museum für naturkunde berlin

Freie Universität Berlin

Leibniz-Gemeinschaft

PROJECTILE–TARGET INTERACTION *and* RAPID, HIGH-TEMPERATURE GEOCHEMICAL PROCESSES *in* IMPACT MELTS

Dissertation
zur Erlangung des akademischen Grades eines
Doktor der Naturwissenschaften
(Dr. rer. nat.)

Vorgelegt von
Christopher Hamann

Eingereicht im Fachbereich Geowissenschaften
der Freien Universität Berlin

Berlin, November 2017

Erster Gutachter
Prof. Dr. Kai Wünnemann
Institut für Geologische
Wissenschaften
Freie Universität Berlin
Malteserstraße 74–100
12249 Berlin, Germany

Zweiter Gutachter und Betreuer
PD Dr. Lutz Hecht
Museum für Naturkunde
Leibniz-Institut für Evoutions-
und Biodiversitätsforschung
Invalidenstraße 43
10115 Berlin, Germany

Dritter Gutachter
Prof. Dr. Alexander Deutsch
Institut für Planetologie
Westfälische Wilhelms-
Universität Münster
Wilhelm-Klemm-Straße 10
48149 Münster, Germany

Tag der Disputation: 19. Februar 2018

Projectile–target interaction and rapid,
high-temperature geochemical processes in impact melts
Christopher Hamann

This research was funded by the Deutsche Forschungsgemeinschaft (DFG), grant He-2893/8-2. It was performed at Museum für Naturkunde, Leibniz-Institut für Evolutions- und Biodiversitätsforschung, Berlin, Germany, in the context of the DFG-funded research unit FOR 887 *Multidisciplinary Experimental and Modeling Impact Research Network* (MEMIN).

If we knew what it was we were doing,
it wouldn't be called research, would it?
—Unknown; often attributed to Albert Einstein

Kurzfassung

Die Kollision fester Körper unter kosmischen Geschwindigkeiten resultiert in einer Vielzahl an physikalischen, morphologischen, und mineralogisch–petrologischen Charakteristika, die in der Natur nur durch Impaktprozesse hervorgerufen werden können. Unter diesen Charakteristika fällt das Aufschmelzen des Projektils und wesentlicher Anteile des Zielgesteins. Die daraus resultierenden *Impaktschmelzen* sind typischerweise Mischungen verschiedener Schmelzen, die verschiedenen Lithologien entstammen, welche sich während der Kraterbildung an verschiedenen stratigraphischen Positionen innerhalb der Schmelzzone des Kraters befinden. In kleinen Kratern können zudem Schmelzen aus Projektilmaterial einen wesentlichen Anteil an dem resultierenden Gesamt-Schmelzvolumen beitragen. All diese verschiedenen Schmelzen werden während der Kraterbildung mechanisch miteinander vermischt, wobei Schmelzen in Kontakt gebracht werden können, die möglicherweise deutlich verschiedene physikalische und chemische Eigenschaften (z.B. chemische Zusammensetzung, Struktur, Dichte, Temperatur etc.) haben, die weitestgehend die Eigenschaften des jeweiligen Gesteins, aus dem sie entstanden sind, reflektieren. Zahlreiche Details bezüglich Genese und Mischung von Impaktschmelzen sind bisher jedoch kaum bekannt. Im Speziellen sind Mischungsprozesse zwischen Impaktschmelzen mit stark verschiedener chemischer Zusammensetzung und Struktur, insbesondere während frühen Phasen der Kraterbildung an der Grenzfläche zwischen Projektil und Zielgestein, sowie nachfolgende chemische und gesteinsbildende Prozesse in Impaktschmelzen während Abkühlung und Ablagerung dieser Schmelzmischungen weitestgehend unverstanden. In der vorliegenden Arbeit werden diese Prozesse sowohl in der Natur als auch im Experiment untersucht und es wird eine bislang einzigartige Kombination aus Einsichten von petrologischen Studien an unverwitterten natürlichen Impaktgläsern und Impaktschmelzgesteinen und Einsichten aus maßgeschneiderten Laserexperimenten und Hochgeschwindigkeits-Impaktexperimenten präsentiert.

Teil II dieser Arbeit befasst sich mit einer In-situ-Rekonstruktion der Grenzfläche zwischen Projektil und Zielgestein in einer Serie von Hochgeschwindigkeits-Impaktexperimenten. Die Versuchsbedingungen (6 km s^{-1} Einschlaggeschwindigkeit, Quarzsand-Ziele mit 42% Porosität, Aluminium-Projektile mit 6 mm Durchmesser) entsprachen weitestgehend den Bedingungen während häufig auftretender Einschläge von (metallischen) Mikrometeoroiden in regolith-bedeckte Oberflächen von Asteroiden im Asteroidengürtel; ein repräsentatives Experiment wurde zudem in einem numerischen Modell simuliert. Es konnte gezeigt werden, dass unter diesen Versuchsbedingungen substantielle Mengen an Projektilschmelze

in Form eines kontinuierlichen Schmelzüberzugs in den resultierenden Impaktkratern zurückbleiben. Zudem wurden heterogene, von Projektilschmelze überzogene Schmelzpartikel mit lagigem Aufbau in den Kratern gefunden und es wurde gezeigt, dass die einzelnen Lagen dieser Schmelzpartikel bestimmten Schockintensitäten (d.h. Spitzendrücken und Post-Schock-Temperaturen) entsprechen, die vom überschreiten des Hugoniot-elastischen Limits in distalen Bereichen bis hin zum vollständigem Schmelzen in proximalen Bereichen der Schmelzpartikel reichen (Kapitel 5). Basierend auf einem Vergleich zwischen numerischem Modell und petrologischen Beobachtungen wurde geschlussfolgert, dass diese Schmelzpartikel weitestgehend den Untergrund des transienten Kraters während frühen Phasen der Kraterbildung (bevor der transiente Krater sein größtes Volumen erreicht; Kapitel 6) abbilden und so die ursprüngliche Grenzschicht zwischen Projektil und Zielgestein konservieren. Anhand petrologischer Beobachtungen wurden mehrere Prozesse an dieser Grenzschicht rekonstruiert: (1) physische Vermischung und Emulgierung von (weitestgehend nicht-mischbarer) Projektilschmelze mit volumetrisch-dominierenden Zielgesteinsschmelzen, (2) Elementaustausch and Redoxreaktionen zwischen diesen beiden Schmelzen, sowie (3) Erzeugung von neuen Schmelzgemischen durch chemische Interaktion dieser beider Schmelzen. Diese Resultate implizieren, dass typische Einschläge von millimeter-großen, metallischen Projektilen auf regolithbedeckte Asteroiden im Asteroidengürtel ähnliche, von Projektilschmelzen überzogene Schmelzpartikeln produzieren und dass solche Oberflächen erhebliche Mengen an fremdartigen (d.h. nicht-endogenem) Material akkumulieren. Sollten solche Schmelzpartikel auf der Asteroidenoberfläche zurückbleiben, ist es wahrscheinlich, dass die nicht-endogene Projektilkomponente einen möglicherweise bedeutenden Anteil an spektralen Daten einnimmt, die von solchen Oberflächen gesammelt werden.

Kapitel 7 in Teil III präsentiert einen neuen experimentellen Ansatz, der es möglich macht, quasi-instantan Schmelzen und Plasmen von natürlichen planetaren Gesteinen auf makroskopischen Skalen durch direkte Laserbestrahlung im Dauerstrichbetrieb zu erzeugen. Es wurde gezeigt, dass diese Experimente Druck- und Temperaturbedingungen während Post-Schock-Phasen von Impaktereignissen mit Einschlaggeschwindigkeiten im Bereich von ca. 4 bis 20 km s^{-1} simulieren und dass die resultierenden experimentellen Produkte (Silikatgläser) thermodynamisch und petrologisch echten Impaktschmelzen (abgeschreckt zu Impaktgläsern) entsprechen, die unter diesen Einschlaggeschwindigkeiten von gleichen Ursprungsmaterialien gebildet wurden. Dies wird erreicht, indem der temperaturbedingte Entropiegewinn der lasererzeugten Schmelze auf den Entropiegewinn abgestimmt wird, der mit dem (theoretischen) thermodynamischen Zustand desselben Materials während bzw. nach eines Impaktereignisses einer bestimmten Einschlaggeschwindigkeit einhergeht. Auf diese Weise werden makroskopische Schmelzvolumina produziert, die sowohl thermodynamisch, als auch petrologisch echten Impaktschmelzen entsprechen, die bei dieser spezifischen Einschlaggeschwindigkeit

erzeugt werden. Darüber hinaus wurden Temperaturkurven bzw. Abkühlraten von Schmelzvolumina, die während der Experimente erzeugt und teilweise aus den Bestrahlungszonen ausgeworfen wurden, mittels eines Infrarot-Mikrobolometers gemessen. Diese Daten wurden genutzt, um Temperaturkurven bzw. Abkühlraten von während der Kraterbildung ballistisch-ejektierten Schmelzen (z.B. Schmelzkügelchen, Tektite etc.) ähnlichen Volumens und chemischer Zusammensetzung näherungsweise zu bestimmen.

Der Rest von Teil III befasst sich mit petrogenetischen Prozessen in Impaktschmelzen, die bislang wenig untersucht (Entmischung von Impaktschmelzen) oder äußerst kontrovers diskutiert (Schicksal von Karbonaten während Impaktprozessen) wurden. In den Kapiteln 8 und 9 wurde das thermodynamisch-bedingte Entmischen von Silikat-Impaktschmelzen unterschiedlichster chemischer Zusammensetzung und Abkühlhistorien untersucht – diese beiden Kapitel stellen die erste umfassende Studie von Schmelzentmischungsprozessen in Impaktschmelzen und den ersten eindeutigen Nachweis von Schmelzentmischungsprozessen in Meteoriten dar. Texturelle Anzeichen von Schmelzentmischungsprozessen wurden präsentiert und diskutiert und es wurde gezeigt, dass die chemischen Zusammensetzungen der jeweiligen entmischten Schmelzpaare (Si-reich und Fe-reich) konsistent mit den Hoch- oder Niedrigtemperatur-Mischungslücken im allgemeinen chemischen System Fe_2SiO_4–$KAlSi_3O_8$–SiO_2–CaO–MgO–TiO_2–P_2O_5 sind. Zudem wurde gezeigt, dass Hauptelement-Verteilungskoeffizienten zwischen den beiden Schmelzpaaren mit dem Grad der Polymerisation der Si-reichen Schmelze korreliert. Diese Resultate zeigen, dass sowohl die Verteilung von Hauptelementen zwischen den beiden Schmelzpaaren als auch die resultierenden Emulsionstexturen denen von tholeiitischen Basalten, lunaren Basalten und experimentellen Analogen gleichen. In Impaktschmelzen können jedoch „quasi binäre“ Hochtemperatur-Mischungslücken (z.B. SiO_2–FeO; $T > 1700\,^{\circ}C$) erreicht werden, die aufgrund der hohen Temperatur und chemischen Zusammensetzung irrelevant für endogene Magmen sind. Die Charakteristika von Inhomogenitäten in Impaktschmelzen, die durch Schmelzentmischung in Mischungslücken hervorgerufen werden, wurden dann mit Inhomogenitäten in Impaktschmelzen verglichen, die durch unvollständige Homogenisierung zweier oder mehrerer (mischbarer oder unmischbarer) Impaktschmelzen hervorgerufen werden. Auf Basis dieses Vergleiches wurden petrologische Hilfsmittel entwickelt, die eine Unterscheidung zwischen diesen beiden Varianten erlauben.

Kapitel 10 präsentiert die Resultate von Laserexperimenten, die das Schicksal von in überhitzen Silikatschmelzen (als Analoge zu Silikat-Impaktschmelzen) mitgeführten Karbonaten (Kalzit, Dolomit) beleuchten. Im Unterschied zu vorherigen Impakt- und Stoßwellenrückgewinnungseperimenten, welche zumeist Kalzit- oder Dolomit-Einkristalle als Ziele hatten, wurden geologisch relevante Gemische aus Silikat- und Karbonatgesteinen als Startmaterialien verwendet. Diese Gemische wurden aus verschiedenen Kombinationen aus Sandstein, Basalt, Kalzitmarmor,

Dolomitmarmor, Kalkstein und dem Eisenmeteorit Campo del Cielo hergestellt. Ein wesentliches Resultat dieser Experimente ist, dass die Zersetzung von Karbonaten durch koexistierende Silikatschmelzen extrem schnell (einige zehner Sekunden) und effektiv ist und in Kontamination von Silikatschmelze mit aus dem Karbonat herrührendem CaO (sowie MgO im Falle von Dolomit) sowie Freisetzung von CO_2 an der Grenzfläche zwischen Silikatschmelze und Karbonat resultiert. Es wurde zudem gezeigt, dass mehrere, teilweise transiente Prozesse an dieser Grenzfläche ablaufen, die weitestgehend denen gleichen, die während der Genese von Calciumskarnen ablaufen. Darüber hinaus weisen die experimentellen Produkte hinsichtlich Mikrotexturen, chemischer Zusammensetzung und Mineralogie zahlreiche Gemeinsamkeiten zu Impaktschmelzen aus karbonatführenden Impaktstrukturen (wie z.B. Barringer, Haughton, Chicxulub, oder West Clearwater Lake) auf. Diese Resultate implizieren, dass das „verzögerte" Zersetzen und Entgasen von Karbonaten durch koexistierende Silikat-Impaktschmelzen während/nach der Druckentlastung ein wichtiger und möglicherweise sogar vorherrschender Prozess während der Genese von Impaktschmelzen aus Silikat–Karbonat-Zielgesteinen ist. Eine Kombination aus diesen experimentellen Resultaten, Resultaten aus vorherigen petrologischen Studien und theoretischen Betrachtungen der Phasendiagramme von Kalzit und Quarz implizieren jedoch, dass Karbonat-Impaktschmelzen – wie in verschiedenen vorherigen Studien postuliert – tatsächlich während der Dekompressionsphase aus Silikat–Karbonat-Zielgesteinen gebildet werden können. Es wird in dieser Dissertation jedoch als unwahrscheinlich erachtet, dass solche Karbonatschmelzen Produkt der *Schmelzentmischung* einer homogenen Ausgangsschmelze sind. Vielmehr wir als wahrscheinlich erachtet, dass Silikat–Karbonat-Schmelzemulsionen in Impaktiten durch starke Kontraste hinsichtlich Dichte und Viskosität der Silikat- und Karbonat-Teilschmelzen begründet sind (so wie im Fall der Unmischbarkeit von Metall- und Silikatschmelzen oder Sulfid- und Silikatschmelzen, vgl. Kapitel 8 and 9). Basierend auf einer Reihe an petrologischen und thermodynamischen Argumenten wurde zudem diskutiert, dass die Erhaltung dieser primären Karbonatschmelzen von mehreren komplexen spezifischen Faktoren (z.B. Unterschiede in der Post-Schock-Temperatur der Karbonat- und Silikatschmelzen, CO_2-Partialdruck, finaler lithostatischer Druck, Reaktionskinetik etc.) abhängt, die sich höchstwahrscheinlich von Impaktszenario zu Impaktszenario unterscheiden. Letztendlich wird in einem zusammenfassenden Modell argumentiert, dass Hochgeschwindigkeitseinschläge in Silikat–Karbonat-Zielgesteine sowohl im Schmelzen als auch im Zersetzen von Karbonaten in spezifischen Zonen/Teilen des Kraters resultiert. Dieses Modell vereint und erklärt widersprüchliche petrologische Beobachtungen an Impaktiten von Impaktstrukturen wie Haughton, dem Ries oder Chicxulub und impliziert, dass die impakt-induzierte CO_2-Entgasung karbonatreicher Zielgesteine wärhend Impaktereignissen komplexer als bisher gedacht ist.

Abstract

The collision of solid bodies at cosmic encounter velocities produces a variety of distinct physical, morphological, mineralogical, and petrological characteristics that are unique to hypervelocity impacts. Among these is melting of the projectile and substantial parts of the target it strikes. The resulting *impact melts* are typically intimate mixtures of melts from different precursor lithologies that initially occupied different stratigraphic positions in the crater's melt zone; at small craters, projectile-derived melts may contribute substantially to the resulting melt mixture. These melts are mixed with each other during crater formation, bringing into contact melts that might have quite diverse physicochemical properties (chemical composition, structure, density, temperature, etc.) that reflect the different precursor lithologies from which they formed. However, many details regarding (1) melt-mixing processes during early time-steps of crater formation at the projectile–target interface, (2) the physical and chemical interaction of impact melts of widely diverse composition and structure, and (3) subsequent petrogenetic processes during cooling of such melt mixtures are not well understood. This PhD thesis tries to contribute to our understanding of these processes by presenting a novel and so-far unique combination of petrologic observations on pristine natural impact glasses and impact melt rocks with results from specifically tailored laser irradiation and hypervelocity impact experiments.

Part II of this thesis is concerned with an in situ reconstruction of the interface between projectile and target in impact experiments. The impact conditions (6 km s^{-1} impact velocity, 42%-porous quartz sand targets, 6-mm-diameter aluminum projectiles) resembled impacts of metallic micrometeoroids into regoliths of asteroids in the main belt; one representative experiment was simulated in a numerical model. The major finding of Part II is that, under these impact conditions, substantial amounts of projectile melt remain as a continuous melt coating within the crater, and that projectile-coated, heterogeneous melt particles are produced that have a layered structure manifested in distinct layers of decreasing shock metamorphism (ranging from complete melting to below Hugoniot elastic limit; Chapter 5). These melt particles essentially sample the floor of the transient crater at early time steps of crater formation (before the transient crater reaches its final dimensions; Chapter 6), and, thus, preserve the original interface between projectile and target. Processes along this interface include (1) physical dissemination and emulsification of (largely immiscible) projectile melt within volumetric dominant target melt, (2) element exchange and redox reactions between the two melts, and (3) production of composite melts due to chemical interaction of these two

melts. These findings not only suggest that impacts of millimeter-size, metallic projectiles into asteroidal regoliths at typical impact velocities in the main belt result in qualitatively similar melt particles, but also that such planetary surfaces might accrete considerable amounts of foreign (i.e. non-endogenic) material. If such melt particles are retained within such regoliths, it is likely that their projectile component might influence surface reflectance spectra obtained from such surfaces.

To further explore the chemical interaction between impact melts of diverse composition and structure, Part III is initially concerned with presenting and discussing a novel experimental approach that is capable of quasi-instantaneously producing, on macroscopic (i.e., hand-specimen) scales, melts and vapors from natural planetary materials by means of direct, continuous-wave laser irradiation (Chapter 7). These experiments simulate postshock P–T conditions of hypervelocity impacts in the 4 to 20 km s^{-1} range, and experimental products (silicate glasses) are shown to be petrologically and thermodynamically similar to true impact melts (quenched to impact glasses) formed from similar starting materials. This is achieved by "matching" the entropy gains of the laser-generated melts to the entropy gains associated with the thermodynamic states produced in hypervelocity impacts at specific velocities. Thus, macroscopic volumes of melt can be produced that thermodynamically as well as petrologically resemble true impact melts formed at that specific impact velocity. Moreover, using temperature measurements of melts formed at/ejected from the irradiation zones, cooling rates of ballistic impact-melt ejecta (e.g., melt spherules, tektites, etc.) of similar size and composition are constrained.

The rest of Part III is then concerned with investigating petrogenetic processes in impact melts that are so-far only poorly constrained. Chapters 8 and 9 investigate unmixing of silicate impact melts of diverse chemical composition and cooling history due to *sensu stricto* liquid immiscibility. This represents not only the first comprehensive study of silicate liquid immiscibility in terrestrial impact melts and experimental analogs, but also the first clear evidence of silicate liquid immiscibility in meteorites. Textural evidence of silicate-melt unmixing is presented, and it is shown that the compositions of the conjugate immiscible liquids (Si-rich and Fe-rich) are consistent with phase separation in the high- or low-temperature two-liquid fields in the general chemical system Fe_2SiO_4–$KAlSi_3O_8$–SiO_2–CaO–MgO–TiO_2–P_2O_5. Moreover, major-element partition coefficients are correlated with the degree of polymerization (NBO/T) of the Si-rich melt. Hence, major-element partitioning between the conjugate liquids as well as the resulting emulsion textures are similar to those known from tholeiitic basalts, lunar basalts, and experimental analogs. However, in impact melts, the high-temperature, "quasi-binary" miscibility gaps (e.g., SiO_2–FeO; $T > 1700\,^{\circ}C$) might be encountered that are inaccessible to endogenous magmatic systems. The characteristics of impact melt inhomogeneity produced by melt unmixing in a miscibility gap (liquid immiscibility *sensu stricto)* are then compared to impact melt inhomogeneity

caused by incomplete homogenization of different (miscible or immiscible) impact melts, and petrographic tools are presented to distinguish between these two.

Chapter 10 presents results from laser irradiation experiments aimed at constraining the fate of carbonates (calcite, dolomite) entrained in superheated silicate melts taken as impact-melt analogs. In contrast to previous impact and shock-reverberation experiments that mainly used calcite or dolomite single crystals, mixed silicate–carbonate composite targets that were produced from various combinations of sandstone, basalt, calcite marble, dolomite marble, and limestone were used in these experiments. Carbonate decomposition by coexisting silicate impact melt is shown to be extremely fast (tens of seconds), and results in contamination of silicate melt with carbonate-derived CaO (and MgO in the case of dolomite) and release of CO_2 at the silicate melt–carbonate interface. Several, partially transient processes were shown to occur at this interface that are largely similar to the formation of calcic skarns during contact metamorphism. In addition, the experimental products show many textural, compositional, and mineralogical features of impact melts known from carbonate-bearing terrestrial craters (e.g., Barringer, Haughton, Chicxulub, or West Clearwater Lake). It is suggested that upon pressure release, "protracted" decomposition of carbonates by heat influx from coexisting silicate impact melt is an important, if not dominant process during impact melting of mixed silicate–carbonate targets. However, a combination of these experimental findings, findings from previous studies, and consideration of the phase diagrams of calcite and quartz suggests that, as envisaged by a number of studies, carbonate impact melts are indeed readily produced during adiabatic decompression. It was discussed that these carbonate melts likely do not form by *unmixing* of a single, homogeneous precursor melt (i.e., liquid immiscibility *sensu stricto*). Rather, carbonate–silicate emulsions in impactites are envisaged to form due to the stark contrast in structure and viscosity of the two melts (e.g., as in the case of metal–silicate or sulfide–silicate emulsions; cf. Chapters 8 and 9). It is discussed that preservation of this primary carbonate melt phase must depend on a complex variety of idiosyncratic factors (e.g., differences in postshock temperature between carbonate melt and silicate melt, CO_2 partial pressure, final lithostatic pressure, reaction kinetics, etc.) that likely differ from impact structure to impact structure. Eventually, a working model is presented that suggests that hypervelocity impacts into mixed silicate–carbonate targets may involve both melting *and* decomposition of carbonates in specific parts of an impact crater, thus bringing together seemingly contrasting previous findings from impactites from terrestrial impact structures like Haughton, Ries, or Chicxulub. The working model also suggests that impact-induced CO_2 degassing of carbonate-bearing targets during hypervelocity impact is more complex than previously thought, which has implications for estimating the net amount of CO_2 that is discharged into the atmosphere immediately after such impacts.

Acknowledgments

No one makes it from naive, initial enthusiasm to finished dissertation without the support, ideas, good will, and friendship of numerous people. During my time at the Museum, I was supported not only by my supervisor, but also by a group of senior colleagues with diverse experience, scientific background, and wisdom, as well as by numerous fellow students that made working in this group extremely satisfying and enjoyable.

First and foremost, I am extremely grateful to Lutz Hecht for being my supervisor and for putting his faith in me for the last four years. Lutz, thank you for your ability to create a balance between advisory guidance and "creative chaos" (this surely teaches to stay on one's own feet!); for always having an open door, ear, and mind for questions, issues, and wishes (not only work-related); for allowing me to look left and right and to follow down paths that were not strictly project-related; for your straightforward way of solving problems and your ability to think out of the box; and simply for your good mood and friendly nature.

I owe much to Alex Deutsch, my co-supervisor, who inspired me from the very beginning of my time in the MEMIN group. Alex, thank you for your ability to talk straight; for inspiring me to challenge and reconsider my own views and results; for your enormous support during the last four years; for your useful suggestions and constructive comments; and for inviting me to Münster.

Thanks are also due to Kai Wünnemann, who—although encumbered with a heavy work load—agreed to review my thesis on very short notice.

Uwe Reimold, in his function as Head of Department, constantly supported me. Shamelessly often did I knock at his door and asked for additional funding or problem-solving, and he always delivered. By internally reviewing most of my manuscripts before submission (mostly on very short notice), Uwe also taught me an eye for details. Uwe, thanks a lot for all the help!

The impact group at the Museum is a motley crew of people with diverse scientific backgrounds, languages, and perceptions. I very much enjoyed the multidisciplinary nature of this group, and bounced many crazy-sounding ideas off Kai Wünnemann and also Natasha Artemieva (one of those ideas is presented in Chapter 6). Kai and Natasha, thank you for all those discussions; for your hospitality and caring; for your raw mental horsepower; and for all the support and good will. It was mainly the two of you who inspired me to think of the impact community as some kind of big family.

Dieter Stöffler wrote landmark papers on impact cratering and meteoritics way before I was born. During the last two years I not only had the

privilege to collaborate with him, but also to tap his enormous amount of wisdom and experience. Dieter, thanks for having faith in me; for the unique experience of assembling a review paper; and, of course, for the nice evening at the Fischerhütte.

There are a number of other people who stepped in at one time or another. Ansgar Greshake always had an open ear for me when I wanted to know something about meteorites, and eventually loaned to me some of his specimens for future plans. Richard Wirth transformed from a teacher to a collaborator and generously allocated TEM-time and supervision. I had a great time with Agnese Fazio and Luigi Folco, who graciously offered to collaborate rather than to compete, and I also enjoyed working with Nadia Van Roosbroek, Lidia Pittarello, and Sean McKibbin. Thanks are also due to Jens Osterholz, Sebastian Schäffer, Dominic Heunoske, and Bernd Lexow at Fraunhofer EMI, who made the laser experiments and, thus, substantial parts of this thesis possible. I am also grateful to my fellow MEMIN colleagues, especially Matthias Ebert, Jakob Wilk, Michael Poelchau, Rebecca Winkler, Thomas Kenkmann, Christoph Michalski, Falko Langenhorst, and Manuel Raith for making the MEMIN experience so awesome. Fred Hörz knows how to write—although we only briefly met in person, I returned to his writing over and over again for inspiration.

A big thank you! is also due to all fellow students and colleagues at the Museum, who made the past years so enjoyable: Robert Luther, Felix Kaufmann, Sanni Siegert, Lukas Manske, Tomke Fröchtenicht, Saskia Bläsing, Elena Martellato, Tanja Mohr-Westheide, Nicole Güldemeister, Astrid Kowitz, Meng-Hua Zhu, Ulli Raschke, Patrice Zaag, Jessica Ecke, Nora Lentge-Maaß, Linus Günther, Sandra Triepel, Melanie Tietje, Michael Bierhaus, Dirk Elbeshausen, Jörg Fritz, Kamila Kotlicki, Kirsten Born, Peter Czaja, Hans-Rudolf Knöfler, Ralf-Thomas Schmitt, Kathrin Krahn, Friederike Schwarz, Rita Schmidt, and many more.

However, none of this would have been possible without the constant support of my family, nor without the love and help of Sylvia. I love you all.

Contents

II Reconstructing the projectile–target interface

III Geochemical processes in impact melts

Part I

Introduction

Chapter 1

The significance of impact cratering

THE HISTORY OF SCIENCE is littered with the remains of cast-off but initially compelling concepts, each of which, at the time of its emergence, soon captured the perception of contemporary scientists. One of those concepts is that the lunar craters (Fig. 1.1a), discovered by Galileo Galilei in the early seventeenth century, are giant volcanoes. This view prevailed until as recently as the 1960s, when planetary exploration, starting with the space programs initiated by the USA and the USSR, and continued geologic research on several terrestrial impact craters (Fig. 1.1b; e.g., Chao et al., 1962; Shoemaker, 1963) gradually put impact cratering into perspective. Today, impact cratering at various scales is recognized as one of the most dominant geological process in the solar system, especially on geologically inactive planetary bodies. It shapes, alters, and scars the surfaces of virtually all solid bodies in the solar system, in particular of those that lack an atmosphere (e.g., the Moon: Fig. 1.1a; or the dwarf planet Ceres: Fig. 1.1c).

"In the minds of many geologists, impact cratering has risen from complete obscurity to become one of the *most fundamental* geologic processes."

—H. Jay Melosh, 1989, *Impact Cratering*, p. iii, Oxford University Press

During the early evolution of the geologically active planetary bodies, impact processes certainly prevailed over endogenic geologic processes. Collisions among differently sized objects—ranging from tiny dust particles to planetesimals of several hundred kilometers diameter—ultimately led to the accretion of planets and moons in the early solar system (e.g., Kokubo and Ida, 2000; Bottke et al., 2006; Raymond et al., 2009, and references therein). After being accreted, some of the early planetesimals experienced continuous and often fatal bombardment by other planetary objects. The Moon, for instance, formed by the impact of a Mars-sized object onto the proto-Earth about 4.5 billion years ago (e.g., Canup and Asphaug, 2001), and the asteroid belt, a cradle of leftover debris located between Mars and Jupiter that might cross Earth's orbit, immediately attests to the violent collision history of the early solar system.

Relics of past and more recent collisions occasionally find their way to Earth's surface in the form of *meteorites*. Among meteorites, pallasites[1] are traditionally believed to represent the boundaries between metallic cores and silicate mantles of already differentiated planetesimals that were shattered through impacts (e.g., Wasson and Choi, 2003). Iron meteorites, consequently, represent remnants of the metallic cores of such

[1] *Pallasites* are a class of stony–iron meteorites that consist of centimeter-size olivine crystals set in FeNi matrix

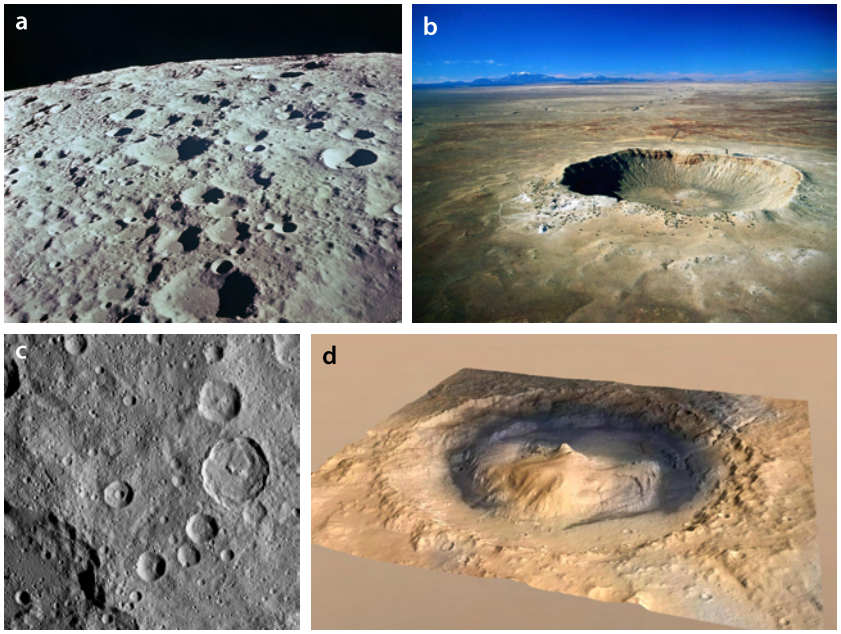

Figure 1.1 Typical examples of impact craters in the solar system. **a** Impact craters on the back side of the Moon, photographed from the lunar orbit during the Apollo 11 mission. Source: NASA. **b** Meteor Crater in Arizona, USA (1.2 km diameter). This simple, bowl-shaped crater was formed some 50 thousand years ago by the impact of an iron meteorite onto sedimentary target rocks (mainly carbonates and sandstones) and is the first recognized and probably best-studied impact crater on Earth. Source: www.meteorcrater.com. **c** Cratered area on the surface of Ceres, photographed from NASA's *Dawn* spacecraft in orbit around the dwarf planet. Source: NASA. **d** Vertically exaggerated, false-color oblique view of Gale Crater on Mars (154 km diameter). Gale Crater was the target of the rover *Curiosity*, which was part of NASA's Mars Science Laboratory mission. Source: NASA/JPL/ESA/DLR/FU Berlin.

differentiated planetesimals (e.g., Goldstein, 1967; Buchwald, 1975; Choi et al., 1995; Benedix et al., 2000), whereas achondrites[2] sample the already differentiated crusts of several meteorite parent bodies. For instance, the howardite–eucrite–diogenite suite of achondrites is believed to originate from the silicate crust of a differentiated meteorite parent body—most likely the asteroid 4 Vesta—that experienced igneous processes not much different from those occurring in Earth's crust and mantle (e.g., McSween et al., 2011).

[2] *Achondrites* are stony meteorites that do not contain chondrules and that consist of material quite similar to terrestrial volcanic or plutonic rocks

After a period of presumably increased impact activity during the so-called Late Heavy Bombardment, thought to occur between 4.1 and 3.8 billion years ago (e.g., Tera et al., 1974; Cohen et al., 2000; Marchi et al., 2013, although this concept is heavily debated; see, e.g., Hartmann, 2003; Boehnke and Harrison, 2016, and references therein), the impact rate has been roughly constant for the last 3.5 billion years (e.g., Neukum et al., 2001). On geologically inactive planetary bodies such as the Moon (Fig. 1.1a) or Ceres (Fig. 1.1c), impact craters have accumulated over geologic times. They are often the dominant surface feature on such bodies, as the only process that may eradicate existing impact structures are additional impacts. Such ancient, heavily cratered planetary surfaces attest

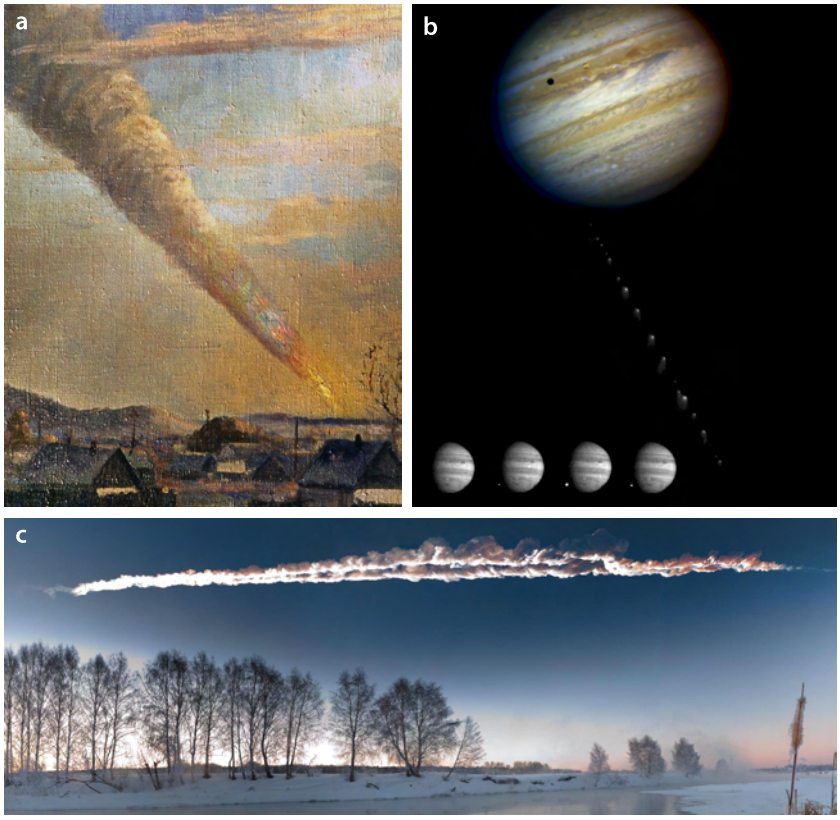

Figure 1.2 Three examples of observed impact events. **a** 1947 painting by P. J. Medvedev, illustrating the impact of the Sikhote-Alin IIAB iron meteorite. Source: www.meteoritegallery.com. **b** Composite Hubble Space Telescope image depicting comet Shoemaker-Levy 9 approaching Jupiter in 1994. The inset shows the night-side impact of fragment W into Jupiter, photographed from NASA's *Galileo* spacecraft. Source: NASA/ESA. **c** The Chelyabinsk meteor streaking through the air over Chelyabinsk, Russia, in 2013. Copyright: M. Ahmetvaleev.

to the frequency of impact processes, and impacts are still observed in present times. For instance, the 1947 impact of the Sikhote-Alin IIAB iron meteorite into Russia was observed by local inhabitants. The event was even painted by one of the witnesses (see Fig. 1.2a), attesting to the impressive nature of the event. Two more recent examples of observed impact events that made it into mainstream media are the 1994 impact of comet Shoemaker-Levy 9 into Jupiter (Fig. 1.2b) and the 2013 Chelyabinsk air burst over Russia (Fig. 1.2c).

Most practical applications of impact cratering are, however, of scientific or economic rather than public interest. For example, in planetary sciences, dating of planetary surfaces is based on the *size–frequency distribution* of impact craters. The size–frequency distribution can be determined by space-borne remote-sensing techniques, that is, by photographing the surface of a given object with sufficient resolution. Assuming that impact craters accumulate at some constant rate, "crater counting" can be used to determine the time span a given surface was exposed to repetitive impacts, which then results in an age estimate (Hartmann, 1966; Neukum, 1983;

Neukum and Ivanov, 1994; Neukum et al., 2001; Hiesinger and Head, 2006; Hiesinger et al., 2012). In analogy to the geologic time scale on Earth, prominent impact events are also used to establish time scales on other planetary bodies (e.g., the Nectarian, Imbrian, Copernican, etc. periods on the Moon; Neukum, 1983; Neukum and Ivanov, 1994; Stöffler and Ryder, 2001; Stöffler et al., 2006). On Mars, impact structures such as Gale Crater (Fig. 1.1d) have been used to determine the Martian paleoclimate (e.g., Miliken et al., 2010). Furthermore, large impact basins have been used to determine the composition and rheological properties of the Martian crust and mantle (e.g., Michalski and Niles, 2010). Some of the largest terrestrial impact structures are also of economic interest: for instance, Sudbury, Canada, hosts one of the world's largest deposits of nickel and copper (e.g., Farrow and Watkinson, 1997), whereas Popigai, Russia, is known for its impact-induced diamond reservoirs (e.g., Masaitis, 1998). In analogy to these examples, future economic interest could possibly focus on similar impact structures on Moon or Mars.

Apart from these practical applications, impact events pose inherent danger to life on Earth. At least one of the five biggest mass extinction events has been proven to be caused by the impact of a large, ca. 10-km-diameter asteroid (Alvarez et al., 1980; Pierazzo and Melosh, 1999) into the Yucatán peninsula in Mexico. The event occurred some 66 million years ago and marked the Cretaceous–Paleogene (K–Pg) boundary and the demise of dinosaurs (Alvarez et al., 1980; Hildebrand et al., 1991; Smit, 1999; Schulte et al., 2010). The resulting Chicxulub crater of some 180–200 km diameter (Pilkington et al., 1994; Collins et al., 2002; Morgan et al., 2016) formed in volatile-bearing sedimentary rocks (carbonates and evaporates), and material associated with the impact was deposited globally in a so-called ejecta layer that contains chemical traces (e.g., iridium) of the impacting asteroid as well as shocked minerals of the target (Alvarez et al., 1980; Smit, 1999). Although the exact mechanism that caused the K–Pg mass extinction is still debated (e.g., Brugger et al., 2017), the most likely scenario is that the impact induced devolatilization of the sedimentary target and released into the atmosphere massive amounts of climatically active chemical species like carbon dioxide, sulfur-bearing gases (SO_2 and SO_3), water vapor, and other aerosols that caused short- and long-term climate changes (e.g., Pierazzo et al., 1998; Pierazzo et al., 2003; Brugger et al., 2017).

More recent impact events were certainly witnessed by *Homo sapiens*: two of the younger impact events in Earth's history are the one that created the 1.2-km-diameter Meteor Crater[3] in Arizona, occurring some 50 thousand years ago (Nishiizumi et al., 1991; Phillips et al., 1991), and the one that created the 100-m-diameter Wabar craters, Saudi Arabia, occurring some 300 years ago (Prescott et al., 2004). The Meteor Crater event may have had lethal effects up to distances of ~24 km from the center of the crater (Kring, 1997), and, if present, likely affected local settlements. Although occurring in a remote area, the Wabar event was potentially witnessed by inhabitants in Yemen: two historical poems, written around

[3] Throughout this thesis, *Meteor Crater* will be used synonymous with *Barringer Meteorite Crater* or simply *Barringer crater*; see Kring (2007)

1704, report of a "wind blown forth with fire" (Basurah, 2003) and might relate to the Wabar event. Slightly more than a century ago, the 1908 Tunguska air burst devastated some 300 km^2 of Siberian forest (Chyba et al., 1993). The most recent event, however, was the 2013 Chelyabinsk air burst (Fig. 1.2c; e.g., Brown et al., 2013) that illustrated the potential danger resulting from atmospheric disruptions of small asteroids. At much smaller scale, continuous impacts of micrometeoroids and man-made orbital debris pose a significant threat to spacecraft personnel and equipment (e.g., Thoma et al., 2004; Christiansen, 2003), as impressively illustrated by impact-damaged spacecraft parts on display in the "Astronaut Gallery" at NASA's Johnson Space Center in Houston, Texas.

Chicxulub-size impact events, or larger ones, may also influence the habitability of planets and the prosperity of potential ecosystems. For instance, repetitive impacts of comets and carbonaceous chondrites might have delivered water (e.g., Dauphas, 2003; Morbidelli et al., 2000) and possibly even simple, pre-biotic organic molecules ("abiogenesis"; e.g., Anders et al., 1973; Chyba and Sagan, 1992) to planetary surfaces. Hence, life in the form of certain microorganisms, so-called extremophiles, is possibly distributed throughout the universe by material that is ejected into space after collisions between planetary objects that may harbor life ("panspermia hypothesis"; e.g., Stöffler and Grieve, 2007; Horneck et al., 2008). Large, Chicxulub-scale impact events have, however, the inherent potential to erode existing planetary atmospheres (e.g., Vickery and Melosh, 1990; Shuvalov, 2009), disturb convective fluxes in planetary mantles (e.g., Reese et al., 2004; Watters et al., 2009; Marchi et al., 2014), or even influence the magnetic field of planets (e.g., Williams and Nimmo, 2004; Reese and Solomatov, 2010). Thus, although planetary impact events may distribute life among planetary surfaces, they may also negatively influence their habitability.

These thoughts collectively demonstrate the significance and complexity of this violent, highly dynamic, extensive, and, not least, fascinating process. Excellent introductory chapters on impact cratering are given in the textbooks of Roddy et al. (1977), Melosh (1989), French (1998), as well as Osinski and Pierazzo (2012). A brief introduction to the impact cratering process and the main research topic of this thesis is given in Chapter 2.

Chapter 2

The impact cratering process

Hypervelocity impacts onto planetary surfaces typically involve impact velocities of a few kilometers per second (e.g., in the asteroid belt) to tens of kilometers per second (e.g., in the Earth–Moon system) and impactor diameters of less than a millimeter (impacts of micrometeoroids) to several hundred kilometers (giant impacts of planetesimals during the early evolution of the solar system). Typical *average* impact velocities vary depending on the position in the solar system: they can be as low as ~5 km s^{-1} in the asteroid belt (e.g., Bottke et al., 1994) and increase to some 15–25 km s^{-1} for the Earth–Moon system (e.g., Chyba et al., 1994; Oberst et al., 2012).

Starting with the initial contact between projectile and target, a rapid but orderly sequence of events occurs in continuous fashion that ends when a crater is fully excavated and ejected debris experiences final motions at the surface of the target (Melosh, 1989). In order to make this highly dynamic process more comprehensible to the human mind, impact cratering is commonly divided into three stages that are based on the most dominant physical phenomena at a given time (e.g., Melosh, 1989; French, 1998). The three stages are: *contact and compression*, *excavation*, and *modification*. In reality, however, these stages continuously grade into another, thus rendering an artificial division into arbitrary stages as well as the exact definition of beginning and end of each stage somewhat pointless.

2.1 Contact and compression

The first stage of impact cratering begins when the projectile contacts the target's surface (Figs. 2.1a and 2.2a). Upon contact, the projectile penetrates the target (Fig. 2.1b), thereby compressing it and accelerating it to a certain fraction of the projectile's initial impact velocity. As the projectile penetrates the target, the resistance of the target to compression gradually decelerates the projectile, which will usually penetrate the target to a depth of about one or two projectile diameters.[4]

[4] This is nicely illustrated in Fig. 2.1

At the point of impact, the kinetic energy of the projectile is released in the form of a *shock wave* that travels through both the projectile and the

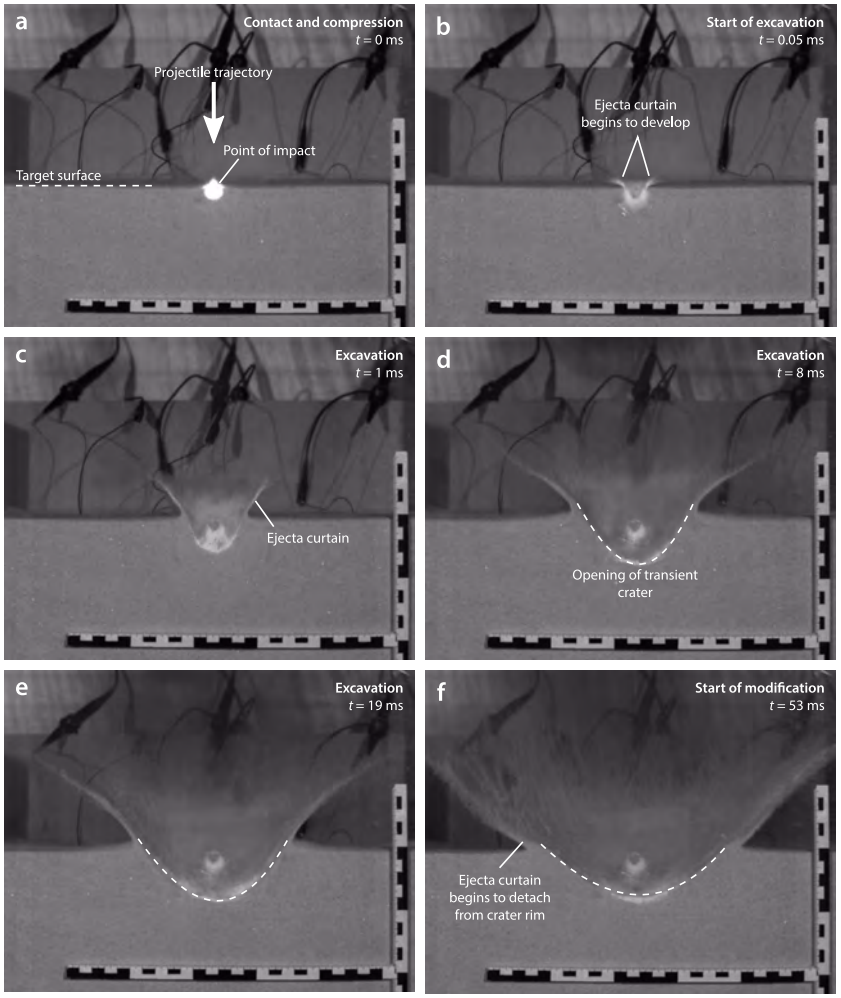

Figure 2.1 Series of video snapshots showing the formation of a small-scale impact crater in sand (video courtesy of Werner Mehl and Kai Wünnemann). In the experiment, a spherical Lexan projectile with a diameter of 6.35 mm and a mass of 2 g was shot at roughly 1.1 km s^{-1} into quartz sand. Although a genuine impact crater formed, the resulting peak shock pressure was insufficient to induce melting or even vaporization. **a** Contact and compression; note that the initial contact between projectile and target is set to $t = 0$ ms. **b** End of contact and compression and beginning of excavation. **c–e** Excavation; note that the depth–diameter ratio of the transient crater changes with time (the transient crater progressively becomes shallower and wider). **f** Modification; note that the angle of the ejecta curtain becomes shallower with time and the crater has developed into a bowl-shaped form.

target (Fig. 2.3; Roddy et al., 1977; Kieffer and Simonds, 1980; Melosh, 1989; O'Keefe and Ahrens, 1993). Contrary to seismic waves, the shock wave travels at velocities much greater than the speed of sound of the projectile and target materials (Zel'dovich and Raizer, 1967; Melosh, 1989; O'Keefe and Ahrens, 1993). Thus, its passage will induce a variety of *irreversible* mechanical effects and physical changes like deformation, solid-state phase transformations, melting, or vaporization in the materials (e.g., Ahrens and O'Keefe, 1972; Stöffler, 1974; Melosh, 1989; Stöffler and Langenhorst, 1994; Pierazzo et al., 1997).

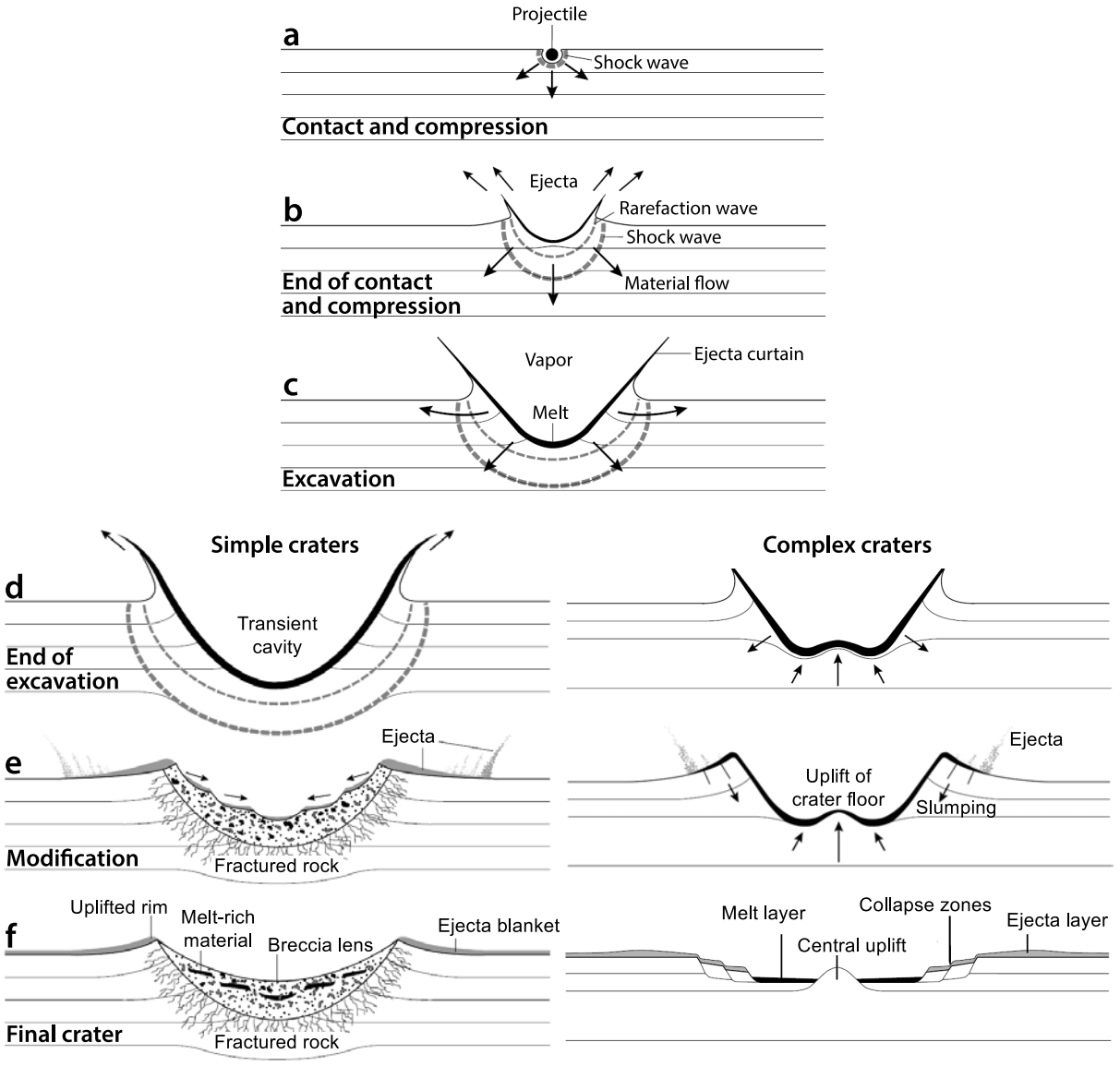

Figure 2.2 Idealized schematic illustration of the different stages of crater formation (modified after French, 1998). The left panel depicts formation of simple craters, the right panel depicts formation of complex craters. Contact and compression as well as excavation are essentially similar for both scenarios, but involve different scales that result in differently sized craters (cf. Fig. 1.1). **a** Contact and compression stage. **b** End of contact and compression stage and beginning of the subsequent excavation stage. **c** Excavation stage; pressure release leads to decompression melting and, if peak shock pressure is high enough, potentially vaporization. Moreover, an ejecta curtain starts to develop that deposits material onto the target's surface. **d** End of excavation stage and start of modification stage. **e** Modification stage. **f** The resulting impact structure.

The shock pressures that are generated in typical impact scenarios can easily reach several hundreds of gigapascals, by far exceeding the yield strength of typical planetary materials such as basalt, FeNi metal, chondrites, anorthosite, or dunite (e.g., Ahrens and O'Keefe, 1972; Melosh, 1989; Pierazzo et al., 1997). The shock pulse duration, that is, the "thickness" of the shock wave, is governed by the diameter of the projectile, and pressure release is initiated as the shock wave reaches the free surface at

the rear of the projectile. Here, the shock wave is reflected in the form of a *rarefaction wave* that follows after passage of the shock wave and that unloads the material from high shock pressures (illustrated in Fig. 2.2b; see Melosh, 1989; O'Keefe and Ahrens, 1993). However, a certain fraction of the energy required to initially compress and heat the material (*internal energy*) remains as heat after passage of the rarefaction wave. If the peak shock pressures generated by the impact are high enough, this residual heat induces melting or even vaporization of large amounts of both projectile and target (see Figs. 2.2c and 2.3; Section 2.4; and, e.g., Ahrens and O'Keefe, 1972; Melosh, 1989; Pierazzo et al., 1997).

Contact and compression is the shortest of all three stages. It ends when the projectile has unloaded from high pressures, that is, as soon as the shock wave and the following rarefaction wave have passed the projectile (Melosh, 1989). The duration of this stage is, thus, governed by the size, composition, and velocity of the projectile: for 10 km s^{-1} impact velocity, unloading of typical silicate projectiles (chondrites or achondrites) of 10 m and 1 km diameter takes ca. 10^{-3} s and 10^{-1} s, respectively (French, 1998). Even for very large impactors, the contact and compression stage is over in less than about 1–2 s. In summary, the major process during contact and compression is transfer of kinetic energy from the projectile into the target and generation of strong shock waves that mediate the velocity differences between projectile and target.

2.2 Excavation

The subsequent excavation stage begins immediately after the end of contact and compression (Figs. 2.1, 2.2c, and 2.3). During excavation, the shock wave expands roughly hemispherically through the target and gradually decays as it engulfs (i.e., compresses, accelerates, deforms, heats) more and more material. As a simplified rule of thumb (the so-called Gault-Heitowit model; see Melosh, 1989, chapter 5), peak shock pressure, P, decays as a function of radius, r. In a simple way, shock wave attenuation around the point of impact might be expressed as

$$P \propto r^{-n} \tag{2.1}$$

Field studies (see references in French, 1998, p. 18), laboratory experiments (e.g., Nakazawa et al., 2002), and theoretical models (e.g., Ahrens and O'Keefe, 1977; Kieffer and Simonds, 1980; Melosh, 1989; Melosh et al., 1992) suggest a pressure–distance relation of $P \propto r^{-2}$ to $P \propto r^{-4.5}$.

Although this simple approximation is inferior to more sophisticated numerical models that use accurate equations of state for the materials involved, it is possible on this basis to regard the point of impact as being surrounded by a series of concentric, roughly hemispherical *shock zones* (Fig. 2.3). Each shock zone is distinguished by a certain range of peak shock pressures and, thus, certain *shock-metamorphic effects* produced in the material (these will be briefly introduced in Section 2.5). At the point of impact, extreme peak shock pressures exist that can easily exceed

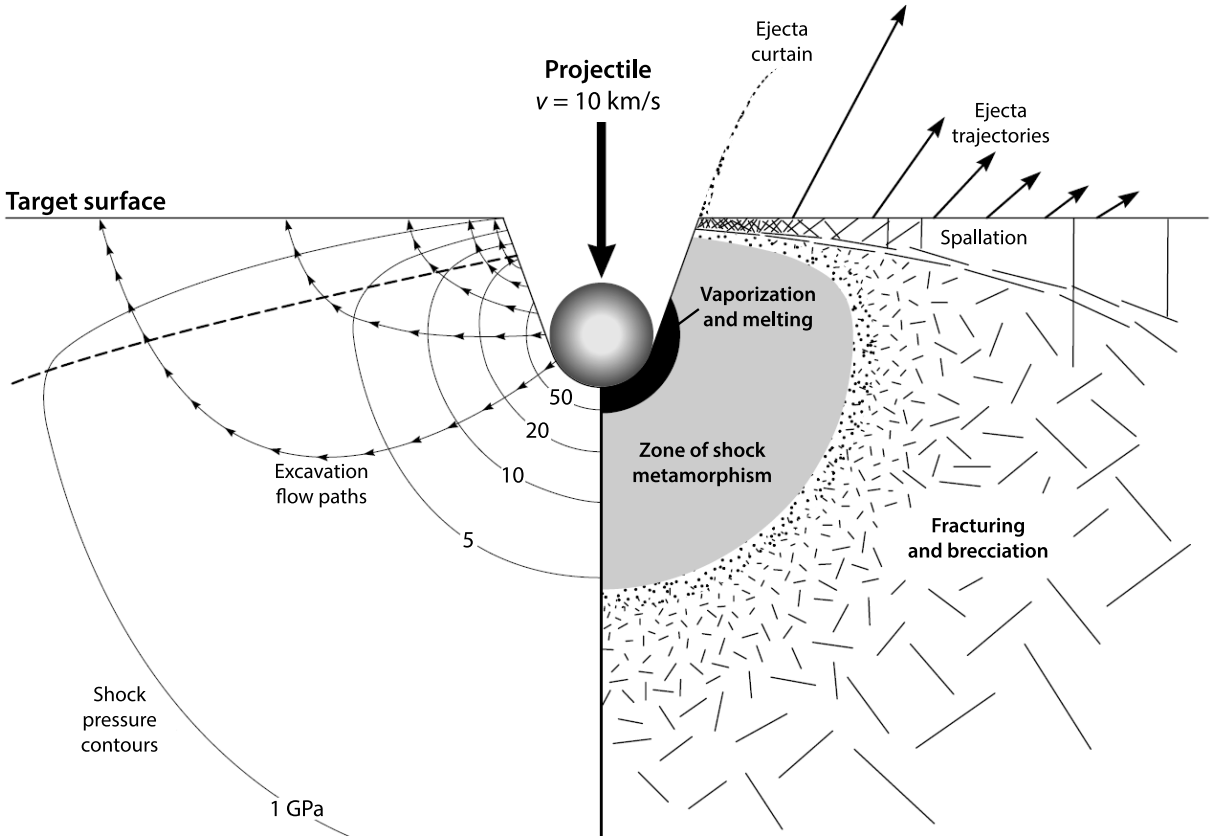

Figure 2.3 Schematic illustration of the contact and compression stage (modified after French, 1998), showing initial shock pressures and excavation trajectories around the impact point in cross section. The point of impact is surrounded by a series of concentric, roughly hemispherical shock zones (**right side**) that correspond to distinct peak shock pressure regimes (**left side**; given in GPa). The projectile, after penetrating the target to about two projectile diameters, is usually completely molten and/or vaporized if impact velocities, and, thus, peak shock pressures are high enough. Shock pressures originating from the point of impact decline rapidly and typically induce the following sequence of effects in the target: (1) melting and vaporization; (2) shock-metamorphic effects and phase transformations; and (3) fracturing and brecciation. The exact shock pressure thresholds for the onset of specific shock effects depend on a variety of factors, the most important ones being the target's porosity (e.g., Wünnemann et al., 2008; Bland et al., 2014; Kowitz et al., 2016) and the target's state variables such as density and preimpact temperature (e.g., Ahrens and O'Keefe, 1972; Melosh, 1989; Pierazzo et al., 1997). The subsequent excavation stage involves: (1) ejection of large, near-surface fragments (spallation) and smaller ejecta (ejecta curtain; right side); and (2) a subsurface flow of target material that forms the transient crater (left side). Close to the target's surface, the shock wave interferes with the free surface, causing upwards deflection of the material trajectories.

100 GPa—after pressure release, these high shock pressures are sufficient to induce complete melting and incipient to even complete vaporization of the projectile and substantial parts of the target (Fig. 2.4). As illustrated by Eq. (2.1), shock pressures drop rapidly with increasing distance from the point of impact. Although the shock wave and, thus, peak shock pressures decay quickly, large volumes of target rock will experience shock pressures of 5–50 GPa. These high shock pressures typically induce a combination of partial melting and solid-state shock-deformation effects and phase transformations in typical planetary rocks (e.g., basalt, chondrites, dunite, anorthosite, "regolith", etc.) and minerals (e.g., olivine, plagioclase, pyroxene, quartz, etc.; see Stöffler et al., 2017). At even greater distances

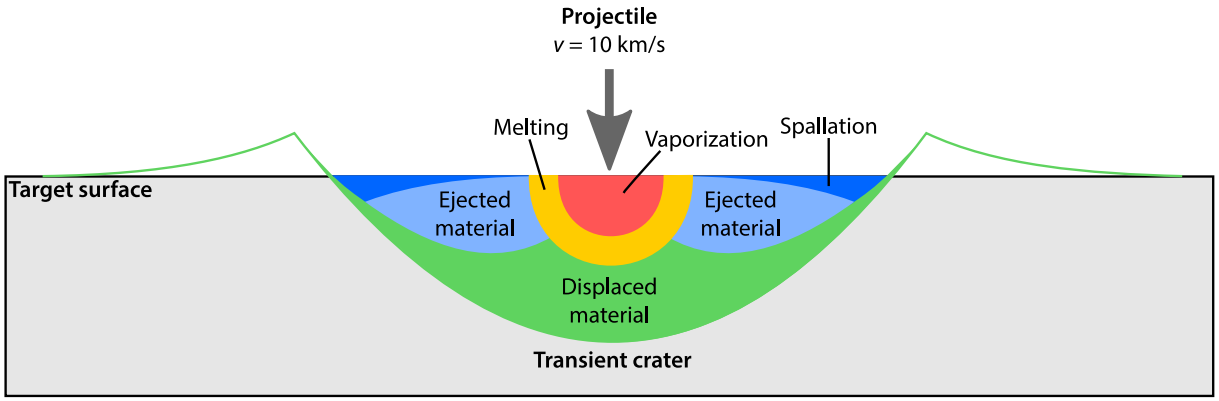

Figure 2.4 Schematic cross section of the transient crater and preimpact locations of displaced/ejected and shock-metamorphosed material (modified after Melosh, 1989). The zone labeled "vaporization" contains a mixture of vaporized projectile and target material that expands upward and outward from the point of impact as a *vapor plume*. The remaining material (including impact melt) is either ejected outward to and also beyond the (transient) crater rim, or is displaced downward and outward along the floor of the transient crater.

from the point of impact, shock pressures drop below 1–2 GPa and the shock wave becomes a regular elastic or seismic wave as its velocity drops to the velocity of sound of the target rock (typically some 5–8 km s^{-1}).

The passages of the shock wave and the following rarefaction wave set material in motion (e.g., Wünnemann et al., 2016) and create a material flow that opens up the transient crater cavity below the target's surface (Figs. 2.1d–f; cf. Fig. 2.4) and that ejects material on upward and outward trajectories above the target's surface (Fig. 2.1d–f; cf. Fig. 2.3). As more and more material is ejected from the opening crater, an *ejecta curtain* (Fig. 2.1) forms that begins to deposit material onto the target's surface around the crater. In contrast to low-velocity, penetration-type craters induced by "slow" projectiles such as gun bullets, the resulting transient crater is many times larger than the projectile. This large ratio of crater diameter to projectile diameter as well as the fact that a supersonic shock wave is induced at the point of impact are two characteristics that set hypervelocity impacts apart from low-velocity, penetration-type impacts (e.g., Melosh, 1989).

The excavation stage lasts many times longer than the contact and compression stage and the major processes are opening of a bowl-shaped transient crater as well as ejection of material from the growing crater. Depending on crater size, the excavation stage requires seconds to minutes for completion, and gravity as well as the target's strength will influence crater growth towards the end of this stage.

2.3 Modification

The modification stage follows after the excavation stage and begins after the crater has been excavated (Fig. 2.2d, e). More precisely, it begins as soon as the transient crater reaches its maximum dimensions (see the time series in Fig. 2.1). Depending on the gravity of the target body (planet,

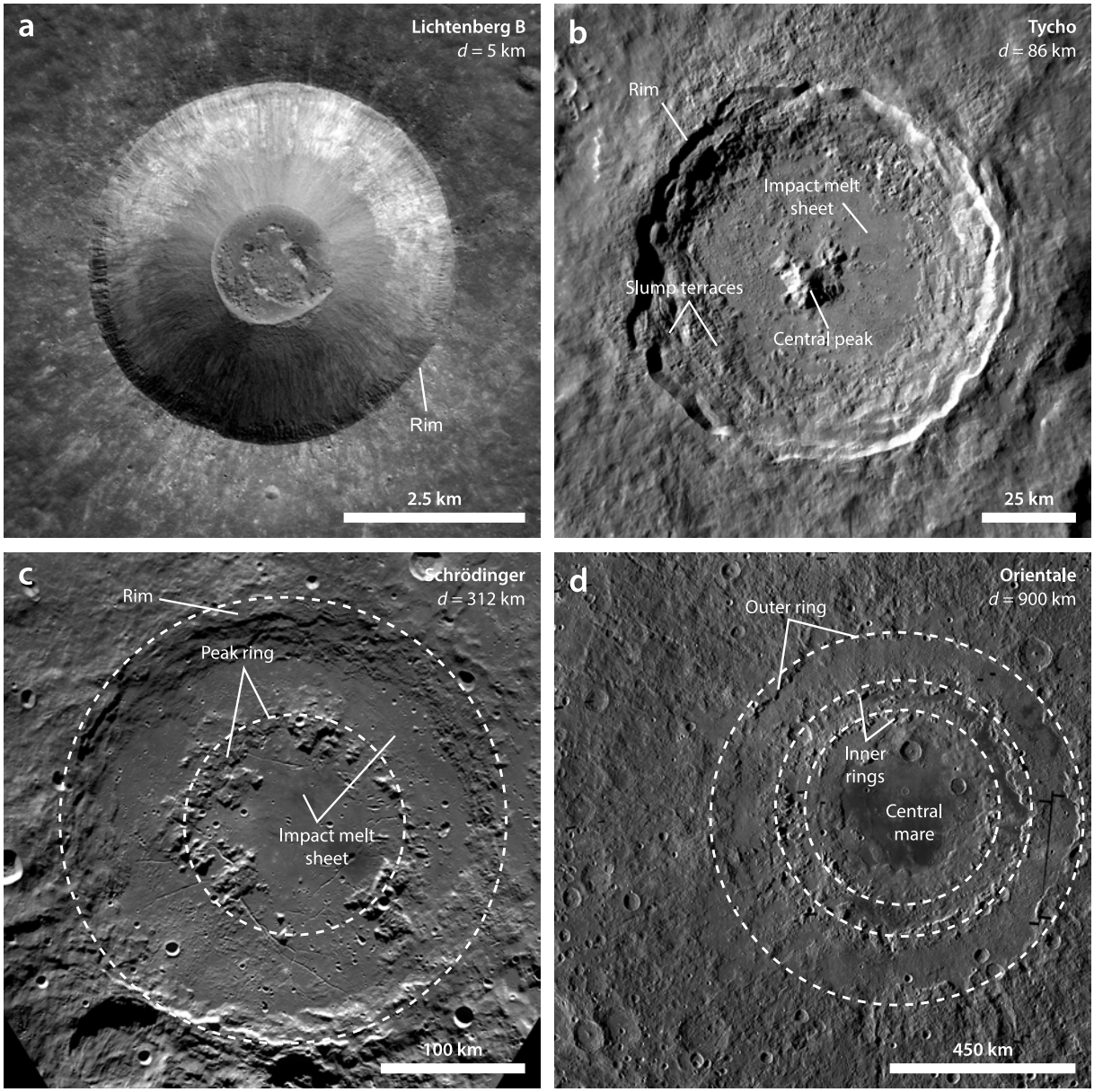

Figure 2.5 Transition from simple to complex impact craters, exemplified by four lunar craters. **a** Lichtenberg B, a simple, bowl-shaped impact crater with a diameter of about 5 km. Source: NASA (mosaic of several *Lunar Reconnaisance Orbiter* images). **b** Tycho, a complex crater featuring a central peak and slumped and terraced walls. Tycho has a diameter of about 86 km. Source: NASA (mosaic of several *Lunar Reconnaisance Orbiter* images). **c** Schrödinger, a peak-ring crater of about 312 km diameter. A well-defined peak ring with a diameter of about half the crater diameter is clearly visible. Note that younger impact craters are superimposed onto Schrödinger (e.g., lower left part of the image) Source: NASA (mosaic of several *Clementine* UVVIS images). **d** Orientale, a multiringed basin of some 900 km diameter with two prominent inner rings. As in the case of Schrödinger, numerous younger impact craters are superimposed onto Orientale (e.g., the complex crater just north of the central mare). Source: NASA (mosaic of several *Lunar Reconnaisance Orbiter* images).

moon, asteroid, etc.) and the diameter of the transient crater, the transient crater that was excavated in the previous stage will collapse under the influence of gravity in more or less spectacular ways. In small, bowl-shaped, so-called *simple craters*, loose debris will slide down the interior crater

walls (see Fig. 2.5a), whereas in large craters, wall terraces, central peaks, flat crater floors (see Fig. 2.5b), or even several inner rings (see Fig. 2.5c, d) will form due to the influence of gravity (for a detailed description of these processes, see, e.g., Melosh, 1989; French, 1998; Osinski and Pierazzo, 2012). Depending on crater morphology, *complex craters* are usually subgrouped into craters with central peaks (Fig. 2.5b), peak-ring craters (Fig. 2.5c) and multiringed basins (Fig. 2.5d).

Whether a simple (left panel of Fig. 2.2) or a complex (right panel of Fig. 2.2) crater forms depends both on the rheological properties of the target (complex craters are formed at smaller diameters in sedimentary targets than in crystalline targets) and the gravity of the target body (transient craters are stabilized to greater sizes with decreasing gravity). On Earth, complex craters generally have diameters greater than some 2–4 km (~2 km for sedimentary targets; ~4 km for crystalline targets), whereas on the Moon, simple craters can have much larger diameters of up to some 15–20 km (e.g., Osinski and Pierazzo, 2012). Hence, the transition from simple to complex craters scales inversely as the gravitational acceleration of the target body on which the craters form (Melosh, 1989). In large craters, two competing processes act during this stage: (1) gravitational collapse of the inner rim, and (2) uplift of the transient crater floor; the latter mechanism may involve fluidization and/or large differential movements of target blocks.

The modification stage is the longest of the three stages. For small, simple craters it might take several minutes to be completed, whereas in the case of large craters (e.g., multiringed basins), this stage can last over geologic time scales and may include long-term effects like isostatic rebound or postimpact volcanism.

2.4 Impact melting and vaporization

A unique feature of hypervelocity impacts is the formation of impact melts and, if peak shock pressures are sufficiently high, of vapor plumes. In general, impact melts are *decompression melts* that form when shock-compressed materials unload after the passage of the rarefaction wave (see Sections 2.1 and 2.2). Thus, impact melting is unlike thermal melting: it is mainly a function of peak shock pressure and the compressibility of the target (Melosh, 1989). Under shock compression, the internal energy of projectile and target is increased as considerable pressure–volume work is done onto the materials (e.g., Melosh, 1989; Pierazzo et al., 1997, and references therein). As discussed in Sections 2.1 and 2.2, release from the shocked state is by rarefaction waves, and decompression occurs via *release adiabats* (Fig. 2.6; see, e.g., Zel'dovich and Raizer, 1967; Ahrens and O'Keefe, 1972; Melosh, 1989; Pierazzo et al., 2005). Due to the unisentropic nature of shock wave compression, a certain fraction of the energy required for compressing and heating the material remains as *residual heat* after the rarefaction wave has passed. Consequently, if the shock pressures generated by an impact are high enough, this residual heat is

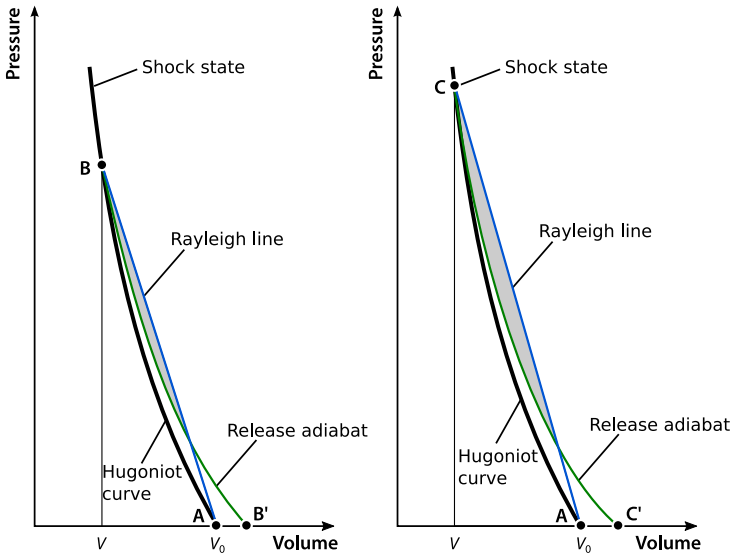

Figure 2.6 Pressure–volume diagram after Melosh (1989, p. 43), illustrating thermodynamic paths during shock loading and unloading. The Rayleigh line connects the initial state A with two shocked states B (**left**) and C (**right**) of different peak shock pressure. If the initial pressure P_0 can be neglected, the specific internal energy of the shocked materials is equal to the areas of the triangles spanned between points V–B–V_0 and V–C–V_0 (third Hugoniot equation). Decompression occurs via the respective release adiabat; the area between the release adiabats and the Rayleigh lines are the net energies per unit mass deposited in the materials in the two scenarios.

sufficient to melt or even vaporize large amounts of material (e.g., Melosh, 1989; Pierazzo et al., 1997). The initial temperature as well as the absolute amount of the melt and/or vapor are a function of the amount of residual heat remaining after decompression (cf. left and right side of Fig. 2.6). Furthermore, compressible (e.g., porous) materials retain generally more waste heat compared to less compressible materials, which hence results in melting/vaporization at lower shock pressures (e.g., Wünnemann et al., 2008; Davison et al., 2010; Bland et al., 2014; Kowitz et al., 2016).

Typical planetary impact events generate strong shock waves and induce vaporization of the projectile as well as melting and vaporization of large volumes of target rock. For most silicates, shock melting is typically induced at impact velocities of 4–7 km s^{-1}, corresponding to shock pressures >50 GPa and postshock temperatures in excess of 2000 °C (Ahrens and O'Keefe, 1972). In porous materials, shock melting starts at much lower shock pressures and, hence, lower impact velocities, because compaction of pore space and friction yields sufficient heat to locally induce melting (e.g., Wünnemann et al., 2008; Davison et al., 2010; Bland et al., 2014; Kowitz et al., 2016). At impact velocities in excess of 7–10 km s^{-1}, the projectile is typically completely molten and/or vaporized (e.g., Ahrens and O'Keefe, 1972; Pierazzo et al., 1997; Hörz et al., 2005), and subsequently admixed into target-derived melts. Consequently, the projectile usually does not survive the impact as discrete pieces, but chemical traces of it

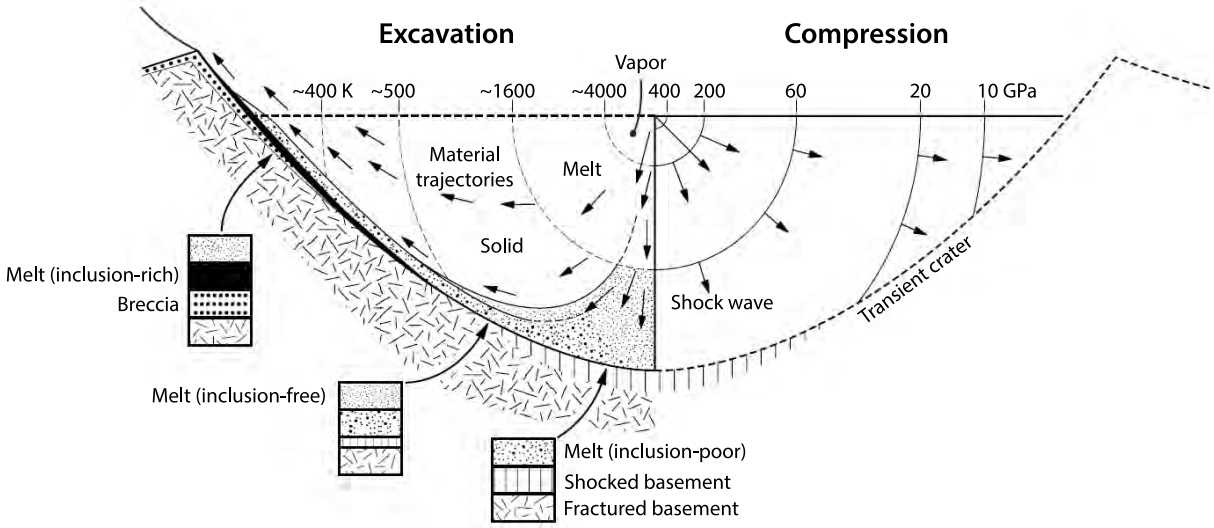

Figure 2.7 Schematic illustration of impact melt formation and displacement/ejection in the transient crater (modified after French, 1998). Shown are concentric zones of different shock regimes (vaporization, melting, and solid-state shock-metamorphic effects) that correspond to certain peak shock pressures (isobars; **right side**) and postshock temperatures (isotherms; **left side**) induced in a typical non-porous, crystalline target (e.g., basalt or granite). Vaporization of a mixture of projectile and target is induced close to the impact point; melting is induced immediately outward of this zone. The boxes illustrate typical idealized stratigraphic columns in different parts of the resulting impact crater.

might be detected in specific melt volumes (see Section 2.5 and Parts II and III). However, especially in the case of complex craters, the projectile contributes much less than 1 vol.% to typical impactites.

The formation of impact melts has no counterpart under endogenous geologic processes. Upon decompression, temperatures far above the melting points of typical silicates are reached, and incipient to complete melting, or even incipient to complete vaporization, occurs almost instantaneously. During the excavation stage, the melt that was just produced is accelerated on downward and outward trajectories (Fig. 2.7) and becomes part of the overall movement of material in the growing crater. As a result, impact melt is both ejected from as well as displaced within the crater. In both cases, the melt might incorporate solid fragments, or mix with other melt volumes originating from other strata of the crater's melt zone (e.g., See et al., 1998; Dressler and Reimold, 2001; Hörz et al., 2002; Schultze et al., 2016, and references therein). Depending on the amount and complexity of the lithologies involved, melt-mixing processes can be quite complex (e.g., See et al., 1998; Mittlefehldt et al., 2005; Schultze et al., 2016; Goderis et al., 2017, and references therein) because melts of quite diverse composition and structure might come into contact. As a result, many processes during melt mixing are poorly constrained, or have been controversially discussed. However, since some scientific applications such as the determination of the impactor type by means of chemical signatures in impact melts (e.g., Goderis et al., 2007; Goderis et al., 2013), reconstruction of the melt zone's stratigraphy of a given crater based on bulk compositions of impact melts (e.g., Hörz et al., 1989; Hörz

et al., 2002; Fazio et al., 2016), or estimation of climatic effects of impacts into carbonate-bearing targets (e.g., Deutsch and Langenhorst, 2007) are sensitive to melt-mixing processes during cratering, understanding of such melt-mixing processes is mandatory (see, e.g., discussion in Mittlefehldt et al., 1992; Ebert et al., 2013; Goderis et al., 2017). Some processes that are so-far only poorly understood but that have particular relevance for this thesis are: (1) mixing of structurally and compositionally diverse impact melts during early time steps of crater formation (e.g., Kearsley et al., 2004; Ebert et al., 2013; Ebert et al., 2014; Goderis et al., 2017), (2) formation of impact melts from carbonate-bearing targets (e.g., Osinski et al., 2008; Osinski et al., 2015; Hörz et al., 2015) and interaction between silicate melts and carbonates (e.g., Martinez et al., 1994; Deutsch and Langenhorst, 2007; Hörz et al., 2015), (3) mixing, chemical interaction, and homogenization of impact melts on small scales (e.g., Hörz et al., 1989; See et al., 1998; Ebert et al., 2013; Ebert et al., 2014; Fazio et al., 2016; Schultze et al., 2016; Goderis et al., 2017; Siegert et al., 2017), and (4) immiscibility of impact melts (Zolensky and Koeberl, 1991; Hamann et al., 2013).

This thesis aims at contributing to our understanding of these processes. An overview of the scientific objectives of this thesis will be given in Chapter 3; the thermodynamics of shock melting and vaporization are further detailed in Chapter 7. Excellent introductions to this topic can be found in Ahrens and O'Keefe (1972) and, in more detail, in chapters 3–5 of Melosh (1989).

2.5 Recognizing impact craters: shock effects and chemical signatures of the projectile

In the previous sections, a brief impression was gained on the extreme physical conditions that are imposed by shock waves on the rocks through which they pass. In nature, shock waves are only generated by hypervelocity impacts—no other geologic process is capable of generating shock waves and related shock-metamorphic effects in rocks and minerals, which are, thus, unique to impact (see introduction to the topic by French, 1998). Consequently, shock-metamorphic effects—in the following simply *shock effects*[5]—have been critical to the identification and verification of impact structures on Earth, and to the identification of similar processes on the Moon and other planetary bodies from which meteorites have been delivered to Earth.

Prior to identification of these *impact-diagnostic* shock effects, the only convincing argument for the occurrence of impact events on Earth was the definite presence of surviving meteorite fragments in and around small, young craters (e.g., at Meteor Crater, Wabar, Henbury, etc.)—crater morphology alone was never regarded as a sufficient argument, because circular depressions may form in a variety of processes such as volcanism, emplacement of salt diapirs, formation of sink holes, etc. Consequently, and due to the aforementioned complete melting and/or vaporization of the impactor in large-scale impact events, only a handful of impact

[5] The recognition of shock effects and high-pressure phases by E. Chao and E. Shoemaker in the melt-bearing breccias (suevites) of the Ries structure (Chao and Shoemaker, 1961) played a crucial role in persuading scientists that impact craters may indeed form frequently on Earth. Until their discovery in 1961, local geologists believed devoutly that the Ries was of volcanic origin, and that the suevites represent volcanic deposits (it was recently discussed by Siegert et al., 2017 that the Ries suevites might have been deposited by a process quite similar to the deposition of pyroclastic density currents).

structures—those with conserved impactor fragments—has been recognized prior to the 1960s. With the acceptance of shock effects as an unequivocal recognition and confirmation criterion for impact, the discovery and confirmation of terrestrial impact structures is no longer limited to small and young structures. To this day, 190 terrestrial impact craters[6] with diameters between ~1 m (Carancas) and more than 100 km (e.g., Sudbury, Chicxulub, and Vredefort) have been confirmed.

[6] See the Earth Impact Database (http://www.passc.net/EarthImpactDatabase/)

2.5.1 Shock effects in rocks and minerals

The term shock effect *sensu stricto* covers all types of shock-induced changes in a rock or mineral. It includes, in progressive order: formation of shatter cones; formation of planar microstructures; phase transformations (e.g., quartz to coesite); decomposition (e.g., of biotite, or of calcite to lime and carbon dioxide); formation of diaplectic glasses (i.e., solid-state amorphization); melting; and vaporization. These changes are typically *irreversible* and are produced when a material is subjected to shock pressures way above its Hugoniot elastic limit (Melosh, 1989; French, 1998), which is defined as "the critical shock pressure at which a solid yields under the uniaxial strain of a plane shock wave" (Stöffler, 1972). For most rock forming minerals, the Hugoniot elastic limit is in the range of 1–10 GPa. Thus, at the surface of a rocky planetary body, only impacts can generate sufficient shock pressures to reach and pass the Hugoniot elastic limit. Figure 2.8 illustrates this by a comparison of typical P–T conditions of shock metamorphism against typical P–T conditions of normal crustal metamorphism.

Although not the focus of this thesis, typical and well-defined shock effects in rocks and minerals are illustrated in Fig. 2.9. Some of these will be encountered in Parts II and III, and they include:

- shatter cones (e.g., Baratoux and Reimold, 2016);
- planar microstructures (planar fractures and planar deformation features; Fig. 2.9a, b; e.g., Stöffler and Langenhorst, 1994; Stöffler et al., 2017) in quartz and feldspar;
- mosaicism (Fig. 2.9c; e.g., Stöffler et al., 2017);
- formation of diaplectic glasses by solid-state transformation (Fig. 2.9d, e; e.g., Stöffler et al., 2017);
- formation of high-pressure polymorphs (e.g., Stöffler and Langenhorst, 1994; Stöffler et al., 2017); and
- formation of mineral and whole-rock glasses (Fig. 2.9f) by impact melting (e.g., Stöffler et al., 2017).

Note, however, that impact melting is not regarded as diagnostic for impact, as mineral and whole rock melts can be produced by other, non-impact processes (e.g., formation of fulgurites by lightning-strike fusion).

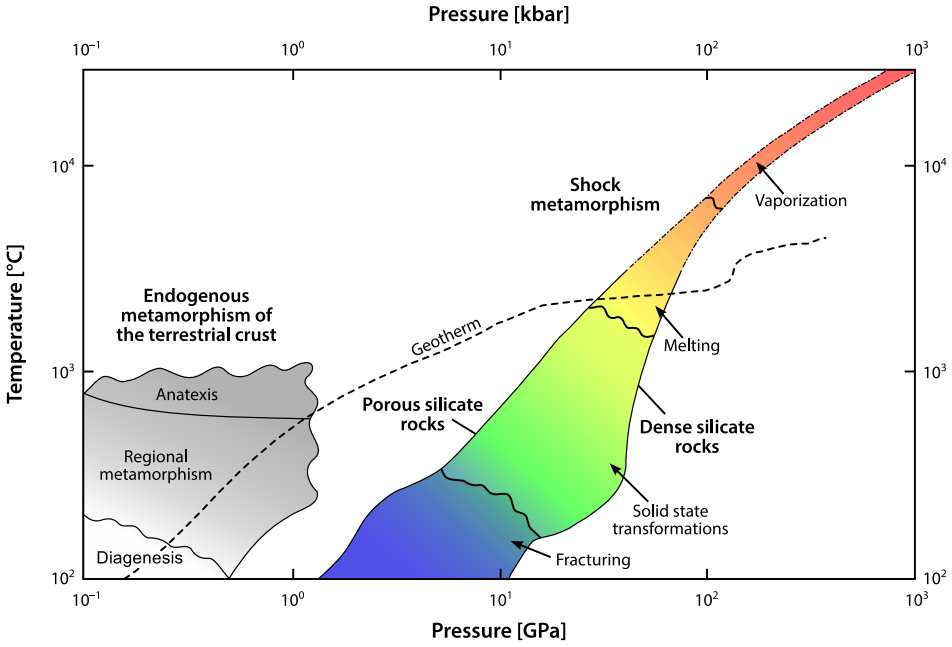

Figure 2.8 Pressure–temperature plot illustrating the conditions of shock metamorphism for typical porous (e.g., sandstone) and non-porous, crystalline (e.g., basalt) rocks, compared against *P–T* conditions of normal crustal metamorphism. Graph modified from Stöffler et al. (2017).

Excellent reviews regarding characteristics and formation conditions of these shock effects can be found in chapter 4 in French (1998), chapter 8 in Osinski and Pierazzo (2012), as well as in Stöffler and Langenhorst (1994), Langenhorst and Deutsch (2012), Baratoux and Reimold (2016), and Stöffler et al. (2017).

2.5.2 Projectile identification

Due to the intense *P–T* conditions during impact cratering, the projectile rarely survives in the form of discrete fragments. However, small amounts of melted and/or condensed projectile material are usually incorporated into impact-generated breccias and melt rocks during crater formation (e.g., Koeberl, 1998; Tagle and Hecht, 2006; Goderis et al., 2007; Koeberl et al., 2012; Goderis et al., 2013). At large (complex) impact structures, *projectile contamination* constitutes usually less than 1 wt.% of the resulting impactite (e.g., Koeberl, 1998; Tagle and Hecht, 2006; Osinski and Pierazzo, 2012; Koeberl et al., 2012): most of the projectile is typically vaporized and the target primarily contributes to the resulting composition. At small (simple) craters, projectile contamination is typically more severe, reaching, in some cases, >10 wt.% of the resulting impactite (e.g., Hörz et al., 1989; Mittlefehldt et al., 1992; Hörz et al., 2002; Hamann et al., 2013; Fazio et al., 2016).

Elements that have high abundances in meteorites, but low abundances in terrestrial rocks—for small craters: crustal rocks—can be used to

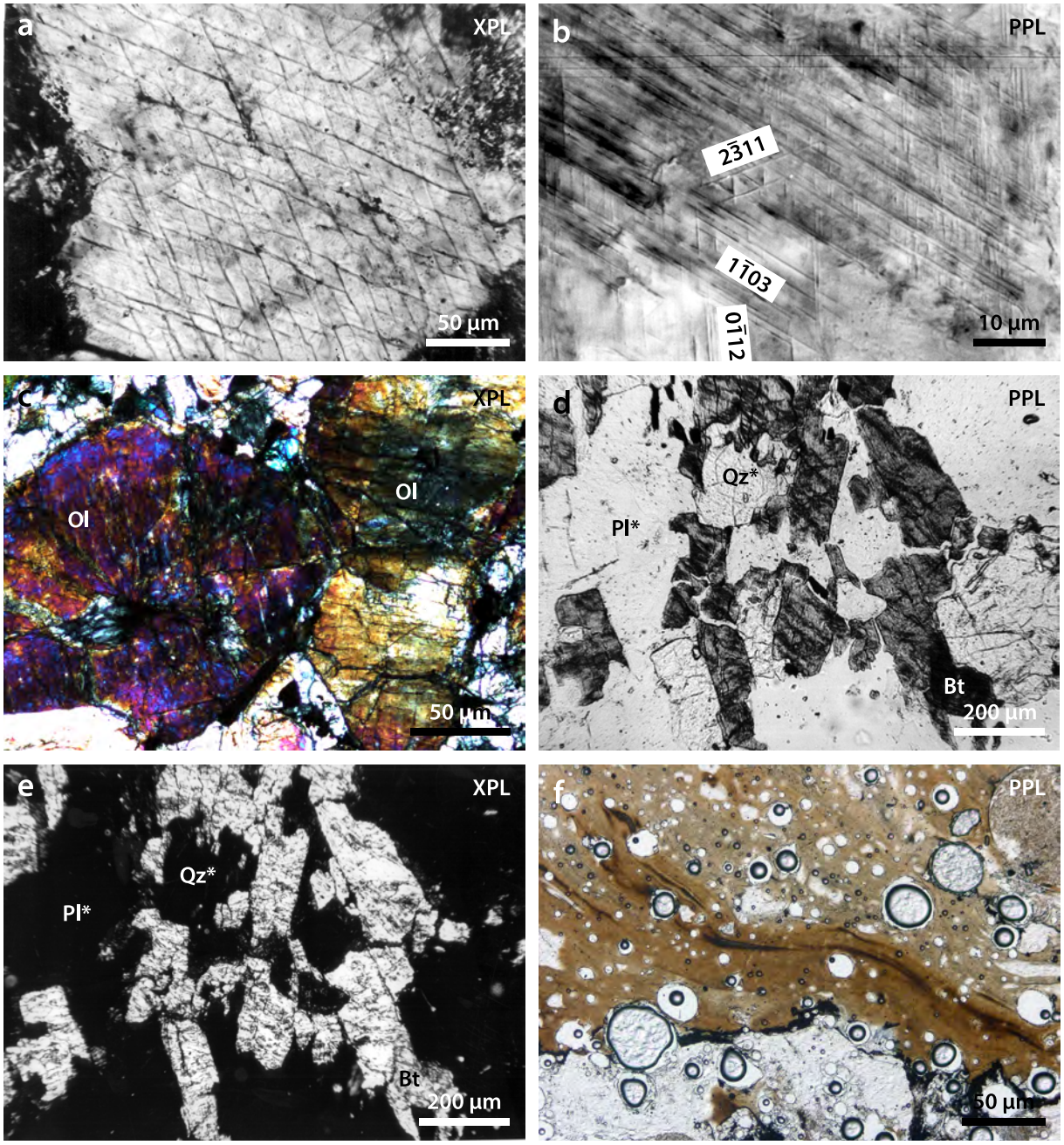

Figure 2.9 Typical shock-metamorphic effects in rocks and minerals. **a** Planar fractures parallel to $\{10\bar{1}1\}$ in quartz of a granite clast of the ejecta blanket (Bunte breccia; polymict lithic breccia) at Ronheim, Ries crater, Germany (sample S 614). Note undulatory extinction of the quartz grain. Image taken under cross-polarized light. **b** Non-decorated planar deformation features in quartz of a gneiss clast in the suevite of Bollstadt (sample B7), Ries crater, Germany. Image taken under plane-polarized light. **c** Strongly shocked euhedral phenocrysts of olivine in the martian meteorite Tissint. Both olivine crystals are in extinct position, but show birefringence due to shock-induced mosaicism. Note the shock-indiced planar fractures running N–S in the left an E–W in the right crystal. Image taken under cross-polarized light. **d, e** Diaplectic quartz glass (Qtz*), diaplectic plagioclase glass (Pl*), and biotite (Bt) with kink bands in a gneiss clast from the suevite of Otting, Ries crater, Germany. d: Plane-polarized light; e: cross-polarized light. **f** Whole-rock melt (now glass) derived from local quartz sand and an iron meteorite impactor, Wabar craters, Saudi Arabia. Note the inclusion of lechatelierite (fused quartz) at the bottom part of the image. Image taken under plane-polarized light. a–e modified from Stöffler et al. (2017).

trace the geochemical signature of the impactor. *Projectile identification* relies predominantly on the moderately siderophile elements Ni, Co, and Cr (although Cr is partially lithophile) and the highly siderophile platinum-group elements (PGE; i.e., Pt, Pd, Os, Ru, Rh, Ir), Re, and Au. These elements occur in significantly higher concentrations in meteorites than in the average terrestrial continental crust (see, e.g., Koeberl, 1998; Dressler and Reimold, 2001; Tagle and Hecht, 2006; Koeberl et al., 2012). This is because crustal rocks are products of planetary *differentiation*, whereas meteorites, except for achondrites, reflect primitive, *undifferentiated* (e.g., chondrites) or *enriched* (e.g., iron meteorites) compositions. Consequently, element abundances and specific inter-element ratios (e.g., Ni/Cr or Ir/Cr) in meteorites differ from those in crustal rocks and, to some extent, mafic or ultramafic mantle rocks. In cases where the *indigenous* component—that is, the abundance of these elements in the target (e.g., Koeberl, 1998; Dressler and Reimold, 2001)—can be estimated, this difference can be used to measure the extraterrestrial contamination and maybe also to determine the type of impactor (e.g., Palme et al., 1978; Evans et al., 1993; Koeberl, 1998; Tagle and Hecht, 2006; Goderis et al., 2007; Koeberl et al., 2012; Goderis et al., 2013, and references therein). However, if mantle-derived lithologies contribute to the target, or are even present in the crater's melt zone, this technique can be insufficient to constrain the impactor type or to even confirm its presence (see discussion in Koeberl, 1998; Dressler and Reimold, 2001; Tagle and Hecht, 2006). This is particularly the case when the projectile contamination is small with respect to the indigenous component; in this case, careful correction for the indigenous component is mandatory (Koeberl, 1998; Dressler and Reimold, 2001; Tagle and Hecht, 2006).

Apart from element ratios, *isotope ratios* of specific elements are nowadays used for fingerprinting the projectile (e.g., Koeberl, 1998; Dressler and Reimold, 2001; Tagle and Hecht, 2006; Koeberl et al., 2012). Commonly used isotope ratios are $^{187}Os/^{188}Os$ and $^{53}Cr/^{52}Cr$, which have not only been used to detect a meteoritic component in impactites, but also to discriminate between specific types of impactors. For instance, the Re–Os isotopic system is particularly sensitive for identifying the presence of minute amounts of a meteoritic component (e.g., Koeberl, 1998; Tagle and Hecht, 2006, and references therein), whereas chromium isotopes have been used to distinguish between certain types of meteorites (e.g., Koeberl, 1998; Tagle and Hecht, 2006). When combined with certain element ratios (e.g., Cr/Ir or PGE element ratios), isotopic systems constitute a powerful method for detecting and identifying projectiles in impactites (e.g., Koeberl, 1998; Dressler and Reimold, 2001; Tagle and Hecht, 2006; Koeberl et al., 2012).

When applying these methods for projectile detection and identification, it is usually tacitly assumed that elements as well as isotopes do not *fractionate* during or after the impact process—that is, they are assumed to largely represent the original ratio of the projectile. However,

element fractionation may be due to a number of processes that occur either during impact, or in its aftermath:

Fractionation during impact Bulk or partial vaporization (e.g., Floss et al., 1996) of the projectile, followed by condensation of this vapor could induce fractionation governed by volatility and condensation temperatures of the elements (Lodders, 2003). Furthermore, partial evaporation of volatile components from superheated impact melts (e.g., Gerasimov et al., 2005) could also change inter-element ratios in impact melts.

Fractionation during projectile–target mixing Heterogeneous admixture of projectile melts and condensates into target-derived melts could induce fractionation. For example, fractionation could be induced by preferential exchange of siderophile elements and/or PGE between impactor-derived metal melts and target-derived silicate melts, governed by distribution coefficients or oxygen fugacity conditions (e.g., Essene and Fisher, 1986; Rowan and Ahrens, 1994; Ebert et al., 2014; Hamann et al., 2013).

Fractionation during crystallization Fractionation could also be induced during crystallization of impact melts, for instance, by preferential, distribution coefficient-governed uptake of siderophile elements and/or PGE by specific minerals (e.g., sulfides, spinels, olivines, etc.). However, this might only be relevant if very small, submicrometer samples are used.

Fractionation after impact Fractionation could also be induced by post-impact, secondary alteration processes, including hydrothermal alteration.

Some of these mechanisms have been documented in experiments and by observations on natural impactites. For instance, it has been shown that elements (e.g., Keller and McKay, 1992; Gerasimov et al., 2005; Warren, 2008) as well as isotopes (e.g., Floss et al., 1996) can fractionate due to evaporation induced by high temperatures, for example, in the vapor plume or in specific parts of the crater's melt zone. Moreover, elements might also fractionate during mixing and chemical interaction of compositionally and structurally different impact melts (e.g., Hörz et al., 1989; Mittlefehldt et al., 1992; Wozniakiewicz et al., 2011; Hamann et al., 2013; Ebert et al., 2013; Ebert et al., 2014; Ebert et al., 2017). This seems especially the case in impact scenarios involving iron meteorites and high-silica targets, as documented by experimental studies (e.g., Ebert et al., 2013; Ebert et al., 2014; Ebert et al., 2017) and studies on pristine impact structures like Barringer (Hörz et al., 2002; Mittlefehldt et al., 2005), Wabar (Hörz et al., 1989; Mittlefehldt et al., 1992; Hamann et al., 2013), and Kamil (e.g., Fazio et al., 2016).

These examples illustrate that without detailed knowledge of elemental and isotopic fractionation processes during or after impact, great care is

needed in assigning specific impactor types to individual impact craters on the basis of inter-element ratios (cf. Mittlefehldt et al., 1992; Ebert et al., 2014) or isotopic ratios (cf. Koeberl et al., 2012) obtained from impact melts. Detailed petrologic–geochemical studies are necessary to reconstruct and understand mechanical and chemical mixing processes between impactor and target. As will be discussed in the next section, reconstruction of these processes is challenging, because impactites—especially those from large, complex impact structures—do not necessarily and fully document all transient processes and physical conditions during crater formation. However, the results of such studies might have implications for the applicability of the above methods and for estimating impactor populations and fluxes throughout solar system history.

2.6 Projectile–target mixing: the fate of the projectile

The fate of the projectile upon impact has ever since been an intriguing question in impact cratering studies. However, the overwhelming majority of petrologic–geochemical studies on natural impactites has focused on other—more readily accessible—aspects of crater formation and impact melting. Among these are: generation, distribution, and emplacement of specific types of impactites (e.g., Dressler and Reimold, 2001; Stöffler and Ryder, 2001; Stöffler et al., 2013; Osinski et al., 2016, and references therein); reconstruction of melt mixing of various individual target lithologies (e.g., See et al., 1998; Dressler and Reimold, 2001; Pratesi et al., 2005; Schultze et al., 2016, and references therein); general geochemistry of impactites (e.g., Koeberl, 1998; Dressler and Reimold, 2001, and references therein); the fate of carbonates and other volatile-bearing lithologies upon impact (e.g., Kieffer and Simonds, 1980; Graup, 1999; Osinski et al., 2008; Hörz et al., 2015, and references therein); and many more.

Early researchers specifically focusing on the fate of the projectile upon impact (e.g., Spencer, 1933; Nininger, 1954) investigated FeNi metal disseminated around small, simple impact structures such as Barringer, Henbury, or Wabar, and recognized that meteoritic material had been incorporated in molten form into silicate impact melts. Later studies (e.g., Brett, 1967; Kelly et al., 1974; Gibbons et al., 1976b), mostly also investigating impact glasses from these craters, suggested that oxidation of FeNi metal from the impactor was induced by the surrounding silicate impact melt, but limited microanalytical techniques in the 1970s did not allow detailed insights into these reactions on the micrometer scale.[7] Subsequent studies eventually showed that Fe (and, to lesser extent, also Ni) from the iron impactors were selectively oxidized during the melt-mixing process: they were partitioned into and became structural parts of the coexisting silicate impact melts as well as of minerals (e.g., olivine, pyroxene, magnetite) that grew from these melts (e.g., Hörz et al., 1989; Mittlefehldt et al., 1992; Hörz et al., 2002; Mittlefehldt et al., 2005; Hamann et al., 2013; Fazio et al., 2016).

Investigation of the chemical interaction between projectile and target

[7] Textural and chemical evidence of this oxidation process was documented much later in the Wabar impact glasses by Hamann et al. (2013) (see Fig. 8.2d in Chapter 8) and in the impact glasses of Ebert et al. (2013) produced in the MEMIN impact experiments (see Fig. 8.6b in Chapter 8)

is obviously limited to those impactites that either preserve projectile remnants in the form of discrete, "quasi-monolithic" melt volumes or even pieces, or to those that preserve primary chemical signatures of the projectile, for instance, in the form of chemical components (e.g., Ni, Ir, PGE) in impact melts. Especially in the case of large and old impact structures, such investigations are challenging to even impossible, because secondary processes such as weathering, hydrothermal activity, devitrification, or simply erosion may severely modify or even completely destroy most traces of the impactor. In addition, subsequent processes in large impact-melt pools may overprint or mask the primary chemical interaction between projectile and target and make reconstruction of the original interface between projectile and target impossible. Due to these reasons, most insights into the chemical interaction between projectile and target came from relatively young, small, and pristine impact craters for which detailed knowledge of both impactor and target exists; among these are Wabar (Brett, 1967; Gibbons et al., 1976a; Hörz et al., 1989; Mittlefehldt et al., 1992; Hamann et al., 2013), Barringer (Kelly et al., 1974; Hörz et al., 2002; Mittlefehldt et al., 2005), Kamil (Fazio et al., 2014b; Fazio et al., 2016), and Henbury (Gibbons et al., 1976a).

Apart from these studies, laboratory experiments are an important tool to investigate the chemical interaction between projectile and target. However, among the vast number of experimental studies focused on the cratering process (e.g., Gault et al., 1968; Braslau, 1970; Stöffler et al., 1975; Cintala and Hörz, 1990; Hörz and Cintala, 1997; Anderson et al., 2004; Hörz et al., 2005; Hermalyn and Schultz, 2011; Daly and Schultz, 2016), only few experimental studies have specifically addressed the physical and chemical dissemination of projectile material during the cratering process (i.e., Hörz et al., 1983; Evans et al., 1994; Wozniakiewicz et al., 2011; Wozniakiewicz et al., 2012; Wozniakiewicz et al., 2015; Ebert et al., 2013; Ebert et al., 2014). In addition, most experiments involved artificial projectiles such as aluminum, copper, lexan, or polyethylene, which, with respect to chemistry, makes the application of experimental results to nature questionable. Those studies that used natural planetary materials as projectile *and* target detailed physical mixing processes between projectile- and target-derived melts; some of them also investigated the chemical interaction between these melts (e.g., Hörz et al., 1983; Wozniakiewicz et al., 2011; Wozniakiewicz et al., 2012; Wozniakiewicz et al., 2015; Ebert et al., 2013; Ebert et al., 2014; Daly and Schultz, 2016) and inter-element fractionation during melt mixing (e.g., Wozniakiewicz et al., 2011; Ebert et al., 2013; Ebert et al., 2014). Despite these examples, the mechanical and chemical interaction between projectile and target—especially during contact and compression and excavation stages of crater formation—is still poorly understood. Many details regarding processes, products, and time scales of mixing of impact melts of diverse composition during these earliest phases of crater formation remain unanswered. This thesis aims at investigating these processes.

Chapter 3

Research aims

The study of impact processes and associated products is a multidisciplinary field of planetary sciences. It involves physics, geology, chemistry, remote sensing, and, with the emergence of high-performance computer clusters, numerical modeling. Traditionally, processes and products of impact cratering in general and impact melting in particular have mainly been studied at terrestrial impact craters (e.g., Spencer, 1933; Kieffer, 1971; Kelly et al., 1974; Kieffer et al., 1976a), by studying extraterrestrial material delivered to Earth in the form of meteorites (e.g., Stöffler et al., 1991, and references therein), and, importantly, by investigation of and experimentation with lunar samples returned during the Apollo era (e.g., Schaal and Hörz, 1977; Schaal et al., 1979; Schaal and Hörz, 1980). In parallel, since the installation of a light-gas gun at NASA Ames Research Center in the 1960s, hypervelocity impact experiments (e.g., Stöffler et al., 1975; Schaal and Hörz, 1977; Schaal et al., 1979; Schaal and Hörz, 1980; Hörz et al., 2005) and shock recovery experiments (e.g., Ahrens and O'Keefe, 1972; Schaal et al., 1979) have been a valuable tool to study the shock behavior of planetary materials. Such impact experiments allowed to investigate impact melting under *controlled* conditions and with the advantage of having knowledge of target *and* projectile properties, impact velocity, impact direction, impact angle, etc. In recent years, numerical models of crater formation have provided detailed insight into numerous aspects of the cratering process, including general cratering mechanics (e.g., Wünnemann et al., 2016), the formation conditions associated with impact melts (e.g., Pierazzo et al., 1997) and vapors (e.g., Pierazzo et al., 1998; Svetsov and Shuvalov, 2016), potential climatic effects of large impacts (e.g., Pierazzo et al., 2003; Pierazzo and Artemieva, 2012), and much more. Modern impact cratering studies are, thus, complex. In the best case, they combine several of the above mentioned approaches into a study that investigates a specific topic or problem from several perspectives. Good examples for this *integrated* approach are Kowitz et al. (2013a), Nagaki et al. (2016), Wünnemann et al. (2016), Rae et al. (in press), and Holm-Alwmark et al. (in press).

3.1 Research framework of this thesis

The PhD research that resulted in this thesis was done in the context of the *Multidisciplinary Experimental and Modeling Impact Research Network* (MEMIN). MEMIN was research unit FOR 887 funded by the Deutsche Forschungsgemeinschaft (DFG). It brought together geoscientists, physicists, and engineers and included studies of natural craters, laboratory experiments, and numerical simulations. Its overall work program (Kenkmann et al., in press) included:

See www.memin.de, Vol. 48 of *Meteoritics & Planetary Science*, and Kenkmann et al. (in press) for an overview of all subprojects

1. complete mineralogical–petrophysical and mechanical characterization of the target prior and after the experiments, using state-of-the-art geophysical tools for meso-scale tomography, as well as state-of-the-art microstructural and chemical analyses of impact products at the (sub-)micrometer-scale;

2. stringent control of the impact experiments with newly developed, in situ, real-time measurements of fracture propagation, stresses, crater growth, and ejecta dynamics;

3. development of new experimental techniques and set-ups (e.g., laser irradiation experiments); and

4. numerical modeling of various aspects of the cratering process (e.g., shock-wave propagation, interaction between ejecta and atmosphere).

Of specific relevance for this thesis was the Subproject "Projectile–target interaction, melting, and vaporization in hypervelocity experiments and natural impactites". The focus of this thesis lies on *transient*, high-temperature processes in impact melts during and immediately after crater formation. It aims at reconstructing the chemical and physical *interaction* between the impactor and the target it strikes, and specifically at investigating the chemical interaction between structurally and/or compositionally diverse impact melts. Due to the complexity of the topic, this thesis comprises results from (1) "conventional" impact experiments performed with two-stage light-gas guns, (2) newly developed and individually tailored laser irradiation experiments, and (3) natural planetary (i.e., terrestrial and extraterrestrial) impact melts. In the respective chapters, these petrologic findings are combined with thermodynamic considerations and, in some cases, results obtained from numerical modeling. The latter was only possible because this thesis was done in the framework of MEMIN, which allowed for interdisciplinary cooperation among different subprojects (e.g., with Subproject 9, "Numerical modeling of impact cratering processes").

As apparent from Chapter 2, the most intense interaction between projectile and target occurs within the first instances of crater formation under, compared to normal conditions in the Earth's crust, excessively high and highly dynamic P–T conditions. All subsequent interaction

between projectile and target happens under petrologically more "common" pressures, but it usually involves temperatures far in excess of those reached in the Earth's crust.[8] It typically involves cooling of and interaction between superheated melts of various compositions and physical properties at relatively low (i.e., near-atmospheric) pressure. Compared to most, if not all, endogenous magmatic processes, impact melting involves extremely short time scales. No one has probably ever witnessed the formation of impact melts with their own eye, and even in the laboratory, sophisticated techniques are required to optically or spectroscopically resolve impact melts and associated chemical processes *during* crater formation. Although one might readily reconstruct all aspects such composition, mineralogy, porosity, density, etc. of the pre-impact target and resulting impact products, *transient processes* operating *during* impact melt formation and cooling are, in most cases, hidden in a black box.

To gain insight into high-temperature chemical processes during impact melting, the prime objective of this thesis is to produce impact melts and relevant analogs from *natural* planetary materials under controlled experimental conditions and to compare the resulting melts against impact melt products (impact glasses and impact melt rocks) formed in *natural* impact craters. The specific scientific aims of this thesis will be discussed in the following.

[8] Recall Fig. 2.8 that compared general P–T conditions of shock metamorphism against typical P–T conditions of metamorphic facies in the Earth's crust

3.2 Scientific objectives and motivation

As will be outlined in Chapter 4, this thesis resorts to several independent articles that build the respective chapters contained within Parts II and III. Each of these chapters is based on individual initial problems and hypotheses that are detailed in the respective introduction and discussion sections. The salient points of these studies are four fundamental and recurring topics related to chemical processes during impact melt formation, to which this thesis will try to contribute. These are stated in the following, and it will be elaborated on each in turn to provide background and motivation.

The overall goal of this thesis is to improve the current understanding of *transient*, high-temperature physical and chemical processes in impact melts in general as well as the chemical interaction between impact melts of diverse structure and composition and subsequent petrogenetic proceses during cooling in particular. Some general questions that will be addressed are:

1. What physical and chemical processes occur immediately at the *projectile–target interface*?

2. What happens during physical and chemical *mixing* of structurally or compositionally diverse impact melts under dynamic disequilibrium conditions? In which respect differs mixing and homogenization of miscible, yet structurally or compositionally diverse

impact melts from mixing and homogenization of immiscible impact melts?

3. What *petrogenetic processes* operate during cooling of compositionally complex impact melts, in particular of those originating from carbonate-bearing targets? Can experiments shed light onto transient petrogenetic processes during melt formation and cooling that are inaccessible from natural impactites?

4. What are typical *time scales* and *cooling rates* involved in formation and cooling of millimeter- to centimeter-sized ballistic melt ejecta (e.g., melt spherules, tektites, etc.)?

5. Are hypervelocity impact experiments a suitable tool to study melt-mixing processes in and petrogenesis of impact melts? Can such results be "scaled up" to natural impact scenarios?

3.2.1 Early physical and chemical processes at the projectile–target interface

Mixing of projectile- and target-derived melts begins with the initial physical contact between projectile and target, upon which the stage is set for all subsequent events (see Fig. 2.1 and Section 2.1). A complete in situ reconstruction of this interface in terrestrial impact structures is, obviously, not possible, and is everything else than straightforward in impact experiments. Numerical modeling can shed light onto transient mechanical and physical processes along the projectile–target interface (e.g., Pierazzo et al., 1998; Bland et al., 2014; Wünnemann et al., 2016; Goderis et al., 2017), however, such models, at the present time, do not address chemical problems. Moreover, they *must* be validated against observations, which brings us back to square one.

Knowledge about chemical processes operating at the projectile–target interface is mainly based on reconstruction of the melt zones of small, simple impact craters. For example, based on a comprehensive petrologic study of glassy impact ejecta (melt spherules), Hörz et al. (1989) and subsequently Mittlefehldt et al. (1992) reconstructed the melt zone of the largest (116 m diameter) of the Wabar craters, Saudi Arabia. At Wabar, two distinct impact melt volumes were formed: a dark or "black" melt that contains ~4.5% meteoritic component, and a transparent or "white" melt that contains <1% meteoritic component. When the meteoritic component is subtracted, both melts were found to be rather similar in terms of bulk chemistry: they both originated from the uppermost parts of the target stratigraphy, but obviously incorporated variable amounts of the projectile. Similar observations were made by Fazio et al. (2016), who described similar melts from the 45-m-diameter Kamil crater, Egypt. At Kamil, the "black" glass variety contains, on average, 11–12 wt.% of projectile component, whereas the "white" glass variety contains <0.1 wt.% projectile component. Based on a comparison between the compositions of individual pre-impact target strata and the compositions of the

two impact glass varieties, Fazio et al. (2016) were able to reconstruct the "stratigraphy" of Kamil's melt zone: the zone of chemical interaction between projectile and target was restricted to the topmost ~1 m of the pre-impact stratigraphic sequence. At both impact structures, the heavily projectile-contaminated impact melts are clast-laden. This indicates that they entrained shocked and unshocked lithic and mineral fragments from the bottom of the transient cavity during crater formation. Similar melts, although of more complex bulk composition reflecting the complex target stratigraphy, are known from the 1.2-km-diameter Barringer crater, Arizona (Hörz et al., 1989; See et al., 1998; Mittlefehldt et al., 2005; Hörz et al., 2015; Osinski et al., 2015). The Barringer impact melts are mixtures of the projectile (~14 wt.% on average) and variable proportions of the topmost two stratigraphic units (Moenkopi calcareous sandstone and siltstone and Kaibab dolomite) depleted in CO_2 (Hörz et al., 1989; Mittlefehldt et al., 2005); the two lowermost stratigraphic units were mostly not involved in melt formation and mixing (Mittlefehldt et al., 2005).

A combination of the generally accepted model of crater formation (Melosh, 1989; French, 1998; Osinski and Pierazzo, 2012), observations on terrestrial impact craters like those mentioned above, and findings from impact experiments (Ebert et al., 2013; Ebert et al., 2014) suggests that the direct interaction between projectile and target is restricted to the uppermost levels of the crater's melt zone. Here, both projectile and target are melted or partially to completely vaporized after passage of the shock and rarefaction waves. The passage of the rarefaction wave also sets material in motion and creates a dynamic and turbulent material flow that facilitates thorough mixing of projectile- and target-derived melts. However, many details regarding the admixture of projectile material into target-derived melts are still not well understood (see discussion in Mittlefehldt et al., 1992; See et al., 1998; Mittlefehldt et al., 2005; Hamann et al., 2013; Ebert et al., 2013; Ebert et al., 2014; Goderis et al., 2017). In particular, the physical and chemical interaction of projectile-derived melt volumes with target-derived melt volumes at the projectile–target interface is poorly constrained. Reconstruction of mixing processes in impact melts, starting with initial contact between projectile and target, is one of the major aims of this thesis. Consequently, one of the greater questions that will be asked is:

- What physical and chemical processes occur immediately at the *projectile–target interface*?

An in situ reconstruction of this interface from impact experiments is presented in Part II, Chapters 5 and 6. The chemical interaction between projectile- and target-derived impact melts is also investigated in Part III, Chapter 8, which contains findings from pristine terrestrial impact melts as well as experimental analogs, and also in Chapter 9, which presents findings from silicate impact melt inclusions in the Netschaëvo IIE iron meteorite.

3.2.2 Mixing of structurally or compositionally different impact melts under disequilibrium conditions

Mixing of structurally or compositionally different impact melts is a recurring topic in most petrologic studies on impact glasses, impact melt rocks, and melt-bearing breccias. Impact melts originating from large, complex impact structures are often described as *homogeneous* in terms of bulk chemical composition (see Dressler and Reimold, 2001, and references therein), whereas impact melts originating from small, simple craters are often described as *heterogeneous* in bulk chemical composition (e.g., Hörz et al., 1989; See et al., 1998; Hörz et al., 2002; Hamann et al., 2013; Fazio et al., 2014b; Schultze et al., 2016). Hence, there seems to exist a positive correlation between crater size and degree of melt homogenization that is likely simply related to the time span available for melt homogenization (cf. discussion in Hörz et al., 1989; See et al., 1998). However, as exceptions to this "rule" exist—for example, the melts of Sudbury (Grieve et al., 1991; Dressler and Reimold, 2001), Chicxulub (Koeberl et al., 1994; Dressler and Reimold, 2001), or East Clearwater Lake (Dressler and Reimold, 2001) are heterogeneous in terms of bulk composition and mineralogy—melt homogenization might also involve other factors. Among these, the presence or absence of a volatile component in the target (e.g., Kieffer and Simonds, 1980; Pierazzo et al., 1997; Osinski et al., 2008; Siegert et al., 2017), the amount of individual lithologies in the target and its structural makeup (e.g., See et al., 1998; Pratesi et al., 2005; Schultze et al., 2016; Siegert et al., 2017), or differential particle velocities of individual melt volumes during crater formation (e.g., See et al., 1998) have been discussed.

From the presence of effectively homogeneous melt volumes >10^4 km^3 in some large terrestrial impact structures (see Dressler and Reimold, 2001, and references therein), it follows that extraordinarily efficient melt-transportation and melt-mixing processes are required to produce intimately mixed and substantially homogeneous melts from quite diverse target volumes that were potentially initially separated by distances of some kilometers (See et al., 1998, p. 937). While melt mixing and homogenization in the case of massive melt sheets might be readily facilitated or enhanced by the flow and pooling of individual melt volumes into massive melt pools, melt mixing and homogenization in the case of small melt volumes—especially ballistic ejecta of millimeter to decimeter size, such as melt spherules or tektites[9]—must be essentially complete within the brief time span between initial contact between projectile and target and the ejection of a specific melt volume from the crater.

The heavily projectile-contaminated melt ejecta present at the Wabar (Hörz et al., 1989; Mittlefehldt et al., 1992; Hamann et al., 2013), Kamil (Fazio et al., 2016), or Barringer (Hörz et al., 2002; Mittlefehldt et al., 2005; Hörz et al., 2015; Osinski et al., 2015) impact structures attest that intimate mixing between projectile and target impact melts must commence during relatively early steps of crater formation (cf. also See et al., 1998; Mittlefehldt et al., 1992). Similar conclusions were drawn by Goderis et al. (2017), who investigated possible projectile signatures in tektites from the

[9] Tektites are distal ejecta that are believed to form within the first instances (contact and compression phase) of crater formation at the interface between projectile and target (Melosh, 1989)

Australasian strewn field. Furthermore, as discussed by See et al. (1998, p. 947), even in the case of large, complex impact structures, melt mixing and homogenization happens on time scales much shorter than the time span required for complete crater growth (i.e., some tens of seconds for melt volumes measured in hundreds or even thousands of cubic kilometers). This requires an intensely turbulent environment to operate during early stages of crater formation that could possibly be induced by differential particle velocities immediately after decompression (e.g., See et al., 1998) and by Kelvin-Helmholtz instabilities that develop along interfaces of individual melt volumes (e.g., Ebert et al., 2017; Goderis et al., 2017).

Mixing of diverse impact melts on microscopic scales will be a recurring topic within the individual chapters comprised within this thesis. In particular, it asks:

- What happens during physical and chemical *mixing* of structurally or compositionally diverse impact melts under dynamic disequilibrium conditions?
- In which respect differs mixing and homogenization of miscible, yet structurally or compositionally diverse impact melts from mixing and homogenization of immiscible impact melts?

While no attempt will be made at investigating melt-mixing processes in massive melt sheets originating in large, complex craters, one objective of this thesis is to explore melt-mixing processes and associated time scales for impact melts formed in small, simple impact craters, such as Wabar, Kamil, or Barringer, as well as in experimental analogs. Due to the absence of massive melt sheets at these craters (see Hörz et al., 1989; Hörz et al., 2002; Kring, 2007; Folco et al., 2010; Fazio et al., 2014b), emphasis will be given on investigation of ballistic melt ejecta of millimeter to decimeter size. Such ejecta are abundant in the solar system (e.g., Heiken et al., 1991, and references therein), hence, the results of this thesis will be applicable to impact scenarios beyond the terrestrial case. Moreover, the findings of this thesis may have immediate relevance for possible impactor signatures and melt-mixing processes in tektites and microtektites (e.g., from the Ivory Coast and Australasian strewn fields; Koeberl et al., 2007; Goderis et al., 2017), whose elevated contents of highly-siderophile (i.e., potentially impactor-derived) elements have been discussed as possibly originating from mantle-derived lithologies (see discussion in Goderis et al., 2017). To this end, this thesis combines petrographic and chemical observations on pristine natural and experimental impact melts (Chapters 5, 8, and 10) with specifically tailored laser irradiation experiments aimed at constraining cooling rates of "typical" ballistic melt ejecta (Chapter 7). Special emphasis will be given to mixing processes between structurally and/or compositionally diverse impact melts (Chapters 8 and 10).

3.2.3 Petrogenetic processes in compositionally complex impact melts, with special emphasis to carbonate-bearing targets

Rock-forming processes in endogenous magmas—for instance, emplacement and crystallization of granitic intrusions in the Earth's crust, or metamorphism of such intrusions during orogeny—are usually thought to occur under *chemical equilibrium* (e.g., Spear, 1993; Philpotts and Ague, 2009). For massive impact-melt sheets in complex impact structures, often measured in volumes of 10^4 km^3 (Dressler and Reimold, 2001) and occasionally showing features like columnar jointing also known from classic petrology, crystallization under chemical equilibrium might be realistic and to be expected. On the other hand, typical impact melts produced in small, simple craters as well as impact melts that are ballistically ejected from the crater form, evolve, and cool on such short time scales that chemical equilibrium is usually not attained during crystallization. Fast cooling is typically manifested in strongly zoned, skeletal mafic minerals (e.g., olivine or pyroxene; Hörz et al., 2002; Schultze et al., 2016), reaction coronas around quartz entrained in more mafic impact melts (e.g., Hamann et al., 2013), heterogeneous chemical composition of melt schlieren on millimeter to centimeter scales (e.g., Hörz et al., 1989; See et al., 1998), quench crystallization textures (see summaries in French, 1998; Dressler and Reimold, 2001), and so on, and many impact glasses and impact melt rocks show textures and mineral compositions indicative of rapid quenching. In this respect, impact melts clearly differ from endogenous magmas, and many rock-forming (or glass-forming) processes in impact melts are not well understood. Furthermore, impact melting typically involves temperatures well above the liquidus of typical silicate minerals and rocks (i.e., production of superheated melts)—thus, in this respect, impact melting differs from endogenous processes involving melting at or above solidus. In addition, many classic petrologic approaches such as thermobarometry or thermodynamic modeling based on crystal–melt distribution coefficients have not yet been shown to be applicable to impact melts (see discussion in Timms et al., 2017), as they are usually only valid or calibrated for "low" temperatures <2000 °C (e.g., Hart, 1978; Lindsley and Andersen, 1983; Sack and Ghiorso, 1991; Asimov and Ghiorso, 1998; Korhonen et al., 2014; Timms et al., 2017).

One recurring problem hampering detailed reconstruction of rock-forming processes in impact melts is the high age and poor state of preservation of many terrestrial impact structures (see the Earth Impact Database under www.passc.net/EarthImpactDatabase/index.html). As glasses are generally prone to chemical weathering, devitrifictaion, and hydrothermal alteration, the high ages and geographic locations of many impact structures in humid regions negatively affect the preservation state of associated impact glasses and impact melt rocks. Furthermore, the poor knowledge of impactor type and composition for the overwhelming part of the terrestrial impact structures (not to speak of their lunar, martian, or asteroidal counterparts) makes reconstruction of rock-forming processes in impact melts difficult, as an important component that clearly

played a major role during crater formation (cf. Chapter 2) is unknown. These thoughts demonstrate that in order to reconstruct melt-mixing and petrogenetic processes in impact melts in general, three prerequisites are paramount: (1) detailed knowledge of the impactor, (2) detailed knowledge of the preimpact lithology, and (3) preservation of pristine impactites (i.e., absence of postimpact, secondary alteration processes). Two examples that combine these three prerequisites are the Wabar (e.g., Hörz et al., 1989; Mittlefehldt et al., 1992; Hamann et al., 2013) and Kamil (e.g., Folco et al., 2010; Fazio et al., 2016) impact structures. Both impact structures served as "ground truth" for the MEMIN experiments of Ebert et al. (2013) and Ebert et al. (2014), and in both cases, detailed petrologic reconstructions of melt-mixing processes in small impact structures were possible (Hamann et al., 2013; Fazio et al., 2016). One aspect of these studies was silicate melt unmixing due to *sensu stricto* liquid immiscibility (Hamann et al., 2013), which is a process that—despite its petrogenetic abundance in endogenous magmas (e.g., Roedder and Weiblen, 1970; Roedder and Weiblen, 1971; Philpotts, 1982; Jakobsen et al., 2005; Bogaerts and Schmidt, 2006; Schmidt, 2006; Veksler et al., 2006; Veksler et al., 2007; Charlier et al., 2011; Charlier et al., 2013; Charlier and Grove, 2012; Veksler and Charlier, 2015)—has so-far been only poorly studied in the context of impact melts (cf. Zolensky and Koeberl, 1991; Hamann et al., 2013). Consequently, the studies of Zolensky and Koeberl (1991) and Hamann et al. (2013) inform a study of origin and significance of silicate liquid immiscibility in other well-known and well-preserved impact glasses and melt rocks that will be presented in Chapter 8. However, even when projectile and target as well as details such as impact angle or velocity of the impact scenario are known to the greatest extent possible for a given impact crater, a complete reconstruction of all rock-forming processes—and one that goes beyond the purely descriptive level—is not straightforward, and often afflicted with considerable debate. Good examples are the numerous studies that investigated impact melt formation at Meteor Crater (e.g., Hörz et al., 2002; Mittlefehldt et al., 2005; Artemieva and Pierazzo, 2011; Hörz et al., 2015; Osinski et al., 2015, and references therein), or, although involving much larger size scales and longer time scales, the continuous debate on the mechanism(s) involved in the formation of the Ries suevites (e.g., Stöffler et al., 2013; Artemieva et al., 2013; Osinski et al., 2016; Siegert et al., 2017, and references therein).

The Meteor Crater and the Ries impact events coincidentally both involved carbonate-bearing targets. In addition to being present at Meteor Crater and Ries, carbonates are present in about one third of the presently 190 known impact structures (Osinski et al., 2008). Thus, carbonates form a considerable and abundant rock type on Earth. As will be outlined in more detail in Chapter 10, the response of carbonates to impact is—despite their abundance—subject of a continuous debate within the planetary sciences community. In contrast to the vast amount of knowledge on the shock behavior of most silicates, metals, or sulfides, which simply melt at a given shock-pressure threshold, the response of carbonates to elevated

shock pressures (i.e., sufficiently high to induce melting of coexisting silicates) is poorly understood. Two hypotheses have been put forward:

1. carbonates *decompose* upon impact into residual oxides (e.g., CaO and MgO) as well as CO_2 (e.g., Kieffer and Simonds, 1980; Boslough et al., 1982; O'Keefe and Ahrens, 1989; Pierazzo and Artemieva, 2012; Hörz et al., 2015); and

2. carbonates *melt* upon impact, thereby producing a primary carbonate impact melt phase that subsequently crystallizes upon quenching (e.g., Graup, 1999; Jones et al., 2000; Osinski and Spray, 2001; Osinski et al., 2008; Osinski et al., 2015).

As will be detailed in Chapter 10, arguments for both hypotheses may be found in terrestrial impactites, for example, from Chicxulub (e.g., Jones et al., 2000; Claeys et al., 2003; Deutsch and Langenhorst, 2007), Ries (e.g., Graup, 1999; Stöffler et al., 2013), or Haughton (e.g., Martinez et al., 1994; Osinski and Spray, 2001), and many experiments have provided contrasting and often ambiguous results (see summary in Bell, 2016).

These examples demonstrate that the fate of carbonates upon impact is a highly topical and still unresolved issue in the planetary sciences. Consequently, this thesis will ask:

- What *petrogenetic processes* operate during cooling in compositionally complex impact melts, in particular in those originating from carbonate-bearing targets?

- Can experiments shed light onto transient petrogenetic processes during melt formation and cooling that are inaccessible from natural impactites?

Since both observations from terrestrial craters and previous experiments are ambiguous, a novel experimental approach will be presented in this dissertation that uses laser irradiation to subject *mixed* carbonate–silicate composite targets to P–T conditions commensurate with post-shock phases of impact crater formation. As will be argued in Chapter 10, the fate of carbonates in terrestrial impact scenarios is intimately linked to the fate of coexisting silicates, and the interaction of silicate impact melts and carbonates involves much longer time scales than realized in conventional shock-recovery experiments.

3.2.4 Time scales and cooling rates involved in formation and cooling of ballistic melt ejecta

As apparent from the thoughts outlined above and in Chapter 2, the time spans associated with the cratering process and the formation and mixing of impact melts are short. While numerical models and cratering mechanics constrain general time scales of the cratering process (see Chapter 2), the time scales required—or better: available—for chemical processes (e.g., melt mixing, diffusion, crystallization, glass formation,

etc.) between melt formation and solidification in discrete impact melt particles, in particular ballistic melt ejecta, are not well constrained from observations. Natural impactites sampling discrete impact melt particles (e.g., tektites, glassy impact spherules, melt shards and "Flädle" in melt-bearing impact breccias, etc.) generally attest that they were virtually instantaneously superheated to high temperatures (generally >1700 °C) and subsequently rapidly quenched during melt ejection from the crater or emplacement inside the crater (Dressler and Reimold, 2001, and references therein). Massive melt volumes such as melt sheets or melt pools, on the other hand, cool substantially slower and, thus, may resemble exposures of normal endogenic igneous rocks (e.g., massive impact melt rocks with columnar joining at Mistastin Lake; see French, 1998, fig. 6.1). However, this thesis will not be concerned with massive melt sheets, but focus on abundant discrete, millimeter to decimeter size melt bodies ubiquitous to many terrestrial (and also lunar) craters that form, evolve, cool, and solidify on very short timescales.

Consequently, one of the questions that will frequently appear within Parts II and III is:

- What are typical *time scales* and *cooling rates* involved in formation and cooling of millimeter- to centimeter-sized ballistic melt ejecta (e.g., melt spherules, tektites, etc.)?

Estimating the *minimum* time scales associated with petrogenetic processes in impact melts is one of the aims of this thesis, as is determination (i.e., measurement) of cooling rates associated with ballistic, millimeter to decimeter size melt ejecta. Of course, this can be readily done using numerical models (e.g., Stöffler et al., 2002) or simple thermodynamic reasoning (e.g., Chapter 7), but this thesis will try to provide some direct constraints in Chapters 7 and 10 by employing specifically tailored experiments.

3.2.5 Application of impact experiments to nature

Impact experiments have been proven to be a valuable tool to study specific aspects of impact cratering and impact melting. Among these are mode of emplacement of impact melts in impact craters (e.g., Stöffler et al., 1975; Evans et al., 1994; Wozniakiewicz et al., 2011; Wozniakiewicz et al., 2012; Wozniakiewicz et al., 2015; Daly and Schultz, 2016; Wünnemann et al., 2016), chemical interaction between projectile and target (e.g., Hörz et al., 1983; Ebert et al., 2013; Ebert et al., 2014), or establishment of shock calibration schemes (e.g., Stöffler et al., 1975; Kieffer et al., 1976a; Ebert et al., 2013). However, laboratory impacts on the meso- to macroscale are currently limited to velocities of ~6–8 km s^{-1}, projectile masses of a few grams, and total impact melt volumes of a few tens of cubic centimeters at best. Thus, one argument that is often put forward against impact experiments is that they only marginally, if at all, reach the magnitudes of typical planetary impact events. Even after some 50 years of application,

the issue of whether or not the results of such experiments may be "scaled up" to natural planetary impact events is still standing.

Although experimental products (glassy impact ejecta) are often compared to terrestrial impactites (e.g., Ebert et al., 2013; Ebert et al., 2014) or vice versa (Fazio et al., 2016), only very few studies have been concerned with an immediate comparison between experimental products and nature. One example is the study of Kieffer et al. (1976a), who compared shock-metamorphosed basalt from Lonar crater, India, to experimentally shocked basalt samples and who concluded that, with respect to the onset of specific shock effects, experiment and nature are indeed similar. In a similar fashion, this thesis will be concerned with evaluating if, and if so, to which extend, chemical and rock-forming processes in some typical, well-preserved terrestrial impact melts are similar to processes in experimentally produced melts. Specifically, two questions are asked:

- Are hypervelocity impact experiments a suitable tool to study melt-mixing processes in and petrogenesis of impact melts?
- Can such results be "scaled up" to natural impact scenarios?

Chapter 4

Personal contribution and structure of this thesis

This dissertation comprises four published, peer-review articles, one manuscript under review at a peer-reviewed journal, and two conference abstract, which each form separate chapters within Parts II and III of this thesis. These previous publications were produced jointly with several colleagues and collaborators, and the results were presented in oral and poster contributions at international conferences (a complete list of all conference abstracts that were produced before or during publication of these articles is given at the end of this chapter). As mentioned before, the scientific work of the articles and conference contributions was conducted in the framework of the DFG research unit FOR 887 MEMIN and on the basis of a research proposal by Lutz Hecht (MfN Berlin) and Alex Deutsch (WWU Münster). In the context of MEMIN, this subproject had the title "Projectile–target interaction, melting, and vaporization in hypervelocity experiments and natural impactites" (DFG grant He-2893/8-2).

4.1 Personal contribution

The four published articles and the submitted manuscript that form Parts II and III are:

1. Hamann, C., Stöffler, D., and Reimold, W. U. (2016). Interaction of aluminum projectiles with quartz sand in impact experiments: formation of khatyrkite ($CuAl_2$) and reduction of SiO_2 to Si, *Geochimica et Cosmochimica Acta* 192, 295–317, http://dx.doi.org/10.1016/j.gca.2016.07.018.

2. Hamann, C., Luther, R., Ebert, M., Hecht, L., Deutsch, A., Wünnemann, K., Schäffer, S., Osterholz, J., and Lexow, B. (2016). Correlating laser-generated melts with impact-generated melts: an integrated thermodynamic–petrologic approach, *Geophysical Research Letters* 43, 10602–10610, http://dx.doi.org/10.1002/2016GL071050.

3. Van Roosbroek, N., Hamann, C., McKibbin, S., Greshake, A., Wirth, R., Pittarello, L., Hecht, L., Claeys, P., and Debaille, V. (2017). Immiscible silicate liquids and phosphoran olivine in Netschaëvo IIE silicate: analogue for planetesimal core–mantle boundaries, *Geochimica et Cosmochimica Acta* 197, 378–395, http://dx.doi.org/10.1016/j.gca.2016.10.042.

4. Hamann, C., Fazio, A., Ebert, M., Hecht, L., Wirth, R., Folco, L., Deutsch, A., and Reimold, W. U. (in press). Silicate liquid immiscibility in impact melts, *Meteoritics & Planetary Science*, http://dx.doi.org/10.1111/maps.12907.

5. Hamann, C., Bläsing, S., Hecht, L., Schäffer, S., Deutsch, A., Osterholz, J., and Lexow, B. The reaction of carbonates in contact to laser-generated, superheated silicate melts: constraining impact metamorphism of carbonate-bearing, sedimentary target rocks, Manuscript submitted to *Meteoritics & Planetary Science*.

Parts I and IV were written especially for this thesis; all individual chapters within these parts were written and revised by the PhD applicant. As each of the chapters contained within Parts II and III is not only concerned with the major research topics outlined in the previous chapter, but also with several side questions and findings that are not immediately relevant to this thesis, brief summaries are given at the beginning of each of these chapters that were written especially for this thesis. These summaries state each chapter's major findings and will serve as a basis for the conclusions presented in Part IV. The remaining text of these chapters is then given as published.

Article 1 forms Chapter 5 of this thesis. The research presented in this article was conducted within the framework of MEMIN, although the experiments were already performed in the 1970s at NASA Ames Vertical Gun Range, Moffett Field, California, by Dieter Stöffler (at that time: WWU Münster; now: MfN Berlin). After relocation of the experimental products from WWU Münster to MfN some 30 years later, the PhD candidate performed a petrologic–geochemical investigation of impact melt particles recovered from impact experiments with aluminum projectiles shot into quartz sand (Series II experiments; see Chapter 5).

The PhD candidate performed all petrologic–geochemical research; interpreted petrographic and geochemical data; carried out a literature survey that served as a basis for the discussion; calculated shock pressures by means of the planar impact approximation; wrote preliminary and final versions of this article and the supplementary information; arranged all figures and tables; and managed the manuscript through the peer-review process under the supervision of Dieter Stöffler and Uwe Reimold (MfN Berlin). Dieter Stöffler and Uwe Reimold contributed to discussions and improved focus and clarity of the manuscript. Hans-Rudolf Knöfler (MfN) prepared some additional thin sections used for this work;

Kathrin Krahn (MfN) and Ralf-Thomas Schmitt (MfN) provided bulk geochemical analyses of the quartz sand target used in these experiments by means of XRF.

Article 2 forms Chapter 7 of this thesis. The research presented in this article was conducted within the framework of MEMIN. The basic idea for the laser irradiation experiments described in this work was provided by Lutz Hecht and Matthias Ebert (ALU Freiburg), who used a similar experimental approach in the first funding round of MEMIN (Ebert et al., 2017). The thermodynamic considerations outlined in Article 2 are based on a suggestion by one of the reviewers that was made during the peer-review process of the article by Ebert et al. (2017). (The PhD applicant is a co-author of this study; the laser irradiation experiments described there were performed earlier, but the methods described in Chapter 7 were subsequently applied to these experiments.) They were subsequently further developed by the PhD candidate under supervision of Kai Wünnemann (MfN Berlin) and Natasha Artemieva (PSI Tucson/Russian Academy of Science). The laser irradiation experiments described in Article 2 were conducted at Fraunhofer-Institut für Kurzzeitdynamik, Freiburg, Germany, by the PhD candidate in cooperation with Sebastian Schäffer (EMI Freiburg) and Dominik Heunoske (EMI Freiburg). Hans-Rudolf Knöfler prepared sections of the experimental products; Kathrin Krahn and Ralf-Thomas Schmitt carried out bulk geochemical analyses of the quartz sand target used in these experiments by means of XRF. Robert Luther (MfN) performed the ANEOS calculations under supervision of Kai Wünnemann and provided data for Fig. 7.3.

The PhD candidate performed all petrologic research; calculated the entropy gains of the materials according to Eq. (7.2); wrote preliminary and final versions of this article and the supplementary information; arranged all figures and tables; and managed the manuscript through the peer-review process under the supervision of Lutz Hecht and Alex Deutsch. All co-authors contributed to discussions and Lutz Hecht and Kai Wünnemann improved focus and clarity of the manuscript.

Article 3 forms Chapter 9 of this thesis. The PhD candidate is the second author of this article and also the corresponding author. This article is a collaboration between the PhD candidate and Nadia Van Roosbroek, a former PhD candidate at Université Libre de Bruxelles and Vrije Universiteit Brussel. For this work, the PhD candidate was supervised by Lutz Hecht and Ansgar Greshake (MfN Berlin); Nadia Van Roosbroek was supervised by Philippe Claeys (Vrije Universiteit Brussel) and Vinciane Debaille (Université Libre de Bruxelles).

The PhD candidate performed all analytical TEM work under supervision of Richard Wirth (GFZ Potsdam); the introduction to the method by Richard Wirth occurred already during a previous study (Hamann et al., 2013). Anja Schreiber (GFZ Potsdam) prepared the relevant TEM foil by FIB preparation. The PhD candidate interpreted all TEM data, arranged all

figures and tables, wrote the results section, wrote the liquid immiscibility-relevant parts of the discussion, and managed the manuscript through the peer-review process with help of Sean McKibbin and Lidia Pittarello (both Vrije Universiteit Brussel) and under the supervision of Lutz Hecht and Philippe Claeys (Nadia Van Roosbroek had finished her PhD by that time and was unavailable for manuscript handling). Nadia Van Roosbroek provided EMPA data on bulk materials, wrote the introduction and specific parts of the discussion, and provided comments and suggestions to the results section. Sean McKibbin performed the geochemical calculations outlined in the discussion and wrote relevant parts of the discussion. All co-authors contributed to discussions and helped in improving focus and clarity of the manuscript.

Article 4 forms Chapter 8 of this thesis. The research presented in this article was conducted within the framework of MEMIN. The PhD candidate conceived the basic idea for this study; did all analytical work (SEM, EMPA, and TEM) with technical assistance of Peter Czaja (MfN Berlin) and Richard Wirth; interpreted petrographic and geochemical data; carried out a literature survey that served as a basis for the discussion; wrote preliminary and final versions of this article; arranged all figures and tables; and managed the manuscript through the peer-review process under the supervision of Lutz Hecht and Alex Deutsch. Agnese Fazio (University of Jena) and Matthias Ebert provided the Kamil and some of the MEMIN samples, respectively, and Lutz Hecht and Wolf Uwe Reimold provided the Tenoumer samples. Agnese Fazio also provided the geologic background for Kamil. All co-authors contributed to discussions and Luigi Folco (University of Pisa), Uwe Reimold, and Lutz Hecht helped in improving focus and clarity of the manuscript.

Article 5 forms Chapter 10 of this thesis. The research presented in this article was conducted within the framework of MEMIN. The laser irradiation experiments described in Article 5 were conducted at Fraunhofer-Institut für Kurzzeitdynamik, Freiburg, Germany, by the PhD candidate in cooperation with Sebastian Schäffer and Dominik Heunoske.

The PhD candidate conceived the basic experimental setup for this study under supervision of Lutz Hecht; did all micro-analytical work with technical assistance of Peter Czaja and Kirstin Born (MfN Berlin); interpreted petrographic and geochemical data; carried out a literature survey that served as a basis for the discussion; wrote preliminary and final versions of this article; arranged all figures and tables; and managed the manuscript through the peer-review process under the supervision of Lutz Hecht and Alex Deutsch. Saskia Bläsing (FU Berlin/MfN Berlin) provided additional carbonate analyses from her MSc project; Kathrin Krahn and Ralf-Thomas Schmitt provided bulk chemical compositions via XRF; Hans-Rudolf Knöfler prepared all sections used in this study. All co-authors contributed to discussions and Lutz Hecht and Alex Deutsch helped in improving focus and clarity of the manuscript.

Conference abstracts Some of the contents of Chapter 6 have been previously presented in the form of two conference abstracts:

1. Hamann, C., Zhu, M.-H., Wünnemann, K., Hecht, L., and Stöffler, D. (2016). Tracing shock wave attenuation in porous, particulate targets: insights from impact experiments and numerical modeling, *79th Annual Meeting of The Meteoritical Society*, Abstract #6335, https://www.hou.usra.edu/meetings/metsoc2016/pdf/6335.pdf.

2. Wünnemann, K., Engelmann, J., Luther, R., Hamann, C., and Zhu, M.-H. (2017). Impact-induced shock melting and ejection of material in an asteroidal environment—implications for the deficit in melt agglutinates in Itokawa samples, *48th Lunar and Planetary Science Conference*, Abstract #2023, https://www.hou.usra.edu/meetings/lpsc2017/pdf/2023.pdf.

Chapter 6 was especially written for this thesis by the PhD candidate, but draws on the material presented in these previous abstracts.

The PhD candidate conceived the basic scientific idea behind Abstract 1; he wrote preliminary and final versions of the abstract and presented the material in an oral contribution at the conference. Meng-Hua Zhu (University of Macau/MfN Berlin) and Kai Wünnemann performed the numerical modeling described in this abstract; the PhD candidate used this model for a time-resolved reconstruction of the P–T conditions at the projectile–target interface.

To Abstract 2, the PhD candidate provided the petrographic observations used in the abstract and discussed the numerical modeling results with the co-authors.

Other publications The following articles were written and published in collaboration with the PhD candidate in 2016 and 2017. Except for Articles 6 and 8, these publications are not immediately concerned with impact melting and, therefore, are not included as individual chapters in this thesis.

6. Ebert, M., Hecht, L., Hamann, C., and Luther, R. (2017). Laser-induced melting experiments: simulation of short-term high-temperature impact processes, *Meteoritics & Planetary Science* 52, 1475–1494, http://dx.doi.org/10.1111/maps.12809.

7. Stöffler, D., Hamann, C., and Metzler, K. (in press). Shock metamorphism of planetary silicate rocks and sediments: proposal for an updated classification system, *Meteoritics & Planetary Science*, http://dx.doi.org/10.1111/maps.12912.

8. Wilk, J., Hamann, C., Fazio, A., Luther, R., Hecht, L., Langenhorst, F., and Kenkmann, T., Melt formation on shatter cones recovered from the MEMIN impact experiments in sandstone, Manuscript submitted to *Meteoritics & Planetary Science*.

9. Kenkmann, T., Deutsch, A., Thoma, K., Ebert, M., Poelchau, M. H., Bulh, E., Carl, E.-R., Danilewsky, A. N., Dresen, G., Dufresne, A., Durr, N., Ehm, L., Hecht, L., Hiermaier, S., Hoerth, T., Grosse, T., Gulde, M., Güldemeister, N., Hamann, C., Kowitz, A., Langenhorst, F., Lexow, B., Liermann, H.-P., Luther, R., Mansfeld, U., Moser, D., Raith, M., Reimold, W. U., Sauer, M., Schäfer, F., Schmitt R. T., Sommer, F., Wilk, J., Winkler, R., and Wünnemann, K. Experimental impact cratering: a summary of the major results of the MEMIN research unit, Manuscript submitted to *Meteoritics & Planetary Science*.

Other conference abstracts The conference abstracts related to Articles 1 to 5 are:

3. Hamann, C., Hecht, L., Schultze, D., Ebert, M., Reimold W. U., and Wirth, R. (2014). Silicate liquid immiscibility in yound impact glasses, *77th Annual Meeting of The Meteoritical Society*, Abstract #5222, https://www.hou.usra.edu/meetings/metsoc2014/pdf/5222.pdf.

4. Hamann, C., Fazio, A., Schultze, D., Ebert, M., Hecht, L., Reimold W. U., and Wirth, R. (2015). Silicate liquid immiscibility in natural and experimental impact melts, *46th Lunar and Planetary Science Conference*, Abstract #2071, https://www.hou.usra.edu/meetings/lpsc2015/pdf/2071.pdf.

5. Hamann, C., Hecht, L., and Deutsch, A. (2015). Shock behavior of calcite and basalt in a MEMIN hypervelocity impact experiment and laser melting experiments, *46th Lunar and Planetary Science Conference*, Abstract #2497, https://www.hou.usra.edu/meetings/lpsc2015/pdf/2497.pdf.

6. Hamann, C., Hecht, L., and Deutsch, A. (2015). Impact-induced devolatilization or melting of calcite? Or both? Answers from MEMIN experiments, *78th Annual Meeting of The Meteoritical Society*, Abstract #5115, https://www.hou.usra.edu/meetings/metsoc2015/pdf/5115.pdf.

7. Hamann, C., Van Roosbroek, N., Greshake, A., Pittarello, L., Hecht, L., Debaille, V., Wirth, R., and Claeys, P. (2015). Occurrence of siliceous impact melt in Netschaëvo IIE? A FIB–TEM study, *78th Annual Meeting of The Meteoritical Society*, Abstract #5117, https://www.hou.usra.edu/meetings/metsoc2015/pdf/5117.pdf.

8. Hamann, C., Hecht, L., and Deutsch, A. (2015). First evidence of calcite melts in recent MEMIN impact experiments, *Goldschmidt 2015*, Abstract #1154, https://goldschmidt.info/2015/uploads/abstracts/finalPDFs/1154.pdf.

9. Hecht, L., Ebert, M., and Hamann, C. (2015). Laser-induced melting experiments: simulation of impact processes, *Goldschmidt 2015*, Abstract #1218, https://goldschmidt.info/2015/uploads/abstracts/finalPDFs/1218.pdf.

10. Van Roosbroek, N., Pittarello, L., Hamann, C., Greshake, A., Debaille, V., Wirth, R., and Claeys, P. (2015). First findings of impact melt in the IIE Netschaëvo meteorite, *Goldschmidt 2015*, Abstract #3241, https://goldschmidt.info/2015/uploads/abstracts/finalPDFs/3241.pdf.

11. Hamann, C., Stöffler, D., and Reimold, W. U. (2015). Experimental impacts of aluminum projectiles into quartz sand: formation of khatyrkite $CuAl_2$ and reduction of quartz to silicon, *Bridging the Gap III*, Abstract #1071, https://www.hou.usra.edu/meetings/gap2015/pdf/1071.pdf.

12. Hamann, C., Hecht, L., and Deutsch, A. (2015). On the shock behavior of calcite: recent results from MEMIN experiments, *Bridging the Gap III*, Abstract #1093, https://www.hou.usra.edu/meetings/gap2015/pdf/1093.pdf.

13. Ebert, M., Hamann, C., Hecht, L., Deutsch, A., and Kenkmann, T. (2015). Bridging the gap between laboratory and nature: geochemical clues form experimental approaches, *Bridging the Gap III*, Abstract #1055, https://www.hou.usra.edu/meetings/gap2015/pdf/1055.pdf.

14. Wilk, J., Hamann, C., Kenkmann, T., and Hecht, L. (2015). Melt formation on shatter cone surfaces in sandstone, Part I: surface morphology, *47th Lunar and Planetary Science Conference*, Abstract #2636, https://www.hou.usra.edu/meetings/lpsc2016/pdf/2636.pdf.

15. Hamann, C., Wilk, J., Hecht, L., and Kenkmann, T. (2015). Melt formation on shatter cone surfaces in sandstone, Part II: melt composition, *47th Lunar and Planetary Science Conference*, Abstract #2381, https://www.hou.usra.edu/meetings/lpsc2016/pdf/2381.pdf.

16. Hamann, C., Hecht, L., Schäffer, S., Deutsch, A., and Lexow, B. (2016). The reaction of carbonates in contact with superheated silicate melts: new insights from MEMIN laser melting experiments, *79th Annual Meeting of The Meteoritical Society*, Abstract #6285, https://www.hou.usra.edu/meetings/metsoc2016/pdf/6285.pdf.

17. Wilk, J., Hamann, C., Hecht, L., and Kenkmann, T. (2016). Melt formation on shatter cone surfaces recovered from the MEMIN hypervelocity impact experiments in sandstone, *79th Annual Meeting of The Meteoritical Society*, Abstract #6523, https://www.hou.usra.edu/meetings/metsoc2016/pdf/6523.pdf.

18. Ebert, M., Hecht, L., and Hamann, C. (2016). Simulation of short-term high-temperature impact processes by using a high-energy laser beam, *79th Annual Meeting of The Meteoritical Society*, Abstract #6382, https://www.hou.usra.edu/meetings/metsoc2016/pdf/6382.pdf.

19. Wilk, J., Kenkmann, T., and Hamann, C. (2017). New insights into shatter cone formation from MEMIN experiments, *European Planetary Science Congress 2017*, Abstract #EPSC2017-912, http://meetingorganizer.copernicus.org/EPSC2017/EPSC2017-912.pdf.

4.2 Structure

This thesis is divided into five consecutive parts. After the stage has been set and an introduction to the research topic has been given in this part, Parts II and III will be concerned with presenting and discussing results. Part IV will be concerned with discussing major results in the light of the four fundamental aspects presented in Chapter 3. Moreover, major conclusions are drawn, and a brief outlook for future studies is presented. Eventually, Part V presents supplementary information.

The contents of Parts II to V are briefly stated in the following.

Part II: reconstructing the projectile–target interface

Chapter 5 deals with an in situ reconstruction of chemical and physical processes at the interface between projectile and target in impact experiments. It presents a detailed petrographic characterization of impact melt particles recovered from the bottoms of impact craters experimentally produced in particulate targets (Section 5.4). Then, it discusses redox reactions between metal projectiles and silicate targets (Subsection 5.5.1) and presents implications for impact melting of asteroidal regoliths under similar impact conditions (Subsection 5.5.2).

Chapter 6 combines the petrographic findings from Chapter 5 with numerical simulations of the experiments. It provides additional evidence that the impact melt particles preserved the projectile–target interface at very early time steps during crater formation, and essentially sample the bottoms of the transient craters.

Part III: geochemical processes in impact melts

Chapter 7 is concerned with basic groundwork carried out to establish direct, continuous-wave laser irradiation as a novel experimental method in the planetary sciences. The basic idea and underlying theory for laser irradiation of planetary materials as a viable experimental approach to the research topic is given (Section 7.2), and a thermodynamic comparison between impact melts and laser-generated melts (Section 7.4) is presented and discussed in the

following. This experimental approach will be the basis for the subsequent Chapters 8 and 10.

Chapters 8–10 are then concerned with petrologic processes in impact melts that originated from a variety of impact scenarios. These include mingling and mixing of structurally/compositionally different, miscible or immiscible impact melts (Chapter 8), chemical interaction of these melts (Chapters 8, 9, and 10), liquid immiscibility (Chapters 8 and 9), carbonate decomposition and carbonate assimilation by silicate melts (Chapter 10), as well as general observations on crystallization and glass formation.

Part IV: conclusions and outlook

Chapter 11 picks up and discusses the four fundamental aspects presented in Chapter 3 and wraps everything up by drawing general conclusions that emerge from this dissertation.

Chapter 12 is eventually concerned with some open questions and a presentation of a brief outlook for future studies.

Part V: appendices

Appendix A presents supporting information to Chapter 5.

Appendix B presents supporting information to Chapter 7.

Appendix C presents supporting information to Chapter 9.

Appendix D presents supporting information to Chapter 10.

Part II

Reconstructing the projectile–target interface

Chapter 5

Reconstructing the projectile–target interface in impact experiments[1]

In this chapter, the interfaces between aluminum projectiles and quartz sand targets are reconstructed based on a petrologic study of layered impact melt particles. These particles were recovered from the floors of impact craters formed in impact experiments that employed similar impact velocities (~6 km s^{-1}) and target properties (e.g, grain size, porosity, impedance contrast, etc.) like small-scale impacts onto regolith-covered planetary surfaces in the asteroid belt. It will be shown that under these impact conditions, projectile-derived, metallic melts coat the surfaces of layered, partially molten, shock-metamorphosed particles that essentially represent the uppermost parts of the crater floors and, thus, also the melt zones of the craters. In the form of distinct layers of successively decreasing shock intensity, ranging from complete melting to below Hugoniot elastic limit, these particles document successive attenuation of the shock wave from highest to lowest peak shock pressure. The topmost, completely molten parts of the quartz sand target reacted in a redox reaction ($3\,SiO_2 + 4\,Al \rightarrow 3\,Si + 2\,Al_2O_3$) with projectile melts along the projectile–target interface, and liquid Al metal was disseminated in the target melts. These findings represent the first *complete* and in situ petrographic documentation of a preserved projectile–target interface, and show that the chemical interaction between projectile and target can be exceptionally fast. Eventually, this Chapter closes with a discussion of these findings with respect to typical small-scale impact scenarios on the Moon and in the asteroid belt, and the applicability to impacts of iron meteorites into silica-rich targets.

Key points:

In situ reconstruction of completely preserved interfaces between metallic projectiles and granular silicate targets

Characterization of a continuous set of petrographic effects induced by shock wave attenuation, ranging from complete melting to below Hugoniot elastic limit

Application of experimental results to impact scenarios of similar scale on the Moon and in the asteroid belt

[1]This chapter has been published as: Hamann, C., Stöffler, D., and Reimold, W. U. (2016). Interaction of aluminum projectiles with quartz sand in impact experiments: formation of khatyrkite ($CuAl_2$) and reduction of SiO_2 to Si, *Geochimica et Cosmochimica Acta* 192, 295–317, http://dx.doi.org/10.1016/j.gca.2016.07.018.

Summary

This is the abstract of the original publication, but its title has been changed to "summary" in order to delimit it from the brief abstract given on the previous page (the original abstract summarizes several findings that are not immediately relevant to this thesis—in this respect, it has more the character of a summary than an abstract). To ensure consistency throughout this thesis, the subfigure labels (a, b, c, etc.) of the original publication have been adjusted to match the style of the previous subfigure captions. The main text, all figure and table captions, the table contents, as well as the supplementary material (Chapter A) are as published.

We analyzed the interaction of spherical, 6.36-mm-diameter, Cu-bearing aluminum projectiles with quartz sand targets in hypervelocity impact experiments performed at NASA Ames Vertical Gun Range. Impact velocities and inferred peak shock pressures varied between 5.9 and 6.5 km s^{-1} and 41 and 48 GPa, respectively. Shocked particles ("impact melt particles") coated with thin crusts of molten projectile material were recovered from the floors of the ca. 33-cm-diameter craters and the respective ejecta blankets. Through petrographic and chemical (optical microscopy, FE-EMPA, SEM-EDX, and XRF) analysis we show that these particles have a layered structure manifested in distinct layers of decreasing shock metamorphism. These can be characterized by the following physical and chemical reactions and alteration products: (1) complete melting and subsequent recrystallization of the projectile, forming a distinct crystallization texture in the fused metal crust; (2) projectile–target mixing, involving a redox reaction between Cu-bearing Al alloy und SiO_2, leading to formation of khatyrkite ($CuAl_2$), Al_2O_3 melt, euhedral silicon crystals, and spherical droplets of silicon; (3) melting of quartz to lechatelierite and formation of planar deformation features in relic quartz grains; and (4) shock lithification of quartz grains with fracturing of grains, grain-boundary melting, planar deformation features, and complete loss of porosity. To our knowledge, this is the first report of khatyrkite formed experimentally in hypervelocity impact experiments. These results have implications for the understanding of a similar redox reaction between Al–Cu metal and siliceous impact melt recently postulated for the Khatyrka CV_3 carbonaceous chondrite. Moreover, these results bear on the processes that lead to layers of regolith on the surfaces of planetary bodies without atmospheres, such as asteroids in the main belt (e.g., 4 Vesta), and on the Moon. Specifically, impacts of mm-sized projectiles at velocities between 4 and 6 km s^{-1} into regolith-covered, asteroidal surfaces in the main belt should yield similar impact melt particles that feature a continuum of shock effects, that is, partially to completely molten projectile remnants adhering to impact-melted regolith agglomerates, as well as projectile-contaminated impact melts and local shock melting along grain boundaries.

5.1 Introduction

It is widely accepted that impact cratering at various scales is a basic geologic process in the solar system. Impact processes certainly prevailed over endogenic geologic processes during the early evolution of the geologically active planetary bodies and were dominant throughout the complete history of geologically inactive, smaller bodies. As most planetary surface layers are highly porous and/or composed of non-cohesive materials (e.g., the lunar regolith or the surfaces of asteroids and comets), understanding of the influence of pore space and lack of cohesion of granular target

materials on the impact mechanism is crucial. To this end, a multitude of theoretical and experimental studies aiming at a better understanding of impacts into porous materials have been, and still are, conducted (e.g., Gault et al., 1968; Braslau, 1970; Stöffler et al., 1975; Cintala and Hörz, 1990; Cintala et al., 1999; Anderson et al., 2004; Hermalyn and Schultz, 2011; Kowitz et al., 2013a; Kowitz et al., 2013b; Ebert et al., 2013; Ebert et al., 2014; Daly and Schultz, 2016). Furthermore, impact experiments have provided insight into the formation mechanisms of lunar (e.g., Hörz and Cintala, 1997) and asteroidal (e.g., Hörz et al., 2005; Daly and Schultz, 2016) regoliths. Only a few of these studies have dealt with the chemical interaction between projectile and target. However, results from impact experiments (e.g., Hörz et al., 1983; Evans et al., 1994; Wozniakiewicz et al., 2011; Wozniakiewicz et al., 2012; Wozniakiewicz et al., 2015; Ebert et al., 2013; Ebert et al., 2014; Daly and Schultz, 2016) and studies of natural impact structures (e.g., Hörz et al., 1989; Hörz et al., 2002; See et al., 1998; Hamann et al., 2013) have clearly indicated the importance of melting, vaporization, and mixing between projectile and target, as well as chemical reaction (e.g., fractionation) processes.

One of the early investigations of impacts into non-cohesive targets is that of Stöffler et al. (1975), which was performed in the 1970s at the NASA Ames Vertical Gun Range (AVGR) in Moffett Field, California. Seventeen impact experiments were performed, shooting cylindrical (7.9 mm in diameter, 0.51 mm in length) Lexan and spherical, 6.36-mm-diameter aluminum alloy (Al–Cu–Mg–Si) projectiles at velocities of 5.86–6.90 km s^{-1} into layers of loose and differently colored quartz sand in order to quantitatively measure the mass distribution and shock-metamorphic properties of resulting ejecta particles. Only the results of the eight experiments using Lexan projectiles (Series I) were published at the time (Stöffler et al., 1975). Although presented at conferences in the early 1980s (Stöffler et al., 1980b; Stöffler et al., 1980a; Jammes et al., 1983), the results of the remaining nine experiments using aluminum projectiles (Series II) have never been published, but recently these experiments were reinvestigated (this work; Hamann et al., 2015; Wünnemann et al., 2015; Wünnemann et al., 2016).

A remarkable result of the previous study of ejecta particles from experiments with aluminum projectiles is the formation of silicon crystals as a consequence of a redox reaction between the aluminum projectile and the quartz sand target, as well as the formation of an Al–Cu-rich phase that is essentially absent in the unshocked projectile(Stöffler et al., 1980b; Stöffler et al., 1980a; Jammes et al., 1983). Specifically, SiO_2 from the target is reduced to Si, whereas Al from the projectile is oxidized to Al_2O_3, following the simple, strongly exothermic ($\Delta H = -619$ kJ) aluminothermic redox reaction $3\,SiO_2 + 4\,Al \rightarrow 3Si + 2\,Al_2O_3$. Although being an interesting fact per se, this finding cannot be applied to impacts of iron meteorites consisting of FeNi metal, as similar reactions involving the oxidation of Fe and Ni are strongly endothermic (e.g., $2\,Fe + SiO_2 \rightarrow 2\,FeO + Si$;

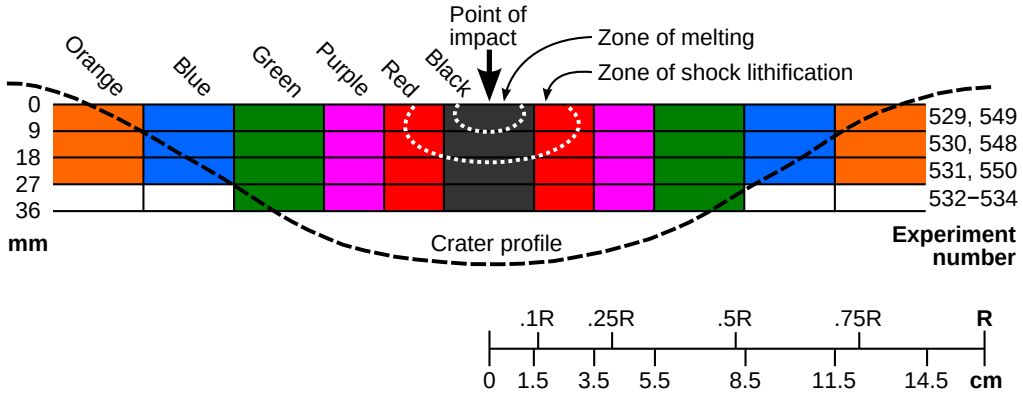

Figure 5.1 The experimental setup of the quartz sand target used for the experiments with Al projectiles (see Table 5.1). Horizontal layers of sand with six concentric, differently colored rings were placed at target depths of 0, 9, 18, and 27 mm, respectively, in order to trace particle movement due to impact. The dashed black line represents the average impact crater profile and the stippled white lines indicate the average zones of melting and shock lithification, respectively, for a series of four experiments (shots 529–532).

ΔH = 2189 kJ). Moreover, oxidation of FeNi metal will take place at far more oxidizing conditions than those required for reducing SiO_2 to Si.

Here, we (1) investigate impact melting and projectile–target interaction in shocked particles, (2) document the aluminothermic redox reaction between aluminum projectile and quartz sand target, and (3) document the formation of khatyrkite ($CuAl_2$) in impact melt particles, a mineral previously identified in the Khatyrka CV3 carbonaceous chondrite (Bindi et al., 2012; Hollister et al., 2014; Hollister et al., 2015, and references therein). Our study is closely related to a more comprehensive reinvestigation of the impact experiments with quartz sand targets performed in 1970/1971 at NASA AVGR (Wünnemann et al., 2016). This paper represents a quantitative analysis of the crater forming process and the mass distribution and shock metamorphism of ejecta using numerical modeling tools involving both Series I (Lexan) and Series II (Al) experiments.

5.2 Experimental and analytical methods

5.2.1 Experimental conditions

The Series II impact experiments under discussion were performed using a two-stage light-gas gun at AVGR. As documented in more detail by Wünnemann et al. (2016), 6.36-mm-diameter aluminum spheres with an average mass of 0.38 g were accelerated to velocities between 5.86 and 6.46 km s^{-1}, corresponding to impact energies between 6.52 and 7.93 kJ (Table 5.1). The projectiles were shot onto a target container (a cylinder of 60 cm diameter and 20.5 cm depth) filled with quartz sand of grain sizes between 0.06 and 0.25 mm. To facilitate tracking of particle movement in the crater and in the ejecta curtain, a 9-mm-thick, horizontal layer of colored sand was included in the target of each experiment. Within the marker bed, differently colored sand strata were used within different, concentric zones to identify the initial radial position of the ejecta

Table 5.1 Experimental conditions and crater parameters for impacts of aluminum projectiles into quartz sand performed at NASA Ames Vertical Gun Range. Samples from experiments 530, 533, and 534 were studied in detail.

Experiment No.	Impact velocity [km/s]	Kinetic energy [kJ]	Shock pressure[a] [GPa]	Crater diameter[b] [cm]
529	6.44	7.88	48(3)	32.8
530	**6.46**	**7.93**	**48(3)**	**33.1**
531	6.17	7.23	45(3)	32.8
532	6.24	7.40	46(3)	32.6
549	5.86	6.52	41(3)	32.0
548	5.99	6.82	42(3)	31.9
550	5.97	6.77	42(3)	32.4
534	**6.32**	**7.59**	**46(3)**	**33.7**
533	**6.11**	**7.09**	**43(3)**	**32.6**

The experiments given in bold were studied in detail.
[a] Shock pressure at the point of impact, calculated using the planar impact approximation (Melosh, 1989, and Figs. A.1 and A.2 in Appendix A). Aluminum projectile parameters: $C = 5.30$ km s^{-1}, $S = 1.37$, $\rho_0 = 2750$ kg m^{-3} (Melosh, 1989); dry sand target parameters: $C = 1.70$ km s^{-1}, $S = 1.31$, $\rho_0 = 1600$ kg m^{-3} (Melosh, 1989); $C = 0.95$ km s^{-1}, $S = 1.34$, $\rho_0 = 1550$ kg m^{-3} (Trunin et al., 2001); $C = 0.62$ km s^{-1}, $S = 1.61$, $\rho_0 = 1510$ kg m^{-3} (Güldemeister et al., 2013). Using these three parameter sets, the estimated uncertainty in calculating the shock pressure is ca. 3 GPa.
[b] Crater diameter measured at rim.

(Fig. 5.1). Four different target configurations were used, with the horizontal marker layer at depths of 0, 9, 18, and 27 mm, respectively; the sand above and below the marker layer was uncolored. For each target configuration, at least two experiments were performed as labeled in Fig. 5.1 to test reproducibility. Peak shock pressures at the point of impact were calculated from the planar impact approximation, using equation-of-state parameters for aluminum and dry sand from Melosh (1989). Because shock pressure will be sensitive to the exact porosity of the sand target, we additionally used Hugoniot data for powdered quartzite (porosity 43%, density 1510 kg m^{-3}) from Güldemeister et al. (2013) and for quartz sand (porosity 43%, density 1550 kg m^{-3}) from Trunin et al. (2001) to present a measure of uncertainty in the pressure estimates. The derivation of the alternative C (y-intercept of a line in a shock velocity vs. particle velocity plot; dimension of km s^{-1}) and S (slope of the line; dimensionless) parameters for the pressure calculations is given in Fig. A.1 in Appendix A. As detailed in Table 5.1 and Fig. A.2, the peak shock pressure at the point of impact for the experiments varied between 41 ± 3 GPa at 5.86 km s^{-1} and 48 ± 3 GPa at 6.46 km s^{-1}. Using Hugoniot data for non-porous quartz and aluminum from Melosh (1989), the upper limit for peak shock pressures is in the range of 64–75 GPa for velocities of 5.86–6.46 km s^{-1} (see Figs. A.1 and A.2). For comparison, Wünnemann et al. (2016) obtained a peak shock pressure of ~59 GPa for experiment 529 by means of numerical modeling. For reasons of internal consistency, we use the shock pressures obtained from the planar impact approximation (Table 5.1).

In order to reduce deceleration of the projectile and turbulent deflection of the ejecta, the target chamber, measuring 2.2 m in width, was evacuated

to 67–400 Pa for the experiments. Using a combination of horizontal and vertical ejecta catchers, ejected material was collected at radial distances between 16 and 105 cm (1 to 6 crater radii) from the point of impact. Sampling within the target pan (from 16 to 30 cm or 1 to 2 crater radii) was facilitated by spraying the preimpact target surface with a thin layer of varnish prior to impact, hence marking the original target surface. For additional information on the experimental setup, see Wünnemann et al. (2016).

5.2.2 Samples

After the experiments were performed at AVGR, the material was transferred to the Institut für Planetologie at Westfälische Wilhelms-Universität (WWU) Münster, Germany. In the following years it was studied at WWU, yielding one publication (Stöffler et al., 1975), three conference abstracts (Stöffler et al., 1980b; Stöffler et al., 1980a; Jammes et al., 1983), and a diploma thesis (Jammes, 1984). After the senior author's relocation from WWU to the Museum für Naturkunde (MfN) Berlin, Germany, the samples used by Jammes (1984) remained at WWU, but were generously made available for the present study.

The analyzed sample suite comprises particulate samples from both the crater floors and the ejecta blankets. It includes (1) partially shock-melted and shock-lithified sand covered with molten projectile material ("impact melt particles"), (2) shock-lithified sand, (3) comminuted quartz sand, and (4) samples of the pre-impact projectile and the target quartz sand. To investigate the geochemical interaction between projectile and target, we focused on those particles that showed visible traces of the aluminum projectiles. A similar approach was taken in comparable experiments with steel or iron meteorite projectiles shot at sandstone targets (Ebert et al., 2013; Ebert et al., 2014).

5.2.3 Analytical methods

The bulk chemical composition of the target quartz sand was determined on glass tablets with X-ray fluorescence (XRF) spectrometry on MfN's Bruker AXS S8 Tiger instrument. The glass tablets were prepared from 0.600 g of pulverized sample material, which was dried for 4 h at 105 °C and subsequently mixed and homogenized with 3.600 g of $B_4Li_2O_7$ (BRA A10 Specflux) and, for oxidization of the sample, with ~0.5 g NH_4NO_3. The mixture was fused into glass tablets using Pt/Au crucibles (950/50) and an OXIFLUX burner chain. The major element composition of the target was measured using an analytical program based on 40 certified international rock standards and ten reference standards (listed in the Appendix A; cf. Govindaraju, 1994). For global detection limits and analytical errors of the XRF analyses, see Table A.1. To determine loss on ignition (LOI), ~1 g of sample powder was dried for 4 h at 105 °C and subsequently heated for 4 h at 1000 °C in a porcelain crucible. LOI was

determined by calculating the mass difference of the sample before and after heating.

The re-polished thin sections of the existing sample suite were briefly examined under the optical microscope, using both reflected and transmitted light. After carbon-coating, back-scattered electron (BSE) imaging of the material was done with MfN's JEOL JSM-6610LV scanning electron microscope (SEM) equipped with a LaB_6 cathode and a Bruker XFlash 5010 energy-dispersive X-ray spectrometer. Both identification and semi-quantitative major element analyses of constituent phases were done with energy-dispersive X-ray spectrometry (EDX). Operating conditions were set to an acceleration voltage of 15 kV and a working distance of ~11 mm, which yielded EDX count rates of 5–10 kcps. X-ray intensity maps were acquired with a fully focused electron beam (spot size ≤1 µm), an acceleration voltage of 15 kV, a resolution of 1600 × 1200 pixel, a dwell time of 128–512 µs per pixel, and a pixel resolution of ≤100 nm. In the maps, only X-ray intensities are shown; neither abundance calibrations nor background corrections were applied. Detection limits for major elements measured with EDX are typically better than ~0.2 wt.%, and the accuracy of such analyses is on the order of 5% for concentrations above a few percent by weight, and 10–30% for concentrations close to the detection limit.

Additionally, the bulk composition of the aluminum projectiles was determined with quantitative electron microprobe analysis (EMPA) using MfN's JEOL JXA-8500F electron microprobe. The microprobe is equipped with a Schottky field-emission cathode, five wavelength-dispersive X-ray spectrometers, and an energy-dispersive X-ray spectrometer. Operating conditions for wavelength-dispersive X-ray spectrometry (WDX) were set to an acceleration voltage of 15 kV, an electron beam current of ~20 nA, and a working distance of 11 mm. A defocused, 20-µm-diameter beam was used for measuring the bulk composition of the aluminum projectile, and 70 individual, randomly performed analyses were averaged to obtain the bulk composition. Conditions for WDX analysis of the projectile are detailed in Table A.2. Briefly, counting time in WDX mode was set to 20 s on peak and 10 s on lower and upper background, respectively, and TAP, PET, and LIF crystals were used. Standardization of the analyses was based on MfN's Astimex and Smithsonian international standard suite for EMPA (e.g., Jarosewich et al., 1980). Furthermore, in order to control data quality, the analysis sequence comprised standard–sample–standard bracketing, that is, standards were measured five times after every twenty sample analyses. Subsequently, raw data were processed for matrix effects using a conventional ZAF routine provided as part of the JEOL operating program. Detection limits for major elements measured with WDX are listed in Table A.2. Typically, the accuracy of WDX major element analyses is much better than 2% for concentrations above a few percent by weight, and 5–10% for concentrations close to the detection limit.

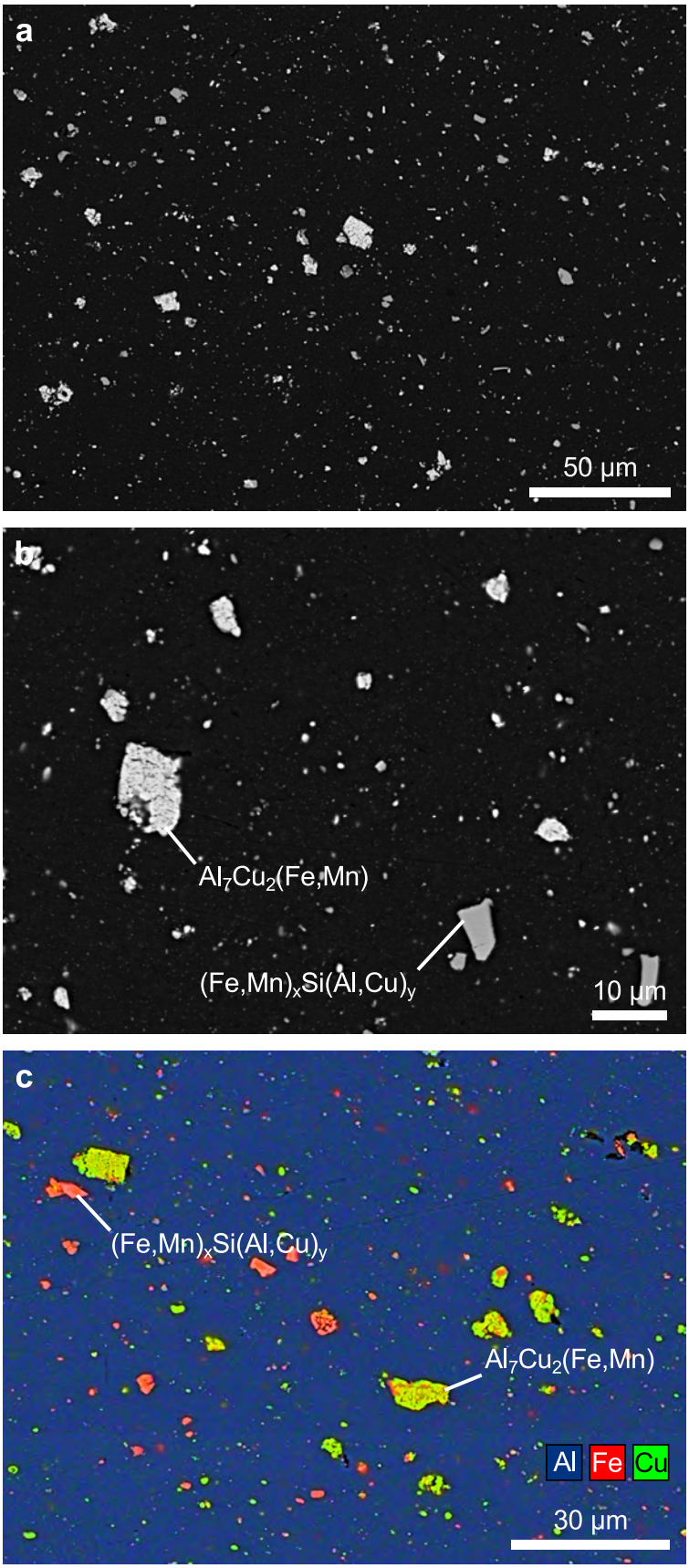

Figure 5.2 Back-scattered electron images (a and b) and elemental distribution map for Al, Fe, and Cu (c) of the aluminum projectile prior to impact. **a** Overview image of the texture of the material, comprising intermetallic phases of up to 10 µm size homogeneously dispersed in Al metal matrix. **b** Close-up BSE image of the intermetallic phases. Specifically, a Cu–Fe-rich phase, most likely $Al_7Cu_2(Fe,Mn)$, is present in form of amoeboid, honeycomb-textured, internally heterogeneous particles. A Fe–Mn-rich phase, most likely $(Fe,Mn)_xSi(Al,Cu)_y$, is present in form of subrounded to angular, internally homogeneous particles. **c** Composite elemental distribution map for Al (blue), Fe (red), and Cu (green) superimposed onto the corresponding BSE image. Note that the Cu–Fe-rich phase (yellowish to greenish) shows compositional domains rich in Fe (as well as Mn and Si; not shown), whereas the Fe–Mn-rich phase (red) is much more homogeneous. For acquisition details, see Subsection 5.2.3.

Table 5.2 Major element composition of the unshocked aluminum projectile.

	Bulk $n = 70$		Al metal matrix $n = 33$		Cu–Fe-rich phase $n = 46$		Fe–Mn-rich phase $n = 17$	
	[wt.%]	[at.%]	[wt.%]	[at.%]	[wt.%]	[at.%]	[wt.%]	[at.%]
Si	0.42(23)	0.41(23)	0.2(1)	0.2(1)	1.2(12)	1.7(16)	5.4(10)	6.9(11)
Al	94.9(17)	96.4(12)	94.5(8)	96.9(5)	46.4(39)	65.3(34)	50.1(38)	65.7(29)
Fe	0.67(83)	0.33(41)	bdl	bdl	14.0(27)	9.5(19)	23.1(36)	14.7(24)
Mn	0.73(32)	0.33(15)	0.4(4)	0.2(2)	4.6(22)	3.2(15)	9.5(16)	6.1(10)
Mg	0.61(3)	0.69(3)	0.8(3)	1.0(3)	bdl	bdl	bdl	bdl
Cu	4.20(124)	1.81(54)	4.0(9)	1.7(4)	33.8(60)	20.3(41)	11.9(57)	6.7(33)
Total	101.5(10)	100.0	100.0	100.0	100.0	100.0	100.0	100.0

Data obtained by EMPA (bulk analysis with defocused, 20-µm-diameter electron beam) and SEM-EDX (point analyses with focused, ~1-µm-diameter electron beam) and reported as average of *n* analyses with twofold standard deviation given in parentheses. SEM-EDX analyses were normalized to 100 wt.% and averages in at.% were calculated from individual data, not from averages in wt.%; bdl—below detection limit.

5.3 Microtexture and composition of projectile and target material prior to impact

5.3.1 Aluminum projectile

The aluminum used for manufacturing the projectiles for the Series II experiments is an Al–Cu–Mg–Si alloy with traces of Fe and Mn. The bulk density of the material is 2800 kg m^{-3}. The alloy is commercially available under the name "Duralumin" and belongs to the Aluminum Association (AA) "2xxx" series of Al–Cu–Mg–Si alloys (Chakrabarti and Laughlin, 2004; Wang and Starink, 2005). The alloy shows a somewhat heterogeneous texture of fine-grained intermetallic phases, generally between <1 and ~10 µm in size, statistically disseminated in the Al metal matrix (Fig. 5.2a). Thus, it shows the characteristic texture of a precipitation-hardened Al–Cu–Mg–Si alloy (e.g., Wang and Starink, 2005). Specifically, the unshocked projectile shows a high-Z, Cu–Fe-rich and a medium-Z, Fe–Mn-rich phase disseminated in the Al metal matrix (Fig. 5.2b; Table 5.2). The Cu–Fe-rich phase is usually ~10 µm in size and shows an internally heterogeneous, honeycomb-like texture and amoeboid shapes (Fig. 5.2b). It is the brightest phase in BSE images and, according to stoichiometry (see below) and structural appearance (Fig. 5.2b), most likely $Al_7Cu_2(Fe,Mn)$ or Al_7Cu_3Fe (Table 5.2; cf. Lin et al., 2014). It shows compositional domains rich in Cu and Fe or in Mn and Si at the submicrometer scale (Fig. 5.2b, c), which makes accurate phase analysis difficult and results in mixed analyses. The Fe–Mn-rich phase is present as subround to angular, internally homogeneous particles that appear slightly darker in BSE images compared to the Cu–Fe-rich phase (Fig. 5.2b). Usually, this phase is ~5 µm in size. According to stoichiometry (see below), this phase is most likely $(Fe,Mn)_xSi(Al,Cu)_y$ (Table 5.2; cf. Boag et al., 2009).

The composition of the unshocked aluminum projectile (reported as averages $\pm 2\sigma$) is given in Table 5.2; major element correlation diagrams are given in Fig. A.3. Its bulk composition (96.4 at.% Al, 1.8 at.% Cu)

is dominated by the composition of the Al metal matrix (96.9 at.% Al, 1.7 at.% Cu). Compared to the Al metal matrix, the Cu–Fe-rich phase is strongly enriched in Cu (20.3 at.%), Fe (9.5 at.%), and Mn (3.2 at.%) and depleted in Al (65.3 at.%), whereas the Fe–Mn-rich phase shows enrichment in Fe (14.7 at.%), Si (6.9 at.%), Cu (6.7 at.%), and Mn (6.1 at.%), and depletion in Al (65.7 at.%). Taking into account that the Cu–Fe-rich phase shows submicrometer-sized compositional domains (Fig. 5.2c), the measured composition of this phase agrees with the α(CuFe) phase known from Al–5.0Cu–0.6Mn–0.5Fe alloys (Lin et al., 2014), that is, $Al_7Cu_2(Fe,Mn)$, which has 70.5 at.% Al, 19.7 at.% Cu, 8.0 at.% Fe, and 1.8 at.% Mn (Fig. A.3). On the other hand, it also agrees with Al_7Cu_3Fe known from, for example, the AA2024-T3 (Al–4.2Cu–1.5Mg–0.6Mn) aluminum alloy (Boag et al., 2009), which has a composition of 70 at.% Al, 18 at.% Cu, 6 at.% Fe, and 1 at.% Mn. The composition of the Fe–Mn-rich phase agrees well with $(Fe,Mn)_xSi(Al,Cu)_y$ (Fig. A.3), which is also encountered in AA2024-T3 and has been reported with variable compositions of 67.8–77.0 at.% Al, 4.0–6.3 at.% Si, 10.0–14.9 at.% Fe, 5.0–6.9 at.% Mn, 4.0–6.3 at.% Mg, and 3.4–5.0 at.% Cu (Gao et al., 1998; Boag et al., 2009).

Notably, the original aluminum projectile seems to be free of $CuAl_2$ (i.e., khatyrkite, also known as "phase Θ" in materials science), $CuAl_2Mg$ (known as "phase S" in materials science), and silicon, which are intermetallic phases frequently reported in the AA2xxx series of aluminum alloys (e.g., Wang and Starink, 2005). However, it has been shown, for example, by Buchheit et al. (1997), that$CuAl_2$ is not necessarily a component in alloys like AA2024-T3.

5.3.2 Quartz sand target

The target material used in the experiments is commercially available quartz sand with grain sizes between 0.063 and 0.250 mm. The bulk density of the sand of different colors, ϕ_s, ranged from 1380 kg m^{-3} to 1558 kg m^{-3}, compared to 1580 kg m^{-3} for plain sand (cf. Stöffler et al., 1975). The bulk porosity is given by $\phi_0 = 1 - (\phi_s/\phi_q)$, where ϕ_q is the density of quartz (2650 kg m^{-3}); hence, the average porosity of the sand is ~42%. For data on grain size distribution by mass, see Wünnemann et al. (2016). Zircon and K-feldspar are trace phases (<5 vol.%) in the quartz sand, whose bulk chemical composition (Table 5.3) is dominated by 98.2 ± 0.5 wt.% SiO_2. Furthermore, Al_2O_3, Fe_2O_3, K_2O, TiO_2, and CaO are present to ~1.5 wt.% and traces of Cu (62 ± 27 μg g^{-1}) and Sr (38 ± 17 μg g^{-1}), as well as ~0.2 wt.% volatiles, were detected.

5.4 Shock metamorphism of quartz sand and projectile–target interaction

5.4.1 Types of shocked particles

In general, the impact experiments of Series II yielded three main types of shocked particles that originated from different zones in the growing crater (Fig. 5.1): (1) impact melt particles, (2) shock-lithified sand, and (3) shock-comminuted quartz grains (cf. Wünnemann et al., 2016). Based on similar experimental data from shock recovery experiments on sand and porous sandstone (cf. Stöffler et al., 1975; Kowitz et al., 2013a; Kowitz et al., 2013b; Buhl et al., 2013, and references therein), and on observations made in natural impact craters (Kieffer, 1971; Kieffer et al., 1976a; Stöffler and Grieve, 2007), we can cautiously define upper and lower limits of shock pressures to which these three types of particles were exposed to. Briefly, impact melting of quartz sand occurs at pressures >13 GPa (see next section), whereas shock-lithified sand with strong shock effects in quartz, such as formation of lechatelierite, diaplectic quartz glass, and planar deformation features (PDF), has been shocked to pressures between ~13 and ~5.5 GPa (Kowitz et al., 2013a; Kowitz et al., 2013b). Shock-lithified sand without distinct shock effects, but with completely crushed pore space, has been shocked to pressures between ~5.5 and ~0.9 GPa (ibid.). Shock-comminuted quartz grains have been shocked to pressures below ~0.9 GPa. In the following section we concentrate on layered melt particles, which reflect shock pressures between ~5.5 and >45 GPa and postshock temperatures from some hundred degrees Celsius to more than 2000 °C (see Subsection 5.4.3).

Table 5.3 Major element composition of the unshocked quartz sand target.

SiO_2	98.2(5)
TiO_2	0.05(1)
Al_2O_3	0.7(1)
Fe_2O_3[a]	0.26(5)
MnO	bdl
MgO	bdl
CaO	0.03(5)
Na_2O	bdl
K_2O	0.50(5)
P_2O_5	bdl
Cu	62(27)
Sr	38(17)
LOI	0.2(1)
Total	99.94

Data obtained by XRF and reported with 1σ measurement error given in parentheses. Major elements are given in wt.%, Cu and Sr in μg g^{-1}. LOI—loss on ignition.
[a] Total Fe reported as Fe_2O_3.

5.4.2 Petrographic characteristics of impact melt particles

Impact melt particles are usually composed of molten and shock-lithified quartz grains coated with molten and subsequently recrystallized metallic projectile residues (Figs. 5.3). In general, four zones can be distinguished both texturally and compositionally in sections taken perpendicular to the Al-coated surface of such particles (Fig. 5.3c and 5.4). Most of the impact melt particles were recovered from the crater floors; however, they were also encountered in the horizontal and vertical ejecta catchers. Notably, their dimensions are negatively correlated with increasing ejection distance. For example, melt particles that were collected from the crater floors are, on average, 1.2 cm in length and 0.8 cm in thickness (measured parallel and perpendicular to the metallic projectile coating, respectively). In contrast, impact melt particles sampled with the ejecta catchers were usually much smaller, measuring up to 0.6 cm in length and 0.4 cm in thickness. For details on mass distribution of melt particles and shock-lithified sand, we refer to Wünnemann et al. (2016).

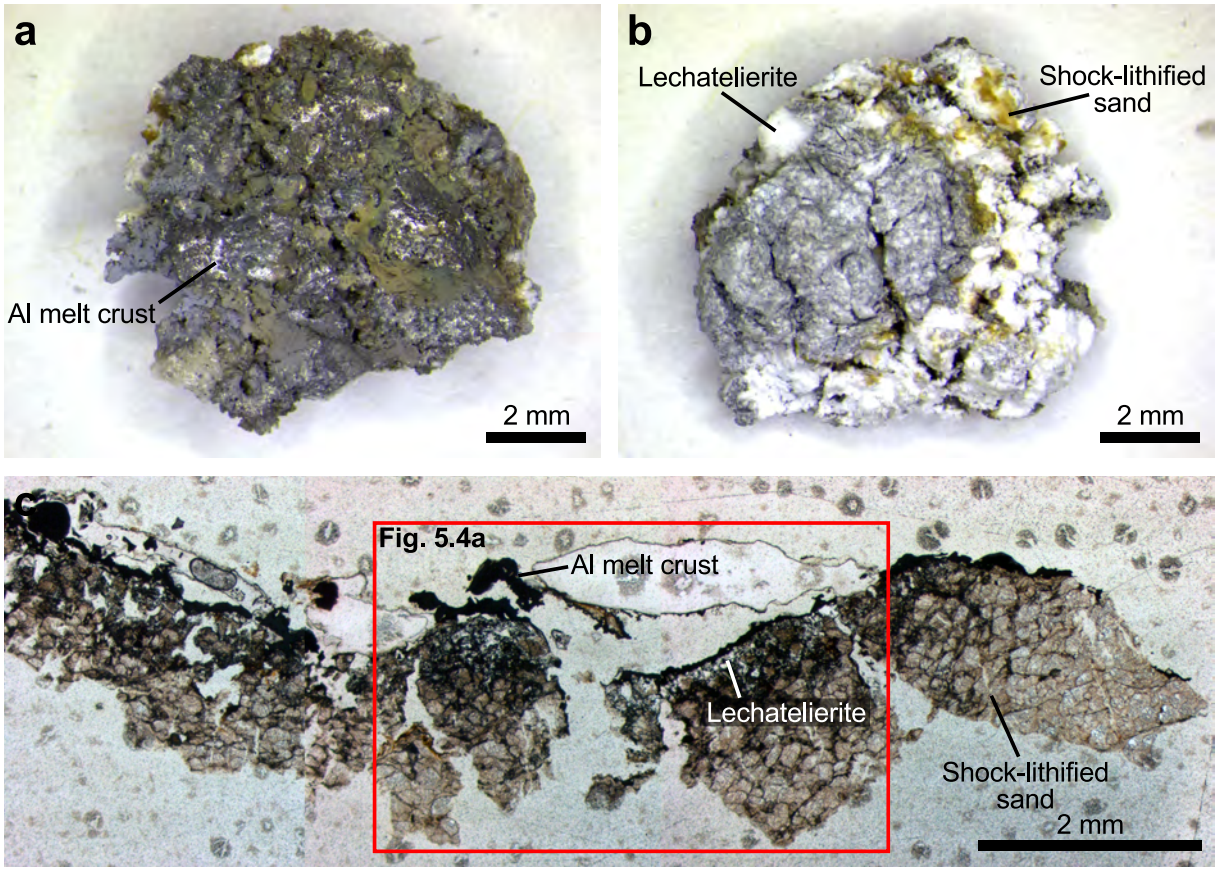

Figure 5.3 Photographs (a and b) and transmitted light photomicrographs (c) of typical impact melt particles. **a** and **b** Top and bottom, respectively, of an impact melt particle recovered from experiment 530 (cf. Table 5.1). Note that the top is coated with metallic projectile material (a), whereas the bottom consists of shock-lithified quartz sand (b). **c** Composite image (plane-polarized light) of a thin-sectioned impact melt particle recovered from experiment 533 (cf. Table 5.1). Note the thin coating of opaque Al metal at the top, as well as the thin layer of translucent lechatelierite (SiO_2 glass) below. The red square indicates the position of Fig. 5.4a.

5.4.3 Chemical projectile–target interaction

The impact melt particles display distinct textural and compositional zoning. In general, four zones can be distinguished both texturally and compositionally in sections taken perpendicular to the Al-coated surface (Figs. 5.3c and 5.4), documenting the chemical interaction between projectile and target in the form of a reaction front between projectile-derived Al and target-derived SiO_2. From the surface downward, the four zones are:

Zone 1 a thin, metallic crust of molten and subsequently recrystallized projectile material;

Zone 2 a reaction front of quenched Al_2O_3 melt at the interface between projectile and target;

Zone 3 lechatelierite with relic, often PDF-bearing quartz grains and projectile inclusions; and

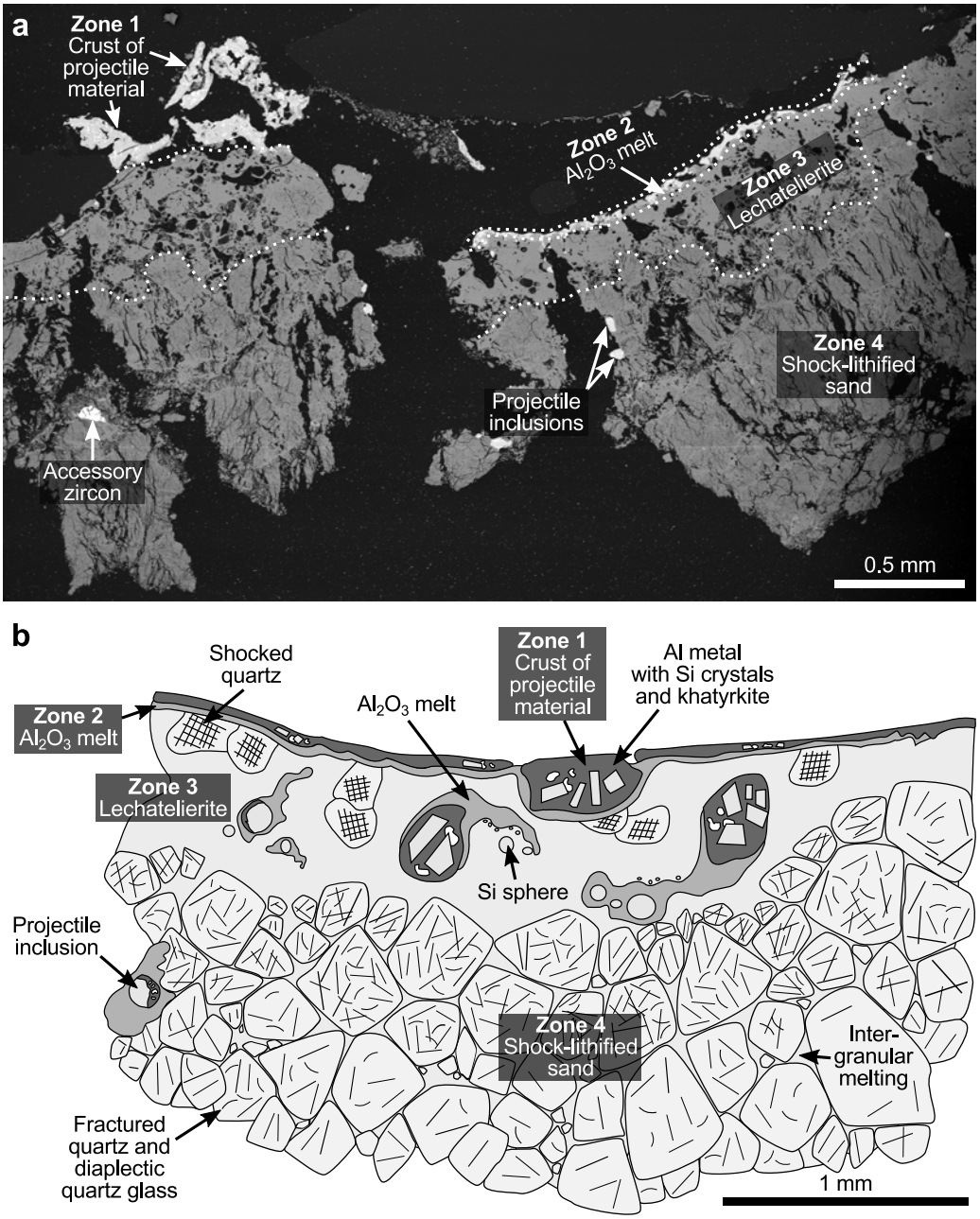

Figure 5.4 Back-scattered electron image (**a**) and schematic illustration (**b**) of the cross section of a typical impact melt particle recovered from the crater bottom of experiment 533 (cf. Table 5.1). Four zones can be recognized texturally and compositionally: Zone 1 is a crust of texturally and compositionally altered, molten, and subsequently recrystallized metallic projectile material; Zone 2 is a reaction front between projectile-derived Al and target-derived SiO_2, composed of quenched Al_2O_3 melt with subhedral to euhedral silicon crystals and silicon spherules in contact with khatyrkite ($CuAl_2$); Zone 3 is a melt zone composed of vesicular lechatelierite, showing relic, highly shocked quartz grains with PDF and inclusions of metallic projectile residues; Zone 4 is a compact aggregate of shock-lithified quartz grains that usually lack PDF but frequently show grain-boundary melting. Projectile inclusions and accessory zircon are occasionally encountered in Zone 4.

Zone 4 shock-lithified quartz sand that shows grain-boundary melting and occasionally contains small inclusions of shock-melted projectile.

Recrystallized crust of molten projectile material (Zone 1)

Impact melt particles are usually coated with molten and recrystallized metallic projectile material, which forms a rugged crust of variable thickness (≤0.4 mm; Figs. 5.3 and 5.4). The material shows a metallic luster in reflected light (Fig. 5.3a) and opacity in transmitted light (Fig. 5.3c). Using optical and electron microscopy, it becomes apparent that the material is texturally and compositionally heterogeneous, showing a eutectic crystallization texture (Fig. 5.5a, b) distinctly different from the texture of the original projectile material (Fig. 5.2a, b). Specifically, subrounded, Al-rich, metallic melt areas are interspersed with intermetallic phases (Fig. 5.5a, b), the latter usually forming a thin, web-like network (Fig. 5.5a, c). Three phases can be identified in this metal crust: (1) lath-shaped to tabular silicon crystals up to ~10 µm in size, showing a medium gray color in reflected light, (2) aggregates or clusters of subrounded khatyrkite ($CuAl_2$) crystallites 1–5 µm in size, which often are in contact with silicon crystals and show a light gray color in reflected light, and (3) aggregates of subrounded crystallites of a medium-*Z*, Fe–Mn-rich phase, most likely $(Fe,Mn)_xSi(Al,Cu)_y$, 1–5 µm in size, and usually interconnected with khatyrkite crystallites, also showing a light gray color in reflected light. Occasionally, $(Fe,Mn)_xSi(Al,Cu)_y$ forms skeletal, so-called "Chinese script" (Hwang et al., 2008) aggregates.

The compositions of the phases encountered in the melt crust are reported in Table 5.4 and Figs. 5.6 and 5.7; a representative elemental distribution map is shown in Fig. 5.5d. Typical EDX spectra for khatyrkite, $(Fe,Mn)_xSi(Al,Cu)_y$, and silicon are given in Fig. A.4. On average, the Al metal matrix is composed of 97.2 at.% Al, 1.2 at.% Cu, and 1.7 at.% Si (Table 5.4). Hence, compared to the Al metal matrix of the unshocked projectile (cf. Table5.2), it is slightly enriched in Si, slightly depleted in Cu, and severely depleted in Mg and Mn. Khatyrkite has, on average, 66.9 at.% Al and 31.4 at.% Cu; Si is present as a minor component (1.6 at.%). Stoichiometric $CuAl_2$ corresponds to 33.33 at.% Cu and 66.66 at.% Al. From the Khatyrka meteorite, khatyrkite with a composition of ~33 at.% Cu and ~66 at.% Al has been reported (Bindi et al., 2012). From materials science, a similar phase is known: for example, Boag et al. (2009) reported a composition of ~70 at.% Al and ~27 at.% Cu with minor amounts (<1 at.%) of Mn, Fe, or Si, whereas Gao et al. (1998) reported a composition of 62.98 at.% Al, 33.83 at.% Cu, and 2.82 at.% Mg. The Fe–Mn-rich phase $(Fe,Mn)_xSi(Al,Cu)_y$ has, on average, 67.6 at.% Al, 11.3 at.% Si, 10.4 at.% Fe, and 8.7 at.% Mn. The silicon crystals are essentially stoichiometric Si (97.9 at.%) with Al and O being present as minor components (totaling ~2 at.%).

Reaction front between projectile and target (Zone 2)

Below the recrystallized crust of metallic projectile material (Zone 1), a narrow, 10–40-µm-thick, heterogeneous melt zone composed predominantly of Al_2O_3 and SiO_2 is present (Figs. 5.4, 5.7, 5.8, and 5.9; Zone 2).

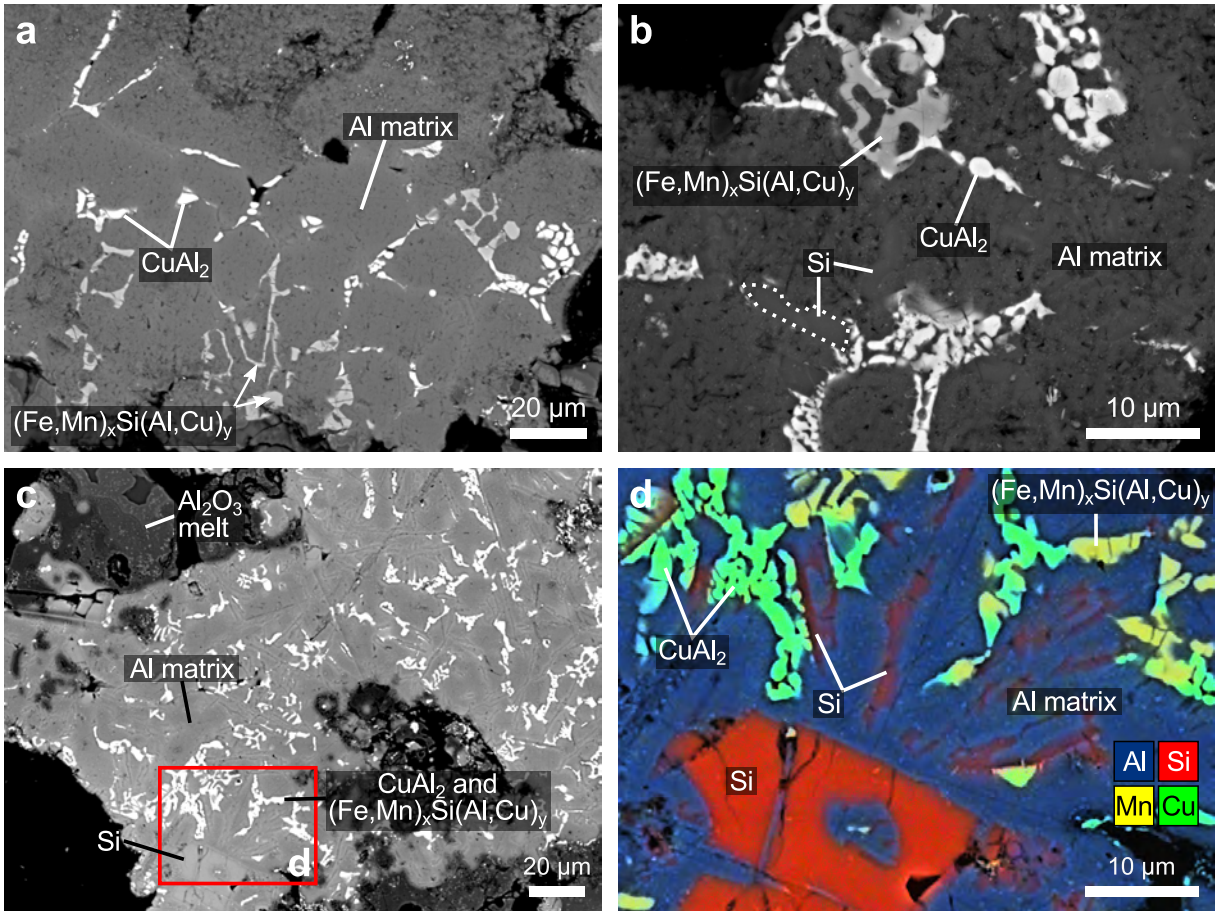

Figure 5.5 Texture and composition of the metallic projectile crust (Zone 1) of impact melt particles from experiments 533 and 534 (cf. Table 5.1). **a** and **b** BSE images of the material in Zone 1, showing the typical eutectic assemblage of khatyrkite ($CuAl_2$) and $(Fe,Mn)_xSi(Al,Cu)_y$ interstitial to subrounded areas of Al metal matrix; experiment 533. Note the presence of euhedral Si crystals in the Al metal matrix (b). **c** BSE image showing the metallic projectile coating (Zone 1) in contact with Si-bearing Al_2O_3 melt (Zone 2); experiment 534. **d** Composite elemental distribution maps for Al (blue), Si (red), Mn (yellow), and Cu (green) superimposed onto the corresponding BSE image. Khatyrkite (green) and $(Fe,Mn)_xSi(Al,Cu)_y$ (yellow) occur in form of clusters mostly in contact with lath-shaped or equant silicon crystals (red). Silicon and khatyrkite are otherwise absent in the original projectile (cf. Fig. 5.2).

This zone shows bulbous and remarkably sharp contacts to the overlying metallic projectile crust in Zone 1 and the underlying lechatelierite in Zone 3 (Fig. 5.8b, c). Occasionally, Zone 2 is also encountered in the vicinity of projectile inclusions in Zone 3. Here, the material is usually present in the form of recrystallized dendrites around subhedral to euhedral, metallic silicon crystals and metallic silicon spherules (see next subsection and Fig. 5.10a). In reflected light, the material shows dark brown colors in contact with the metallic projectile crust, whereas it shows light brown to tan colors in contact with lechatelierite. In transmitted light, the material is opaque. In BSE images, the dark brown layer in contact with the metallic projectile crust shows a darker signal than the light brown layer in contact with lechatelierite (Fig. 5.8b, c). The internal boundary between these two differently colored layers is usually irregular and serrated. Occasion-

Table 5.4 Major element compositions of phases in the recrystallized crust of molten projectile material (Zone 1) and in projectile inclusions (Zone 3 and Zone 4).

	Al metal matrix $n = 32$		Khatyrkite ($CuAl_2$) $n = 47$		$(Fe,Mn)_xSi(Al,Cu)_y$ $n = 58$		Silicon $n = 25$	
	[wt.%]	[at.%]	[wt.%]	[at.%]	[wt.%]	[at.%]	[wt.%]	[at.%]
O	bdl	bdl	bdl	bdl	bdl	bdl	0.7(3)	1.3(5)
Si	1.7(9)	1.7(8)	1.1(5)	1.6(7)	9.5(13)	11.3(16)	98.5(7)	97.9(8)
Al	95.6(21)	97.2(10)	47.0(41)	66.9(35)	54.9(37)	67.7(32)	0.8(5)	0.8(5)
Fe	bdl	bdl	bdl	bdl	17.4(27)	10.4(18)	bdl	bdl
Mn	bdl	bdl	bdl	bdl	14.3(42)	8.7(26)	bdl	bdl
Mg	bdl	bdl	bdl	bdl	bdl	bdl	bdl	bdl
Cu	2.7(22)	1.2(10)	51.9(43)	31.4(37)	3.8(36)	2.0(19)	bdl	bdl

Data obtained by SEM-EDX (point analyses with focused, ≤1-µm-diameter electron beam) and reported as average of *n* analyses with twofold standard deviation given in parentheses. Data were normalized to 100 wt.% and averages in at.% were calculated from individual data, not from averages in wt.%; bdl—below detection limit.

ally, the contact appears diffuse and material from the dark brown layer may be mixed with material from the underlying light brown layer and vice versa, indicating interaction between the two materials in the liquid state. Moreover, incipient crystallization of nanometer-sized, dendritic, medium- to high-*Z* crystallites is indicated in both layers (Fig. 5.8b, c). However, due to the small dimensions of these crystallites, exact point analyses and phase identification were not feasible with SEM-EDX or EMPA.

Compositionally, the Al_2O_3-rich melt in the dark brown and light brown layers (Table 5.5) differs significantly from the Al metal matrix in the overlying Zone 1 (Table 5.4). In comparison, both layers of the reaction front are thoroughly oxidized (Figs. 5.7 and 5.9). The dark brown layer is predominantly composed of Al_2O_3 (97.3 wt.%, on average), with SiO_2 being present as a minor component (<4.4 wt.%, averaging 1.8 wt.%). In Fig. 5.9 the data obtained from the dark brown, Si-poor layer plot at ~39 at.% Al and ≤1.5 at.% Si, whereas the Al metal matrix plots at ~97 at.% Al and ≤3 at.% Si. The light brown, Si-rich layer shows higher contents of SiO_2 (between 2.4 and 37.6 wt.%, averaging 9.7 wt.%) and lower contents of Al_2O_3 (between 61.7 and 96.6 wt.%, averaging 89.2 wt.%) compared to the dark brown, Si-poor layer. Consequently, the data obtained from the light brown, Si-rich layer follow a trend that is defined by a mixing line between pure Al_2O_3 and pure SiO_2 (Fig. 5.9).

Lechatelierite with relic quartz grains showing planar deformation features (PDF) and projectile inclusions (Zone 3)

The reaction front of Zone 2 is underlain by vesicular lechatelierite (Figs. 5.4 and 5.8), which occasionally shows relic, PDF-bearing quartz grains and spheroidal or irregularly shaped inclusions of projectile material (Fig. 5.10a). Usually, lechatelierite is present in the form of large (≤500 µm), highly vesicular, homogeneous patches and, occasionally, flow bands.

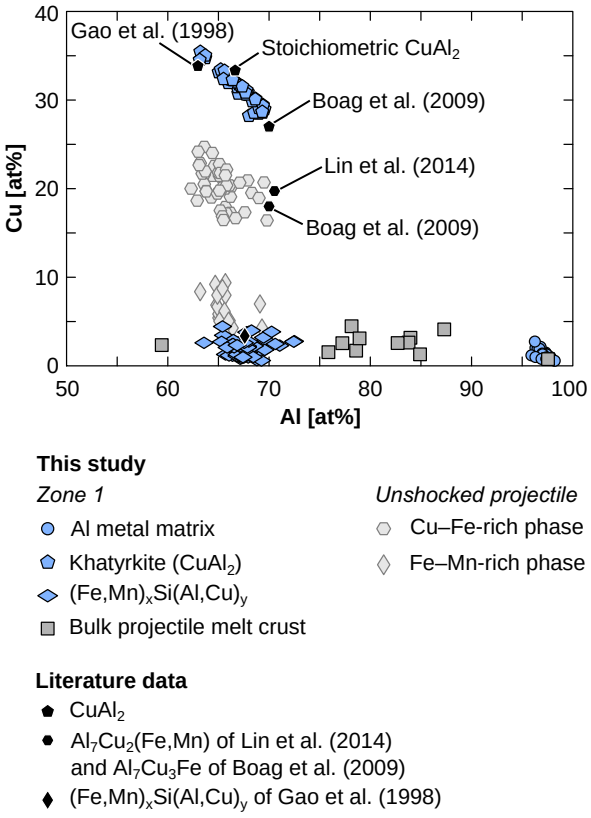

Figure 5.6 Al vs. Cu contents (in at.%) of phases encountered in Zone 1 (recrystallized crust of molten projectile material) of impact melt particles compared to intermetallic phases of the unshocked aluminum projectile and literature data on typical phases encountered in aluminum alloys of type AA2xxx (Gao et al., 1998; Boag et al., 2009; Lin et al., 2014). Note that most khatyrkite data fall onto a mixing line between Al metal matrix and stoichiometric $CuAl_2$, indicating mixed analyses of both khatyrkite and matrix material due to the very small dimensions of the khatyrkite crystallites. All data were obtained from experiments 533 and 534 (cf. Table 5.1).

Based on constant BSE brightness (Figs. 5.4a and 5.8) and on elemental distribution maps (Fig. 5.11a), lechatelierite is compositionally homogeneous, essentially representing monomineralic quartz melt. The crystallographic orientations of 72 sets of PDF in 35 quartz grains were measured by Jammes (1984). In summary, the majority of PDF show poles to c-axis angles >45°. The most frequent orientations are $11\bar{2}1$, $10\bar{1}1$, and $11\bar{2}2$ with 29%, 14%, and 8%, respectively; 35% of the PDF could not be indexed due to the intrinsic limitations of the optical universal stage technique.

Occasionally, textures indicative of melting along PDF were detected in the form of broadened PDF. These are subplanar and subparallel, amorphous lamellae which are distinctly thicker (~0.3–1 µm) than normal PDF (<0.2 µm). Similar features have been described by Ebert et al. (2013) and Fazio et al. (2014b). The projectile inclusions usually comprise euhedral silicon crystals embedded in a matrix of Al_2O_3-rich, amorphous or dendritically recrystallized material (Fig. 5.10a), or Al metal (Fig. 5.10b). Tiny, ~1-µm-diameter metallic silicon spherules are usually associated with and disseminated in the Al_2O_3 melt zone surrounding the projectile inclusions (Fig. 5.10a), and khatyrkite is often present adjacent to silicon crystals (Fig. 5.10b). The latter kind of inclusion is also occasionally found in the underlying Zone 4 (see next subsection and Fig. 5.10b).

Compositionally, the phases present in the projectile inclusions are indistinguishable from the phases encountered in Zones 1 and 2; therefore, data obtained from these phases have been included in the averages

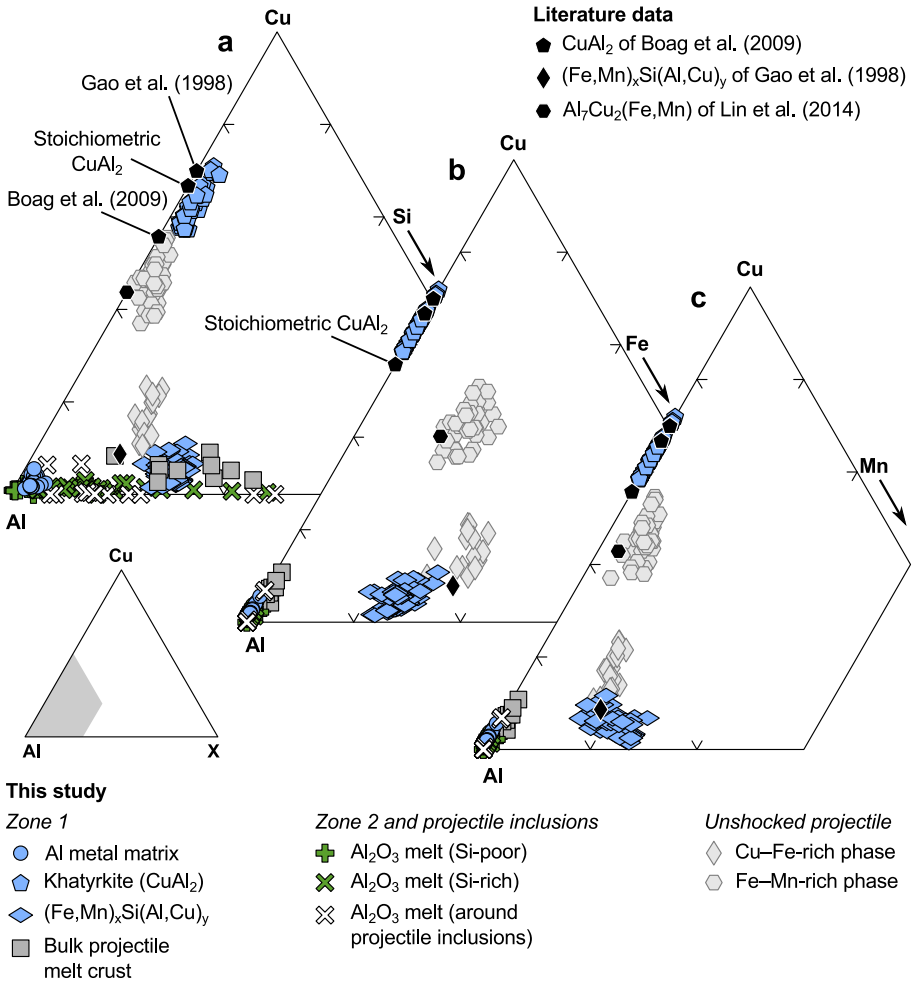

Figure 5.7 Compositional variations of phases encountered in Zone 1 (recrystallized crust of molten projectile material) and Zone 2 (reaction front between projectile and target) of impact melt particles plotted in the ternary systems Al–Cu–Si (**a**), Al–Cu–Fe (**b**), and Al–Cu–Mn (**c**). Intermetallic phases of the unshocked projectile and literature data (Gao et al., 1998; Boag et al., 2009; Lin et al., 2014) for $CuAl_2$, $(Fe,Mn)_xSi(Al,Cu)_y$, and $Al_7Cu_2(Fe,Mn)$ are plotted for comparison. Data are given in at.% and the diagrams are truncated according to the inset in the lower left corner. All data were obtained from experiments 533 and 534 (cf. Table 5.1).

given in Tables 5.4 and 5.5. Moreover, as shown in Table 5.6, lechatelierite is nearly pure SiO_2 (99.6 wt.%) with subordinate amounts of Al_2O_3 (0.4 wt.%).

Shock-lithified sand (Zone 4)

The vesicular lechatelierite of Zone 3 is underlain by a thick, irregular (sawtooth-shaped) layer of shock-lithified sand (Figs. 5.3c and 5.4), in which the quartz grains are partially to completely fractured. They usually lack PDF or planar fractures; however, the primary porosity of the original quartz sand target has been lost and the quartz grains are densely packed. Moreover, incipient melting of quartz and, locally, zircon is observed (Fig. 5.12), forming thin, vesicular flow bands and veins of melt surrounded by fractured quartz grains. These melts obviously formed by

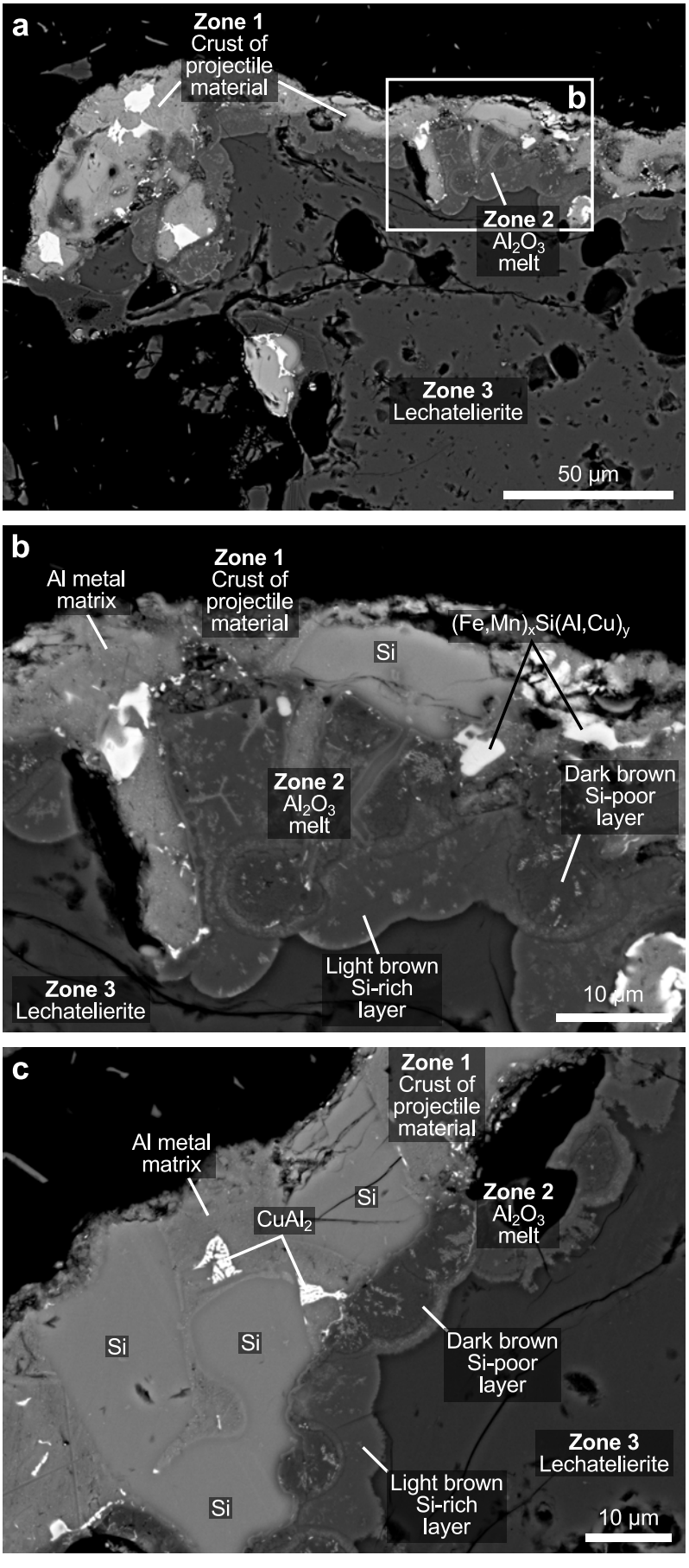

Figure 5.8 Back-scattered electron images of an impact melt particle from experiment 533, showing the reaction front (Zone 2) between projectile-derived Al and target-derived SiO_2, which forms a narrow zone of quenched Al_2O_3 melt at the interface of Zone 1 and Zone 3. **a** Overview BSE image of the overall textural context of Zone 2. **b** and **c** Close-up BSE images of the 5–20-µm-thick Al_2O_3 melt zone in contact to Al metal matrix, silicon crystals, khatyrkite, and $(Fe,Mn)_xSi(Al,Cu)_y$ of Zone 1 and lechatelierite of Zone 3. Note that the material shows compositional heterogeneity in the form of two differently colored internal layers (Si-poor and Si-rich; dark gray and medium gray in the BSE images; dark brown and light brown in reflected-light microscopy) that show dendritic crystallites of a medium- to high-*Z* material.

grain-boundary melting. However, it is reasonable to assume that a certain proportion of the quartz grains was transformed to diaplectic quartz glass. In fact, Jammes (1984) was able to document a continuous sequence of progressively decreasing shock metamorphism of quartz in Zones 3 and 4. This was established on the basis of refractive index measurements of 50 grains taken from impact melt particles of experiment No. 529. Grains of lechatelierite showed a refractive index very near to 1.459 (compared to 1.4585 of synthetic SiO_2 glass), whereas the refractive index of grains

Table 5.5 Major element compositions of dark brown, Si-poor and light brown, Si-rich Al_2O_3 reaction front between projectile and target (Zone 2) and of Al_2O_3 melt around projectile inclusions.

	Dark brown, Si-poor layer		Light brown, Si-rich layer		Rims around projectile inclusions	
[wt.%]	Range	Avg. (n = 13)	Range	Avg. (n = 30)	Range	Avg. (n = 14)
SiO_2	0.1–4.4	1.8(29)	2.4–37.6	9.7(159)	2.1–80.15	15.8(384)
Al_2O_3	95.1–99.4	97.3(31)	61.7–96.6	89.2(156)	19.3–93.2	82.7(377)
FeO[a]	bdl	bdl	bdl	bdl	bdl	bdl
MnO	bdl	bdl	bdl	bdl	0.1–1.0	0.7(4)
MgO	0.1–1.6	0.6(12)	0.1–1.5	0.5(7)	0.5–1.4	0.9(6)
Cu	0.1–1.7	0.7(7)	0.1–1.4	0.8(7)	0.1–4.0	1.7(37)

Data obtained by SEM-EDX (point analyses with focused, ≤1-µm-diameter electron beam; normalized to 100 wt.%) and reported as range and average (Avg.) of n analyses with twofold standard deviation given in parentheses; bdl—below detection limit.

[a] All Fe reported as FeO.

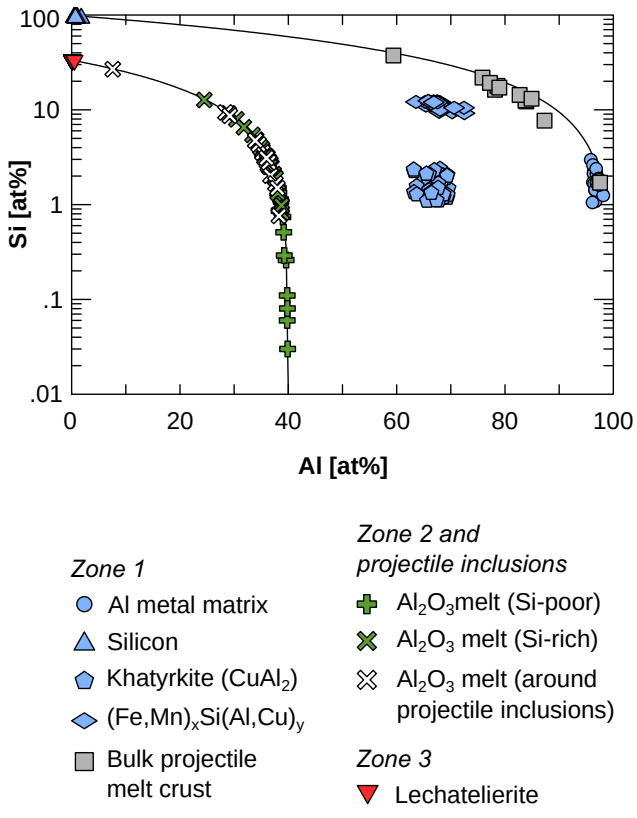

Figure 5.9 Al vs. Si contents (in at.%) of the phases in Zone 1 (recrystallized crust of molten projectile material), Zone 2 (reaction front between projectile and target), and Zone 3 (lechatelierite) of impact melt particles from experiments 533 and 534 (cf. Table 5.1). Note that the Al_2O_3-rich melt plots onto a mixing line between stoichiometric Al_2O_3 (40 at.% Al, 60 at.% O) and SiO_2 (33.33 at.% Si, 66.66 at.% O). The bulk projectile closely follows a mixing line defined by Al metal matrix and silicon crystals; the slight shift to lower Si contents is caused by the presence of khatyrkite ($CuAl_2$) and $(Fe,Mn)_xSi(Al,Cu)_y$ in the melt crust.

of diaplectic glass was found to range from 1.460 to 1.485. The refractive index for quartz grains with PDF varied from 1.528 to 1.546 (compared to 1.5533 of unshocked quartz). These results are in good agreement with the database of Stöffler and Langenhorst (1994). Furthermore, irregularly shaped projectile inclusions, akin to those encountered in Zone 3, are occasionally disseminated in Zone 4 (Figs. 5.4 and 5.10b).

Compositionally, the phases present in projectile inclusions in Zone 4, that is, silicon crystals, khatyrkite, and $(Fe,Mn)_xSi(Al,Cu)_y$, are similar to the phases in projectile inclusions of Zone 3 and, therefore, have been included in the calculation of averages given in Tables 5.4 and 5.5.

5.5 Discussion and implications for planetary regoliths

The following discussion is subdivided into five parts. First, we focus on more general aspects of the impact experiments, discussing the petrologic evidence of the reaction between projectile and target, and elucidating *P*–*T* and oxygen fugacity conditions for the experiments. Then, implications of the results for the Khatyrka CV3 chondrite, in which khatyrkite was first discovered (Bindi et al., 2012), are discussed. Furthermore, the applicability of the experiments to impacts of iron meteorites into silica-rich targets and, finally, some implications for regolith-forming processes on planetary surfaces are evaluated.

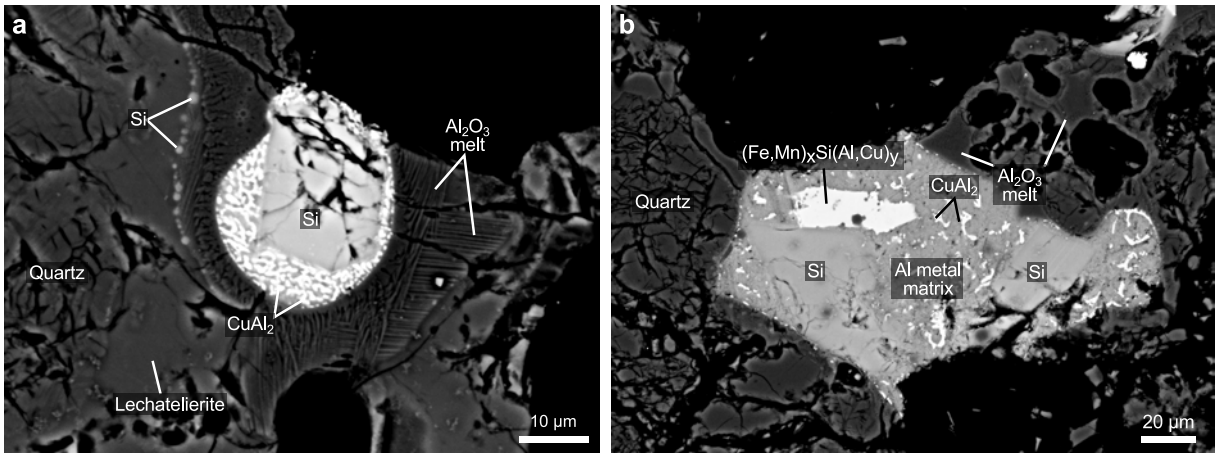

Figure 5.10 Back-scattered electron images of typical projectile inclusions in Zone 3 (a) and Zone 4 (b) of an impact melt particle from experiment 534 (cf. Table 5.1; Fig. 5.4). **a** Spherical inclusion in lechatelierite of Zone 3, comprising a euhedral silicon crystal and khatyrkite ($CuAl_2$) crystallites surrounded by dendritically recrystallized Al_2O_3 melt. Note the presence of tiny metallic silicon spherules disseminated in lechatelierite at the interface between lechatelierite and the Al_2O_3 melt zone. **b** Irregularly-shaped projectile inclusion in fractured quartz grains of Zone 4, comprising silicon, khatyrkite, and $(Fe,Mn)_xSi(Al,Cu)_y$ crystals in Al metal matrix. Note the presence of quenched Al_2O_3 melt at the interface between the metallic projectile inclusion and t he quartz grains.

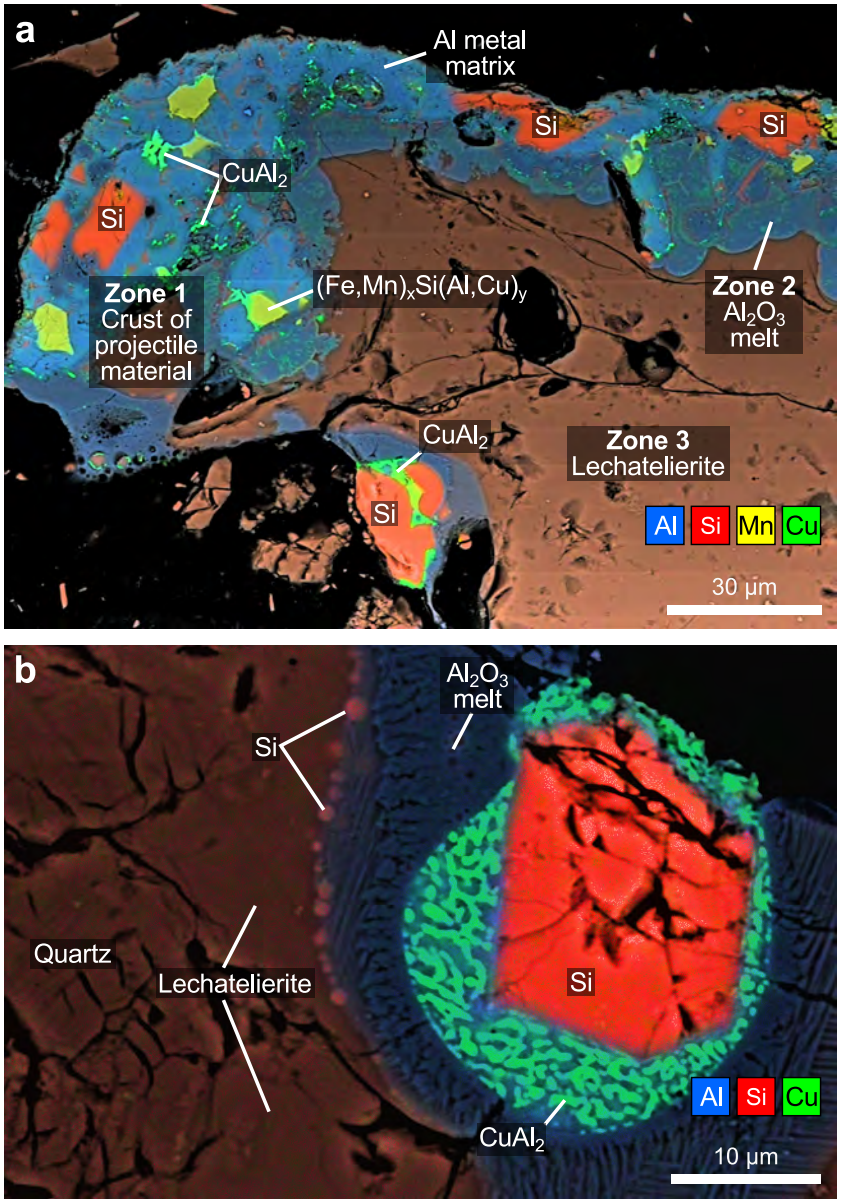

Figure 5.11 Composite elemental distribution maps superimposed onto the corresponding BSE images of impact melt particles from experiments 533 and 534 (cf. Table 5.1). **a** Elemental distribution of Al, Si, Mn, and Cu among Zones 1–3 (cf. Fig. 5.4); experiment 533. The Al metal matrix of Zone 1 (light blue) contains inclusions of silicon (red), khatyrkite (green), and $(Fe,Mn)_xSi(Al,Cu)_y$ (yellow). Underneath Zone 1, a reaction front of quenched Al_2O_3 melt (dark blue) has formed between projectile and target materials (Zone 3). See Fig. 5.8a for the corresponding BSE image. **b** Spheroidal, projectile-derived melt inclusion in lechatelierite of Zone 3, comprising a euhedral silicon crystal (red) and crystallites of khatyrkite ($CuAl_2$; green); experiment 534. Note that dendritically recrystallized Al_2O_3 melt formed at the interface between a projectile inclusion and lechatelierite, quite similar to the observation in Zone 2 shown in (a). Note also the presence of metallic silicon spherules at the interface between Al_2O_3 melt and lechatelierite. See Fig. 5.10a for the corresponding BSE image.

5.5.1 *P–T* conditions, aluminothermic reaction, and oxygen fugacity

P–T conditions and aluminothermic reaction

Hypervelocity impacts of aluminum projectiles into quartz sand result in (1) complete melting of the aluminum projectile, (2) partial melting of the quartz sand target, and (3) redox reactions between projectile-derived Al and target-derived SiO_2. Compared to "normal" endogenic geologic processes, *P–T* conditions during contact and compression stage, as well as during the immediately following decompression stage, are extreme, even for the kind of small-scale, low-velocity impacts discussed here (e.g., Melosh, 1989). Based on the planar impact approximation (Melosh, 1989), shock pressures between 41 ± 3 GPa and 48 ± 3 GPa were reached at the point of impact (Table 5.1); in the three experiments studied in detail

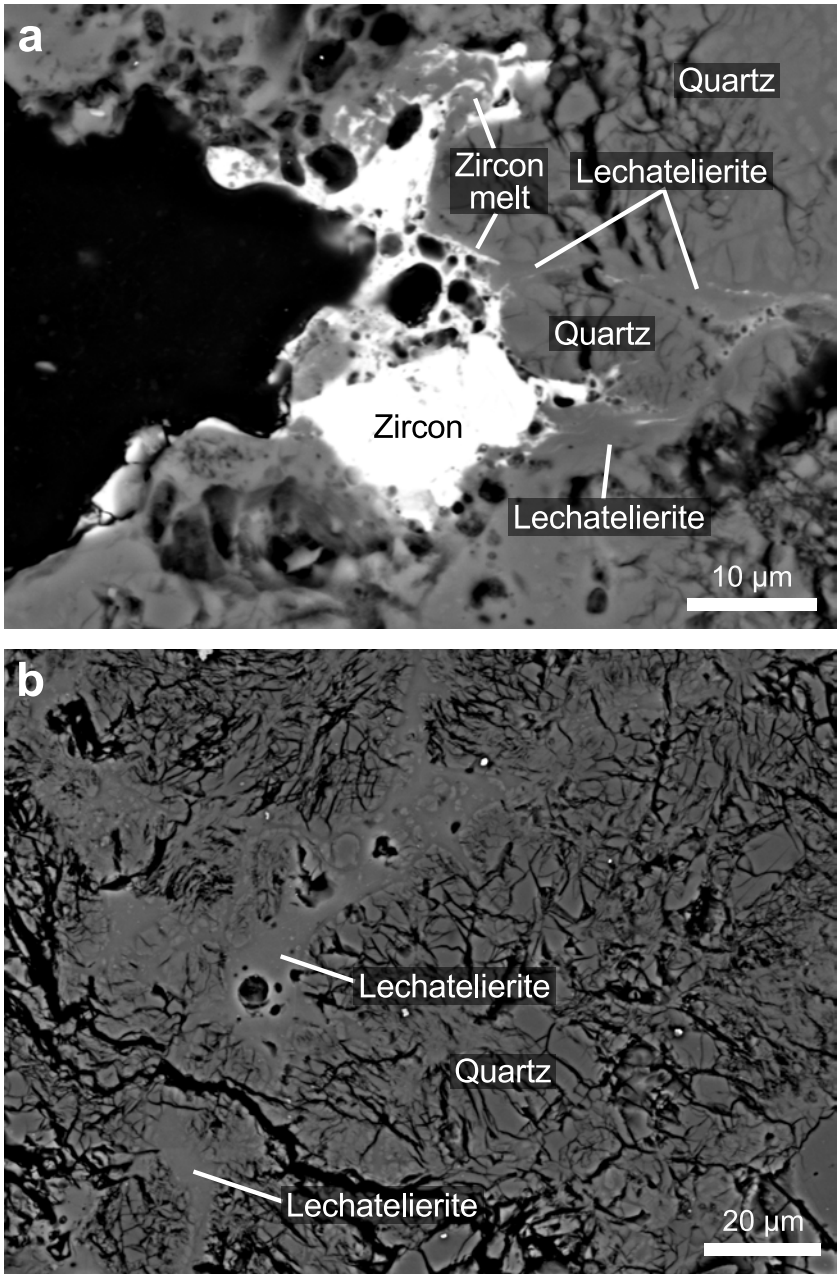

Figure 5.12 Back-scattered electron images documenting incipient melting of accessory zircon (a) and shock-lithified quartz (b) in Zone 4 of impact melt particles from experiments 533 and 534 (cf. Table 5.1). **a** Incipient melting of zircon (note the high-*Z* schlieren in the lechatelierite veins) locally indicates postshock temperatures in excess of 2000 °C (Robie et al., 1995); experiment 533. **b** Incipient melting of quartz locally indicates postshock temperatures in excess of 1713 °C, which is the melting point of quartz at ambient pressure (Robie et al., 1995); experiment 534.

(530, 533, and 534), 48 ± 3 GPa, 43 ± 3 GPa, and 46 ± 3 GPa were reached, respectively. As shown by Wünnemann et al. (2016) on the basis of numerical modeling, pressures in excess of 13 GPa occurred in an elliptical zone[10] (at ~0.8 cm depth and ~0.5 cm radial distance) around the point of impact (Fig. 5.1). Material in this region will undergo shock melting and, depending on its initial position, will either remain in the final crater or be ejected. As shown in the previous section (e.g., Fig. 5.4), the uppermost parts of the impact melt particles are composed of molten and subsequently recrystallized Al metal, quenched and partially recrystallized Al_2O_3 melt, and lechatelierite. This indicates postshock temperatures in excess of 2000 °C, as alumina, quartz, and aluminum have melting points

[10] The zones of decreasing shock metamorphism documented in the melt particles will be immediately correlated to the shock zones obtained from the model in Chapter 6

Table 5.6 Major element compositions of lechatelierite in Zone 3 and accessory zircon in Zone 4.

[wt.%]	Lechatelierite $n = 11$	Zircon $n = 8$
SiO_2	99.6(1)	31.8(3)
Al_2O_3	0.4(1)	bdl
FeO[a]	bdl	bdl
MnO	bdl	bdl
MgO	bdl	bdl
ZrO	bdl	67.0(6)
HfO	bdl	1.2(5)

Data obtained by SEM-EDX (point analyses with focused, ≤1-µm-diameter electron beam) and reported as average of *n* analyses with twofold standard deviation given in parentheses; bdl—below detection limit.
[a] All Fe reported as FeO.

of 2072, 1713, and 660 °C, respectively (Robie et al., 1995). Although it is obvious that melting of both the aluminum projectile and the uppermost parts of the sand target occurred (Figs. 5.3, 5.4, and 5.5), it seems that theoretical considerations regarding the shock pressure thresholds for incipient and complete melting of aluminum (73 and 106 GPa, respectively; Pierazzo et al., 1997) are at odds with the observations made in this study (see Table 5.1). Using Hugoniot data for non-porous quartz from Melosh (1989), we can place an upper limit of 64–75 GPa for impact velocities between 5.9 and 6.5 km s^{-1} (see Figs. A.1 and A.2). These values are close to or slightly below the pressure threshold of 73 GPa from Pierazzo et al. (1997), that is, shock pressures in this scenario would still be too low to facilitate wholesale melting of the projectile.

We recognize two mechanisms that led to pronounced melting of both projectile and target: (1) the effect of pore crushing and (2) the release of heat from the redox reaction between projectile and target.

1. *Pore crushing* can locally amplify shock pressure and postshock temperature due to collapse of pore space in porous materials. In general, for impacts into porous targets, shock melting occurs at lower pressures and, hence, lower impact velocities compared to impacts into dense targets (e.g., Wünnemann et al., 2008; Davison et al., 2010; Kowitz et al., 2013a; Kowitz et al., 2013b; Bland et al., 2014). Specifically, a major effect of pore crushing in porous sandstone is that incipient melting of quartz grains is facilitated at shock pressures as low as ~5 GPa (Kowitz et al., 2013a; Kowitz et al., 2013b), which is significantly below the pressure threshold of ~50 GPa that is required for melting single quartz crystals (Stöffler and Langenhorst, 1994). Consequently, postshock temperatures were increased in the projectile due to the crushing of nearby pores in the quartz sand target immediately below the projectile–target interface (Zone 2 and 3). The effect of pore crushing is also demonstrated in Zone 4 of the impact melt particles, where it accounts for incipient melting of quartz and zircon along grain boundaries (Fig. 5.12). The locally

increased temperatures leading to incipient melting were caused by localized shock pressure amplifications which occurred at grain contacts, even though the average temperature increase over a large volume remained small.

2. The most obvious additional heat source is the *redox reaction* between projectile and target, $3\ SiO_2 + 4\ Al \rightarrow 3\ Si + 2\ Al_2O_3$. This reaction is strongly exothermic ($\Delta H = -619$ kJ); thus, progressive oxidation of Al metal from the projectile must have released excess heat that further promoted melting of the projectile and the uppermost parts of the quartz sand target.

In conclusion, the impact melt particles experienced average shock pressures and average postshock temperatures ranging from >45 GPa and >2000 °C at their top sides (Zones 1–3) to ~5.5 GPa and some hundred degrees Celsius at their bottom sides (Zone 4), which relates to the decaying shock front within the sand target. Taken together, these P–T conditions are rather typical for small-scale impact experiments in the velocity range of ~4 to ~10 km s^{-1} into porous targets (e.g., Hörz et al., 1983; Poelchau et al., 2013; Ebert et al., 2013; Ebert et al., 2014, and references therein).

Oxygen fugacity

The observations documented above show that the shock-fused projectile is spread over the shock-lithified target in the center of the crater, becoming an integral part of the impact melt particles and mixing with the shock-melted, chemically altered parts of the target. Notably, silicon—forming subhedral to euhedral crystals or spherules—is an important component in the projectile melt crust and in projectile inclusions (Figs. 5.5, 5.7, and 5.9; Table 5.4), but not in the unshocked aluminum projectile (Figs. 5.2 and A.3; Table 5.2). The reaction front of quenched Al_2O_3 melt (Zone 2), which is present between the metallic projectile melt crust (Zone 1) and lechatelierite (Zone 3), documents the chemical reaction between projectile and target. Specifically, owing to the highly reducing nature of Al (see below) and in keeping with the reaction

$$3\ SiO_2 + 4\ Al \rightarrow 3\ Si + 2\ Al_2O_3 \qquad \text{(R 5.1)}$$

SiO_2 of the target was reduced to metallic Si, incorporated into the projectile melt, and precipitated in form of silicon crystals or spherules. Conversely, Al metal of the projectile, being the reducing agent, was oxidized, forming a thin reaction front of Al_2O_3 melt. This aluminothermic reaction is strongly exothermic ($\Delta H = -619$ kJ), producing excess heat that possibly caused further melting of projectile and target. Furthermore, this reaction imposed extremely reducing conditions on the materials, which are otherwise rarely encountered in natural materials, either terrestrial or extraterrestrial.

Whether metals, such as iron, occur in a more oxidized or more reduced state is mainly governed by oxygen fugacity (fO_2), which can be

considered as the pressure that would be applied by 1 molecule of oxygen in a cubic meter of space (for a detailed explanation, see, e.g., Frost, 1991). In natural systems, fO_2 is mainly a function of the Mg/Fe ratio in silicates and the content of titanium in oxides. Hence, it is usually governed by the mineral assemblage in a rock and not imposed from the environment. However, for our experiments the opposite holds true, as metallic aluminum requires highly reducing conditions to be stable and will, if allowed to react with oxides or free oxygen, immediately oxidize. As we will see below, this imposed highly reducing conditions on the materials used in the experiments.

As outlined above, Reaction (R 5.1) involves oxidation of Al metal (Zone 1) to Al_2O_3 melt (Zone 2). Written with respect to 1 mol of oxygen, the following reaction

$$\frac{2}{3}\,Al_2O_3 \leftrightarrow \frac{4}{3}\,Al + O_2 \tag{R 5.2}$$

describes one half of Reaction (R 5.1). The equilibrium constant K for Reaction (R 5.2) is

$$K_{\text{R 5.2}} = \frac{(a_{Al})^{\frac{4}{3}}\, fO_2}{(a_{Al_2O_3})^{\frac{2}{3}}} \tag{5.1}$$

where a_i are the activities of Al in the metallic melt crust of Zone 1 and Al_2O_3 in the dark brown, Si-poor melt phase of Zone 2. Following general methods outlined by Fogel et al. (1989) and Frost (1991), the following expression may be written:

$$\log K_{\text{R 5.2}} = \frac{A}{T} - B - C\frac{(P-1)}{T} \tag{5.2}$$

where T is the temperature in Kelvin and P is the total pressure in bar. A, B, and C are given by

$$A = \Delta H_r/2.303R \tag{5.3}$$

$$B = \Delta S_r/2.303R \tag{5.4}$$

$$C = \Delta V_{r,\,\text{solids}}/2.303R \tag{5.5}$$

where ΔH_r, ΔS_r, and $\Delta H_{r,\,\text{solids}}$ are the change in standard enthalpy, the standard entropy, and the standard-state molar volumes of the reaction, respectively, R is the universal gas constant, and the term 2.303 is a conversion factor derived from converting ln (fO_2) to log (fO_2). For the following discussion, we will assume a pressure of 1 bar, hence $C(P-1)/T = 0$. Substituting Eq. (5.1) into Eq. (5.2), the following equation emerges that expresses fO_2 as a function of T, P, and the activities of Al in the metallic melt crust (Zone 1) and Al_2O_3 in the reaction front (Zone 2):

$$\log fO_2 = -\frac{A}{T} + B - \frac{4}{3}\log a_{Al} + \frac{2}{3}\log a_{Al_2O_3}. \tag{5.6}$$

We assume that the activity of Al_2O_3 in the dark brown, Si-poor melt phase of Zone 2 is approximated by the mole fraction of Al_2O_3, that is, $a_{Al_2O_3} = \chi_{Al_2O_3} = 0.98$. Moreover, $a_{Al} = \chi_{Al}\,\gamma_{Al}$, whereby χ_{Al} and γ_{Al} are the mole fraction and activity coefficient, respectively, of Al in Al metal of Zone 1. Using the activity coefficients of Desai (1987) for binary Al–Si alloys and $\chi_{Al} = 0.96$, we estimate $a_{Al} = 0.95$.

Using Eq. (5.6) and thermodynamic data from Robie et al. (1995), we can calculate a fO_2 vs. T equilibrium curve for Reaction (R 5.2) and compare it with petrologically more common redox buffers (Myers and Eugster, 1983; Frost, 1991). The result (Fig. 5.13) coincides with the Al–Al_2O_3 buffer (Essene and Fisher, 1986; Bindi et al., 2012), confirming that extremely reducing conditions are imposed by Reaction (R 5.2). Specifically, at 1000 and 2000 K, log fO_2 values of ΔIW −26 and ΔIW −11 (ΔSi–SiO_2 −9 or ΔSi–SiO_2 −3), respectively, are indicated, which explains the presence of metallic silicon at the metal–silicate interface and in the metallic melt crust of Zone 1. Similarly reducing conditions were reached in some other shock experiments involving reactions between silicates and metals. For example, Rowan and Ahrens (1994) shocked molten basalt targets enclosed in molybdenum capsules to pressures between 0.8 and 6 GPa. They described Fe–Si–Mo-rich metallic spheres in low-FeO basaltic melt (0.1 wt.% compared to an initial concentration of 9 wt.%) in their samples, originating from in situ reduction of SiO_2 and FeO and oxidation of Mo. Using a similar approach as described above, Rowan and Ahrens (1994) estimated oxygen fugacities in their experiments around the Si–SiO_2 buffer (10–17 bar at 1670 K). For comparison, the most reduced meteorites, such as enstatite chondrites, usually yield log fO_2 values of ΔIW −6 to ΔIW −8 at 1000 K (e.g., Fogel et al., 1989), and, thus, contain Fe in metallic form. Moreover, metallic silicon and iron silicides, such as FeSi or Fe_3Si_7, are known from lunar meteorites, for example, Dhofar 280 (Nazarov et al., 2015), and the Apollo 16 lunar regolith (Spicuzza et al., 2011). On Earth, such reducing conditions are known from fulgurites (rocks formed by lightning strike fusion). For example, Essene and Fisher (1986) described a specimen that seems to have locally equilibrated around the Si–SiO_2 buffer and, hence, contains metallic silicon in form of lath-shaped crystals and globules quite similar in appearance to the ones described from our experiments (cf. fig. 2 of Essene and Fisher, 1986). These examples demonstrate that extremely reducing conditions far below the IW or QIF buffers may occur in natural materials, both terrestrial and extraterrestrial.

Implications for the Khatyrka CV3 carbonaceous chondrite

The most relevant comparison to our study arises from recent descriptions of khatyrkite ($CuAl_2$) in the Khatyrka CV3 carbonaceous chondrite by Bindi et al. (2012). As outlined by these authors and shown in Fig. 5.13, khatyrkite requires fO_2 conditions a few log units above the Si–SiO_2 buffer in order to keep this phase stable. Interestingly, a similar redox reaction between khatyrkite and FeO in siliceous impact melt was recently

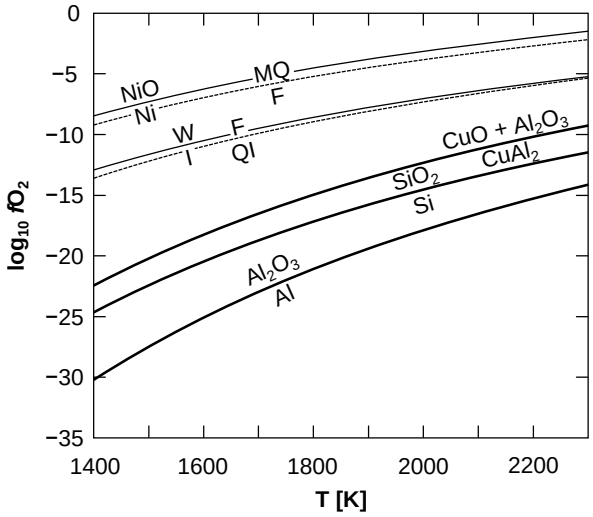

Figure 5.13 Calculated log fO_2 vs. T (in K) equilibrium curves for relevant metal–metal oxide buffers and common petrologic redox buffers. Heavy continuous lines: fO_2 conditions for materials encountered in the impact melt particles; thin continuous lines: petrologically significant metal–metal oxide buffers; thin dotted lines: petrologically significant mineral redox buffers. The equilibrium curves were obtained by the methods outlined by Myers and Eugster (1983), Fogel et al. (1989), and Frost (1991), and using thermodynamic data from Robie et al. (1995). FMQ: fayalite–magnetite–quartz; IW: iron–wüstite; QIF: quartz–iron–fayalite.

described from Khatyrka grain #129,[11] yielding Ni-free Fe metal spherules at the interface between khatyrkite and impact melt (Hollister et al., 2015).

The Khatyrka carbonaceous chondrite, recovered in 2011 in eastern Siberia (MacPherson et al., 2013), has constituted a mystery as to what (extraterrestrial?) process could have led to the formation of a unique assemblage of Al metal alloys and silicates. For instance, the discoveries of icosahedrite ($Al_{63}Cu_{24}Fe_{13}$), a naturally occurring quasicrystal, as well as khatyrkite and cupalite (CuAl) in Khatyrka (Bindi et al., 2012; Hollister et al., 2014) challenge our understanding of how Al–Cu-rich, metallic phases can form under conditions of equilibrium nebular condensation. Given the fact that Al and Cu have greatly contrasting chemical properties, the presence of these phases in Khatyrka has remained an enigma. Specifically, Al condenses at high temperatures (>1600 °C) into corundum (Al_2O_3), hibonite ($CaAl_{12}O_{19}$), and grossite ($CaAl_4O_7$), which later are converted to gehlenite ($CaAl_2SiO_7$), whereas Cu condenses at much lower temperatures (1000–1100 °C, based on its 50% condensation temperature) into Fe metal (Lodders, 2003).

Moreover, explaining the presence of metallic Al in Khatyrka, which requires extremely reducing conditions to be stable (see previous subsection), is challenging. Hence, the possibility that Khatyrka is actually the result of anthropogenic activity has been discussed in some detail (see, e.g., Bindi et al., 2012). However, a recent description of an assemblage comprising a CAI, impact-melted ferromagnesian CV3 matrix, and khatyrkite in mutual contact in Khatyrka grain #129 by Hollister et al. (2015) sheds

[11] The redox reaction in Khatyrka was later documented in more detail by Lin et al. (2017); see below

some light on the formation history of Khatyrka. Furthermore, oxygen isotopic compositions of olivine, pyroxene, and spinel encountered in various grains of Khatyrka coincide with the carbonaceous chondrite anhydrous mineral (CCAM) line (Bindi et al., 2012; Hollister et al., 2014). The CCAM line discriminates terrestrial from extraterrestrial sources, thus ultimately proving an extraterrestrial origin of Khatyrka. Besides these facts, the discovery of a stishovite grain containing a 5-nm-diameter inclusion of icosahedrite indicates that an impact event must have played a role in Khatyrka's history (Bindi et al., 2012).

The impact melt particles of our study show some similarities to grain #129 of Khatyrka described by Hollister et al. (2015). For example, grain #129 features a crust of khatyrkite and Al metal adhering to an impact melt droplet derived from CV3 matrix material, quite similar in structure to Zones 1–3 of our impact melt particles. Hollister et al. (2015) further discussed a redox reaction between Al–Cu metal and impact melt, which yielded Ni-free Fe spherules ≤1 µm in size at the interface between Al–Cu alloy and Fe-depleted impact melt (see figs. 2 and 3 in Hollister et al., 2015). These Ni-free Fe spherules differ in composition from FeNi spherules encountered in the interior of the impact melt droplet, indicating in situ reduction of FeO-bearing glass. Similarly, redox reactions in our experiments between Al metal projectile and SiO_2 target (see above) yielded silicon spherules in lechatelierite at the interface to projectile inclusions, which are surrounded by a reaction zone of Al_2O_3 melt (Figs. 5.10a and 5.11b). A similar reaction zone seems to be missing in Khatyrka,[12] but the Ni-free Fe spherules could be regarded as analogs to the silicon spherules found in our experiments. However, the presence of carbonaceous and/or organic material in Khatyrka could also have played a role in creating the highly reducing conditions. As discussed by Essene and Fisher (1986) and Rowan and Ahrens (1994), possible reducing agents include C and N, which may effectively scavenge oxygen from a melt and locally facilitate reduction of oxides to produce elemental metals. This form of "smelting" was also discussed for the formation of iron silicides in dust particles from comet 81P/Wild 2, which were trapped in the silica aerogel capture medium of the *Stardust* spacecraft (Rietmeijer et al., 2008). Thus, we raise the question whether organic matter could have played a role in Khatyrka's history as well. In conclusion, searching for a reaction zone between Al–Cu alloy and impact melt (e.g., in the form of Al_2O_3-enriched impact melt?) in grain #129 could further illuminate the redox process(es) in Khatyrka and ultimately prove that Al–Cu alloy and impact-melted CV3 matrix have a mutual history.

[12] After publicatiof of this study in 2016, the discovery of a similar reaction zone between Al metal alloys and silicate melt in a grain of Khatyrka was indeed published in 2017 by Lin et al. (2017), who reported several phases such as Ni-free Fe metal, Al spinel, and Al-rich glass around khatyrkite

Applicability to impacts of iron meteorites into silica-rich targets

The aluminum projectiles used in this study have, admittedly, no counterpart in nature. Thus, applying the petrologic and geochemical results of this study to impacts of iron meteorites into silica-rich targets (e.g., quartz sand or sandstone) seems a bit of a stretch, yet several small impact craters on Earth feature impactites similar in texture to the impact melt particles

described above. For example, impact melting of quartz sand at the Wabar craters, Saudi Arabia, yielded impact melts that incorporated remnants of the impacting IIAB iron meteorite in the form of FeNi spherules (see Chapter 8 and Hörz et al., 1989; Hamann et al., 2013). Occasionally, inclusions of molten target material (i.e., lechatelierite and a melt derived from accessory minerals in the target) surrounded by metallic projectile melts are found disseminated in these impact melts (see figs. 1d–f and 2c of Hamann et al., 2013), which texturally strongly resemble Zones 1 and 3 of this study. Of course, as outlined in Section 5.1 and documented by Fig. 5.13, the chemical reaction between metallic Fe from the Wabar IIAB projectile and SiO_2 of the quartz sand target must have been strongly endothermic (ΔH = 2189 kJ), and Fe in the metal should equilibrate with FeO in the impact melt close to the IW buffer. Hence, no metallic Si is expected to be found in these melt particles.

However, several textural characteristics of the impact melts produced in our experiments are commonly recognized in natural impact melts from small impact craters formed by iron meteorites, such as Barringer, Arizona, Wabar, Saudi Arabia, or Kamil, Egypt—to name only a few. The most striking common textural features are:

1. formation of PDF in quartz (e.g., Kieffer, 1971);
2. occurrence of relic, PDF-bearing quartz grains in impact melt and lechatelierite (e.g., Gnos et al., 2013; Fazio et al., 2014b);
3. melting of quartz to vesicular, often flow-banded lechatelierite (e.g., Hörz et al., 1989; See et al., 1998; Hamann et al., 2013; Fazio et al., 2014b);
4. dissemination of metallic projectile spherules in siliceous impact melts (e.g., Gibbons et al., 1976b; Hörz et al., 1989; Hörz et al., 2002; Hamann et al., 2013; Fazio et al., 2014b);
5. crystallization of minerals, such as olivine or pyroxene, from impact melts that are (chemical) mixtures of projectile and target (e.g., See et al., 1998; Hörz et al., 2002); and
6. formation of thin veneers of projectile-rich melts around target fragments (e.g., Kearsley et al., 2004; Hamann et al., 2013).

Hence, albeit of different chemistry, in respect to the interaction process between projectile and target, the impactites produced in this study share some common features with natural impactites formed in small, simple impact craters.

Comparison with other shock experiments involving aluminum

Geochemical studies of impacts of aluminum projectiles are rare, as such projectiles have no counterpart in nature. One example is the study of Fiske et al. (1995), who investigated chemical reactions between quartz

discs and aluminum capsules shocked to pressures of 42 and 56 GPa. For both experiments they described diaplectic quartz glass cross-cut by veins of black glass, which consists of 20–400 nm size spheres of crystalline Si and Al in a matrix of amorphous SiO_2. They did, however, not detect metallic silicon in quartz discs enclosed in steel capsules shocked to 56 GPa and, consequently, attributed the presence of metallic Si in the experiments with aluminum capsules to in situ reduction of SiO_2 by highly reactive Al metal.

Moreover, Wozniakiewicz et al. (2011), Wozniakiewicz et al. (2012), and Wozniakiewicz et al. (2015) investigated impactor residues of, for example, pyrrhotite ($Fe_{1-x}S$), pentlandite [$(Ni,Fe)_9S_8$], olivine, diopside, phyllosilicate, and calcite micro-projectiles shot onto aluminum foils used for NASA's *Stardust* mission. These experiments were designed to simulate impacts of interplanetary dust particles onto Al foils that were intended to secure aerogel blocks (the actual particle catchers) of the spacecraft. Although compositionally different and significantly smaller projectiles with sizes <53 μm were used by them, their impact velocities of ~5.8–6.2 km s^{-1} are comparable to those of our study. Using a combination of SEM and scanning transmission electron microscopy, Wozniakiewicz et al. (2011), Wozniakiewicz et al. (2012), and Wozniakiewicz et al. (2015) showed that projectile residues and impact melts remain inside the impact craters created in the aluminum foils. Specifically, Wozniakiewicz et al. (2011) detected fractured particles of pyrrhotite and pentlandite adhering to Al metal in the craters. Moreover, melting and mixing of projectiles and targets is indicated at the interfaces, yielding impact melts that are mixtures of pyrrhotite and Al with constant Fe/S ratios, but variable Fe/Al and S/Al ratios. These impact melts are analogs to the reaction zone between aluminum projectile and quartz sand (Zone 2) in our experiments, which shows highly variable Si/Al ratios (Figs. 5.7 and 5.9), indicating mixing between projectile and target. Furthermore, Wozniakiewicz et al. (2015) investigated impact melting of Mg–Fe-rich phyllosilicate projectiles shot onto *Stardust* aluminum foils and described projectile–target mixing in impact melts that locally encountered reducing conditions due to the presence of molten Al. Comparable to our study, this resulted in the production of <50-nm-diameter, metallic silicon beads and Fe-silicides via reduction of SiO_2 and FeO in silicate melts derived from impact melting of the phyllosilicate projectiles.

Another example is that of Daly and Schultz (2016), who performed impact experiments with 6.35-mm-diameter basalt and aluminum projectiles shot at 4.5–5 km s^{-1} into porous, powdered pumice targets (~43% porosity; 1300 kg m^{-3} bulk density). Their study was designed to investigate the effect of impact angle (30°, 45°, 60°, and 90° with respect to the horizontal) on the projectile retention for impacts into the regolith of asteroid 4 Vesta. They found that projectile retention is sensitive to the impact angle, with high impact angles (with respect to horizontal) favoring projectile retention in the target. For example, in the case of vertical impacts, ~72% of the projectile remains inside and near the crater, whereas

in the case of 30° impacts, only ~7% of the projectile is retained. Moreover, they detected "projectile-contaminated breccia pieces" that show coatings of partially molten projectile material adhering to partially molten and projectile-contaminated target fragments similar in appearance to the impact melt particles from our study. In the case of the aluminum projectile, shot at 5.58 km s^{-1}, Daly and Schultz (2016) described projectile–target mixing processes and partial melting of the projectile, but did not report a pronounced reaction front between projectile and target, nor did they give a detailed characterization of shock-metamorphic effects in the target. In comparison, it seems that the Al projectiles in our study are substantially more molten than theirs, which is most likely due to the slightly higher impact velocities in our experiments, as well as the lower density of the target in their experiment. To estimate the difference in shock pressure between the two studies, we used Hugoniot data for powdered basalt from Pierazzo et al. (2005) and quartz sand from Trunin et al. (2001) as a first approximation for powdered pumice (see Figs. A.1 and A.2). Hugoniot data for the aluminum projectile were taken from Melosh (1989). Compared to the 41–48 GPa of our experiments, the estimated shock pressure for the experiment by Daly and Schultz (2016) is ~35 GPa.

5.5.2 Implications for regolith formation on planetary bodies

Implications for impacts into the lunar regolith

The results of this study bear on our understanding of regolith-forming processes on planetary surfaces. Specifically, so-called "agglutinates" are abundant in the lunar regolith, which were sampled at all six Apollo landing sites (see summaries in McKay et al., 1991; Lucey et al., 2006). They are defined as individual particles made up of smaller lunar soil particles in the form of mineral fragments, glasses, and older agglutinates, bonded together by vesicular, often flow-banded glass (McKay et al., 1991). The glass in many lunar agglutinates has roughly the same composition as the soil in which they are found (e.g., Engelhardt, 1970; Marvin et al., 1971; Taylor et al., 1972; Gibbons et al., 1976a; Hu and Taylor, 1977). Agglutinates are believed to form by melting and mixing produced by bombardment of micrometeoroids striking the lunar regolith (McKay et al., 1991). They make up, on average, some 25–30% of the lunar soil, although their abundances occasionally range from rare 5% to about 65% (McKay et al., 1991). Obviously, formation of agglutinates requires (1) a constant influx of micrometeoroids impacting the surface of an airless body with high velocity and (2) a target surface consisting of regolith that formed by prior bombardment.

Although the aluminum projectiles of this study have no counterpart in nature, impact melting and sintering of the quartz sand target shows some qualitative similarities to lunar agglutinates. For example, target-derived, vesicular melts (lechatelierite) that incorporate shocked mineral fragments (PDF-bearing quartz) in Zone 1, as well as the glass-bonded

rock fragments (shock-lithified quartz grains) in Zone 4, bear some resemblance to glasses and glass-bonded lithic fragments in lunar agglutinates, notwithstanding the difference in chemical composition. However, typical lunar agglutinates usually lack intact meteoritic fragments (Rubin, 1997) and are substantially more melt-rich, if not melt-dominated (Hörz and Cintala, 1997). The paucity of lunar agglutinates showing projectile fragments is born out of the fact that the average lunar impact velocity ranges from 13 to 18 km s^{-1} (Zook, 1975; Cintala and Grieve, 1998), which corresponds to peak shock pressures in regolith material of far beyond 40 GPa, the threshold pressure for complete melting (e.g., Stöffler and Grieve, 2007). Specifically, less than 2% of the impacting projectiles should survive as intact fragments, whereas the vast majority should be extensively melted or vaporized (Zook, 1975; Rubin, 1997).

Despite these facts, scenarios can be envisaged that involve much lower impact velocities, which would allow the survival of projectile remnants impacting the Moon. For example, the minimum relative lunar impact velocity is ~3 km s^{-1}, resulting from both the gravitational escape velocity due to the lunar gravity and the gravitational influence of the Earth at lunar orbit (Zook, 1975). Moreover, based on the velocity distribution of meteoroids as they impact the Moon, a certain fraction (maybe <10%) of projectiles impact the lunar surface at velocities of 4–6 km s^{-1}. If one assumes that melting of impactors starts at velocities of ~5 km s^{-1}, we find that between 1 and 5% of the impacting projectiles should survive the impact as partially molten fragments, whereas 12–32% will undergo whole-rock melting and 50–90% vaporization (Zook, 1975). Indeed, several reports exist that document intact projectile fragments in the lunar regolith. These reports include the Hadley Rille enstatite chondrite, recovered from the Apollo 15 landing site, which documents partial impact melting of the lunar regolith in the form of an agglutinate-like rim around the preserved chondritic projectile (Rubin, 1997). As shown by this author, the chondrite accreted to the lunar regolith at a relative impact velocity of at least 3 km s^{-1}. Due to the impact, portions of the lunar regolith were melted, forming the agglutinate-like rim composed of flow-banded, vesicular silicate glass, blebs and spherules of troilite and low-Ni Fe metal, rock fragments, and mineral grains. The mineral grains in the rim include enstatite, as well as a poorly characterized phase heavily enriched in light rare earth elements. Both of these phases are otherwise absent in the lunar regolith surrounding the Apollo 15 landing site, thus documenting the chemical interaction between projectile and target. Another example for natural projectile–target interaction was reported by Jolliff et al. (1993), who described a 0.3 × 0.4 mm iron meteoroid fragment enclosed in an agglutinate containing glass and fine-grained soil particles from Apollo 16 regolith core sample 60014. As initially hypothesized by Jolliff et al. (1993) and later discussed by Rubin (1997), it seems likely that the agglutinate formed directly around the iron meteoroid fragment as a result of impact melting of the lunar regolith. Other examples of impactor remnants in the lunar regolith, in the form of mineral and lithic fragments, were reported

by Quaide and Bunch (1970), Zolensky (1997), Day et al. (2006), and Joy et al. (2012).

A comparison between our experimental results and typical lunar agglutinates may constrain formation conditions of the unusual agglutinate-like rims around projectile remnants, such as in the case of the Hadley Rille enstatite chondrite described by Rubin (1997). It seems reasonable that agglutinates that lack surviving projectile fragments were formed by projectiles impacting at velocities high enough to facilitate complete melting or vaporization of the impactor. In the case of impactor melting, chemical remnants of the impactor melt should either reside at the point of impact, that is, in a crater, or mix with target-derived impact melt. Early workers tried to discern extralunar components in lunar microcraters and in agglutinates (see summaries in Hörz et al., 1975; McKay et al., 1991), yet failed to identify the chemical properties of the projectiles. The only direct evidence for the chemical composition of micrometeoroids impacting the Moon is based on trace element analysis of lunar soils, hinting at CI chondrites as the most abundant impactors (e.g., Anders et al., 1973), and on the detection of projectile residues in regolith and breccia samples (e.g., Day et al., 2006; Joy et al., 2012). Furthermore, projectiles that form agglutinate-like rims around them upon impact, for example, the Hadley Rille enstatite chondrite or the iron meteoroid of Jolliff et al. (1993), are appreciably larger than the submillimeter micrometeoroids that typically produce agglutinates. For example, the Hadley Rille enstatite chondrite fragment is 1.1 × 1.2 mm in size (Rubin, 1997), which is slightly larger than the 0.3 × 0.4 mm iron meteoroid of Jolliff et al. (1993). In comparison, the projectile melt crust of Zone 1 in our experiments is ≤0.4 mm in thickness (Figs. 5.3 and 5.4). The agglutinate-like rim around the Hadley Rille enstatite chondrite has a maximum thickness of ~360 µm (Rubin, 1997), which is comparable to the ≤500-µm-thick layer of lechatelierite (Zone 3) in our experiments.

The compositions and physical properties of the materials involved in the examples given above are, admittedly, different from our projectile and target materials. Nevertheless, it is tempting to speculate that low-velocity (~4–6 km s^{-1}) impacts of mm-sized projectiles into the lunar regolith would yield similar petrographic effects, that is, agglutinate-like rims of impact-melted lunar soil around (partially) molten impactors. Moreover, as outlined by Hörz and Cintala (1997), projectiles that impact at velocities high enough to facilitate whole-rock melting and formation of true agglutinates should also produce a continuum of lower shock pressures further away from the point of impact. These lower shock pressures lead to incipient grain-boundary melting, forming "glass-welded aggregates" (Hörz and Cintala, 1997) akin to the melt-bonded quartz grains in Zone 4 of our experiments. This hypothesis is in keeping with shock recovery experiments with granulated lunar basalt (Schaal et al., 1979) and lunar soil (Schaal and Hörz, 1980), which show that progressive grain-boundary melting develops as a response to collapse of pore space in samples shocked to pressures between ~17 and ~65 GPa. Whole-rock

melting, forming frothy impact glass that mimics the bulk composition of the precursor rock, starts at pressures in excess of 60–65 GPa in these experiments. This is in general agreement with recent numerical modeling studies (e.g., Wünnemann et al., 2008; Davison et al., 2010; Kowitz et al., 2013a; Kowitz et al., 2013b; Bland et al., 2014), which have shown that for impacts into porous materials, shock melting occurs at lower pressure and, hence, lower impact velocities compared to dense materials. Moreover, as suggested in these studies and verified in our experiments, compaction of heterogeneous, porous materials during shock loading can produce enough localized postshock heat to facilitate grain boundary melting.

Implications for impacts into the regolith of asteroids in the main belt

Compared to the Moon, the average impact velocity in the main belt decreases to ~5 km s^{-1} (Bottke et al., 1994), which is in the range of the impact experiments under discussion here and of those performed by Daly and Schultz (2016). This velocity is believed to be marginally capable of producing impact melts; hence, the products of typical mm-sized impacts into asteroidal regoliths will differ from much faster impacts of comparable projectiles into the lunar regolith (see above and, e.g., Hörz et al., 2005, as well as references therein).

Several workers have experimentally investigated shock metamorphism of powdered chondritic materials. For example, Bischoff and Lange (1984) impacted fine-grained (<120 μm) powders derived from the Forest City H5 chondrite with aluminum and stainless steel flyer plates at velocities between 1 and 1.7 km s^{-1}, inducing shock pressures of 4–38 GPa. They described complete consolidation of the shocked chondrite powder starting at pressures as low as ~4 GPa and reported grain-boundary melting of feldspar grains at pressures between 28 and 38 GPa. However, the most detailed experimental study on shock metamorphism in chondrite powders is that of Hörz et al. (2005), who reported on shock reverberation experiments in the pressure range of 14.5–67 GPa performed with a "regolith" powder derived from the ALH 85017 L6 chondrite. Hörz et al. (2005) found that the initial pore space (40–50%) of the material is completely closed at 14.58 GPa. Furthermore, they detected incipient grain-boundary melting to start at ~27 GPa. At ~67 GPa, corresponding to ~5 km s^{-1} impact velocity, ~50% of the sample was molten. Ultimately, Hörz et al. (2005) hypothesized that whole-rock melting of the chondrite powder will require shock pressures in excess of 80 GPa, which would correspond to impact velocities in excess of 8 km s^{-1}.

By combining our results presented above with those of Hörz et al. (2005) and Daly and Schultz (2016), we conclude that impact melting along grain boundaries will be a common, if not dominant, process in asteroidal regoliths. Contrary to agglutinates in the lunar regolith, impact melt agglomerates in asteroidal regoliths, for example, on 4 Vesta, will feature heterogeneous impact melts that result from incipient melting along grain boundaries. Appreciable parts of the impacting projectiles

will be retained in these regoliths, not only in the form of partially to completely molten crusts adhering to regolith agglomerates, but also in the form of projectile-contaminated impact melts.

5.6 Summary and conclusions

Impacts of aluminum projectiles into quartz sand at ~6 km s^{-1} result in complete melting of the projectile, partial melting of the target, exothermic redox reactions between Al metal and SiO_2, and mixing between the liquid projectile and the partially molten target. The liquid projectile is spread over the shock-lithified and partially molten target and becomes an integral part of impact melt particles. Aluminum of the projectiles causes extremely reducing conditions around the Al–Al_2O_3 buffer (ΔIW –26 or ΔSi–SiO_2 –9 at 1000 K), which, upon cooling, leads to the formation of metallic silicon, khatyrkite ($CuAl_2$), and $(Fe,Mn)_xSi(Al,Cu)_y$ in the projectile melt crust. Moreover, a reaction front of Al_2O_3 melt forms at the interface between projectile and target as a result of the redox reaction.

Although artificial projectiles have been used that have no counterpart in nature, the results of this study have implications for the unusual coexistence of Al–Cu–Fe alloys (e.g., icosahedrite, khatyrkite, and cupalite), silicates (e.g., olivine and clinopyroxene), and siliceous impact melt in the Khatyrka CV3 carbonaceous chondrite. For instance, a redox reaction similar to that documented in our experimental results is expected between the Al–Cu–Fe alloys and the siliceous impact melt of Khatyrka.[13] Furthermore, the results of this study bear on our understanding of regolith-forming processes on planetary bodies lacking an atmosphere. Specifically, impacts of mm-sized projectiles at velocities between 4 and 6 km s^{-1} into regolith-covered surfaces of large asteroids in the main belt should yield similar layered impact melt particles that feature a continuum of shock effects, including partially to completely molten projectile remnants adhering to impact-melted regolith agglomerates, as well as projectile-contaminated impact melts and local shock melting along grain boundaries.

[13] As mentioned before, this redox reaction was recently documented by Lin et al. (2017)

Acknowledgments

We greatly appreciate editorial handling by Alex Nemchin. Constructive reviews by Penny Wozniakiewicz and Gareth Collins led to a much improved article. We thank the 1970s staff of NASA Ames Vertical Gun Range for performing the experiments and the Institut für Planetologie of the Westfälische Wilhelms-Universität Münster for allocation of the samples. Thanks are also due to Hans-Rudolf Knöfler for sample preparation, to Peter Czaja for assistance at the electron microprobe, as well as to Kathrin Krahn and Ralf-Thomas Schmitt for XRF sample preparation and analysis. Fruitful discussions with Kai Wünnemann, Meng-Hua Zhu, Natasha Artemieva, Lutz Hecht, and Robert Luther are greatly appreciated. This publication is part of the PhD thesis of CH, performed in the

framework of the Multidisciplinary Experimental and Modeling Impact Research Network (MEMIN). The MEMIN research unit (FOR 887) is funded by the Deutsche Forschungsgemeinschaft (DFG). CH gratefully acknowledges the DFG for funding (grant He-2893/8-2). We dedicate this publication to Claudia Jammes, who conducted the initial mineralogical study of the impact products of the experiments to achieve her Diploma degree at the Westfälische Wilhelms-Universität Münster (awarded in 1984).

Associate editor: Alexander Nemchin

Chapter 6

Shock wave attenuation in porous, particulate targets: insights from impact experiments and numerical modeling[1]

Key points:

Petrologic observations of layered impact melt particles recovered from the floors of experimental impact craters (see Chapter 5) are compared to numerical models of crater formation under similar starting conditions

The shock zones preserved in the particles agree with modeled shock zones at very early time steps of crater formation, which indicates that the melt particles sample the uppermost parts of the transient cavity at very early time steps of crater formation

These findings suggest that chemical processes along the projectile–target interface can effectively operate on time scales measured in fractions of total crater growth time

Hypervelocity impacts create shock waves that attenuate with increasing distance from the point of impact, which can be regarded as being surrounded by hemispherical zones of decreasing shock pressure and, hence, by a continuum of decreasingly intense shock-metamorphic effects. Shock attenuation—or better: the resulting sequence of successively decreasing shock effects—has been, in part, reconstructed at some terrestrial craters by either using well-documented shock effects (e.g., shatter cones, PDF, diaplectic glasses, etc.) to estimate shock pressures, or by using combinations of petrographic observations and numerical modeling. However, descriptions of successively decreasing shock effects that cover large, *uninterrupted* pressure ranges (i.e., from complete melting to below Hugoniot elastic limit) are rare. In this chapter, shock wave attenuation in quartz sand targets is reconstructed by comparing the shock zoning documented in impact melt particles from impact experiments (see Chapter 5) against a numerical model that simulates shock wave attenuation under starting conditions similar to the experiments. The melt particles essentially represent the uppermost parts of the transient cavity at *very* early time steps of crater formation. Combined with the petrologic findings of the previous chapter, this suggests that chemical processes along the projectile–target interface can effectively operate on time scales measured in fractions of total crater growth time.

[1]Some of the contents of this chapter were presented at the 79th Annual Meeting of The Meteoritical Society. To meet the requirements of this dissertation, the conference abstract has been rewritten and extended. The original abstract is: Hamann, C., Zhu, M.-H., Wünnemann, K., Hecht, L., and Stöffler, D. (2016). Tracing shock wave attenuation in porous, particulate targets: insights from impact experiments and numerical modeling, *79th Annual Meeting of The Meteoritical Society*, Abstract #6335. Additional material is derived from a second abstract: Wünnemann, K., Engelmann, J., Luther, R., Hamann, C., and Zhu, M.-H. (2017). Impact-induced shock melting and ejection of material in an asteroidal environment—implications for the deficit in melt agglutinates in Itokawa samples, *48th Lunar and Planetary Science Conference*, Abstract #2023.

6.1 Introduction

Regolith-covered surfaces of atmosphere-less bodies (e.g., on the Moon, or on asteroids and comets) are subject to a continuous flux of impactors that range from millimeter-size micrometeoroids to large, meter-size, crater-forming objects. Independent from the size scale, hypervelocity impacts generate shock waves that lead to distinct shock-metamorphic effects in both projectile and target. Depending on the initial impact velocity, the rheological properties (e.g., density, prorosity) of the materials involved, and the distance from the point of impact, shock effects in rocks and minerals range from mechanical loading (e.g., fracturing), to solid-state transformations (e.g., formation of diaplectic glasses), to melting, and ultimately to vaporization.

Based on physical considerations in the form of Eq. (2.1) on page 12, the point of impact can be regarded as being surrounded by hemispherical zones of decreasing shock pressure and, hence, by a continuum of decreasingly intense shock-metamorphic effects in the target material (Melosh, 1989). This shock attenuation has, in part, been reconstructed at some terrestrial craters on the basis of well-documented shock effects in rocks and minerals (e.g., Kieffer, 1971), or by using a combination of petrographic observations and numerical modeling (e.g., Rae et al., in press). However, descriptions of successively decreasing shock-metamorphic effects that cover large, *uninterrupted* pressure ranges (from complete melting to below Hugoniot elastic limit) in a given sample are rare (e.g., Stöffler et al., 1975; Nagaki et al., 2016).

Here, shock wave attenuation and impact melt formation in porous, "regolith-like" targets is studied by comparing the sequence of shock effects documented in the impact melt particles recovered from the impact experiments detailed in Chapter 5 with results obtained from numerical modeling. The results of this comparison will then be discussed in the light of abundantly occurring, small-scale impacts of micrometeoroids into regolith-covered, asteroidal surfaces.

6.2 Methods

6.36-mm-diameter aluminum spheres were shot vertically at velocities of 5.9–6.5 km s^{-1} onto quartz sand targets of ~42% porosity, producing impact craters of ~33 cm diameter and ~6 cm depth (see Fig. 6.1 and cf. Chapter 5). Tracing of particle movement was facilitated by 9-mm-thick, horizontal strata of differently colored quartz sand that were placed at different positions in the target (see Fig. 5.1). Ejecta were collected up to distances of 6 crater radii, but this study focuses exclusively on large, centimeter-size, layered melt particles that were recovered from the crater floors (cf. Chapter 5). Subsequent petrographic investigation of the melt particles was done on petrographic thin sections, using similar micro-analytical methods as described in Chapter 5.

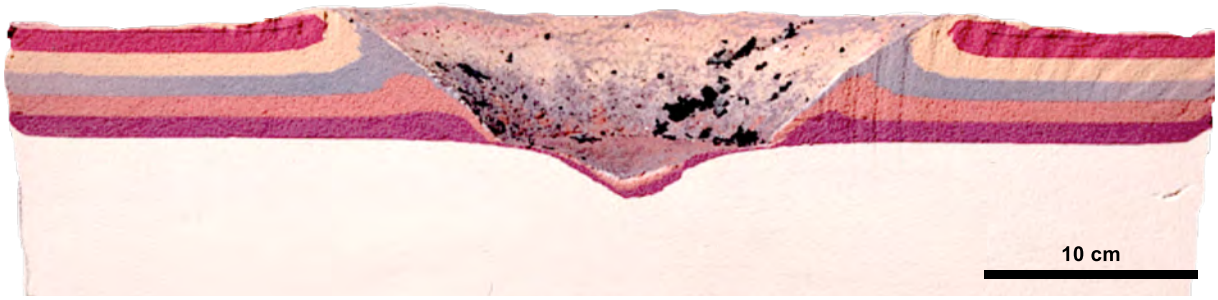

Figure 6.1 Cross-section through an experimental crater formed in quartz sand. Note the presence of dark melt particles on the crater floor. Similar melt particles were investigated here. Image courtesy of D. Stöffler.

The iSALE shock physics code (Wünnemann et al., 2006) was used to simulate a representative experiment (529; see Table 5.1) in a representative model (Fig. 6.2; see also Wünnemann et al., 2016). For the model, the behavior and the thermodynamic properties of the quartz sand target was modeled using a Drucker–Prager rheology and the well-tested ANEOS (analytical equation of state) version of SiO_2 (Melosh, 2007). To account for porosity and its effect on the reduction of the critical shock pressure required for melting, the ε–α compaction model of Wünnemann et al. (2006) was used. In analogy to the differently colored strata in the experiments, tracer particles were used in the model to record shock conditions (e.g., peak shock pressure) and particle trajectories inside the crater and in the ejecta curtain. To calculate the ejected melt volume, the contours for material that is ejected at a certain ejection velocity (white dots in Figs. 6.3 and 6.4 for minimum ejection velocity) were superimposed onto the contours for peak shock pressure in tracers that were plotted at their original location (Figs. 6.3 and 6.4; see also Wünnemann et al., 2016). The geometric overlap then corresponds to the amount of melted or shocked material that remains inside the crater or that is ejected.

6.3 Results

As documented in detail in Chapter 5, the melt particles have a layered structure of decreasing shock metamorphism (Figs. 5.3 and 5.4). A topmost layer consists of fused Al metal that documents complete melting of the Al projectile. This Al metal crust is underlain by vesicular lechatelierite, in which relic, PDF-bearing quartz grains and spheres of Al metal are embedded. These two layers are underlain by shock-lithified and fractured quartz grains that show grain-boundary melting. Based on previous attempts to calibrate shock effects in sandstone (Kowitz et al., 2016), the following shock pressure and postshock temperature ranges are assigned under which these layers have presumably formed: the uppermost layers (Al metal melt and lechatelierite) formed at >13 GPa and >2000 °C, whereas the bottom layer (glass-welded sand with PDF-bearing quartz grains) formed between 5 and 13 GPa and several hundred degrees Celsius. Grain-boundary melting in the bottom layer was induced by pore col-

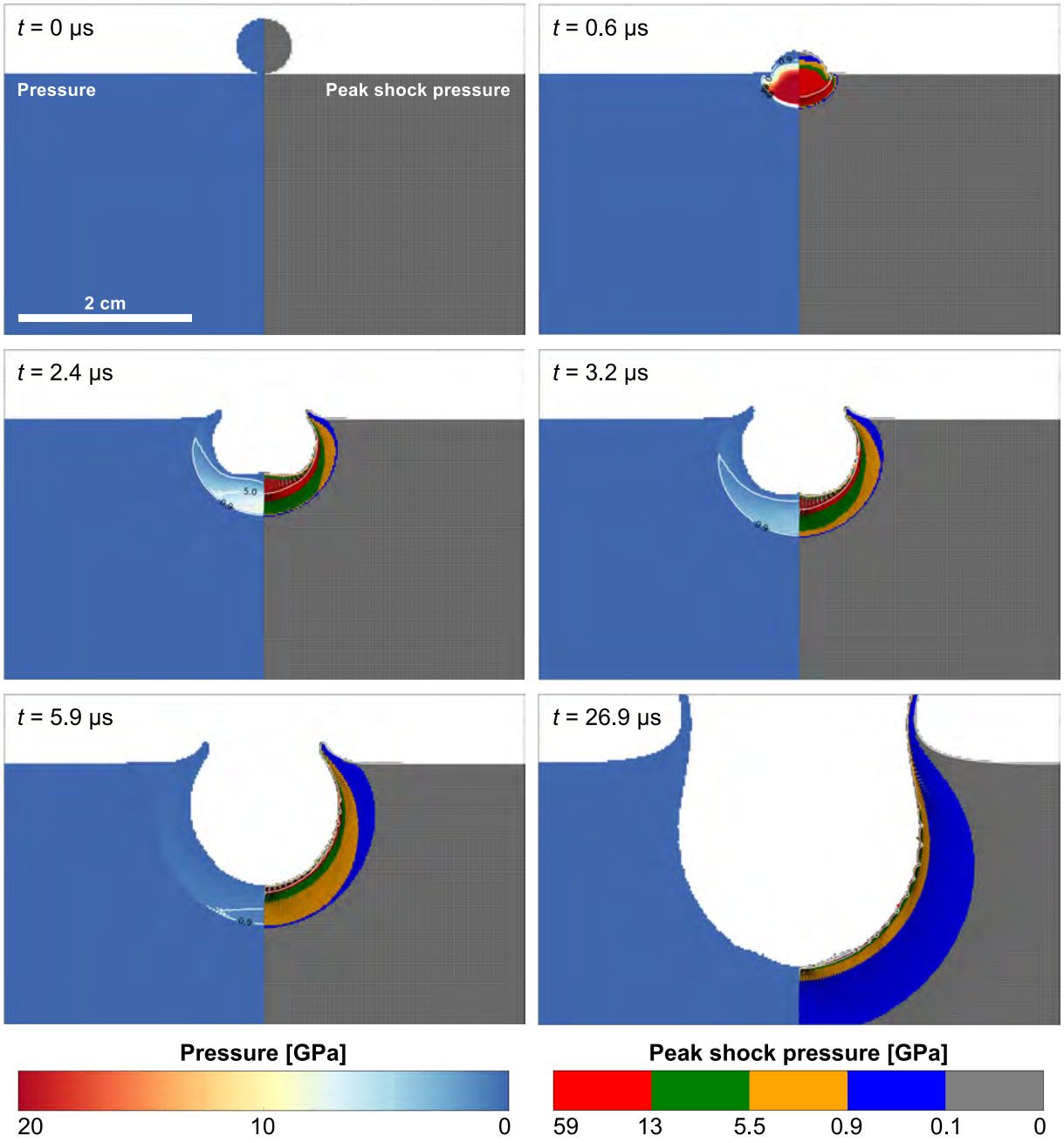

Figure 6.2 Snap shots of the numerical simulation of Experiment No. 529, which involved the impact of a 6.36-mm-diameter aluminum projectile at 6.44 km s^{-1} into quartz sand of 42% porosity. Left panels: pressure; right panels: peak shock pressure recorded by tracer particles. Model courtesy of M.-H. Zhu.

lapse, which locally increased shock pressure and post-shock temperature (Wünnemann et al., 2008; Kowitz et al., 2013b; Bland et al., 2014; Kowitz et al., 2016).

Figures 6.3 and 6.4 compare the shock zoning preserved in the melt particles to the shock zones obtained from the model. In the model, shock wave attenuation around the point of impact results in roughly hemispherical zones of discrete, successively decreasing peak shock pressures

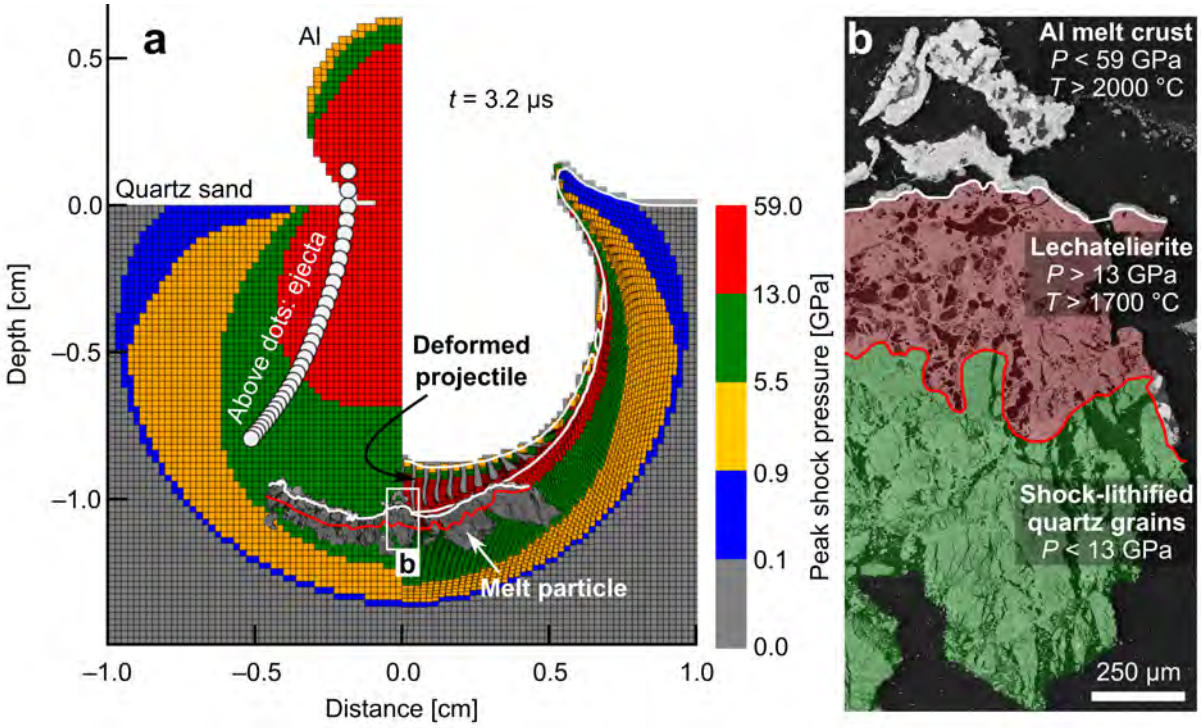

Figure 6.3 Comparison of shock zones documented in a melt particle from Experiment 533 against the shock zoning obtained from the model. **a** Model snap shot at $t = 3.2$ µs (left: pressure isobars; right: material flow and peak pressure during crater formation) with superimposed cross-section (mosaic of BSE images) of the melt particle at a similar scale like the model. **b** Detail of the cross section shown in a. The three shock zones documented petrographically are outlined to facilitate comparison with the model.

(left sides of the model snapshots) that are successively deformed and displaced during opening of the transient cavity (right sides of the model snapshots). As a first-order approximation, peak shock pressures at the point of impact range from ~59 to ~13 GPa for a depth of about 1 projectile radius, and from ~13 to ~5 GPa at depths between 1 and 2 projectile radii. At depths >2 projectile radii, peak shock pressures drop to <1 GPa and, thus, below the target's Hugoniot elastic limit. As illustrated in Fig. 6.2, the high-pressure shock zones (red and green in the model) become thinner and thinner with time, as the projectile and target melts in these zones are "smeared" along the floor of the opening transient cavity.

Interestingly, there seems to be a narrow, very early time frame (~3 µs after initial contact between projectile and target) in the model in which shape as well as vertical and lateral extent of the shock zones best match the extent of the shock zones documented in the melt particles (Figs. 6.3a and 6.4a). Moreover, the shapes of the melt particles and the curvature of the layers are identical to the curvature of the transient crater bottom at these time steps in the model. At subsequent time steps (>3 µs; Fig. 6.2), shape and extent of the modeled shock zones start to differ more and more form the documented shock zones in the melt particles, that is, the shock zones in the model become thinner and thinner with increasing time. Eventually, in the model the projectile is smeared along the bottom of the

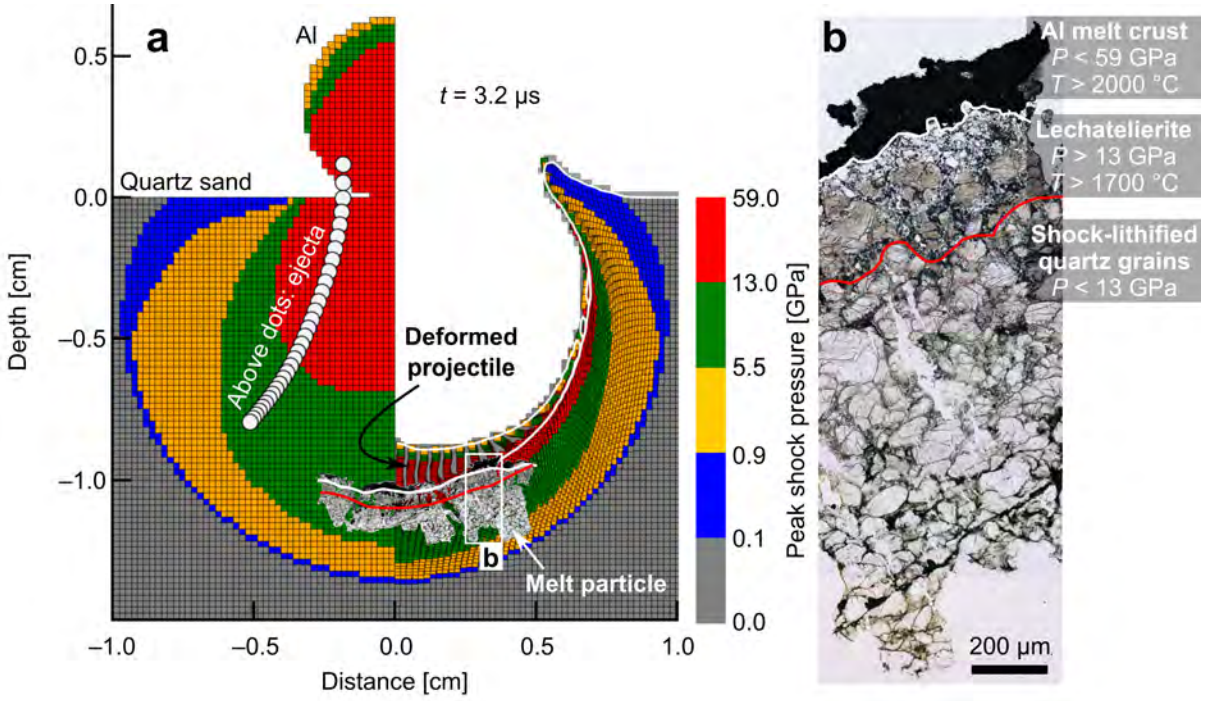

Figure 6.4 Comparison of shock zones documented in a melt particle from Experiment 530 against the shock zoning obtained from the model. **a** Model snap shot at $t = 3.2$ µs (left: pressure isobars; right: material flow and peak pressure during crater formation) with superimposed cross-section (mosaic of thin-section images taken in plane-polarized light) of the melt particle at a similar scale like the model. **b** Detail of the cross section shown in a. The three shock zones documented petrographically are outlined to facilitate comparison with the model.

transient crater, forming a thin, nearly infinitesimal coating. Similarly, the layer of target material residing within the crater's melt zone (i.e., in the high-pressure shock zones at $P > 13$ GPa) also becomes thinner and thinner with increasing time in the model.

6.4 Discussion and conclusions

The melt particles document the effect of shock wave attenuation in a porous, particulate target that can be considered as a regolith analog. Shock wave attenuation in the numerical model is in excellent agreement with shock wave attenuation documented in the layered melt particles, thus validating the model. Moreover, with respect to distribution and shock-metamorphic overprint of ejecta, the model is also in excellent agreement with observations from the experiments (Wünnemann et al., 2016), again validating the model. Hence, the combination between petrologic observation and numerical model suggests that (1) the melt particles formed at very early time steps during crater formation (~3 µs after initial contact between projectile and target, i.e., before the transient crater reached its maximum dimensions) and (2) that the melt particles essentially sample the floors of the transient craters, including all chemical processes that occurred at the projectile–target interface (cf. Chapter 5). Furthermore, to the best of our knowledge, these melt

particles represent the first documented in situ samples of a projectile–target interface. Interestingly, the petrologic zones preserved in the melt particles—generally speaking and from top to bottom: (1) projectile melt, (2) heavily projectile-contaminated target melt, (3) largely projectile-free target melt, (4) shocked target—are qualitatively similar to the reconstructed stratigraphy of the melt zones of Wabar (Hörz et al., 1989; Mittlefehldt et al., 1992), Barringer (Hörz et al., 2002; Mittlefehldt et al., 2005) and Kamil (Fazio et al., 2016). At these much larger craters, melt zones existed during cratering that produced, also from top to bottom: (1) projectile melts (preserved in the form of FeNi spheres; cf. Chapter 8), (2) heavily projectile-contaminated target melts ("black melt"; cf. Chapter 8), (3) largely projectile-free target melts ("white melt"; cf. Hörz et al., 1989; Fazio et al., 2016), and (4) shocked target rocks (e.g., Fazio et al., 2014a). Specifically, for Kamil's melt zone (crater diameter = 45 m), Fazio et al. (2016) estimated that the direct interaction between liquid projectile and liquid target was restricted to the uppermost ~1 m of the melt zone, thus contaminating only shallow portions of the preimpact target. Similar conclusions can be drawn from the experiments, where the most intense interaction between the Al projectiles and the quartz sand target occurred in the uppermost portions of the preimpact target.

General impact conditions such as impact velocity, target porosity, impactor size, and impedance contrast between projectile and target in the experiments were quite similar to abundant impacts of micrometeoroids of similar size into regoliths of asteroids in the main belt (cf. Chapter 5; Daly and Schultz, 2016). Thus, it is to be expected that qualitatively similar melt particles are produced during such impacts, with composition and mineralogy of such melt particles depending on the materials involved. Moreover, these results suggest that asteroidal regoliths may accrete measurable quantities of foreign (i.e., non-endogenous) material in the form of projectile melts. Obviously, the amount of foreign material that is retained in the regolith over time will depend on a variety of factors such as porosity, grain size, and composition of the regolith, impact angle and impact velocity, and probably size and, thus, gravity of the asteroid. Oblique impacts were not simulated in the experiments, although these are statistically much more frequent than vertical impacts and impact obliquity will probably have the greatest influence on projectile retention. For example, the impact experiments of Daly and Schultz (2016) included oblique impacts and clearly showed that projectile retention is sensitive to impact angle, ranging from 7% for 30° impacts to 72% for vertical impacts (averaging 17% of the mass of the projectile retained over all probable impact angles). Nevertheless, such experiments have one common, inevitable problem that makes transfer of results to asteroidal environments questionable: gravity However, the parameter study of Wünnemann et al. (2017)—although also assuming vertical impacts only—suggests that in case of an Itokawa-size body with a reduced gravity ($g = 0.0162\ \mathrm{m\,s^{-2}}$) and a 20–60%-porous regolith, significant amounts of melt both derived from the projectile and the target remains inside the crater. Specifically,

at 5 km s^{-1} impact velocity, >90$ of the melt will be retained on the asteroid on case of a 60%-porous target, >40$ of the melt will be retained on the asteroid on case of a 20%-porous target. In other words, even on a body with reduced gravity, projectile material may accrete in substantial amounts if it does not leave the crater on ejection trajectories that favor escape into open space. As noted by Wünnemann et al. (2017), gravity does neither produce melt production, nor ejection dynamics, hence, it is to be expected that similar impacts into astroidal regoliths in the main belt indeed should produce similar impact melt particles as described here and in Chapter 5. Given the fact that ejection dynamics change significantly in case of oblique impacts, the biggest limitation of this study clearly is the vertical impact simplification. Overall, this study nevertheless demonstrates, that—in agreement with Hörz et al. (2005)—significant amounts of melting occur at relatively low impact velocities if the target is porous. Moreover, the experiments and the model also predict that in case of vertical impacts, a significant amount of the generated melt remains inside the crater and is not ejected from the asteroid. Future studies should obviously investigate the effect of impact angle on melt ejection and projectile retention in hope to explore the causes for the paucity of asteroidal agglutinates, or the paucity of melt particles in the samples returned from Itokawa. If substantial amounts of foreign components indeed accrete in such regoliths, great care would be needed in interpreting surface reflectance spectra from such regoliths.

Part III

Geochemical processes in impact melts

Chapter 7

Correlating laser-generated melts with impact-generated melts: an integrated thermodynamic–petrologic approach[1]

In this chapter, an experimental approach that uses direct laser irradiation to melt and vaporize planetary materials under highly dynamic conditions is presented. These experiments simulate postshock P–T conditions of hypervelocity impacts, and experimental products (silicate glasses) are shown to be petrologically and thermodynamically similar to true impact melts (quenched to impact glasses) formed from the same materials. It will be shown that by "matching" the *entropy gains* of the laser-generated melts to the entropy gains associated with the thermodynamic states produced in hypervelocity impacts at specific velocities, melts can be produced that thermodynamically and mineralogically resemble true impact melts formed at that specific impact velocity. By using temperature measurements of centimeter-size melt volumes ejected from the irradiation zones during the experiments, cooling rates of similarly sized ballistic melt ejecta (e.g., discrete bodies of impact melt, melt spherules, tektites, etc.) formed during hypervelocity impacts will be constrained. In conclusion, these experiments allow to study the formation and mixing of macroscopic (hand-specimen scale) volumes of impact-melt analogs under dynamic conditions in high-fidelity scenarios. Moreover, these experiments extend the currently attainable "postshock" temperatures in impact experiments to ranges commensurate with impacts in the velocity range of 4 to some 20 km s^{-1} (in comparison to some 7 km s^{-1} achieved in conventional, light-gas gun-based impact experiments).

Key points:

Laser melting of planetary materials forms melts with thermodynamic properties of impact melts originating from adiabatic decompression

Laser-generated melts are petrologically similar to impact melts and allow for estimating time scales of impact melt formation and cooling

Direct laser irradiation of planetary materials simulates effectively the formation of impact melts and vapors in the 4–20 km s^{-1} range

[1]This chapter has been published as: Hamann, C., Luther, R., Ebert, M., Hecht, L., Deutsch, A., Wünnemann, K., Schäffer, S., Osterholz, J., and Lexow, B. (2016). Correlating laser-generated melts with impact-generated melts: an integrated thermodynamic–petrologic approach, *Geophysical Research Letters* 43, 10602–10610, http://dx.doi.org/10.1002/2016GL071050.

Summary

This is the abstract of the original publication, but its title has been changed to "summary" in order to delimit it from the brief abstract given on the previous page. The main text and all figure captions, as well as the contents of the supplementary material (Chapter B), are as published.

Planetary collisions in the solar system typically induce melting and vaporization of the impactor and a certain volume of the target. To study the dynamics of quasi-instantaneous melting and subsequent quenching under postshock P–T conditions of impact melting, we used continuous-wave laser irradiation to melt and vaporize sandstone, iron meteorite, and basalt. Using high-speed imaging, temperature measurements, and petrologic investigations of the irradiation targets, we show that laser-generated melts exhibit typical characteristics of impact melts (particularly ballistic ejecta). We then calculate the entropy gains of the laser-generated melts and compare them with the entropy gains associated with the thermodynamic states produced in hypervelocity impacts at various velocities. In conclusion, our experiments extend currently attainable postshock temperatures in impact experiments to ranges commensurate with impacts in the velocity range of 4–20 km s^{-1} and allow to study timescales and magnitudes of petrogenetic processes in impact melts.

7.1 Introduction

A unique feature of hypervelocity impacts is the formation of impact melts, which are generated when shock-compressed materials unload after the passage of the impact-induced shock wave. Unloading from high pressure is often described by the concept of the propagation of a rarefaction wave (Melosh, 1989). Due to the unisentropic nature of shock wave compression, a certain fraction of the energy required for compressing and heating matter (internal energy) remains as residual heat after the rarefaction wave has passed. Consequently, if the shock pressures generated by an impact are high enough, the residual heat is sufficient to melt or even vaporize large amounts of material (Pierazzo et al., 1997). For most silicates, shock melting is typically induced at impact velocities of 4–7 km s^{-1}, corresponding to shock pressures >50 GPa and postshock temperatures >2300 K (Ahrens and O'Keefe, 1972). In porous materials, shock melting starts at much lower shock pressures and, hence, lower impact velocities, because compaction of pore space and friction yields sufficient heat to locally induce melting (Wünnemann et al., 2008; Davison et al., 2010; Kowitz et al., 2013b; Bland et al., 2014).

Impact melting of planetary materials is usually studied either in experiments (e.g., Hörz and Cintala, 1997; Hörz et al., 2005; Ebert et al., 2013; Ebert et al., 2014; Wozniakiewicz et al., 2015) or at natural terrestrial impact structures (e.g., Hörz et al., 1989; Hörz et al., 2002; Hamann et al., 2013; Fazio et al., 2016) and in lunar regolith samples (Heiken et al., 1991). On Earth, only a few young impact structures, such as Meteor Crater (Hörz et al., 2002; Osinski et al., 2015), Wabar (e.g., Hörz et al., 1989; Hamann et al., 2013), or Kamil (e.g., Fazio et al., 2016), combine the most paramount prerequisites for reconstructing physicochemical mechanisms of impact melt formation: (1) detailed knowledge of the impactor, (2)

detailed knowledge of the preimpact lithology, and (3) preservation of pristine impactites.

Impact experiments are a valuable tool to study impact melting, yet only rarely were typical planetary materials used as targets and projectiles (e.g., Hörz et al., 2005; Ebert et al., 2013; Ebert et al., 2014; Wozniakiewicz et al., 2015). Moreover, the maximum impact velocities currently obtained for macroscopic (>1–2 mm) projectiles accelerated in the laboratory are limited to 6–8 km s^{-1}. Such high-velocity shots are bought dearly by heavily stressing or even damaging the gun barrel. Consequently, impact experiments do not reach the magnitudes of typical impact events in the Earth–Moon system, which mostly involve impact velocities of 15–25 km s^{-1} (Chyba et al., 1994; Oberst et al., 2012). These impacts typically induce partial and total vaporization of the projectile and large amounts of target rocks, and they also create a continuum of successively decreasing shock pressures around the point of impact that induce melting (Pierazzo et al., 1997). Furthermore, there remain several outstanding questions regarding impact melting that are difficult to assess from natural impactites and, due to experimental limitations, are hard to address in conventional experiments.

Here we establish direct laser irradiation of planetary materials as an experimental approach that allows for the study of quasi-instantaneous melting and subsequent quenching processes commensurate with impact melting in typical planetary impact scenarios. Our experiments are focused on postshock thermal processes of impact melt formation and cooling. Therefore, we explicitly exclude shock-metamorphic effects in minerals from our discussion, as our experimental approach is not capable of, and does not intend to, produce shock-induced solid-state transformations.

7.2 Rationale

Pulsed laser irradiation with peak intensities of 10^7–10^{14} W cm^{-2} and with pulse durations in the nanosecond to millisecond range was used in previous experiments (Gerasimov et al., 1998; Kadono et al., 2002; Ohno et al., 2004; Ishibashi et al., 2013) to investigate impact vaporization of planetary materials and to study the physicochemical properties of the laser-produced vapor plumes in analogy to impact processes. However, as a consequence of the high irradiation intensities used in these studies, the laser-generated vapor plumes were thermodynamically comparable to vapor plumes generated in impact scenarios with extremely high impact velocities (50–120 km s^{-1}). These impact velocities resemble cosmic encounter velocities of long-range comets, but not the average impact velocities of 15–25 km s^{-1} encountered in the Earth-Moon system (Olsson-Steel, 1990; Chyba et al., 1994; Oberst et al., 2012) or of 5 km s^{-1} encountered in the asteroid belt (Bottke et al., 1994). Consequently, if we want to simulate impact melting in typical impact scenarios with direct laser irradiation, we have to use a laser with just enough intensity to induce melting and in-

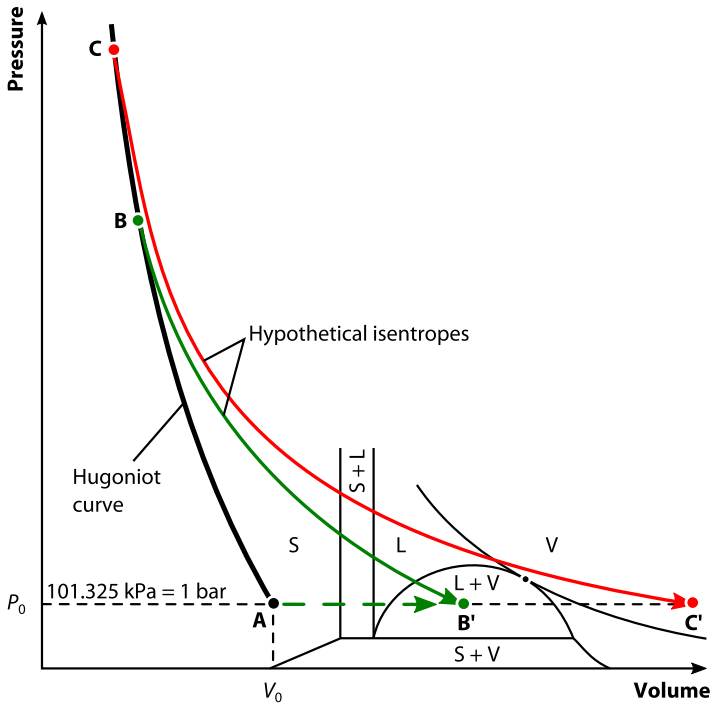

Figure 7.1 Pressure–volume relation for a hypothetical silicate that undergoes shock-induced phase changes (based on Melosh, 1989). Point B corresponds to an impact scenario in which the material is compressed to state B and released to state B′, inducing melting and incipient vaporization. Shocking the material to higher pressure (state C) induces complete vaporization (state C′). Using laser irradiation in the parameter region of this study (dashed green arrow), the material directly achieves state B′. S = solid; L = liquid; and V = vapor.

cipient vaporization of the target material. This experimental setup could bridge the gap between dynamic impact experiments and static heating experiments, essentially combining the dynamic, quasi-instantaneous production of superheated melts with rapid quenching—in other words, simulating postshock conditions of impact melt formation.

Here we consider direct, continuous-wave (CW) laser irradiation of planetary materials with intensities of $1.1–5.3 \times 10^4$ W cm^{-2}, which are easily achieved with commercial lasers with powers of 2–10 kW and beam diameters of a few millimeters. The absorption of a fraction of the laser energy results in the rapid formation of a melt layer at the surface of the sample, followed by evaporation of the molten material and the formation of a vapor cloud. These processes have been studied in detail for metal samples in the parameter region considered here (Horak et al., 2015).

A schematic P–V diagram of impact-induced melting and vaporization of a hypothetical silicate is given in Fig. 7.1. In a typical impact scenario, material is compressed to, say, state B. After the passage of the shock front, the material is released via adiabatic decompression from high pressures, following release adiabats (Zel'dovich and Raizer, 1967; Ahrens and O'Keefe, 1972; Melosh, 1989). Point B' corresponds to a postshock condi-

tion sufficient to induce melting and incipient vaporization of the material. Now, we assume (1) that all entropy production is taking place during shock compression and (2) that entropy during decompression remains constant, because release adiabats correspond to isentropes (Ahrens and O'Keefe, 1972; Kadono et al., 2002; Pierazzo et al., 2005). Consequently, if we know the thermodynamic state of point B', we can reconstruct point B on the Hugoniot, as B and B' are connected through the corresponding isentrope. Thus, by matching the entropy change of a laser-generated melt with the entropy change of an impact-generated melt, we can directly compare laser melting with postshock impact melting.

Another argument for the validity of our approach comes from the consideration of chemical equilibria and the dynamics of the impact process. Impact melts form and cool under strong chemical disequilibrium (See et al., 1998; Hörz et al., 2002; Schultze et al., 2016). Conventional furnace or piston cylinder experiments usually use slow heating rates and long run durations to attain chemical equilibrium among phases. This is usually a necessity because they are designed to elucidate endogenous petrologic processes that operate on much longer time scales. Impact experiments are a way to achieve extreme chemical disequilibria in the resulting melts (e.g., Ebert et al., 2014; Wozniakiewicz et al., 2015). However, as stated above, impact velocities and involved masses are limited in the laboratory; hence, only small amounts of melt and even less vapor (if any) are produced. Using a laser to quasi-instantaneously melt and mix all constituent phases of a rock under dynamic conditions will obviously produce chemical disequilibrium. When combined with rapid quenching (cf. Basilevsky et al., 2000), two prerequisites are met to not only produce chemical disequilibrium in melts and newly crystallizing phases but also to preserve it during quenching. We therefore argue that laser melting should produce melts that are similar to true impact melts.

7.3 Methods

We used a CW infrared fiber laser with a wavelength of 1.07 µm situated at Fraunhofer-Institut für Kurzzeitdynamik, Freiburg, Germany, to irradiate sandstone, Campo del Cielo iron meteorite, and basalt. Petrographic descriptions and bulk chemical compositions of the materials are detailed in Texts B.1–B.3 and Table B.1 in Appendix B; the experimental setup is illustrated in Fig. B.1. In experiment 887, a plate of iron meteorite attached onto a cube of sandstone was irradiated (Fig. B.2). Experiment 892 involved the irradiation of a plate of basalt (Fig. B.3). The CW laser emitted a power of 2–8 kW over a specified time (2–6 s) during which the target was moved either horizontally or vertically (i.e., the laser irradiated a line onto the target's surface). The beam intensity of the laser was close to a Gaussian distribution and the beam diameter was between 2.0 and 5.9 mm. The laser intensity was in the range of $1.1–5.3 \times 10^4$ W cm^{-2} and the laser–matter interaction zone was recorded with a video camera and a high-speed framing camera (recording with 1.1×10^4 fps and exposure

times of 1–20 µs). Time- and space-resolved surface temperature measurements were done with an infrared microbolometer (recording with 50 fps and between 373 and 2373 K).

The irradiated samples were recovered after the experiments, molded in epoxy, and thin sectioned to expose profiles of the melt zones. After carbon coating, the sections were studied with scanning electron microscopy in order to validate the temperature measurements against petrological observations. Specifically, we used incipient to complete transformation of mineral phases to melts/glasses to estimate minimum temperatures, whereas the boiling points of the materials were taken as upper temperature limits.

To describe the thermodynamic properties of the materials in hypothetical impact scenarios, we used the ANEOS (Thompson and Lauson, 1972). Specifically, we used well-tested ANEOS versions for quartz (Melosh, 2007), iron (Thompson, 1990), and basalt (cf. Pierazzo et al., 2005) to compute the change in entropy ΔS as a function of particle velocity u_p and shock pressure P. We then used the ΔS values obtained from ANEOS to correlate the laser-generated melts with impact-generated melts and to find specific impact scenarios that would yield impact melts similar to the laser-generated melts. We are aware that compared to more recent data (e.g., Kurosawa et al., 2012; Kraus et al., 2012; Kraus et al., 2015), the used ANEOS versions fail to accurately describe the shock states at pressures higher than those required for incipient vaporization. However, given the fact that we focus on impact melts and considering the widespread use of these ANEOS versions, we are certain that ANEOS describes the material behavior in the shock pressure range of interest sufficiently accurate.

7.4 Results and discussion

7.4.1 High-speed imaging and temperature measurements

Direct CW laser irradiation of sandstone, iron meteorite, and basalt with laser intensities of $1.1–5.3 \times 10^4$ W cm^{-2} resulted in melting and vaporization of specific parts of the samples. Directly at the irradiation points, the laser vaporized all materials, producing vapor plumes (Fig.7.2a, b) that existed until cease of laser irradiation. Typically, the irradiation of materials under these conditions leads to the formation of a partially ionized vapor with a temperature of several thousand Kelvin. This is in agreement with the emission of light in the visible spectral range observed with the high-speed camera and with the emission of radiation in the infrared wavelength range observed with the microbolometer. Close to the irradiation zones, melts formed at the sample surfaces and spherical melt droplets were ejected (Fig.7.2a, b). In the basalt experiment, the laser also formed a tube of basaltic melt that eventually separated a spherical melt droplet that dripped onto the specimen stage (Fig.7.2b).

Using the temperature readings from the microbolometer (Fig. 7.2a, b) allowed for estimating surface temperatures and cooling rates of the laser-generated melts (Fig. 7.2e, f and Text B.4). Moreover, we validated

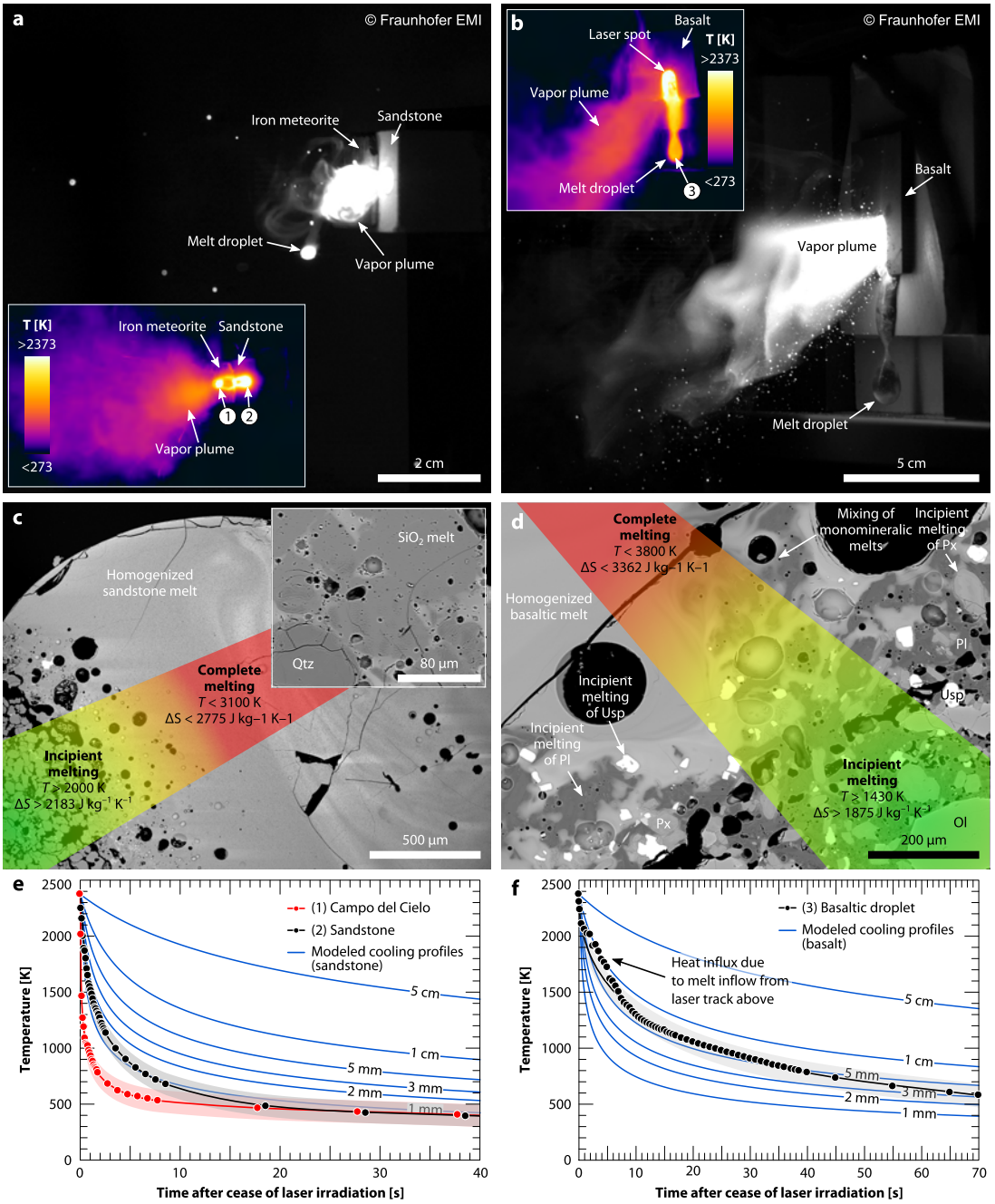

Figure 7.2 Laser irradiation of sandstone, iron meteorite, and basalt. **a** Example high-speed camera image of experiment 887. In this frame, the laser irradiates the sandstone, forming a vapor plume and melt droplets. The inset shows the corresponding microbolometer image used to extract cooling profiles (1) and (2) in (e). **b** Example high-speed camera image of experiment 892. A vapor plume and a tube of melt formed in this experiment that eventually separated a ~1-cm-diameter melt droplet. The inset shows the corresponding microbolometer image used to extract cooling profile (3) in (f). **c** and **d** Representative back-scattered electron images of laser-generated melts in sandstone and basalt. Incipient to complete melting of the sandstone indicates temperatures between 1996 and 3157 K (see c). The inset shows incipient melting of quartz in detail. Incipient to complete melting of the basalt indicates temperatures between 1430 and 3800 K (see d). The monomineralic melts eventually homogenized during laser irradiation. **e** and **f** Cooling profiles for experiments 887 and 892 and modeled temperature profiles for sandstone and basalt melt droplets of various diameters (see Text B.5 and cf. Bouley et al., 2012). The shaded areas denote the estimated inaccuracy of the temperature measurements (Text B.4). Qtz = quartz; Ol = olivine; Pl = plagioclase; Px = pyroxene; and Usp = ulvöspinel.

the measured temperatures against petrologic observations after the experiments (Section 7.4.2 and Fig. 7.2c, d) and modeled the thermal evolution of the sandstone and basalt melts (Fig. 7.2e, f and Text B.5). In experiment 887, sandstone and iron meteorite melts achieved temperatures >2373 K close to the irradiation zone (Fig. 7.2a, e). The measured (and modeled) cooling profiles follow power laws with negative exponents. Since we only measured surface temperatures, the cooling rates can be regarded as maximum estimates. The iron meteorite melt quenched within 2 s from >2373 to ~773 K ($dT/dt \approx -800\,K\,s^{-1}$) and then within additional 3 s to ~573 K ($dT/dt \approx -67\,K\,s^{-1}$); the sandstone melt quenched within 7 s from >2373 to ~773 K ($dT/dt \approx -300\,K\,s^{-1}$) and then within additional 10 s to ~573 K ($dT/dt \approx -20\,K\,s^{-1}$). The basaltic melt droplet of experiment 892 (Fig. 7.2b, f) had an initial temperature of >2373 K and quenched within 11 s to ~1273 K ($dT/dt \approx -100\,K\,s^{-1}$), then within additional 30 s to ~573 K ($dT/dt \approx -23\,K\,s^{-1}$). Qualitatively, the measured and modeled data constrain the time scales available for petrogenetic processes in impact melts of similar volume (cf. Hörz et al., 1989; Hörz et al., 2002; See et al., 1998); in particular, they should be applicable to millimeter- to centimeter-sized ballistic ejecta.

7.4.2 Petrographic observations

The recovered samples document temperature gradients ranging from (1) partial melting of those components with the lowest melting temperatures, to (2) incipient melting of all target components, to (3) complete melting of all target components and begin of mixing between monomineralic precursor melts, to (4) melt homogenization (Fig. 7.2c, d). Furthermore, the irradiation targets experienced vaporization close to the laser irradiation point (Fig. 7.2a, b).

In terms of microtextures and mineralogy, laser melting of sandstone (Fig. 7.2c) resembles progressive impact melting of Coconino sandstone at Meteor Crater, Arizona (Kieffer, 1971), or of Seeberger sandstone used in the MEMIN (Multidisciplinary Experimental and Modeling Impact Research Network) shock recovery and impact experiments (Kowitz et al., 2013a; Ebert et al., 2013), whereas laser melting of iron meteorite resembles impact melting of Campo del Cielo (Ebert et al., 2013). Moreover, laser melting of basalt (Fig. 7.2d) resembles progressive impact melting of basalt at Lonar, India (Kieffer et al., 1976a). We conclude that the laser-generated melts show typical characteristics of rapidly quenched impact melts from small terrestrial impact craters and ballistic ejecta in particular (cf. Hörz et al., 1989; Hörz et al., 2002; See et al., 1998; Hamann et al., 2013).

7.4.3 Correlating laser-generated melts with impact-generated melts

Following Zel'dovich and Raizer (1967) and Ahrens and O'Keefe (1972), we calculate the entropy change for laser melting of quartz, iron, and basalt

using the thermodynamic approach

$$\mathrm{d}S = \frac{c_p}{T}\mathrm{d}T - V\mathrm{d}P, \tag{7.1}$$

where S is the entropy of the material, c_p is the isobaric specific heat capacity of the material, T is the temperature, V is the volume of the material, and P is the pressure. Since the laser-generated melts were only surrounded by the ambient atmosphere, we assume that melting took place at a constant pressure of 1 bar. Moreover, we assume that the volume change during melting is small, contributing only insignificantly to the entropy increase. Hence, we assume that $V\mathrm{d}P$ equals zero. The change in entropy ΔS within a given temperature interval is then calculated by

$$\Delta S = \int_{T_1}^{T_2} \frac{c_p}{T}\mathrm{d}T + \frac{\Delta H^0_{\mathrm{fus}}}{T_{\mathrm{fus}}} \tag{7.2}$$

where T_1 is the initial temperature (~300 K), T_2 is the temperature of the melt, $\Delta H^0_{\mathrm{fus}}$ is the enthalpy of melting at 1 bar pressure, and T_{fus} is the melting temperature of the material at 1 bar pressure. The term $\Delta H^0_{\mathrm{fus}}/T_{\mathrm{fus}}$ accounts for the latent heat of fusion at the melting point of the material, that is, we only consider melting. The latent heat of vaporization when passing the boiling point is therefore not included in Eq. (7.2).

The melting and boiling temperatures for quartz, iron, and basalt used in this study are given in Table B.2. For quartz, we used the c_p values given in the NIST-JANAF thermochemical tables (Chase, 1998), for iron, we used the c_p values of Desai (1986), and for basalt, we used the c_p values of Bouhifd et al. (2007) (Figs. B.4–B.6). For the basalt, we assume that the incipient melting and vaporization entropies (or temperatures) correspond to the lowest incipient melting and vaporization entropies (or temperatures) of its main minerals (diopside, anorthite, and forsterite). Moreover, we exemplarily used the Melosh (2007) ANEOS to calculate the entropy gain for melting of quartz at 1 bar to compare the results of our calculations against an independent set of thermodynamic variables.

The resulting entropy changes from incipient melting to incipient vaporization of the materials are given in Fig 7.3. For quartz (Fig 7.3a), incipient melting at 1996 K yields ΔS = 2183 J kg^{-1} K^{-1} and incipient vaporization at 3157 K yields ΔS = 2775 J kg^{-1} K^{-1}. For T = 2400 K (slightly above the upper temperature limit recorded by the microbolometer), the entropy change is 2420 J kg^{-1} K^{-1}. Comparing these entropy changes to the entropy changes of nonporous quartz for a given Hugoniot state upon shock compression, the laser-generated melts cover entropy and temperature gradients that correspond to impact-generated melts originating from shock pressures and particle velocities between ~66 GPa and ~3.3 km s^{-1} (incipient melting) and ~98 GPa and ~4.1 km s^{-1} (incipient vaporization). For comparison, the shock pressure required for incipient melting of α-quartz is in excess of 50 GPa (Stöffler and Langenhorst, 1994), whereas incipient and 50% vaporization requires shock pressures in excess of 95 and 255 GPa, respectively (Melosh, 2007; Kraus et al., 2012). However,

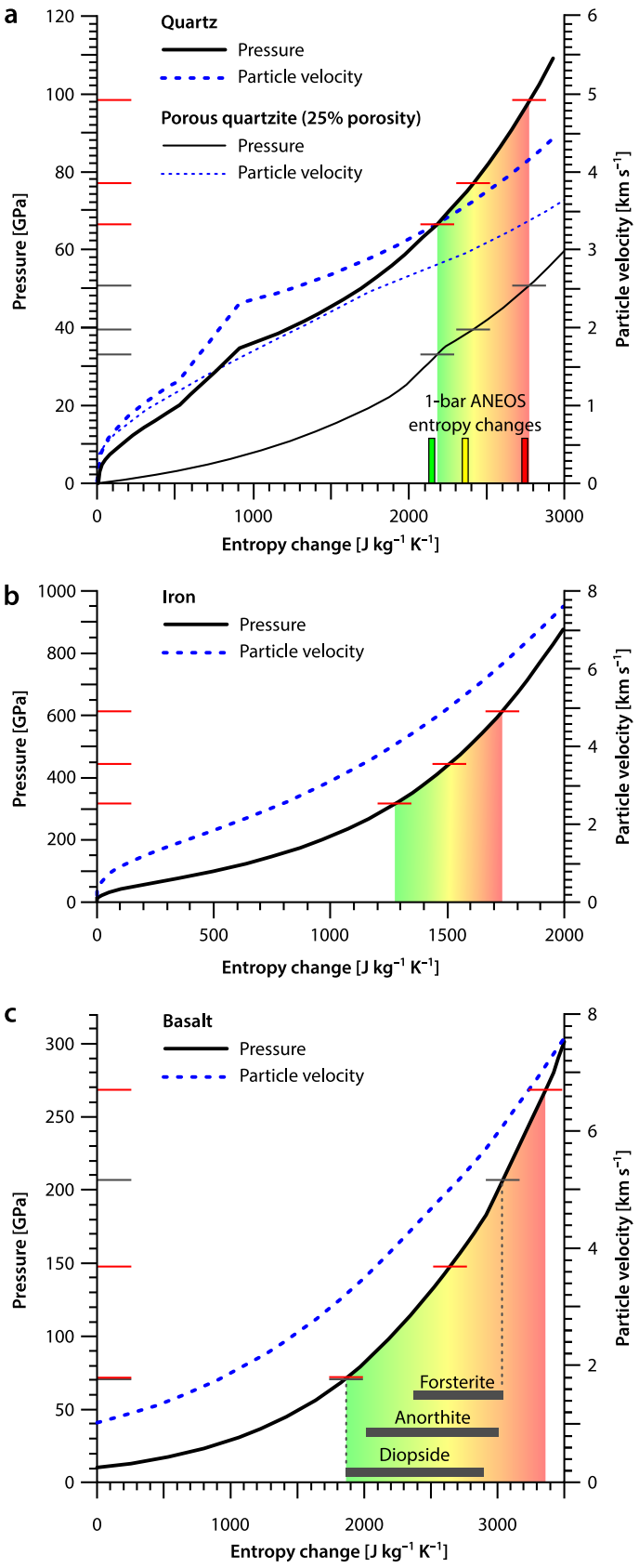

Figure 7.3 ANEOS Hugoniots for **a** nonporous and 25% porous quartz, **b** iron, and **c** basalt. The colored fields correspond to calculated entropy changes of incipient melting (green), complete melting (yellow), and incipient vaporization (red) of quartz (a), iron (b), and basalt (c), respectively. The dashed curves give the particle velocities in hypothetical impact scenarios (the laser-generated melts do not achieve these particle velocities) and the colored vertical bars in (a) correspond to a 1 bar entropy calculation using the Melosh (2007) ANEOS. For the basalt, incipient melting and incipient vaporization entropy ranges at a reference pressure of 1 bar are shown as thick horizontal lines for main constituent minerals.

assuming a nonporous quartz target is unreasonable, since the irradiated sandstone had an initial porosity of ~23% that would effectively reduce the peak shock pressure required to induce melting (Kowitz et al., 2013a). For comparison, Fig 7.3a also gives the shock pressures and particle velocities of 25%-porous quartzite that would correspond to the calculated entropy changes: ~34 GPa and ~2.8 km s^{-1} for incipient melting and ~51 GPa and ~3.4 km s^{-1} for incipient vaporization (cf. Wünnemann et al., 2008).

For iron (Fig 7.3b), incipient melting at a temperature of 1811 K yields ΔS = 1275 J kg^{-1} K^{-1} and incipient vaporization at 3130 K yields ΔS = 1732 J kg^{-1} K^{-1}; for the intermediate temperate of 2400 K, ΔS was found to be 1510 J kg^{-1} K^{-1}. These entropy changes correspond to shock pressures and particle velocities of ~320 GPa and ~4.0 km s^{-1} (incipient melting) and ~610 GPa and ~6.1 km s^{-1} (incipient vaporization), respectively. For comparison, the estimated shock pressure required for melting of iron lies between 260 and 390 GPa, whereas incipient vaporization requires 420–884 GPa (Ahrens and O'Keefe, 1977; Pierazzo et al., 1997), the most recent estimate being 507 (+65, −85) GPa (Kraus et al., 2015).

For the basalt (Fig 7.3c), incipient melting at a temperature of 1430 K yields ΔS = 1875 J kg^{-1} K^{-1}, whereas incipient vaporization at ~3800 K yields ΔS = 3362 J kg^{-1} K^{-1}. Complete melting of the basalt was readily achieved at 2373 K (Fig 7.3b), which yields ΔS = 2646 J kg^{-1} K^{-1}. Using the basalt Hugoniot and the thermodynamic data of the basalt, we find that the laser-generated basaltic melt covers entropy and temperature gradients that correspond to impact-generated melts originating from shock pressures and particle velocities of ~70 GPa and ~3.2 km s^{-1} (incipient melting) and ~270 GPa and ~7.1 km s^{-1} (incipient vaporization), respectively. By using the thermodynamic data of the main constituent minerals and the basalt Hugoniot as a first-order estimate, the laser-generated, monomineralic feldspar, pyroxene, and olivine melts (Fig. 7.2d) would correspond to shock pressures between 70 and 205 GPa. These estimates agree with shock pressure estimates for incipient to complete melting observed in experimentally shocked basalt (Kieffer et al., 1976a). Specifically, incipient melting of plagioclase and pyroxene starts at shock pressures between 40 and 60 GPa, whereas complete melting of the basalt requires shock pressures in excess of 80 to 100 GPa.

7.4.4 Estimation of impact conditions and experimental limitations

Using the planar impact approximation (Melosh, 1989) and Hugoniot data for quartz and iron (Fig. B.7), we find that an iron projectile impacting a nonporous quartz target at a minimum impact velocity of ~6 km s^{-1} would induce peak shock pressures of ~100 GPa at the point of impact, which would gradually decrease as the shock front attenuates with distance. Upon decompression, this impact would produce impact melts originating from shock pressures of 60–100 GPa, which would correspond to the laser-generated sandstone melts of experiment 887. If we take vaporization of the sandstone target at the point of laser irradiation into account, we find that experiment 887 corresponds to postshock thermal conditions of the

impact of an iron meteorite at much higher impact velocities, most likely in the range of 7 to 11 km s^{-1} (cf. Ahrens and O'Keefe, 1972). An impact scenario that would induce shock pressure ranges commensurate with the entropy changes in the basalt experiment would be the impact of a basalt projectile (a quasi-chondritic impactor) into a basalt target at a minimum velocity of 14 km s^{-1}. In this scenario, peak shock pressures of ~270 GPa would be created at the point of impact, inducing incipient vaporization of the basalt target and also giving rise to acontinuum of lower shock pressures.

When comparing our experiments to impact experiments or even impact events, we clearly face several experimental limitations. The most obvious is that direct laser melting under the conditions described above is unable to create shock-metamorphic effects in minerals. Moreover, since we focus on postshock thermal effects, our experimental setup is obviously not able to reproduce typical structural features (craters, ejecta deposits, etc.) of impact events.

7.5 Conclusions

Direct laser irradiation of planetary materials with laser intensities in the range of 1.1–5.3 × 10^4 W cm^{-2} is a suitable tool to simulate impact melting and incipient vaporization in typical impact scenarios in the solar system. Although not capable of creating high shock pressures, our experiments produce superheated melts that thermodynamically, texturally, and mineralogically resemble impact melts formed during adiabatic decompression. In particular, laser-generated melts of sandstone, iron meteorite, and basalt resemble true impact melts known from terrestrial impact structures and from impact experiments. Temperature gradients documented in the irradiated materials, ranging from incipient melting to complete vaporization, correspond to postshock temperature gradients obtained in impact scenarios involving impact velocities high enough to induce complete vaporization at the point of impact and, as the shock wave gradually attenuates, also inducing successively decreasing temperatures with increasing distance that lead to various stages of melting.

A combination of laser melting with time- and space-resolved temperature measurements, petrologic investigations of the resulting melts, and modeling of cooling curves allows for estimating cooling rates in ballistic impact melt ejecta. This approach may effectively be used to study timescales and magnitudes of petrogenetic processes in natural impact melts. Specifically, millimeter- to centimeter-sized melt ejecta will fully solidify within several seconds, and cooling rates are governed by melt volume and material properties. Ultimately, our experiments extend currently attainable postshock temperatures in impact experiments to ranges commensurate with impact scenarios in the velocity range of 4 to possibly 20 km s^{-1}. Thus, they bridge the gap between impact experiments, previous high-intensity laser ablation experiments, and natural observations.

Acknowledgments

This work was funded by the German Science Foundation DFG (grants He-2893/8-2 and Wu-355/6-2). It is part of the PhD theses of CH and RL conducted in the Multidisciplinary Experimental and Modeling Impact Research Network (MEMIN; DFG FOR 887). We gratefully acknowledge the reviews of Kosuke Kurosawa and Boris Ivanov who helped to improve the quality of this paper, as well as editorial handling by Andrew Dombard. We appreciate fruitful discussions with Natasha Artemieva and thank Kosuke Kurosawa for stimulating this study and Dominic Heunoske for assistance.

Associate editor: Andrew Dombard

Chapter 8

Silicate liquid immiscibility in impact melts[1]

This chapter is concerned with structural and compositional heterogeneities in silicate impact melts that either arise from melt unmixing in miscibility gaps (liquid immiscibility *sensu stricto*), or from incomplete mixing and homogenization of compositionally diverse impact melts. At the core of the chapter is a detailed documentation of silicate liquid immiscibility in ballistic impact-melt ejecta (quenched to impact glasses and impact melt rocks) from a variety of pristine, well-studied terrestrial impact structures (Wabar, Kamil, Barringer, and Tenoumer) and glasses produced in the MEMIN hypervelocity impact and laser irradiation experiments. It is shown that the compositions of the conjugate immiscible liquids (Si-rich and Fe-rich) are consistent with phase separation in the high- or low-temperature two-liquid fields in the general chemical system Fe_2SiO_4–$KAlSi_3O_8$–SiO_2–CaO–MgO–TiO_2–P_2O_5, and that major-element partition coefficients are correlated with the degree of polymerization (NBO/T) of the Si-rich melt. Then, this chapter is concerned with a discussion of the thermodynamic and structural reasons of melt unmixing in silicate impact melts of diverse bulk chemical composition. After this, genuine melt unmixing in a miscibility gap is compared against incomplete mixing and homogenization of compositionally diverse impact melts that originate from different parts of a crater's melt zone, or by mixing projectile-derived with target-derived impact melts during early stages of crater formation. Since this chapter presents findings from rapidly quenched ballistic ejecta, these observations constrain the minimum time scales of petrogenetic processes in impact melts—for example, interaction between projectile- and target-derived melts, melt mixing and mingling, melt unmixing, diffusion-controlled element exchange, crystallization, and glass formation—to a few seconds.

Key points:

A comprehensive petrologic and thermodynamic study of silicate liquid immiscibility in impact melts is presented

Unmixing of silicate impact melt is either *directly* (e.g., mixing of iron meteorite-derived melts and high-silica target melts produces bulk compositions that coincide with a miscibility gap) or *indirectly* (e.g., the bulk composition of a residual melt is shifted into a miscibility gap due to crystallization) induced

A working model that classifies heterogeneities in silicate impact melts that either arise from melt unmixing (i.e., liquid immiscibility *sensu stricto*) or from incomplete mixing and homogenization of compositionally diverse impact melts is established

[1]This chapter has been submitted to Meteoritics & Planetary Science and was accepted for publication on May 15, 2017. It will be published as: Hamann, C., Fazio, A., Ebert, M., Hecht, L., Wirth, R., Folco, L., Deutsch, A., and Reimold, W. U. (2017). Silicate liquid immiscibility in impact melts, *Meteoritics & Planetary Science*, DOI: 10.1111/maps.12907.

This chapter has been published as

Christopher Hamann, Agnese Fazio, Matthias Ebert, Lutz Hecht, Richard Wirth, Luigi Folco, Alex Deutsch, and Wolf Uwe Reimold

SILICATE LIQUID IMMISCIBILITY IN IMPACT MELTS

Meteoritics & Planetary Science
Vol. 53, pp. 1594–1632

first published September 11, 2017

It is not included in the online version of this thesis, but is available at the journal's homepage:

http://dx.doi.org/10.1111/maps.12907

Chapter 9

Disequilibrium crystallization and liquid immiscibility in silicate impact melt in the Netschaëvo IIE iron meteorite[1]

Following up on the previous chapter, this chapter is concerned with understanding petrogenetic processes in silicate melt preserved in the Netschaëvo IIE iron meteorite. The silicate inclusion shows compositional variations related to element exchange with the surrounding metal, and textures indicative of shock melting, rapid cooling, fast crystallization upon quenching, and silicate liquid immiscibility. Specifically, crystal morphology (e.g., hopper-shaped olivine, acicular Cl-apatite), mineral composition (e.g., P in olivine), and phase-separated silicate glass droplets document fast cooling rates that are inconsistent with endogenic models involving slow cooling. In contrast, the silicate melt resembles quenched impact melts described in the previous chapter, and many processes documented in terrestrial and experimental impact melts—that is, chemical interaction between metal and silicate, silicate melt unmixing, rapid crystallization under disequilibrium conditions—can be transferred to the Netschaëvo silicate inclusion. The picture that emerges from these results is that impact processes played an important role in the formation of the IIE group of meteorites and, thus, on the IIE parent body.

Key points:

The silicate melt preserved in the Netschaëvo IIE iron meteorite is rapidly quenched, presumably chondritic impact melt

Unmixing of silicate melt was likely induced after partitioning of phosphorous from the host metal into the silicate impact melt

These findings suggests that impact processes probably played an important role in the history of the IIE parent body

[1]This chapter has been published as: Van Roosbroek, N., Hamann, C., McKibbin, S., Greshake, A., Wirth, R., Pittarello, L., Hecht, L., Claeys, P., and Debaille, V. (2017). Immiscible silicate liquids and phosphoran olivine in Netschaëvo IIE silicate: analogue for planetesimal core–mantle boundaries, *Geochimica et Cosmochimica Acta* 197, 378–395, http://dx.doi.org/10.1016/j.gca.2016.10.042.

Summary

This is the abstract of the original publication, but its title has been changed to "summary" in order to delimit it from the brief abstract given on the previous page (the original abstract summarizes several findings that are not immediately relevant to this thesis—in this respect, it has more the character of a summary than an abstract). To ensure consistency throughout this thesis, the subfigure labels (a, b, c, etc.) of the original publication have been changed from uppercase to lowercase letters. The main text, all figure and table captions, the table content, as well as the supplementary material (Chapter C) are as published.

We have investigated a piece of the Netschaëvo IIE iron meteorite containing a silicate inclusion by means of electron microprobe analysis (EMPA) and transmission electron microscopy (TEM). Netschaëvo contains chondrule-bearing clasts and impact melt rock clasts were also recently found. The examined inclusion belongs to the latter and is characterized by a porphyritic texture dominated by clusters of coarse-grained olivine and pyroxene, set in a fine-grained groundmass that consists of new crystals of olivine and a hyaline matrix. This matrix material has a quasi-basaltic composition in the inner part of the inclusion, whereas the edge of the inclusion has a lower SiO_2 concentration and is enriched in MgO, P_2O_5, CaO, and FeO. Close to the metal host, the inclusion also contains euhedral Mg-chromite crystals and small (<2 μm), Si-rich globules. A TEM foil was cut from this glassy, silico-phosphate material. It shows that the material consists of elongated olivine crystallites containing up to 14 wt.% P_2O_5, amorphous material, and interstitial Cl-apatite crystals. The Si-rich silicate glass globules show a second population of Fe-rich silicate glass droplets, indicating they formed by silicate liquid immiscibility. Together with the presence of phosphoran olivine and quenched Cl-apatite, these textures suggest rapid cooling and quenching as a consequence of an impact event. Moreover, the enrichment of phosphorus in the silicate inclusion close to the metal host (phosphoran olivine and Cl-apatite) indicates that phosphorus re-partitioned from the metal into the silicate phase upon cooling. This probably also took place in pallasite meteorites that contain late-crystallizing phases rich in phosphorus. Accordingly, our findings suggest that oxidation of phosphorus might be a general process in core–mantle environments, bearing on our understanding of planetesimal evolution. Thus, the Netschaëvo sample serves as a natural planetesimal core–mantle boundary experiment, and based on our temperature estimates, the following sequence of events takes place: (1) precipitation of olivine (1400–1360 °C), (2) re-partitioning of phosphorus from the metal into the silicate phase, and (3) formation of immiscible melts (1230–1115 °C).

9.1 Introduction

Two varieties of iron meteorites can be distinguished: (1) the fractionally crystallized *magmatic* iron meteorites (IC, IIAB, IIC, IID, IIIAB, IIIE, IIIF, IVA, and IVB) and (2) the silicate-bearing, so-called *non-magmatic* iron meteorites (IAB/IIICD and IIE), with several members containing silicate inclusions of various nature (Choi et al., 1995; Goldstein et al., 2009). While fractional crystallization of slowly cooling metallic liquids (Scott, 1972) is the process that formed the first variety, the exact formation conditions of the silicate-bearing irons are less clear. Their formation is inconsistent with extensive fractional crystallization, and these irons may

have come from bodies that were not sufficiently heated to form metallic cores (Haack and McCoy, 2004).

The iron meteorites belonging to the IIE group possess silicate inclusions representing a wide variety of characteristics, ranging from large chondritic clasts to smaller, molten, feldspar-rich globules (Ruzicka, 2014). Mittlefehldt et al. (1998) classified these different types into five groups while Ruzicka (2014), on the other hand, prefers to divide the silicate-bearing IIE into a *fractionated* and an *unfractionated* subgroup. Given the observation of a silicate inclusion made of impact melt lithology in Netschaëvo (Van Roosbroek et al., 2016), it is possible that IIE are *impact melt breccias*. This illustrates that there is no appropriate way to classify the very broad range of mineralogical and petrological characteristics the IIE represent.

Looking at their radioisotopic ages, the silicate-bearing IIE form two groups that do not correspond to the fractionated and unfractionated subgroups based on mineralogy. An "old" IIE group, having a formation age of ~4.5 Ga, consists of 6 meteorites: Weekeroo Station, Colomera, Miles, Techado, Taramuhara, and the recently described Mont Dieu, whereas meteorites sharing ages of around 3.6 Ga are called the "young" IIE; this group consists of Netschaëvo, Kodaikanal, and Watson (Bogard et al., 2000).

Over the past decades, several formation scenarios were proposed for the IIE group, trying to incorporate all their different features. These can be subdivided into *exogenic*, *endogenic*, and *hybrid* models. In exogenic models, IIE are formed by impact mixing with limited to complete impact melting (Burnett and Wasserburg, 1967; Bence and Burnett, 1969; Scott and Wasson, 1976; Osadchii et al., 1981; Rubin et al., 1986; Wasson and Wang, 1986; Olsen et al., 1994; Ikeda and Prinz, 1996; Ikeda et al., 1997). In endogenic models, IIE are formed as an internal process inside an early planetesimal, involving internal radiogenic heating followed by incomplete separation of metal and troilite from silicate (Wasserburg et al., 1968; Prinz et al., 1982; Prinz et al., 1983; McCoy, 1995). Hybrid models consist of a combination of both extremes (Bunch et al., 1970; Armstrong et al., 1990; Casanova et al., 1995; Ruzicka et al., 1999; Bogard et al., 2000; Hsu, 2003; Takeda et al., 2003; Ruzicka and Hutson, 2010). Ruzicka (2014) subdivided them into three groups:

1. *"cold crust"* models where metallic melt is mixed with cold silicate at the surface of an asteroid as a consequence of an impact event;

2. *"hot mixing"* models where metallic melt is injected, also as a consequence of an impact event, in an internally heated chondritic body; and

3. *"collisional disruption and re-accretion"* models where the internally heated parent body broke up and re-accreted afterwards.

All these formation models involve a chondritic parent body, the main H chondrite or a related H chondrite-like parent body.

Netschaëvo is the first iron meteorite where the occurrence of chondrules has been discovered and has long been regarded as the most primitive member of the IIE group. However, Van Roosbroek et al. (2016) described silicate inclusions not corresponding to the chondrule-bearing clasts, which can be classified as impact melt rocks. This suggests that Netschaëvo is a breccia containing metamorphosed and impact melt rock clasts (Van Roosbroek et al., 2016) and, consequently, that collisions must have played an important role in its formation history.

Following up on the initial petrographic description of the Netschaëvo impact melt rock inclusions by Van Roosbroek et al. (2016), the present study sets out a detailed nano-analytical investigation of the glassy material in the silicate inclusions of Netschaëvo IIE by means of electron microprobe analysis and transmission electron microscopy in order to gain more detailed insight into their formation mechanism. We show that the occurrence of phosphoran olivine (containing several wt.% P_2O_5; cf. Boesenberg and Hewins, 2010) and the presence of silicate emulsion textures strengthen the impact formation hypothesis. We also constrain the temperature at which transfer of phosphorus from the metal into the silicate melt occurs—a process which may be important for core–mantle boundaries or other silicate–metal interaction zones, for example, in the source of pallasite meteorites (cf. McKibbin et al., 2016).

9.2 Analytical techniques

9.2.1 Electron microprobe analysis

Back-scattered electron (BSE) imaging and quantitative electron microprobe analysis (EMPA) of the fine-grained, siliceous material in the Netschaëvo sample were done with the JEOL JXA-8500F field-emission electron microprobe at Museum für Naturkunde, Berlin, Germany, which is equipped with five wavelength-dispersive X-ray spectrometers and an energy-dispersive X-ray spectrometer. Operating conditions for wavelength-dispersive X-ray spectrometry (WDX) were set to an acceleration voltage of 15 kV, a beam current of 15 nA, and a working distance of ~11 mm. A slightly defocused beam (spot size ~5 µm) was used for measuring the bulk composition of the fine-grained, siliceous material. Standardization was based on the main Astimex and Smithsonian international standards suite of the micro-analytical facilities at Museum für Naturkunde; see Table C.1 (Appendix C) for details. Raw data were then processed for matrix effects using a conventional ZAF routine in the JEOL series operating system. Normalization of WDX analyses to 100 wt.% was not applied and results are reported in oxides. Detection limits varied between 48 ± 1 ppm for Cl and 210 ± 1 ppm for Mn; see Table C.1 for average values. Accuracy of the WDX analyses is much better than 3% for major elements >5 wt.% and in the range of 10−% for minor elements <0.5 wt.%. Precision is much better than 5% for major elements >5 wt.% and in the range of several ten percent for minor elements <0.5 wt.%.

9.2.2 Transmission electron microscopy

Sample preparation as well as transmission electron microscopy (TEM) were both carried out at the TEM laboratory of the Deutsches GeoForschungsZentrum, Potsdam, Germany. Preparation of a electron-transparent sample was done with a FEI FIB200TEM focused ion beam (FIB) device (for a detailed description of the FIB preparation method, see Wirth, 2009). A TEM-ready foil with final dimensions of 15 × 10 × 0.1 µm was cut directly from the polished and carbon-coated section using a gallium ion beam under high-vacuum conditions. Then, it was placed on a carbon film on top of a copper grid. Further carbon-coating to prevent charging of the TEM sample was not applied (for a discussion on the need of TEM sample carbon-coating, see Wirth, 2009).

The FIB-cut TEM foil was then surveyed and analyzed with a FEI Tecnai G^2 F20 X-Twin transmission electron microscope. The microscope is equipped with an EDAX ultra-thin window EDX system, a Fishione high-angle annular dark-field (HAADF) detector, and a Gatan imaging filter. Operating conditions were set to an acceleration voltage of 200 kV, using normal imaging mode for bright-field (BF) and dark-field (DF) imaging and scanning transmission electron microscopy (STEM) mode for HAADF imaging and analytical electron microscopy (AEM). All HAADF images were acquired with a camera length of either 75 or 330 mm. In general, the brightness of such images follows a Z^2 dependency (e.g., Wirth, 2009). Specifically, a short camera length (75 mm) allows to image Z contrast (by collecting only electrons that were scattered under high angles from inner shell electrons), whereas a long camera length (330 mm) allows to simultaneously image Z contrast and diffraction contrast (by collecting electrons that were scattered under low angles from outer shell electrons). Bright-field images were digitally recorded; only electron diffraction patterns were recorded on image plates. Compositional information on both crystalline and amorphous phases was obtained semi-quantitatively from EDX spectra. Each EDX spectrum was obtained within 60–120 s live time. Beam size in STEM mode was ~1 to 2 nm. However, to avoid specimen damage and mass loss (especially of Na), the electron beam was scanned across a preselected area during data acquisition. Depending on specific count rates, the dead time of the utilized EDX spectrometer was mostly between 5 and 10%. For quantification, the k_{ab} factors of the TIA software package were used and all data were normalized to 100 wt.%. Total errors for AEM are ~4% for concentrations of 5–30 wt.% and >50% for concentrations below a few percent by weight. Structural information on crystalline and amorphous phases was either directly obtained with selected area electron diffraction (SAED) patterns recorded on image plates (allowing high precision), or by calculating diffraction patterns with a fast Fourier transform (FFT) from high-resolution lattice fringe images of lattice fringes (allowing fast data acquisition). Interpretation of acquired diffraction patterns was done with the program Digital Micrograph by Gatan.

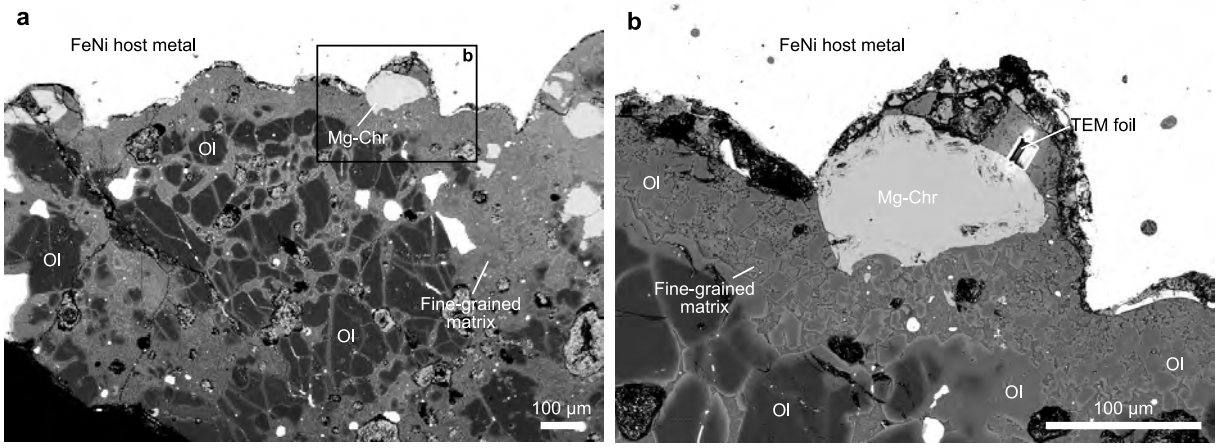

Figure 9.1 Back-scattered electron images of the studied Netschaëvo silicate inclusion in contact with the host FeNi metal. **a** Typical texture of the silicate inclusion, showing coarse-grained olivine (Ol) and Mg-chromite (Mg-Chr) crystals in fine-grained matrix. **b** Location of the TEM foil (Fig. 9.2a) representatively sampling the fine-grained matrix in contact with the FeNi host metal. Note the presence of silicate droplets in the FeNi host metal.

Table 9.1 Average composition and standard deviation of the glassy matrix material in Netschaëvo determined by electron microprobe analysis.

		Silico-phosphate material	
[wt.%]	Quasi-basaltic material	SiO_2-poor	SiO_2–CaO-poor
SiO_2	53.4(45)	36.2(30)	40.7(59)
TiO_2	0.4(1)	0.3(1)	0.10(5)
Al_2O_3	7.6(9)	4.5(11)	3.3(19)
Cr_2O_3	0.2(1)	0.7(3)	0.5(2)
FeO	16.9(29)	21.9(19)	26.0(19)
MnO	0.3(1)	0.3(1)	0.30(4)
MgO	3.9(13)	7.2(28)	18.3(78)
CaO	10.6(26)	14.2(30)	1.7(16)
Na_2O	2.1(6)	1.1(3)	0.5(5)
K_2O	0.3(2)	0.2(1)	0.1(1)
P_2O_5	3.0(20)	12.1(22)	8.0(7)
NiO	bdl	0.04(2)	0.04(2)
Cl	1.3(3)	1.9(4)	0.2(2)
Total	100.0	100.6	99.7
No. of analyses	10	12	4

Data were obtained by EMPA-WDX and are given in wt.%; bdl = below detection limit.

9.3 Petrography

The silicate inclusions of the impact melt rocks of Netschaëvo (Fig. 9.1) are characterized by a porphyritic texture dominated by coarse-grained olivine and, to a lesser extent, by pyroxene crystals. They are embedded in a groundmass containing fine-grained, euhedral olivine crystals set in quenched melt that is partially crystallized with microlitic domains consisting of olivine. Several opaque phases are present in the Netschaëvo

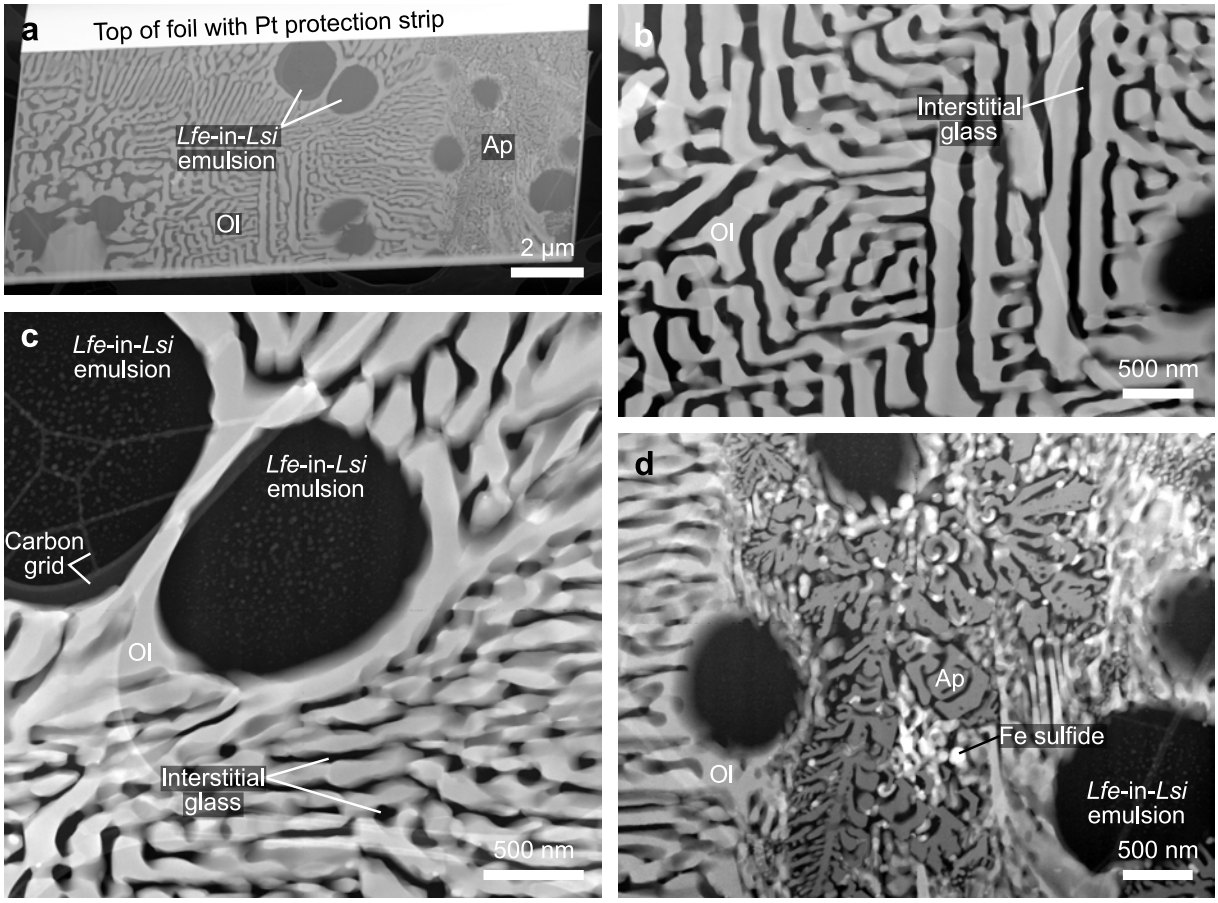

Figure 9.2 High-angle annular dark-field TEM images showing the entire foil (**a**) and typical details (**b**–**d**). Phosphoran olivine (Ol) crystallites, grown in symplectite-like fashion (b), enclose globules of Si-rich glass and Cl-apatite (Ap) hopper crystals (c and d). Note that tiny droplets some 10–50 nm in diameter are disseminated in the globules (c), hinting at further (metastable?) liquid–liquid phase separation. The TEM carbon grid is weakly visible seemingly in front of the images. The first-order (stable) liquid immiscibility is indicated by *Lfe* (Fe-rich liquid) and *Lsi* (Si-rich liquid).

silicate inclusions, the majority consisting of kamacite and taenite, usually present as large, irregular grains (300–400 µm) with lesser amounts of troilite. Metal is also found as rounded metal blebs (5–20 µm) surrounded by metal dendrites (1–5 µm) with an interstitial P,S-rich phase. Such globules are contained in the glassy material and also between and within olivine and pyroxene crystals. The glassy matrix material in the inner part of the silicate inclusion has a quasi-basaltic composition and contains a relatively high SiO_2 content, whereas the matrix material closer to the contact with the surrounding metal has lower SiO_2 and is enriched in P_2O_5, CaO, and FeO. The latter will be referred to as "silico-phosphate material" (Table 9.1). In the area containing the silico-phosphate material, euhedral Mg-chromite crystals of 10–100 µm and small (<2 µm), Si-rich globules are present. Olivine and pyroxene crystals have the same composition throughout the silicate inclusion, independent of the type of matrix material present. A detailed description of these samples is provided by Van Roosbroek et al. (2016).

9.4 Mineralogy of fine-grained material

As some microstructural features are smaller than the resolution limit of the microprobe, TEM is required in order to characterize the fine-grained material in the inclusion. Thus, a TEM foil (Fig. 9.2a) was FIB-cut from a representative area of the silico-phosphate matrix material present at the outer rim of the silicate inclusion (cf. Fig. 9.1b).

9.4.1 Phosphoran olivine

Olivine is the most abundant phase in the fine-grained material. The olivine crystallites generally have elongated shapes and their sizes range from <500 nm to ~2 µm length and ~100 to ~400 nm width. They occur in a geometric, symplectitic network with interstitial glass (see Subsection 9.4.3) between individual olivine laths (Figs. 9.1b and 9.3a). Selected-area electron diffraction patterns (Fig. 9.4a) and HRTEM lattice fringe images (Fig. 9.5) indicate that olivine grains are perfectly crystalline, showing little or no signs of lattice defects or twinning. A SAED pattern of a typical olivine lath (Fig. 9.4a) was obtained with a low-index zone axis orientation (i.e., electron beam parallel to *c* axis) and could be unequivocally identified as olivine. Specifically, lattice spacing between the (100), (010), and (110) planes is ~4.65 Å, ~10 Å, and ~4.17 Å, respectively. Moreover, the angles between the (110) and (100) and the (110) and (010) planes are 24.7° and ~65°, respectively. Thus, the obtained SAED pattern agrees well with the olivine structure.

TEM-EDX analyses (Table 9.2) show that olivine contains up to 14 wt.% of P_2O_5 and that olivine has an intermediate fayalite (Fa) content ranging from Fa_{42}–Fa_{47} on the left side of the TEM foil (where Cl-bearing apatite is absent) to Fa_{64} on the right side of the TEM foil (where it is in assemblage with Cl-bearing apatite and Fe sulfides). As apparent from the number of cations on the basis of four oxygen atoms (Table 9.2), Si deficiency is approximately counterbalanced by the presence of P, suggesting that Si + P ≈ 1 and that phosphorus replaces silicon in the olivine structure. This is best illustrated by olivine analysis Ol.2 (Table 9.2), which has an unusually low SiO_2 content of 21.4 wt.% (equaling 0.72 Si atoms per formula unit) paired with the highest P_2O_5 content of 14 wt.% (equaling 0.40 P atoms per formula unit). Although TEM-EDX analyses are less precise (and notoriously lack the high accuracy and precision of microprobe data), with Si + P ≈ 1 and the sum of the remaining cations close to 2, it seems likely that phosphorus is substituting for silicon in the olivine structure.

9.4.2 Cl-Apatite

Cl-apatite occurs as interstitial dendritic chains consisting of intergrown apatite crystallites showing typical hopper morphologies and dimensions of ~250 nm (Figs. 9.2d, 9.3b, and 9.6). The chains are usually between 500 nm and 1 µm long, a single chain reaching a length of ~4 µm. Individual crystallites often show hollow cavities and are delicately intergrown

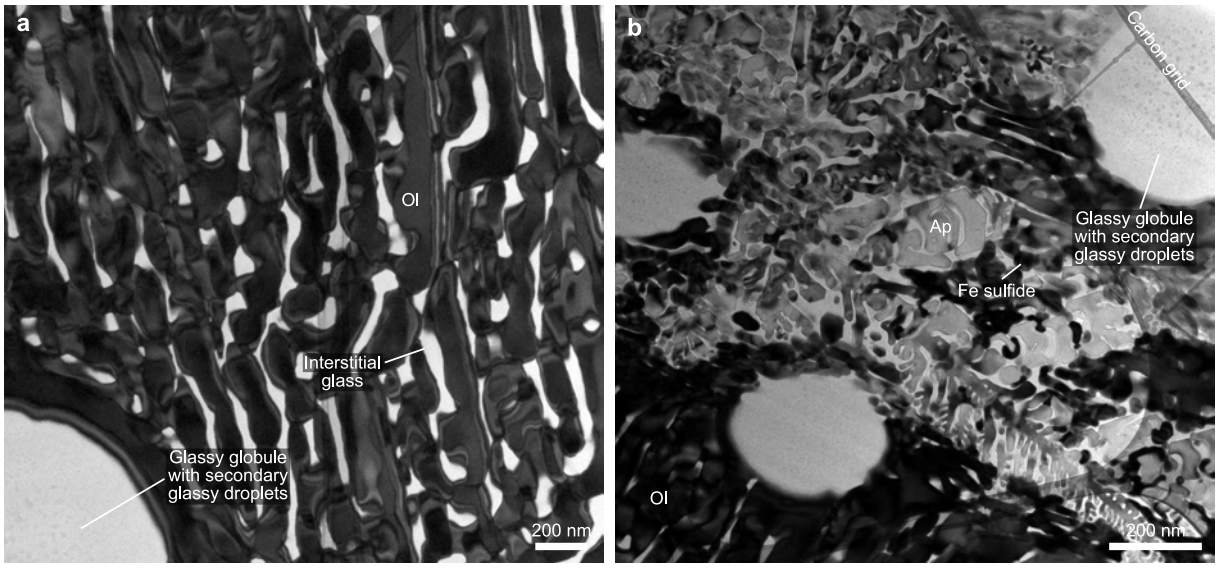

Figure 9.3 Bright-field TEM images of phosphoran olivine, Cl-apatite, and glassy globules. **a** Symplectite-like texture of phosphoran olivine (Ol) crystallites and interstitial glass. The olivine crystallites show a common crystallographic orientation, as indicated by rather uniform diffraction conditions. Note that the glassy globule is surrounded by an olivine grain that grew around the globule. **b** Delicate intergrowth of phosphoran olivine, Cl-apatite (Ap) hopper crystals, glassy globules, and Fe sulfide blebs. Note the difference in diffraction contrast between crystalline (diffraction contrast visible) and amorphous phases (diffraction contrast absent).

with olivine crystallites, Fe-sulfide blebs, and interstitial glass (Fig. 9.6). A SAED pattern (Fig. 9.4b) was indexed as apatite; lattice spacing in $[11\bar{2}1]$, $[1\bar{1}00]$, and $[20\bar{2}1]$ direction is 3.86 Å, 8.19 Å, and 3.51 Å, respectively, and the angles between the $[11\bar{2}1]$ and $[20\bar{2}1]$ and the $[1\bar{1}00]$ and $[20\bar{2}1]$ directions are 25.3° and 64.4°, respectively. Additionally, TEM-EDX analyses show that Cl-apatite contains up to 4.5 wt.% Cl (Table 9.2).

9.4.3 Amorphous material

A third phase in the residual material is not only present in the form of amorphous globules of about 500 nm to 1.5 µm diameter, but also as an amorphous groundmass interstitial to phosphoran olivine and Cl-apatite crystallites (Fig. 9.2 and 9.3). In the globules, amorphous secondary droplets of 10–50 nm diameter are finely dispersed (Figs. 9.2c, d, and 9.3a, b). Both materials—the globules with secondary droplets, as well as the groundmass interstitial to the crystalline phases—lack the typical diffraction contrast of crystalline materials in BF images (Fig. 9.3). Furthermore, SAED patterns (Fig. 9.4c, d) show sets of diffuse, concentric scattering intensity, ultimately confirming that both materials are completely amorphous.

In HAADF images (Fig. 9.2c), the globules show dark contrast, whereas the nanometer-sized droplets show bright contrast. Hence, the host material is composed of low-Z material, whereas the secondary droplets are composed of high-Z material (Z denotes atomic number). Specifically, the globules usually show a bulk composition rich in SiO_2 (75.0–86.5 wt.%)

Table 9.2 Composition of phosphoran olivine and Cl-apatite crystallites in the fine-grained matrix of the silicate inclusions in Netschaëvo determined by analytical transmission electron microscopy.

	Olivine					Apatite	
	Ol.1	Ol.2	Ol.3	Ol.4	Ol.5	Ap.1	Ap.2
Oxide wt.%							
SiO_2	30.8	21.4	33.1	31.5	31.9	3.8	6.4
Al_2O_3	0.6	0.5	bdl	bdl	bdl	bdl	0.6
Cr_2O_3	bdl	bdl	bdl	bdl	bdl	bdl	bdl
FeO[a]	32.3	38.4	38.8	34.5	46.4	2.5	2.0
MnO	bdl	1.4	0.5	0.3	0.4	bdl	bdl
MgO	24.4	24.3	27.6	25.5	14.8	1.1	bdl
CaO	bdl	bdl	bdl	bdl	0.2	48.1	50.8
P_2O_5	11.8	14.0	bdl	7.1	6.3	40.2	35.8
Cl	bdl	bdl	bdl	bdl	bdl	4.3	4.5
Number of cations on the basis of four O							
Si	0.94	0.72	0.94	0.94	1.00	0.30	0.51
Al	0.02	0.02	—	—	—	—	0.06
Cr	—	—	—	0.02	—	—	—
Fe	0.82	1.08	0.93	0.86	1.21	0.16	0.13
Mn	—	0.04	0.01	0.01	0.01	—	—
Mg	1.11	1.22	1.17	1.13	0.69	0.13	—
Ca	—	—	—	—	0.01	4.08	4.37
P	0.30	0.40	—	0.18	0.17	2.69	2.43
Cl	—	—	—	—	—	0.58	0.61
Total	3.19	3.48	3.05	3.14	3.09	7.95	8.12
Fa[b]	42	47	44	43	64	—	—

Data were obtained by TEM-EDX and are fixed to 100 wt.%; bdl = below detection limit.
[a] All Fe reported as FeO.
[b] Fa = 100 × Fe/(Fe + Mg + Mn).

with lesser amounts of Al_2O_3 (9.3–12.2 wt.%) and FeO (2.8–4.1 wt.%; see Table 9.3). Moreover, considerable compositional heterogeneity from globule to globule exists for Na_2O (below detection limit to 5.5 wt.%), K_2O (<0.2–1.2 wt.%) and CaO (0.9–2.1 wt.%), which is often associated with the presence or absence of the small, nanometer-sized, high-*Z* contrast droplets. Due to the small dimensions of these droplets, reliable TEM-EDX analyses were not possible on individual droplets, as focusing the electron beam for EDX analyses immediately resulted in sputtering material from the TEM foil. The glass interstitial to phosphoran olivine and Cl-apatite is dominated by SiO_2 (79.1–89.2 wt.%), with Al_2O_3 (8.9–11.3 wt.%) and FeO (1.0–6.9 wt.%) being present as minor components. Thus, it is compositionally similar to the glassy globules.

The glassy globules are usually surrounded by phosphoran olivine crystallites, which, in some cases, seemingly grew around the glassy globules (Fig. 9.2c). The interface between host silicate glass and secondary glass droplets is, even under highest magnification, always a sharp meniscus rather than a gradual transition of composition. Furthermore, the sec-

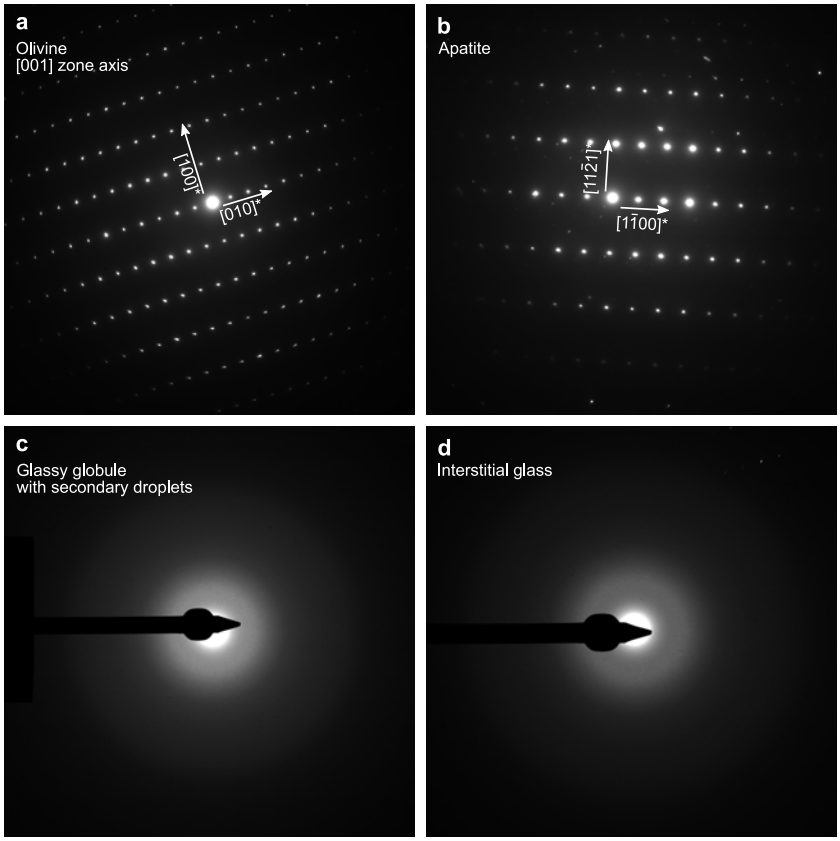

Figure 9.4 Selected area electron diffraction patterns of crystalline (a and b) and amorphous (c and d) phases in the studied TEM foil. **a** Olivine diffraction pattern, obtained with an incident electron beam parallel to *c* axis. Lattice spacing between the (100), (010), and (110) planes is ~4.65 Å, ~10 Å, and ~4.17 Å, respectively. The angles between the (110) and (100) and the (110) and (010) planes are 24.7°and ~65°, respectively. **b** Apatite diffraction pattern; lattice spacing in [11$\bar{2}$1], [1$\bar{1}$00], and [20$\bar{2}$1] direction is ~3.86 Å, ~8.19 Å, and ~3.51 Å, respectively. The angles between the [11$\bar{2}$1] and [20$\bar{2}$1] and the [1$\bar{1}$00] and [20$\bar{2}$1] directions are 25.3°and 64.4°, respectively. **c** Diffraction pattern of a glassy globule with secondary droplets (obtained from the large globule in the upper right corner of Fig. 9.3b), showing a set of diffuse, concentric rings that prove that the material is truly amorphous. **d** Diffraction pattern of the glass interstitial to olivine crystallites, also yielding a set of diffuse, concentric rings.

ondary droplets cluster in the cores of their host globules, leaving a narrow zone almost free of secondary droplets adjacent to the interface with the surrounding olivine (Fig. 9.2c).

9.4.4 Metallic globules

Metallic globules of 100 nm to 60 μm diameter are disseminated in the silicate inclusion. Usually, these globules consist of an intergrowth of two or three phases (Fe-rich, S-rich, and possibly with an additional P-rich phase). Microprobe measurements indicate that the Fe-rich phase in the globules comprising the three phases consist of a Ni-poor phase (87.3 wt.% Fe and 10.1 wt.% Ni) and a Ni-rich phase (66.9 wt.% Fe and 32.4 wt.% Ni). The S-rich phase consists of 62.6 wt.% Fe and 33.8 wt.%

Table 9.3 Composition of interstitial glass and Si-rich, amorphous droplets (*Lsi*) in the fine-grained matrix of the silicate inclusions in Netschaëvo determined by analytical transmission electron microscopy.

	Interstitial glass, $n = 2$				Silica-rich, amorphous droplets (*Lsi*), $n = 5$						
[wt.%]	G.1	G.2	Average	σ	*Lsi*.1	*Lsi*.2	*Lsi*.3	*Lsi*.4	*Lsi*.5	Average	σ
SiO_2	89.2	79.1	84.2	2.3	75.0	86.5	85.0	85.0	80.9	82.5	1.9
TiO_2	bdl	0.6	<0.6	—	bdl	bdl	bdl	bdl	bdl	bdl	—
Al_2O_3	8.9	11.3	10.1	0.5	10.8	9.3	10.2	10.2	12.2	10.5	0.4
Cr_2O_3	bdl	bdl	bdl	—	bdl	bdl	bdl	bdl	bdl	bdl	—
FeO[a]	1.0	6.9	3.9	1.3	4.1	3.2	2.8	2.8	3.6	3.3	0.2
MnO	bdl	bdl	bdl	—	bdl	bdl	bdl	bdl	bdl	bdl	—
MgO	0.4	1.5	1.0	0.3	1.7	0.5	0.6	0.7	0.9	0.9	0.2
CaO	0.5	0.5	0.5	0.0	2.1	bdl	0.9	0.9	1.0	1.0	0.3
Na_2O	bdl	bdl	bdl	—	5.5	bdl	bdl	bdl	bdl	<5.5	—
K_2O	bdl	bdl	bdl	—	bdl	0.4	0.2	0.3	1.2	0.4	0.2
P_2O_5	bdl	bdl	bdl	—	bdl	bdl	bdl	bdl	bdl	bdl	—
Cl	bdl	bdl	bdl	—	0.8	0.1	0.2	bdl	0.1	0.3	0.1

Data were obtained by TEM-EDX and are fixed to 100 wt.%; σ = standard error; bdl = below detection limit.
[a] All Fe reported as FeO.

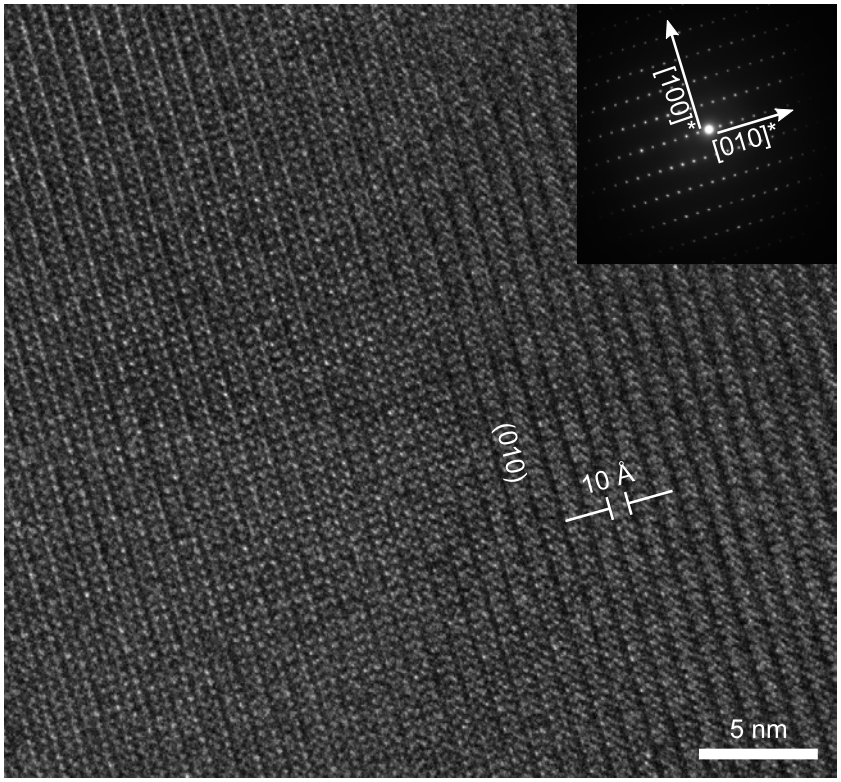

Figure 9.5 High-resolution TEM image picturing lattice planes in a typical phosphoran olivine crystallite with a zone axis of [001]. The olivine crystal lattice is free of lattice defects or twinning, and lattice spacing of the (010) plane is ~10 Å. The inset shows the corresponding SAED pattern; see Fig. 9.4a for details.

S, whereas the P-rich phase consists of 60.7 wt.% Fe, 24.5 wt.% Ni, and 13.8 wt.% P.

9.5 Discussion

9.5.1 Phosphoran olivine

Phosphoran olivine is an extremely rare phase, being described for the first time in pallasites (Buseck, 1977; Buseck and Clark, 1984). It is generally referred to as "phosphoran" if more than 1 wt.% P_2O_5 is present (Boesenberg and Hewins, 2010). For example, Wasson et al. (1999) found up to 7.4 wt.% P_2O_5 in phosphoran olivine from the Brenham pallasite. This mineral has also been found in terrestrial (Goodrich, 1984; Agrell et al., 1998) and other extraterrestrial samples (Buseck and Clark, 1984; Wasson et al., 1999; Goodrich, 2003; Wang et al., 2006), as well as in manufactured objects (Tropper et al., 2004; Boesenberg, 2006). In olivine, P^{5+} will replace Si^{4+} in the silica tetrahedron, but requires charge balancing with another cation. Early studies suggested that P^{5+} and Na^{+} substitute for Si^{4+} and Mg^{2+} (or Ca^{2+}), as is the case for garnets (Thompson, 1975; Bishop et al., 1976). However, Na^{+} cannot be accommodated by olivine, as there is no structural site available for this cation (Goodrich, 1984). Buseck and Clark (1984) were the first to propose the possibility of vacant octahedral sites that compensate for the charge of P^{5+}. Goodrich (1984) supported this idea, based on structural formula of olivine showing cation deficiencies. The vacancy of the octahedral site was experimentally confirmed by Boesenberg and Hewins (2010), who proposed the charge balancing scheme $4\ {}^{VI}M^{2+} + 2\ {}^{IV}Si^{4+} \leftrightarrow 3\ {}^{VI}M^{2+} + 2\ {}^{IV}P^{5+} + {}^{VI}\square$.

Boesenberg and Hewins (2010) carried out experiments to constrain the formation conditions of phosphoran olivine and concluded that three requirements need to be met: (1) enrichment of P_2O_5 in the parental melt, (2) depletion of SiO_2 in the parental melt, and (3) rapid crystallization from a melt or rapid cooling in an un-equilibrated system. The latter is inferred from their findings that P behaves compatibly within the first tens of hours of the experiments ($D^{Ol/Liq} > 1$), resulting in the incorporation of P into the olivine, but becomes highly incompatible ($D^{Ol/Liq}$ is 0.001–0.3) after a timescale of days to weeks, and will be expelled from the crystal lattice and be replaced by Si. Based on their experiments, Boesenberg and Hewins (2010) concluded that phosphoran olivine crystallized from a melt supersaturated in P, by igneous activity or a pyrometamorphic reaction.

9.5.2 Crystal shape and crystallization of Cl-apatite

The skeletal and parallel arrangements of apatite crystals in the Netschaëvo silicate inclusions can be produced by quenching from a liquid (Wyllie et al., 1962), while near-equilibrium growth produces smaller, equant apatites co-existing with liquid or vapor. Quench apatites produced experimentally (Wyllie et al., 1962) are generally closely-packed bundles of parallel or radiating needle aggregates. These bundles exhibit a hexagonal

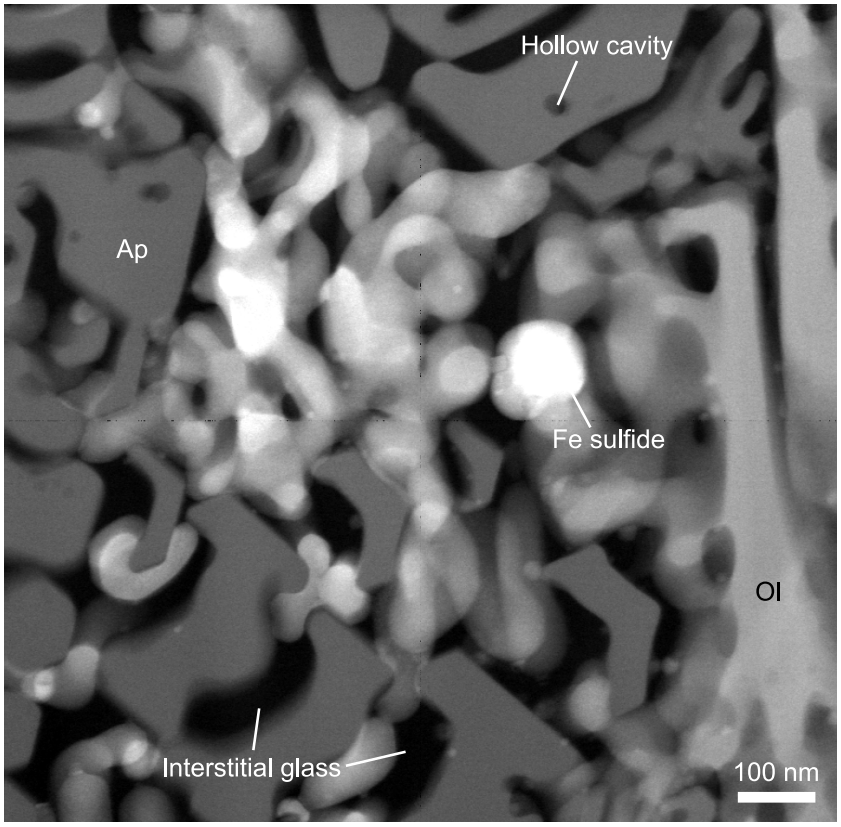

Figure 9.6 High-angle annular dark-field TEM image showing the delicate intergrowth of Cl-apatite (Ap), phosphoran olivine (Ol), Fe-sulfides, and interstitial glass in detail (cf. Fig. 9.2d for an overview). Note the presence of hollow cavities in the Cl-apatite hopper crystals.

outline with interstitial, quenched glass in cross-section. Acicular crystals are greatly elongated parallel to the *c*-axis and can locally contain a hollow cavity along the length of the crystal. Wyllie et al. (1962) concluded that these crystal habits are present in experimental and natural systems over a wide range of compositions, indicating that the physical control of precipitation from a cooling liquid is the main driving force to form these crystals, while its chemical environment seems less important. Furthermore, acicular apatite crystals have been found in several environments (Girault, 1966; Capdevilla, 1967; Bargossi et al., 1999) and their presence has often been used to infer rapid cooling conditions and/or the presence of a fluid (Piccoli and Candela, 2002).

Several studies have investigated the solubility of apatite in melts. Although most studies have focused on felsic systems, Watson (1979) reported that saturation of apatite in basic to intermediate magmas is controlled by three variables, that is, concentration of P_2O_5, concentration of SiO_2, and temperature. The experiments were carried out over a temperature range of 1165–1275 °C and at 1 atm pressure. In a magma containing about 45 wt.% SiO_2, ~6 wt.% P_2O_5 is required for apatite saturation at 1200 °C. With increasing amounts of SiO_2 and with decreasing temper-

ature, the amount of P_2O_5 needed to saturate the melt decreases. This indicates that higher P_2O_5 concentrations are needed to saturate basaltic liquids. Furthermore, the amount of CaO has also an effect on apatite saturation (Tollari et al., 2006). In contrast to SiO_2, which is negatively correlated to the apatite saturation temperature, CaO encourages apatite saturation (Tollari et al., 2008). Furthermore, all experiments performed on ferrobasaltic liquids (Watson, 1980; Tollari et al., 2006; Tollari et al., 2008) showed that pressure only has a minor effect on apatite saturation.

9.5.3 Silicate liquid immiscibility

From the observations made above—that is, Si-rich silicate glass globules showing a secondary population of (presumably Fe-rich) silicate glass droplets—it has to be considered that silicate liquid immiscibility affected the crystallization history of the fine-grained silicate matrix during cooling. In fact, liquid–liquid phase separation through immiscibility is a common phenomenon in glass-forming binary and multicomponent silicate systems. For example, it is frequently encountered and utilized in the production of technological glasses (e.g., Shelby, 2005). On the contrary, in geosciences, the relevance of silicate liquid immiscibility has been debated since the early 20th century (e.g., Daly, 1914; Bowen, 1928; Roedder, 1979; Philpotts, 1982; Veksler et al., 2007; Charlier et al., 2013, and references therein), and thus far, it seems that no consensus has been reached regarding its petrogenetic role and importance. However, despite its controversial reputation in geologic and planetary sciences, a large number of case studies on silicate emulsions exist in the literature. These have addressed terrestrial (e.g., Philpotts, 1982) and lunar (e.g., Roedder and Weiblen, 1970; Roedder and Weiblen, 1971) basalts, terrestrial layered intrusions (e.g., Jakobsen et al., 2005), natural (Chapter 8 and, e.g., Zolensky and Koeberl, 1991; Hamann et al., 2013) and experimental (Chapter 8 and Ebert et al., 2013) impact melts, and meteorites (e.g., Ruzicka et al., 2006).

The physical mechanism behind the unmixing process is quite universal and based on thermodynamics and the behavior of a system's Gibbs free energy of mixing, ΔG_m. Briefly, if mixing of two components yields a lower ΔG_m, the mixture will remain homogeneous, whereas if separation of the mixture into two components yields a lower ΔG_m, the mixture will (if allowed by kinetics) separate into two phases (James, 1975; Wood and Hess, 1980; Shelby, 2005). Phase separation in glass-forming silicate systems is, in addition, a consequence of the poor steric compatibility between network-forming (mainly Si^{4+}) and network-modifying (e.g., Fe^{2+}, Mg^{2+}, and Ca^{2+}) cations and, furthermore, the Coulomb repulsion between poorly shielded network-modifying cations (Hudon and Baker, 2002). In a silicate melt, network-modifying cations are surrounded by bridging (Si–O–Si) and non-bridging (Si–O–M, where M is a network-modifying cation) oxygens that isolate the network-modifying cations from each other by masking the positive charges (Charlier et al., 2015).

However, the bridging oxygens are connected to Si^{4+} by strong covalent bonds and, therefore, the network-modifiers are not well protected from each other, resulting in Coulomb repulsions and eventually in melt unmixing (Hudon and Baker, 2002). Typical textures of immiscibility comprise spherical globules or droplets of one phase disseminated in a continuous matrix phase. The interface between the two phases is always a sharp meniscus, which proves to be a good test for true immiscibility (e.g., Roedder, 1978), since incomplete mixing of two (or more) melts with differing compositions will produce compositional gradients.[15] Geologically relevant compositions tend to split up into a Si-rich liquid (*Lsi*) showing the composition of a granite, and an Fe-rich liquid (*Lfe*) showing the composition of an Fe-rich pyroxenite (Philpotts, 1982). Moreover, aluminum and alkalis tend to concentrate in *Lsi*, whereas the remaining major elements (especially Fe, Mg, Ca, and P) tend to concentrate in *Lfe*. After phase separation in the liquid state, rapid quenching is required in order to preserve the two phases, as crystallization (especially of the Fe-rich liquid, forming magnetite, Fe-rich olivine, or Fe-rich pyroxene) tends to destroy the evidence for liquid immiscibility (e.g., Roedder, 1978; Philpotts, 2008).

[15] This was discussed in Chapter 8; see Subsection 8.6.3 and Fig. 8.17

The textures presented in Figs. 9.2 and 9.3 are unequivocally consistent with phase separation through silicate liquid immiscibility and they are the first clear occurrence of silicate liquid immiscibility in meteorites. They show globules of *Lsi* disseminated in an Fe,Mg,P-rich matrix, which crystallized to phosphoran olivine and Cl-apatite. Hence, the presence of one of the two phases (i.e., *Lsi*) produced by liquid immiscibility is immediately apparent, whereas the conjugate matrix phase (i.e., *Lfe*) crystallized during quenching to phosphoran olivine and Cl-apatite. However, the mechanism of phase separation is less clear. On one hand, the large glassy globules are consistent with phase separation through nucleation and growth of individual droplets (cf. Subsection 8.6.1; James, 1975; Shelby, 2005). In this case, immiscible droplets nucleate randomly upon unmixing from the conjugate matrix phase, continuously growing by a process called Ostwald ripening. Phase separation by nucleation and growth is restricted to a region between the binodal and the spinodal of a miscibility gap (for a discussion of the binodal and the spinodal, see Subsection 8.6.1; James, 1975; Shelby, 2005). Typical emulsion textures produced by nucleation and growth comprise spherical droplets of the dispersed phase randomly distributed in the matrix phase. On the other hand, the symplectitic texture formed by the phosphoran olivine and the interstitial *Lsi* is reminiscent of phase separation through spinodal decomposition (cf. Fig. 8.7; Subsection 8.6.1; James, 1975; Shelby, 2005), which ultimately results in an emulsion texture with high connectivity. Phase separation through spinodal decomposition will occur in that region of a miscibility gap that is defined by the spinodal. In that case, the dispersed phase will be regularly instead of randomly distributed in the matrix phase, forming tubes or continuous pathways. Hence, it is entirely possible that the sili-

cate inclusions in this impact melt rock document both mechanisms of phase separation in a miscibility gap.

9.5.4 Formation of the silicate inclusion

Based on their similar composition (cf. Van Roosbroek et al., 2016), the impact melt rocks of Netschaëvo were probably produced by shock melting and likely originated from the same parent material as the chondrule-bearing clasts. High temperatures must have been reached to melt a large part of the olivine. Large low-Ca pyroxene and olivine grains were preserved from melting, whereas small olivine and low-Ca pyroxene, together with calcic pyroxene, plagioclase, and phosphates, completely melted (cf. Van Roosbroek et al., 2016). At this stage the metal must also have been partially molten, as evidenced by the presence of quench features in the metal host and the scalloped contact between the silicate inclusion and surrounding metal (cf. Van Roosbroek et al., 2016). Upon cooling of the metal–silicate assemblage, several events took place that probably occurred in the following order:

1. precipitation of olivine and pyroxene from the liquid;
2. phosphorus in liquid metal–sulfide is oxidized and re-partitions into the silicate melt;
3. silicate liquid immiscibility occurs, possibly due to high P_2O_5 contents; and
4. phosphoran olivine and Cl-apatite crystallize during a late quenching event from *Lfe*, whereas *Lsi* quenched to a glass.

In the following subsections, we place some quantitative constraints on these events.

Precipitation of olivine from the melt: estimation of temperature

Roeder and Emslie (1970) experimentally investigated olivine–liquid equilibria and presented a model to predict the temperature at which olivine will saturate in a liquid. This model is based on two important observations. The first is that the ratio

$$\frac{\left(X_{\mathrm{FeO}}^{\mathrm{Ol}}\right)\left(X_{\mathrm{MgO}}^{\mathrm{Liq}}\right)}{\left(X_{\mathrm{FeO}}^{\mathrm{Liq}}\right)\left(X_{\mathrm{MgO}}^{\mathrm{Ol}}\right)}$$

is nearly constant over a wide range of temperatures. The second observation is that the ratio

$$\frac{X_{\mathrm{MgO}}^{\mathrm{Ol}}}{X_{\mathrm{MgO}}^{\mathrm{Liq}}}$$

is highly temperature-dependent. Putirka (2005) recalibrated the model of Roeder and Emslie (1970), incorporating the effect of temperature, SiO_2, Na_2O, K_2O, and H_2O with the parameterizations:

$$\begin{aligned}\ln K_D(\mathrm{Mg}) = {} & \frac{-2.11(\pm 0.07) + 3063.2(\pm 87.4)}{T(^\circ\mathrm{C})} \\ & + 0.019(\pm 0.001)[\mathrm{SiO_2}]^{\mathrm{Liq}} \\ & + 0.080(\pm 0.002)[\mathrm{Na_2O} + \mathrm{K_2O}]^{\mathrm{Liq}}\end{aligned} \tag{9.1}$$

$$\begin{aligned}\ln K_D(\mathrm{Fe}) = {} & \frac{-3.25(\pm 0.09) + 2556.4(\pm 114.6)}{T(^\circ\mathrm{C})} \\ & + 0.028(\pm 0.002)[\mathrm{SiO_2}]^{\mathrm{Liq}} \\ & + 0.052(\pm 0.003)[\mathrm{Na_2O} + \mathrm{K_2O}]^{\mathrm{Liq}}\end{aligned} \tag{9.2}$$

and obtained an olivine saturation surface that was temperature-sensitive and independent of olivine-composition. This model is used here to find the temperature at which fine-grained olivines precipitate from the Netschaëvo quasi-basaltic liquid. The average composition of the fine-grained olivines ($Fa_{24.5 \pm 3.8}$; Van Roosbroek et al., 2016) and the average composition of the quasi-basaltic melt (Table 9.1) is used to reconstruct a Netschaëvo parental melt as a mixture of the observed 80% quasi-basaltic groundmass and 20% olivine crystals (i.e., in-situ crystallization of the quasi-basalt with an olivine component being removed from the melt). The quasi-basaltic melt is the most likely parental composition, because high phosphorus contents are only observed at the margins of the silicate inclusion, and phosphorus had not yet partitioned into the silicate melt by the time of fine-grained olivine precipitation (before separation of immiscible silicate melts). This is also based on the observation that there is no detectable P_2O_5 in the fine-grained olivine (i.e., it is not phosphoran olivine) and on the likely temperature range at which these immiscible melts formed (see Subsection 9.5.4). Based on this model, a temperature of 1350–1400 °C best reproduces the composition of the Netschaëvo parental melt. The best matching composition, calculated by the model, was then used to calculate $X^{\mathrm{Ol}}_{\mathrm{MgO}}$ and $X^{\mathrm{Ol}}_{\mathrm{FeO}}$. The calculated composition of olivine is 35.5 wt.% MgO and 21.1 wt.% FeO, which corresponds well to the composition of the fine-grained olivines (37.9 ± 3.1 wt.% MgO and 21.9 ± 2.9 wt.%; Van Roosbroek et al., 2016), indicating that the model is internally consistent. The calculated exchange coefficient K_D

$$K_D = \frac{X^{\mathrm{Liq}}_{\mathrm{Mg}} / X^{\mathrm{Ol}}_{\mathrm{Mg}}}{X^{\mathrm{Liq}}_{\mathrm{Fe^{2+}}} / X^{\mathrm{Ol}}_{\mathrm{Fe^{2+}}}} \tag{9.3}$$

from the model, using these olivine compositions and the composition of the best-matching melt, is 0.32, in good agreement with typical K_D values of 0.31–0.34 for experiments on similar meteoritic melts (e.g., experiments of Usui et al., 2015) and clearly in the general range of 0.17–0.45 for basaltic systems (e.g., Putirka, 2005). These calculations further indicate that

olivine precipitated in the Netschaëvo silicate inclusion in the relatively high temperature range of 1350–1400 °C.

Re-partitioning of phosphorus from the metal into the silicate phase

The silico-phosphate matrix material is concentrated in a 100-µm-wide rim at the edge of the silicate inclusion, close to the contact with the metal host. The area also contains small, SiO_2-rich globules spread in the fine-grained matrix and 10–100-µm-size Mg-chromite grains (Fig. 9.1). Based on the presence of Mg-chromite grains and the high amount of phosphorus in this region, resulting in the presence of phosphoran olivine and apatite, we can reasonably assume that phosphorus and chromium from the surrounding metal partitioned into the silicate melt. This is supported by:

1. the low amounts of Cr_2O_3 and P_2O_5 in the chondrule-bearing Netschaëvo silicates, representing the original material (0.59 wt.% and 0.54 wt.% in the bulk silicate, respectively; e.g., Olsen and Jarosewich, 1971);

2. the low concentration of P_2O_5 in the quasi-basaltic melt and the absence of chromite grains in the inner part of the silicate inclusion; and

3. the presence of elongated intergrowths in the metal host of the investigated Netschaëvo silicate inclusion (Van Roosbroek et al., 2016), consisting of a P-rich, a S-rich, and a FeNi phase.

These intergrowths are connected to the edge of the silicate inclusion (fig. 1b in Van Roosbroek et al., 2016), indicating that phosphorus was supplied to the silicate melt from the metal via these structures. A similar situation is present in olivine coronas on olivine grains in the Morristown and Emery mesosiderites. In these coronas, P and Cr are enriched and this can be explained by the diffusion of P and Cr from the metal (Ruzicka et al., 1994).

Several authors have investigated the metal–silicate partitioning of phosphorus (Newsom and Drake, 1983; Jana and Walker, 1997b; Jana and Walker, 1997a; Pak and Fruehan, 1986; Young et al., 1992). The most recent study by Righter et al. (2010) experimentally investigated the effect of temperature and melt composition on $D_P^{Met/Sil}$ and observed that $D_P^{Met/Sil}$ increases with increasing temperature and decreases with increasing polymerization of the melt. However, the findings of these studies are not easily applied quantitatively, because silicate and metal in Netschaëvo meet at a reaction zone, and clear zoning of olivine crystals in the silicate and the presence of discrete taenite crystals in the metal indicate a cooling and crystallization history. With cooling, the partitioning of phosphorus between metal and silicate changed, resulting locally in high P_2O_5 in silicate along reaction boundaries with the metal. This means that the

composition of the silicate melt, and thus the polymerization degree, cannot be used to deduce a $D_P^{Met/Sil}$ value. Righter et al. (2010) showed that $D_P^{Met/Sil}$ depends mainly on the composition of the silicate material and much less on the temperature. Although no $D_P^{Met/Sil}$ value can be defined for Netschaëvo, the process is probably similar to the process responsible for the precipitation of oxide phases (e.g., phosphates and chromites) in IIIAB iron meteorites (Olsen et al., 1999). During cooling and solidification of the metal, fractional crystallization takes place and taenite precipitates. Other elements are concentrated in the residual liquid, such as Na, Mg, K, Ca, Mn, P, Cr, (Olsen et al., 1999) and, importantly, O (Kracher, 1983). A large degree of taenite crystallization, or in another sense a low degree of partial melting, would yield a high concentration of O and P in the liquid metal. This concentration could also be explained by an unusual metal composition. The metal in Netschaëvo has a P concentration of 0.15 wt.% (Buchwald, 1975), which can be compared to the P concentration in other IIE metal (0.15, 0.7, 0.3, 0.47, and 0.38 wt.% for Weekeroo Station, Colomera, Kodaikanal, Elga, and Mont Dieu, respectively; Buchwald, 1975; Van Roosbroek et al., 2015. Therefore, the build-up of P and O can best be explained by fractional crystallization of the metal. With increasing oxygen fugacity, phosphorus can become oxidized. Initially, phosphorus preferentially resides in the molten metal, because $D_P^{Met/Sil}$ is high at high temperature (Schmitt et al., 1989; Chabot and Drake, 2000; Righter and Drake, 2000; Righter et al., 2010). However, during cooling, $D_P^{Met/Sil}$ decreases and phosphorus is expelled from the metal, partitioning into the silicate melt that is enclosed by the metallic liquid. The outer part of the silicate inclusion is enriched in P_2O_5, close to the contact with the metal host, while the inner part of the inclusion retains its quasi-basaltic composition. The presence of P_2O_5-rich rims on silicate inclusions and elongated intergrowths in the metal host consisting of a P-rich, a S-rich, and a FeNi phase (Van Roosbroek et al., 2016) indicates that the system might approximate a phosphide–phosphate redox buffer, that is, part-way through the oxidation reaction (cf. Olsen et al., 1999).

The same probably also happened for Cr, enriching the melt in Cr_2O_3, which can explain the presence of Mg-chromite grains in the silicate inclusion along the contact with the surrounding metal (Fig. 9.1). It should be noted that chromite is a very early-crystallizing phase in IIIAB irons and pallasites, while phosphates are late-crystallizing phases. However, the situation may not be directly comparable with Netschaëvo because of the more complex silicate mineralogy (including pyroxene) and the presence of more major-element components (e.g., Al_2O_3 and TiO_2) likely influencing relative phase stabilities and, hence, crystallization order or timing. In terrestrial systems, chromite can crystallize directly from Fe–S–O mattes, and at chromite saturation there may be several tenths of a percent each of Cr and O in the melt (e.g., Ulff-Møller, 1985; Ulff-Møller, 1998; Fonseca et al., 2008). The in situ generation of oxide, including phosphate, minerals from a low-degree melt of meteoritic iron therefore

appears possible; nevertheless the introduction of an *additional* oxidizing agent cannot yet be entirely ruled out.

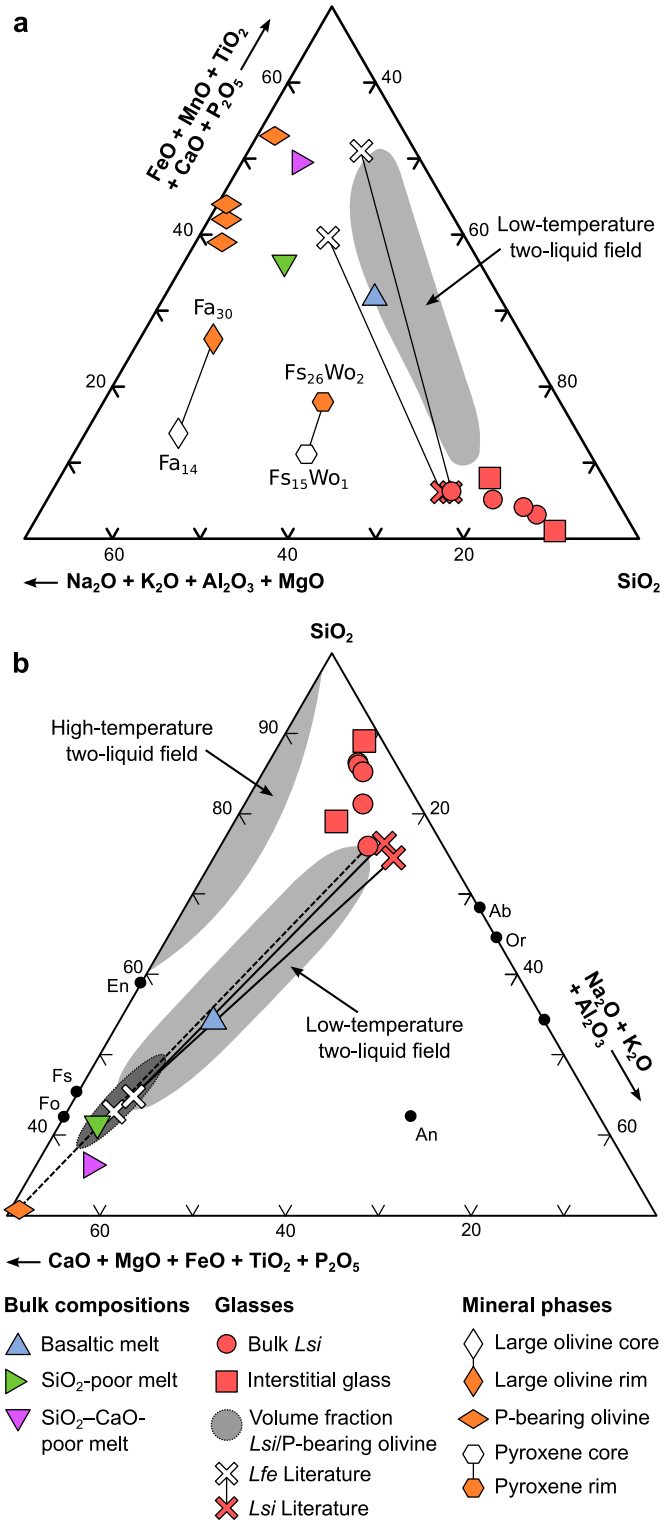

Figure 9.7 Liquid immiscibility in the Netschaëvo silicate inclusion. **a** Pseudo-ternary system (Na_2O + K_2O + Al_2O_3 + MgO)–(FeO + MnO–TiO_2 + CaO–P_2O_5)–SiO_2 after Philpotts (1982). **b** Pseudo-ternary system (CaO + MgO–FeO + TiO_2 + P_2O_5)–SiO_2–(Na_2O + K_2O + Al_2O_3) after Roedder (1978). Bulk melt composition is from Van Roosbroek et al. (2016), data of immiscible melts typically encountered in terrestrial volcanic rocks are from Philpotts (1982) and Sensarma and Palme (2013).

The effect of high phosphorus contents on silicate liquid structure

has been investigated by several authors (Toplis et al., 1994; Bogaerts and Schmidt, 2006; Charlier and Grove, 2012). High P_2O_5 in a silicate melt will form PO^{4-} complexes (Mysen and Richet, 2005) and, as a consequence, silicate polymerization increases, with a decrease in the number of non-bridging oxygens per tetrahedral cations (NBO/T). Higher polymerization results in a lower capacity to accommodate network-modifying cations (such as Ca^{2+}, Mg^{2+}, and Fe^{2+}). The PO^{4-} complexes fit poorly into the silicate network and the free energy of the system increases, consequently expanding the liquid–liquid miscibility gap (Bogaerts and Schmidt, 2006). This, together with the fact that addition of phosphorus into the silicate liquid lowers the liquidus temperature (Toplis et al., 1994), promotes unmixing (Charlier and Grove, 2012). Phosphorus is, thus, enriched in the poorly polymerized melt *Lfe*, whereas silica is enriched in the polymerized melt *Lsi*. The same holds for other network-modifying cations, such as Ca^{2+}, Mg^{2+}, and Fe^{2+}.

Formation of immiscible melts

As outlined above, partitioning of phosphorus from the host metal into the silicate melt most likely induced liquid–liquid phase separation of *Lfe* and *Lsi*. Constraining a temperature at which unmixing was induced is, however, difficult, since laboratory experiments aiming at confining two-liquid fields (e.g., Roedder, 1978; Bogaerts and Schmidt, 2006; Veksler et al., 2008, and references therein) for geologically relevant compositions are generally conducted under idealized equilibrium conditions. Attainment of chemical equilibrium is questionable for impact melts (cf. Chapter 7), mainly due to fast cooling rates and the short duration at which materials stay in the liquid state. However, when plotted in the pseudo-ternary system ($CaO–MgO–FeO–TiO_2–P_2O_5$)–SiO_2–($Na_2O–K_2O–Al_2O_3$), *Lsi* and the interstitial glass between phosphoran olivine crystallites fall close to *Lsi* encountered in the mesostasis of terrestrial basalts (Fig. 9.7; cf. Philpotts, 1982). Moreover, the bulk composition of the quasi-basaltic melt (Table 9.1) falls right within the low-temperature two-liquid field, and tie lines connecting individual *Lsi* analyses with analyses obtained from phosphoran olivine—which is presumed to have crystallized from the conjugate melt, *Lfe*—are more or less parallel to the low-temperature two-liquid field (Fig. 9.7b). Furthermore, if we calculate a theoretical bulk composition of the assemblage phosphoran olivine + *Lsi* by means of calculating the volume fraction of both phases from HAADF images with the program ImageJ, we find that this (theoretical) bulk composition also falls within, or close to, the low-temperature two-liquid field. Thus, unmixing was most likely due to low-temperature liquid immiscibility, yet it remains questionable whether the textures described above show the result of *stable* or *metastable* unmixing. Stable unmixing in laboratory experiments is usually recognized by the presence of large (>10 µm diameter) droplets of one liquid disseminated in the conjugate matrix liquid, whereas metastable unmixing (which is due to insufficient time for crystallization during quenching) results in minute, nm-sized

quench droplets (Hess, 1977; Freestone and Powell, 1983). As noted by Philpotts (2008) and demonstrated in Chapter 8 for impact melts, stable immiscible droplets tend to develop a second set of minute immiscible quench droplets. The silicate inclusions in Netschaëvo show *Lsi* droplets ≤1.5 µm that show a second set of quench droplets in their cores, quite similar to the *Lsi* phases known from impact melts from the Wabar, Saudi Arabia (Chapter 8; Hamann et al., 2013), and Kamil, Egypt (Chapter 8), impact craters. Hence, it has to be concluded that unmixing—whether stable or metastable—was due to low-temperature liquid immiscibility.

Constraining a temperature at which unmixing could have happened is not as straightforward as recognizing unmixing in the first place. Experimental data on the extent of the stable low-temperature two-liquid field constrain stable melt unmixing to temperatures between 1115 and 1230 °C in the system K_2O–FeO–Al_2O_3–SiO_2 (Roedder, 1978). Therefore we can cautiously define a temperature interval of ~1115 to ~1230 °C for final equilibration of the two melts before solidification of *Lsi* and crystallization of phosphoran olivine and Cl-apatite. This temperature range also provides a minimum temperature for the oxidation of P and Cr in the metallic melt, the redistribution of P and Cr between metal and silicate, and the unmixing of the liquids.

Formation of apatite and phosphoran olivine

Phosphoran olivine and Cl-apatite appear interwoven with each other, indicating they co-precipitated. The typical hopper morphology of the Cl-apatite crystals and the fact that the preservation of phosphoran olivine in the presence of a melt is limited to only a few weeks (Boesenberg and Hewins, 2010) indicates that these phases were formed during very rapid cooling and that the sample was not heated again after their formation. For phosphate saturation, Tollari et al. (2006) experimentally defined an equation to predict the P_2O_5 content of the coexisting silicate liquid:

$$M^{\mathrm{Liq}}_{\mathrm{P_2O_5}} = \exp\left[T\left(\frac{-0.8579}{139.0000 - M^{\mathrm{Liq}}_{\mathrm{SiO_2}}} + 0.0165\right) - 3.3333\ln\left(M^{\mathrm{Liq}}_{\mathrm{CaO}}\right)\right] \tag{9.4}$$

where M represents the molar percentage of the oxides and T is the temperature in K. Here, we want to deduce a temperature at which Cl-apatite saturated. As discussed previously, Cl-apatite probably precipitated from *Lfe*. Using the average concentration of SiO_2, CaO, and P_2O_5 measured in the SiO_2-poor silico-phosphate melt (Table 9.1), a temperature of 1150 °C is calculated. This means that quenching occurred near or below 1150 °C. This temperature is based on the average composition and was probably locally higher or lower, depending on the availability of SiO_2, CaO, and P_2O_5 in the melt.

9.6 Implications

One of the most important observations from this study is the high amount of phosphorus in the outer parts of the silicate inclusion, situated close to the metal host. This indicates that phosphorus, originally contained in the metal host of Netschaëvo, re-partitions into the silicate melt upon cooling. In other meteorite groups, such as the IIIAB irons, this process was responsible for the presence of oxide phases, formed as a consequence of oxygen build-up in the metallic liquid during cooling and fractional crystallization. In silicate-free irons, the lack of a lithophile component results in a peculiar Fe,Mn phosphate mineralogy with no phosphoran olivine (Olsen et al., 1999). In contrast, oxidation processes were responsible for the conspicuous mineralogies of the stony-iron pallasite achondrites (Boesenberg et al., 2012; McKibbin and Claeys, 2014; Fowler-Gerace and Tait, 2015; McKibbin et al., 2015; McKibbin et al., 2016), which consist mainly of olivine and metal and are thought to have formed by mixing of mantle and core material (e.g., Buseck, 1977). Like in Netschaëvo, phosphoran olivine is present in some pallasite meteorites, where it crystallized from a P_2O_5-rich silicate liquid (Boesenberg and Hewins, 2010).

Apart from phosphoran olivine, at least four primary (probably igneous or metamorphic) phosphate minerals are present in pallasites: merrillite $[Ca_{18}Na_2Mg_2(PO_4)_2]$, stanfieldite $[Ca_3Mg_3(PO_4)_4]$, farringtonite $[Mg_3(PO_4)_2]$, and a silico-phosphate (summarized in Boesenberg et al., 2012). These phosphates can be divided into two groups based on their REE pattern: one that has low REE concentrations and is enriched in HREE, and one that has high REE concentrations, is enriched in LREE, and has negative europium anomalies (Davis and Olsen, 1991). This probably indicates that two different processes were responsible for their formation, such as a near- or possibly slightly sub-solidus oxidation reaction for the first group, and formation from a melt for the second group (Boesenberg et al., 2012). It should, however, be noted that these magmatic processes are distinct from the far sub-solidus (~700 °C and below) kamacite–taenite exsolution and inferred slow cooling rates, which occurred after magmatic evolution ceased (Yang et al., 2010). The presence of these near-solidus crystallizing phases rich in phosphorus, present in pallasites (from more than one parent body: Davis and Olsen, 1991; Hutcheon and Olsen, 1991) and in this study, indicates that re-partitioning of phosphorus might be a general process in planetesimal core–mantle environments. Thus, the Netschaëvo sample might serve as a natural planetesimal core–mantle boundary experiment and can be used to constrain the temperature range over which phosphorus oxidation and re-partitioning takes place during planetesimal evolution.

In the previous sections, we have provided estimates for several processes taking place in the formation of Netschaëvo. It is clear that phosphorus re-partitioning must have taken place after the crystallization of olivine and before the formation of immiscible melts. From our temperature estimates, this takes place between ~1400–1350 °C and ~1230–1115 °C.

9.7 Summary and conclusions

The examined impact melt rock of Netschaëvo contains fine-grained matrix material of quasi-basaltic composition in the inner part of the inclusions, evolving towards a silico-phosphate matrix towards the contact with the metal host. A detailed nano-analytical investigation of the glassy silico-phosphate matrix material of Netschaëvo IIE by FIB-TEM shows that this material consists of phase-separated glass, phosphoran olivine, and quenched Cl-apatite. The presence of Si-rich amorphous globules containing finely-dispersed secondary droplets, as well as textures resembling emulsions formed by spinodal decomposition, indicate the action of silicate liquid immiscibility. Although this has been observed in several terrestrial impact melts, the investigated sample of Netschaëvo constitutes the first clear evidence of silicate liquid immiscibility in meteorites.

Several processes took place during cooling of the silicate–metal assemblage, probably occurring in the following order:

1. precipitation of olivine from the liquid;
2. re-partitioning of phosphorus from the metal into the silicate phase;
3. formation of immiscible melts; and
4. crystallization of phosphoran olivine and Cl-apatite in a late quenching event.

Re-partitioning of phosphorus from the metal into the silicate phase is a process that probably also took place in pallasite meteorites. These silicate–metal meteorites also contain several late-crystallizing, P-bearing phases and are formed in a core–mantle environment on several parent bodies, indicating that re-partitioning of phosphorus could be a general process in these environments. By means of the Netschaëvo sample, providing a natural planetesimal core–mantle boundary experiment, the temperature at which this process takes place is estimated. Based on temperature ranges defined for olivine precipitation and the formation of immiscible melts, oxidation of phosphorus and re-partitioning must have occurred between ~1400–1350 °C and ~1230–1115 °C.

Acknowledgments

We are grateful for the thorough reviews and constructive comments by Alan Rubin and an anonymous reviewer, who greatly helped to improve our manuscript. Moreover, we thank Chris Herd for editorial handling and the Natural History Museum of London for providing the sample of Netschaëvo (registration number: BM.33953). NVR and VD thank the FRS-FNRS for funding through an incentive grant. CH thanks the Barringer Family Fund for a student travel grant and the DFG for funding (MEMIN research unit FOR 887, grant He-2893/8-2). SMcK is a postdoctoral fellow of the Research Foundation Flanders (FWO). PhC thanks

the FWO (grants: G.A078.11 & G.0021.11). Skillful FIB preparation by Anja Schreiber (GFZ) is greatly acknowledged, and we thank Peter Czaja (MfN) for assistance at the electron microprobe. This research has partly been funded by the Interuniversity Attraction Poles Program "Planet Topers", initiated by the Belgian Science Policy Office.

Associate editor: Chris Herd

Chapter 10

Silicate melt–carbonate interaction: constraining impact metamorphism of carbonate-bearing target rocks[1]

Carbonates are abundant target components in one third of the presently known terrestrial impact strucures. Despite their abundance, it remains controversial whether carbonates shocked to pressures sufficient to melt coexisting silicates decompose into residual oxides (mainly CaO and MgO) and CO_2, or are preserved as primary carbonate impact melts. This chapter presents a novel experimental approach that uses direct laser irradiation to subject carbonate–silicate composite targets to *P*–*T* conditions typical of post-shock stages of hypervelocity impacts. It will be shown that, under these conditions, carbonate decomposition by coexisting silicate melt is extremely fast (tens of seconds), and results in contamination of silicate melt with carbonate-derived CaO and MgO and release of CO_2 at the silicate melt–carbonate interface. The experiments reproduce many textural, compositional, and mineralogical features of impact melts produced in carbonate-bearing terrestrial craters (Barringer, Haughton, West Clearwater Lake). These findings suggest that upon pressure release, *protracted* decomposition of carbonates by heat influx from coexisting silicate impact melt is the dominant process during impact melting of mixed silicate–carbonate targets. A combination of these findings, findings from previous studies, and consideration of the phase diagrams of calcite and quartz suggest, however, that carbonate impact melts are readily produced during adiabatic decompression; preservation of this primary melt phase depends on a complex variety of idiosyncratic factors. This chapter concludes with a working model that suggests that hypervelocity impacts into mixed silicate–carbonate targets may involve both melting *and* decomposition of carbonates.

Key points:

Experiments constrain that decomposition of carbonates (calcite, dolomite) by coexisting silicate melts is extremely fast (tens of seconds) and produces residual oxides (CaO and MgO) and CO_2 along the silicate melt–carbonate interface

Incorporation of residual oxides into silicate melt is probably diffusion-controlled and yields heavily Ca- or Ca,Mg-enriched silicate melts as well as a variety of Ca- or Ca,Mg-rich skarn minerals (e.g., Ca-rich olivine, wollastonite, melilite, spurrite, calcite, ferropericlase)

A working model is presented that suggests that impacts into mixed silicate–carbonate targets may involve both melting *and* decomposition of carbonates; preservation of primary carbonate impact melts depends on a complex variety of idiosyncratic factors

[1]This chapter was submitted on June 14, 2017 to *Meteoritics & Planetary Science* and was accepted on May 14, 2018 in revised form for publication as: Hamann, C., Bläsing, S., Hecht, L., Schäffer, S., Deutsch, A., Osterholz, J., and Lexow, B. (2018). The reaction of carbonates in contact with laser-generated, superheated silicate melts: constraining impact metamorphism of carbonate-bearing target rocks, *Meteoritics & Planetary Science* 53, 1644–1686.

Summary

This is the abstract of the submitted manuscript, but its title has been changed to "summary" in order to delimit it from the brief abstract given on the previous page. Moreover, some typos that were found to occur in the submitted manuscript have been edited and corrected.

We simulated entrainment of carbonates (calcite, dolomite) in silicate impact melts by 1-bar laser melting of silicate–carbonate composite targets, using sandstone, basalt, calcite marble, limestone, dolomite marble, and iron meteorite as starting materials. We demonstrate that carbonate assimilation by silicate melts of variable composition is extremely fast (seconds to minutes), resulting in contamination of silicate melt with carbonate-derived CaO and MgO and release of CO_2 at the carbonate–silicate interface. We identify several major processes: (1) thermal decomposition of carbonate releases CO_2 and produces residual oxides (CaO, MgO); (2) incorporation of residual oxides from proximally dissociating carbonate into silicate melt; (3) rapid back-reactions between residual CaO and CO_2 form equant calcite crystallites and porous carbonate quench products; (4) high-temperature reactions between Ca-contaminated silicate melt and carbonate yield typical skarn minerals and residual oxide melt; (5) mixing and mingling between Ca- or Ca,Mg-contaminated and unaffected silicate melts; (6) precipitation of Ca- or Ca,Mg-rich silicates in contaminated silicate melt upon quenching. Our experiments reproduce textural and compositional features of typical impact melts originating from silicate–carbonate targets. They reinforce hypotheses that thermal decomposition of carbonates, rapid back-reactions between decomposition products, and incorporation of residual oxides into silicate impact melts are the dominant processes during impact melting of mixed silicate–carbonate targets. However, by comparing our results with previous studies and thermodynamic considerations on the phase diagrams of calcite and quartz, we envisage that carbonate impact melt is readily produced during adiabatic decompression from high shock pressure, but, as pressure returns to normal, subsequently decomposes due to heat influx from coexisting silicate impact melt. Under certain circumstances, post-shock conditions may favor production *and* conservation of carbonate impact melt. Thus, the response of carbonate–silicate targets to impact might involve melting *and* decomposition of carbonates, the dominant response being governed by a complex variety of factors.

10.1 Introduction

Carbonates such as calcite, $CaCO_3$, or dolomite, $CaMg(CO_3)_2$, are abundant in the solar system. They not only occur in sedimentary and magmatic rocks on Earth, but are also present on Mars (Ehlmann et al., 2008; Michalski and Niles, 2010), are envisaged to occur on Venus (Kargel et al., 1994), and are found in meteorites (Leuw et al., 2010). Owing to their abundance, they are, thus, possible target rocks involved in planetary impact events.

On Earth, carbonates are present in the target rocks of about one third of the presently 190 known impact structures (Osinski et al., 2008). Despite their abundance and in contrast to siliceous sedimentary or crystalline

targets, the reaction of carbonate-bearing targets to hypervelocity impact is not well understood (see review by Langenhorst and Deutsch, 2012). In particular, the question is whether carbonates released from high shock pressures will decompose and liberate CO_2 (e.g., Kieffer and Simonds, 1980; Boslough et al., 1982; O'Keefe and Ahrens, 1989; Pierazzo and Artemieva, 2012; Hörz et al., 2015, and references therein), or whether they will be preserved as recrystallized carbonate impact melts in impactites (e.g., Graup, 1999; Jones et al., 2000; Osinski and Spray, 2001; Osinski, 2003; Osinski et al., 2008; Osinski et al., 2015, and references therein). Answering this question is of general interest to planetary sciences, because impact-induced release of CO_2 from carbonates into planetary atmospheres can affect atmosphere composition, climate stability, and even the evolution of life (Alvarez et al., 1980; O'Keefe and Ahrens, 1989; Pierazzo et al., 1998; Brugger et al., 2017). Quantification of shock-released CO_2 from carbonates, especially following the mass extinction at the Cretaceous–Paleogene (K–Pg) boundary (e.g., Alvarez et al., 1980; Hildebrand et al., 1991; Smit, 1999; Schulte et al., 2010; Morgan et al., 2016), is still a highly topical and unresolved issue in planetary sciences. Although sulfate aerosols possibly have had a dominant role in changing the Earth's climate across the K–Pg boundary (Pierazzo et al., 1998; Brugger et al., 2017), detailed knowledge of the total amount of CO_2 released into the atmosphere following Chicxulub is mandatory for modeling Earth's atmosphere and impact-induced climate changes at the end of the Cretaceous (Brugger et al., 2017).

The study of the response of carbonates to high shock stresses has progressed along three axes:

1. *impact* and *shock reverberation experiments* with carbonates (Vizgirda and Ahrens, 1982; Lange and Ahrens, 1986; Tyburczy and Ahrens, 1986; Martinez et al., 1995; Gupta et al., 2000; Agrinier et al., 2001; Langenhorst, 2002; Skála et al., 2002; Kurosawa et al., 2012; Bell, 2016);

2. *petrologic studies* of impactites from terrestrial impact structures (Martinez et al., 1994; Graup, 1999; Osinski and Spray, 2001; Osinski et al., 2008; Hörz et al., 2015; Osinski et al., 2015); and

3. *numerical modeling* (Pierazzo et al., 1998; Ivanov and Deutsch, 2002).

So far, experiments with carbonates yielded contrasting results, illustrated in particular by disagreeing estimates for the shock pressure threshold that governs the onset of calcite decomposition (see summaries in Osinski et al., 2008; Bell, 2016). Although different experimental techniques were used, these pressure estimates range from as low as some 20 GPa (e.g., Lange and Ahrens, 1986; Kurosawa et al., 2012) to as high as some 60 GPa (e.g., Bell, 2016). Such discrepancies are puzzling, but might simply arise from different experimental techniques (e.g., single shock vs. shock reverberation; Martinez et al., 1995), shock pulse durations, water

content and grain size of starting materials (Agrinier et al., 2001), CO_2 partial pressure during the experiments (Agrinier et al., 2001), or reaction kinetics (Ivanov and Deutsch, 2002). Consensus, however, exists on the *timing* of gas release: devolatilization of carbonates is strictly regarded as a post-shock effect triggered by residual heat, that is, occurring *after* passage of the rarefaction wave (see Agrinier et al., 2001; Ivanov and Deutsch, 2002).

Findings from terrestrial impact structures, such as Ries (Graup, 1999; Osinski, 2003; Stöffler et al., 2013), Haughton (Martinez et al., 1994; Osinski and Spray, 2001) or Barringer (Hörz et al., 2015; Osinski et al., 2015), are also contrasting. Direct evidence for decomposition of carbonates are, for example:

1. Ca,Mg-enriched silicate impact glasses related to the Barringer (Hörz et al., 2015), Haughton (Martinez et al., 1994), and Chicxulub (Sigurdsson et al., 1991) impact structures;

2. the presence of periclase, MgO, and larnite, Ca_2SiO_4, in impactites from Haughton (Martinez et al., 1994); and

3. Ca-rich pyroxene ($Wo_{44–48}$) around carbonate clasts at Chicxulub (Deutsch and Langenhorst, 2007).

Contrary to these findings, the existence of carbonate impact melts has been postulated for Chicxulub (Jones et al., 2000), Ries (Graup, 1999; Osinski, 2003), Haughton (Osinski and Spray, 2001), Barringer (Osinski et al., 2015), Tenoumer (Pratesi et al., 2005), and Steinheim (Anders et al., 2011). The salient point of the studies advocating the presence of true carbonate impact melts is the existence of blebs, globules, and spheres of microcrystalline calcite intimately intermingled with silicate impact glasses. These textures have been interpreted as being formed by immiscibility between coexisting carbonate and silicate impact melts (Graup, 1999; Pratesi et al., 2005; Osinski et al., 2008), thus, seemingly documenting the existence of quenched, immiscible carbonate melts. Others (e.g., Hörz et al., 2015), however, argued that these textures may simply reflect post-impact, hydrothermal or evaporative alteration processes, such as the formation of caliche. In addition, a robust identification of primary carbonate melts in impactites may be complicated by in situ sequestration of CO_2 from decomposed carbonates, as released CO_2 rapidly reacts with initially produced, highly reactive CaO (Agrinier et al., 2001), forming new calcite that may be mistaken for calcite that crystallized from a true carbonate melt.

In analogy to shock experiments with silicates, previous experimental studies with carbonates were mainly concerned with establishing the peak pressure thresholds that govern devolatilization and melting of pure carbonates. The most recent study of that kind is from Bell (2016), who shocked single crystal calcite to pressures of up to 60.8 GPa (which is sufficient to completely melt silicate minerals such as quartz, olivine, or pyroxene; Ahrens and O'Keefe, 1972; Stöffler and Langenhorst, 1994),

but neither detected decomposition nor melting of the recovered calcite. While studies with pure materials are highly relevant to delimit the response of pure materials to elevated shock pressures, we argue that the fate of carbonates in natural impact scenarios is more complex, and intimately linked to the fate of coexisting silicates. For example, the (pre-impact) stratigraphic columns of most, if not all, carbonate-bearing terrestrial impact structures also contain silicates in the form of sedimentary, crystalline, or metamorphic strata (The Earth Impact Database; Osinski et al., 2008), prominent examples being the Barringer, Haughton, Tenoumer, Chicxulub, or Ries impact structures. Moreover, hypervelocity impacts typically produce melts that are intimate mixtures of all lithologies that resided in the crater's melt zone (Dressler and Reimold, 2001). As a consequence, carbonate melts at terrestrial impact structures seem to occur intimately associated with silicate melts (Hörz et al., 2015), yielding the typical emulsion-like melt textures that are ascribed to carbonate–silicate immiscibility (Graup, 1999; Osinski and Spray, 2001; Pratesi et al., 2005; Osinski et al., 2008). In contrast to monolithic silicate impact melts generated in quasi-monolithic silicate targets, for example, at Wabar (Hörz et al., 1989; Hamann et al., 2013), Kamil (Fazio et al., 2016), or Lonar (Kieffer et al., 1976b), no pure carbonate impact melt volumes are known or have been recognized so far. Thus, we envisage that entrainment of carbonates in superheated silicate impact melts or hot melt-bearing breccias during excavation and modification stages of crater formation will inevitably submit carbonates to low-P, high-T environments. Thus, we envisage that elevated temperatures (not pressures) of silicate impact melts or silicate clasts are the dominant factor governing the fate of such carbonate clasts in these environments. Indeed, dendritic crystals of Ca-rich pyroxene (Wo_{47}) surround round calcite crystals in impactites from Haughton have been ascribed to in situ reactions of calcite with silicate impact melt (Martinez et al., 1994). Similar reactions of carbonate clasts with silicates are documented in impactites from Chicxulub, were Ca-rich pyroxene ($Wo_{44–48}$) coronas (reaction fronts) developed around calcite fragments (Deutsch and Langenhorst, 2007), and from West Clearwater Lake, where thermally metamorphosed limestone xenoliths are associated with silicate impact melt (Rosa and Martin, 2010). These examples suggest that *protracted* decomposition and outgassing of carbonates entrained in superheated silicate impact melts or hot melt-bearing breccias could be a process that occurs on time scales much longer than the initial shock pulse (cf. Deutsch and Langenhorst, 2007).

Here, we hypothesize that the fates of carbonates and carbonate impact melts, if produced, are predominantly governed by post-shock cooling processes, especially when in coexistence with silicate impact melts or when entrained in melt-bearing breccias. In the context of the Multidisciplinary Experimental and Modeling Impact Research Network (MEMIN), we present an experimental study that uses direct, continuous-wave (CW) laser irradiation to melt silicate–carbonate composite targets. We aim at constraining the fate of calcite and dolomite entrained in superheated

silicate melts that are taken as impact melt analogs (see Chapter 7; Ebert et al., 2017). Thus, we explicitly give focus on post-shock stages of impact events, when pressure release and melting through residual heat are the dominant factors that govern the formation of impact melts.

10.2 Materials and methods

10.2.1 Laser melting experiments

We used a CW infrared fiber laser (IPG YLS 10000) with a wavelength of 1.07 µm at Fraunhofer Institute for High-Speed Dynamics, Freiburg, Germany, to irradiate silicate–carbonate composite targets following the rationale and experimental setup of Chapter 7. The CW laser emitted a power of 8 kW over a specified time of 2–6 s. The profile of the laser beam was close to a Gaussian distribution with a $1/e^2$ diameter of 5.9 mm on the target for all experiments. While the position of the laser beam was fixed, the target was moved vertically at a speed of 5 or 10 mm s^{-1}; that is, the targets were irradiated along lines on their surfaces. The average laser intensity within the $1/e^2$ diameter was 2.5×10^4 W cm^{-2} for all experiments and the laser–matter interaction zone was observed by several cameras, using the same instrumentation as detailed in Chapter 7. The instrumentation included time- and space-resolved surface temperature measurements with an infrared microbolometer that recorded with 50 frames per second and within a temperature interval of 373–2373 K. All experiments were conducted in the ambient atmosphere under a pressure of ~1 bar.

The experimental conditions are summarized in Table 10.1; exemplary video snapshots during the experiments are given in Fig. D.1 (Appendix D). Experiment 889 (Fig. D.1a) was performed with a layered target composed of an alternating sequence of sandstone layers and calcite marble layers; this experiment will be referred to as "sandstone–carbonate experiment". Experiments 891 and 892 (Fig. D.1b, c) were performed with basalt plates layered on top of a limestone (891) and a calcite marble (892) plate, respectively; these experiments will be referred to as "basalt–carbonate experiments". For experiment 893 (Fig. D.1d), a fine-grained, three-component powder mixture was prepared from representative hand specimen of the Campo del Cielo iron meteorite, dolomite marble, and sandstone. We will refer to experiment 893 as "iron meteorite–carbonate–sandstone experiment" or "powder experiment". The dolomite marble and the sandstone were comminuted using a jaw crusher and a swing mill, yielding powders with intentionally heterogeneous grain sizes between <100 µm and ~5 mm. From the iron meteorite, millimeter-size chips and pieces were produced using a metal rasp. The powder mixture was then prepared from 6.0 g Campo del Cielo, 18.0 g dolomite, and 6.0 g sandstone, homogenized using an agate mortar and pestle, and tightly filled into an aluminum cylinder (4 cm inner diameter, 2 cm depth) that was previously glued onto a glass plate. To secure the powder mixture during the experiment, a 2-mm-thick, 4-cm-diameter, circular sandstone cover plate was

Table 10.1 Experimental conditions of laser irradiation.

Experiment	Materials	Emitted power [kW]	Laser intensity [10^4 W/cm^2]	Irradiation time [s]	Traverse length [mm]	Movement speed of target [mm/s]	Estimated cooling rate [K/s]
889	Alternating sequence of sandstone and calcite marble plates	8	2.5	6	30	5	106
891	Basalt plate on top of limestone plate	8	2.5	6	30	5	44
892	Basalt plate on top of calcite marble plate	8	2.5	6	30	5	44
893	Powder target[a]	8	2.5	2	20	10	47

[a] 6 g Campo del Cielo iron meteorite, 18 g dolomite marble, and 6 g sandstone.

attached to the aluminum cylinder on top of the powder mixture (see Fig. D.1d). Laser irradiation of the powder was then facilitated through the sandstone cover plate (i.e., the laser vaporized/melted the sandstone plate immediately after start of laser irradiation).

10.2.2 Starting materials

The bulk chemical compositions of the starting materials are given in Table 10.2; individual mineral compositions are given in Table D.1. For the carbonate layers, we used Carrara marble from Italy (e.g., De Bresser et al., 2005) and Savonnières limestone from France (e.g., Roels et al., 2003); for the powder experiment we used a dolomite marble from the Fichtel Moutains, Germany (Hecht et al., 1999). The Carrara marble was used in experiments 889 (sandstone–carbonate target) and 892 (basalt–carbonate target). It is a holocrystalline, dense, calcite-dominated marble with equigranular fabric and calcite grain sizes between 100 and 300 μm, a porosity of ~0.1 vol.%, and an arithmetic mean grain size of ~150 μm. It is generally homogeneous in composition and grain size, except for fine-grained dolomite veins that occasionally pervade the material and locally reduce the grain size to ~50 μm. Accessory minerals are pyrite, fluorite, apatite, and albite with grain sizes ≤20 μm. The Savonnières limestone was used in experiment 891 (basalt–carbonate target). It is a calcareous oolite with oval, ~0.5-mm-diameter ooids in a fine-grained, crystalline matrix of calcite. The Savonnières has an average porosity of ~30 vol.% and a heterogeneous microtexture. Often, calcareous bivalve shell fragments some millimeters in size are disseminated in the material and the ooids are primarily matrix-supported. The dolomite marble was used in experiment 893 (iron meteorite–carbonate–sandstone target) and is described in Hecht et al. (1999). It is a calcite-bearing dolomite marble of fine-grained, polygonal texture and predominantly composed of dolomite grains of 0.1 to 1 mm size and of calcite grains of 1 to 4 mm size. Calcite typically shows more irregular grain boundaries than dolomite and usually

Table 10.2 Bulk chemical compositions of the starting materials.

[wt.%]	Carrara marble†	Savonnières limestone*	Dolomite marble[a]	Seeberger sandstone[b]	Hoffelder basalt†	[wt.%]	Campo del Cielo[c]
SiO_2	0.13(5)	bdl	1.05	94.77(90)	43.50(30)	Fe	92.6
TiO_2	bdl	bdl	0.01	0.36(4)	2.36(1)	Ni	6.62
Al_2O_3	0.03(2)	bdl	bdl	3.11(10)	14.78(38)	Co	0.43
FeO_t	0.02(1)	0.36(10)	0.18	0.45(9)	12.38(28)	P	0.25
MnO	bdl	bdl	0.017	bdl	0.18(1)	Total	99.9
MgO	0.87(20)	0.60(10)	19.2	0.12(2)	10.65(45)		
CaO	55.55(95)	55.61(10)	35.6	0.05(1)	9.78(5)		
Na_2O	bdl	bdl	bdl	0.15(5)	3.69(4)		
K_2O	bdl	bdl	0.03	0.23(1)	1.53(2)		
P_2O_5	0.01(1)	0.02(2)	0.03	0.03(1)	0.49(1)		
LOI	43.95(5)	43.80(20)	42.4	1.29(30)	0.76(12)		
Total	100.6	100.4	98.5	100.6	100.1		

All data are given in wt.% and reported with 2σ in parentheses; total iron (FeO_t) is reported as FeO + Fe_2O_3.
bdl = below detection limit; LOI = loss on ignition.
† Data determined by ICP-AES.
* Data determined by XRF.
[a] Data from Hecht et al. (1999); original sample description: 12661-1.
[b] Data from Ebert et al. (2013).
[c] Data from Buchwald (1975).

contains fine-grained exsolutions of dolomite. The calcites in all three carbonates are relatively pure $CaCO_3$ with ~0.8 wt.% MgO on average, whereas the dolomite in the dolomite marble and the accessory dolomite grains in the Carrara are stoichiometric $CaMg(CO_3)_2$.

For the silicate layers and the powder mixture, we used Seeberger sandstone—this sandstone was also used in previous MEMIN impact and shock recovery experiments (Ebert et al., 2013; Kowitz et al., 2013b; Poelchau et al., 2013)—as well as Hoffelder basalt from Hoffeld, Germany. The sandstone was used in experiments 889 (sandstone–carbonate target) and 893 (iron meteorite–carbonate–sandstone target). It is a well-sorted, porous, quartz-dominated sandstone with an average grain size of 100 ± 25 µm and a porosity of 23.1 ± 0.5 vol.%. It consists of ~89 vol.% quartz, ~10 vol.% phyllosilicates (kaolinite ± muscovite ± illite; Ebert et al., in press), and ~1 vol.% accessory minerals (rutile ± altered ilmenite ± zircon ± iron oxides/hydroxides). The basalt was used in experiments 891 and 892 (basalt–carbonate targets). It is a dense, aphanitic, holocrystalline, porphyritic, ultramafic rock with olivine phenocrysts ($Fo_{79\pm4}$) in a fine-grained matrix of plagioclase (labradorite, $An_{62}Ab_{36}Or_2$), pyroxene (salite, $En_{39\pm3}Fs_{13\pm1}Wo_{49\pm2}$), Fe,Ti oxides (ulvöspinel and rare ilmenite), and feldspathoids. The olivine phenocrysts show sizes between ~200 and ~800 µm, whereas the matrix shows grain sizes ≤100 µm. On a TAS diagram (Le Bas et al., 1986), the bulk composition of the "basalt" plots close to the limit between the fields of tephrite and basanite.

10.2.3 Analytical techniques

The bulk chemical compositions of the Carrara marble and the Hoffelder basalt were determined prior to the experiments at ALS Geochemistry, North Vancouver, Canada, by using inductively coupled plasma atomic emission spectroscopy (ICP-AES) on lithium borate fusions of representative samples. The bulk chemical composition of the Savonnières limestone was determined at Museum für Naturkunde (MfN), Berlin, Germany, by using X-ray fluorescence spectrometry (XRF) and similar sample preparation and analysis procedures as outlined in Chapter 5 and Appendix A. The detection limits for major element analysis by ICP-AES and XRF are on the order of 0.01 wt.% and the analytical range for the oxides given in Table 10.2 is about 0.01–100 wt.% (see Appendix A).

Immediately after the experiments, the irradiated targets were investigated under the binocular microscope to identify and designate specific surface areas of interest for subsequent scanning electron microscopy (SEM) characterization. Petrographic surface analysis via SEM employed MfN's JEOL JSM-6610LV scanning electron microscope that is equipped with a LaB_6 cathode and a Bruker XFlash 5010 silicon drift detector for energy-dispersive X-ray spectroscopy (EDX). Back-scattered electron (BSE) and secondary electron (SE) imaging as well as semi-quantitative phase characterization with EDX were performed using the "low vacuum" mode of the SEM, 15 kV acceleration voltage, and variable beam currents. Subsequently, the irradiated targets were molded in epoxy and cut to dimensions that allowed for thin-section manufacture. Polished thin sections (either perpendicular or parallel to the laser tracks) were prepared and investigated at MfN by using a combination of optical and electron microscopy, electron microprobe analysis, and Raman spectroscopy. Prior to applying the more specialized methods (see below), we investigated the sections in transmitted light using a Leica petrographic microscope.

Raman spectra were collected at MfN by using a confocal Horiba LabRAM HR800 Raman microscope (600 lines per millimeter grating, lateral resolution ≤0.5 µm, axial resolution ≤1.2 µm) and different laser excitation wavelengths (473, 633, and 784 nm) on thin sections free of carbon coating. Calibration of the spectrometer was done prior to each measurement session using the most prominent mode of silicon at 520.7 cm^{-1}. The acquired spectra were compared against reference spectra taken from the RRUFF database (www.rruff.info) and against natural mineral standards provided by MfN's mineralogical collection.

Analytical scanning electron microscopy was performed on carbon-coated samples, using MfN's JEOL JSM-6610LV SEM and similar analytical conditions as described above but using the "high vacuum" mode of the instrument. To correct for the effects of carbon coating in quantification of EDX spectra acquired from carbonates or carbonate decomposition products, we used the correction routine provided by the Bruker Esprit 2.0 software. Specifically, we used the coating-induced carbon K_α peak in spectra obtained from silicate minerals present in the samples that we assumed to be free of carbon (e.g., quartz, plagioclase, olivine, or pyrox-

ene) to correct the carbon content of measured spectra obtained from the carbonate phases.

After initial reconnaissance analysis with EDX, electron microprobe analysis (EMPA) of glasses, mineral phases, and carbonate decomposition products was done with MfN's JEOL JXA-8500F field-emission electron microprobe. The microprobe is equipped with a Schottky field-emission cathode, five wavelength-dispersive X-ray spectrometers, and a Bruker XFlash 6|10 energy-dispersive X-ray spectrometer. Quantitative major and minor element abundances were determined by point analyses that were obtained against Smithsonian microbeam standards (Jarosewich et al., 1980) with wavelength-dispersive X-ray spectroscopy (WDX). Compositional EMPA was done using 15 kV acceleration voltage and 10–15 nA beam current. In order to minimize loss of sodium and electron beam-induced decomposition of carbonates during analysis, we used a defocused electron beam (2–20 µm diameter, depending on dimension and composition of the analyzed phase) as often as possible. Electron microprobe WDX raw data were processed and corrected for matrix effects using the ZAF routine provided by the JEOL operating program. Precision and accuracy of the WDX measurements were constantly monitored by measuring the composition of specific Smithsonian glass and minerals standards (Jarosewich et al., 1980) several times before, during, and after each analysis session. Typically, precision was much better than 1% for all analyzed elements; accuracy was better than 5% for elements with concentrations above 1 wt.% and better than 10% for elements with concentrations below 1 wt.%. Due to the small dimensions of most mineral phases, defocusing of the electron beam was not always possible. Care was taken to visually recognize damaging of the glasses and carbonates due to electron bombardment by inspecting BSE and/or SE images before and after WDX measurements; affected analyses were abandoned. Moreover, the highly vesicular nature of the carbonate decomposition products (see Section 10.3) made a robust quantitative phase analysis via EMPA difficult and resulted in mixed analyses between the spongy decomposition products and the infiltrated epoxy resin. To overcome these issues, we used X-ray maps to semi-quantitatively determine the composition of the spongy carbonate decomposition products. To this end, we collected high-magnification K_α X-ray maps with 2000 × 1500 pixels and, depending on magnification, theoretical pixel sizes as small as 60 nm via EDX by using MfN's JEOL JXA-8500F field-emission electron microprobe. The X-ray maps were acquired with 15 kV, 15 nA, and a fully focused electron beam (spot size <1 µm). To minimize beam damage during acquisition of the maps, dwell times of 16 µs were used and the total acquisition time was held between 2 and 5 hours. The resultant maps were interpolated and quantified by using the Bruker Esprit 2.0 software, and the color contrast was usually adjusted to best show the elemental distribution patterns. EDX spectra of phases of interest were then produced from the maps by integrating a sufficient number of individual

pixel spectra, and we used the carbon correction routine described above to account for the excess carbon induced by the carbon coating.

10.3 Results

10.3.1 Petrographic overview of the experimental products

Representative macroscopic characteristics of the samples after laser irradiation are illustrated in Fig. 10.1; typical sections taken parallel to the extent of the laser tracks are illustrated in Fig. 10.2. Direct laser irradiation of the mixed silicate–carbonate targets yielded melts that were either ejected in the form of melt droplets or resided in the form of coherent melt tubes, or melt pools, in, at, and around the irradiation traverses (Figs. 10.1, 10.2, and D.1). In some experiments (891, 892, and 893), tubes of melt formed in the irradiation traverses that eventually separated cm-size, spherical melt globes that dripped onto the specimen stage (Figs. D.1b–c and 10.2e and cf. Chapter 7). All melts quenched to holohyaline or hyaline glasses of variable color, ranging from transparent to blue to green to dark brown to black in reflected light (Figs. 10.1 and 10.2) and from transparent to tan to dark brown in transmitted light (Fig. 10.2c, d). Newly grown mineral phases were generally too small to be reliably identified under the polarizing microscope.

Using the readings from the infrared microbolometer (see Chapter 7), we measured the surface temperatures and, hence, approximate cooling rates of the melts during the experiments. The average cooling rates for the most typical melt volumes of each experiment are given in Table 10.1. The measured cooling profiles generally follow power laws with negative exponents. As we only measured surface temperatures, the cooling rates can be regarded as maximum estimates (see discussion in Chapter 7). All melts had initial temperatures >2373 K, which is the upper temperature limit of the infrared microbolometer. Typical melt volumes of experiment 889 quenched within ~7 s from >2373 to ~773 K ($dT/dt \approx -300\,K\,s^{-1}$) and then within additional ~10 s to ~573 K ($dT/dt \approx -20\,K\,s^{-1}$); the average cooling rate from >2373 to 573 K (i.e., presumably below glass transition) was about $106\,K\,s^{-1}$. Quenching from >2373 to ~1273 K of typical melt volumes in the experiments 891 and 892 took ~11 s ($dT/dt \approx -100\,K\,s^{-1}$) and subsequent quenching from 1273 to ~573 K took additional ~30 s ($dT/dt \approx -23\,K\,s^{-1}$); the average cooling rate from >2373 to 573 K was about $44\,K\,s^{-1}$. Typical melt volumes of experiment 893 quenched within ~10 s from >2373 to ~1350 K ($dT/dt \approx -200\,K\,s^{-1}$) and within another ~10 s from ~1350 to ~1000 K ($dT/dt \approx -30\,K\,s^{-1}$). Subsequent quenching to ~700 K took additional ~20 s ($dT/dt \approx -15\,K\,s^{-1}$); the average cooling rate from >2373 to ~700 K was about $47\,K\,s^{-1}$.

Notwithstanding differences in melt compositions and microtextures, the experiments with the layered targets (889, 891, and 892) yielded qualitatively similar features. Silicate glasses (representing melts) were found to volumetrically dominate the melt zones in all three experiments—this

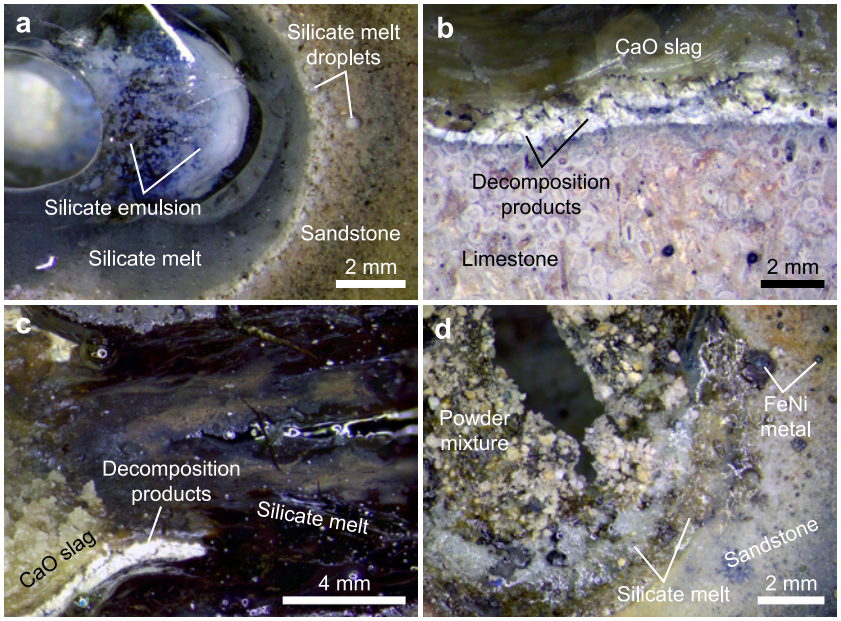

Figure 10.1 Representative reflected light photomicrographs of the laser-irradiated targets prior to thin-sectioning. **a** Silicate melt and silicate melt droplets (now quenched to glasses) resting on top of the sandstone plate of experiment 889 (sandstone–carbonate target). The milky white to blue color of the glass indicates emulsification. **b** Thermal decomposition of limestone in experiment 891 (basalt–carbonate target) resulted in formation of white decomposition products and, eventually, in lustrous-green CaO slag. **c** Transition zone between the molten basalt layer (right) and the limestone layer (left) of experiment 891. **d** Excavated powder mixture and silicate melt resting on top of the sandstone cover plate of experiment 893 (iron meteorite–carbonate–sandstone target). Note the presence of FeNi metal droplets that splashed onto the cover plate.

is not surprising given the fact that we used silicates for the upper layers. Incipient melting of the silicate layers generally started at the outer margins of the melt tracks (Fig. 10.2a) and is identical to laser melting of pure sandstone and basalt described in Chapter 7 and Ebert et al. (2017), which is, thus, not detailed here. Briefly, melting usually starts along grain boundaries and then proceeds to the interior parts of individual crystals, forming micrometer-thin, sub-parallel melt veins that pervade the material. Generally, melting starts with those components that have the lowest melting points (either the phyllosilicates in case of the sandstone or plagioclase/feldspathoids in case of the basalt) and the zone in which incipient grain-boundary melting dominates is some 0.5 to 1 mm in (apparent) diameter. Incipient melting successively but rapidly grades into wholesale melting and mixing of all components as the laser power reaches its full intensity, forming well-homogenized, occasionally schlieren-rich melts that tend to mimic the bulk composition of the silicate starting material.

The response of the carbonate layers to direct laser irradiation was in stark contrast to laser-induced melting of the silicate layers and will be detailed in Subsection 10.3.2. In the experiments with the layered targets, a zone of texturally complex, friable carbonate decomposition

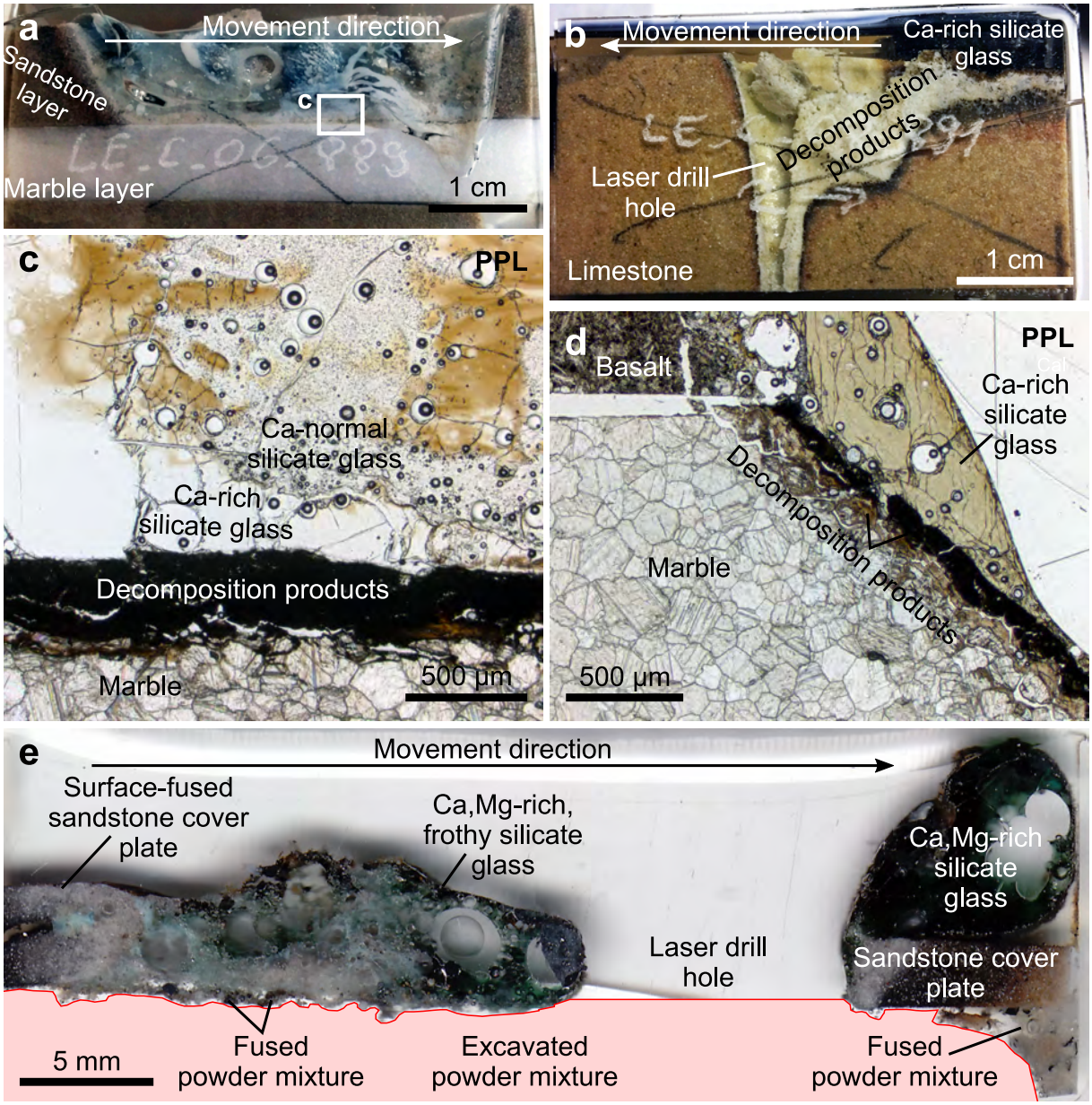

Figure 10.2 Representative photomicrographs in reflected light (a, b, e) and transmitted light (c, d) of the laser-irradiated targets after sectioning. **a** Cross section through laser traverse of experiment 889 (sandstone–carbonate target). The target moved from left to right; irradiation direction was perpendicular to movement direction. The laser melted the sandstone layer and also penetrated the marble layer towards the end of the traverse, forming a melt that quenched to a transparent to blue glass with milky white schlieren (cf. Fig. 10.1a). **b** Cross section through one end of the laser traverse of experiment 891 (basalt–carbonate target). The target moved from right to left; irradiation direction was perpendicular to movement direction. The laser melted the basalt layer and also penetrated the limestone layer at the end of the traverse. The white material in the limestone layer is CaO slag resulting from laser-induced carbonate decomposition (cf. Fig. 10.1b). **c** and **d** Typical interfaces between Ca-rich silicate glasses and carbonate layers in the experiments with layered targets (plane-polarized light). Note that calcite decomposition products separate the carbonate layers from the silicate glasses. **e** Cross section through the laser traverse of experiment 893 (iron meteorite–carbonate–sandstone target). The target moved from left to right; irradiation direction was perpendicular to movement direction. The laser surface-fused the sandstone cover plate at the start of the traverse and eventually penetrated the powder mixture. The red area corresponds to the original position of the powder mixture, which was subsequently either excavated by the laser or lost during thin-sectioning.

products always separates silicate glasses from carbonates (Fig. 10.2b–d). The silicate glasses were never observed coexisting with or wetting the surfaces of pristine calcite crystals—rather, carbonate decomposition products invariably separate pristine calcite crystals from silicate glass. Due to the different experimental setup, a similar zone is usually missing in the powder experiment (893)—here, relict dolomite and calcite mineral clasts showing variable degrees of decomposition are usually, but not exclusively, enclosed by silicate glass. Furthermore, we detected texturally complex, recrystallized carbonate-rich inclusions with fluidal shapes in the silicate glasses of the basalt–carbonate experiments (891 and 892) that are missing in the sandstone–carbonate experiment (889) or the powder experiment (893).

10.3.2 Thermal decomposition of calcite

To characterize the response of calcite affected by direct laser irradiation, we applied SEM methods immediately after performing the experiments with the layered targets in hope that residual and highly reactive CaO (cf. Agrinier et al., 2001) might still be detectable, if produced. Calcite grains that were affected by direct laser irradiation, for example at the ends of the laser traverses of the basalt–carbonate experiments 891 and 892 (Fig. 10.2b), as well as those grains that are in contact to the silicate glasses (e.g., Fig. 10.2c, d), exhibit textures indicative of thermal decomposition. Direct laser irradiation of the carbonate layers resulted in successive but ultimately complete thermal decomposition of calcite, following the reaction

$$CaCO_3 \rightarrow CaO + CO_2 \qquad \text{(R 10.1)}$$

in which calcite decomposes into residual, highly reactive CaO and gaseous CO_2. Figure 10.3 illustrates laser-induced thermal breakdown of the limestone layer at the outermost end of the laser traverse of experiment 891 (cf. Figs. D.1b, 10.1b, and 10.2b). Moving along the decarbonation zone (from left to right in Fig. 10.3a), we observe first intact calcite, then calcite grains start to show increasing BSE brightness and Ca contents as well as decreasing O and C contents, and finally we observe a smooth, in BSE images bright and in reflected light lustrous green CaO slag that shows compositions consistent with lime. Both texture (smooth, melt-like material and individual melt droplets) and composition (almost pure CaO) of the slag suggest that the laser induced temperatures in excess of ~2900 K, which is the temperature at which a mixture of solid CaO and gaseous CO_2 is transformed into a mixture of liquid CaO and gaseous CO_2 (Ivanov and Deutsch, 2002).

Utilizing BSE imaging (Fig. 10.4) and transmitted light microscopy (Fig. 10.5), it appears that calcite decomposition involves several stages. Incipient decomposition is often indicated by the appearance of micrometer-size vesicles in grains that are otherwise intact (Fig. 10.4a). Advanced decomposition of calcite results in grains that show local disaggregation

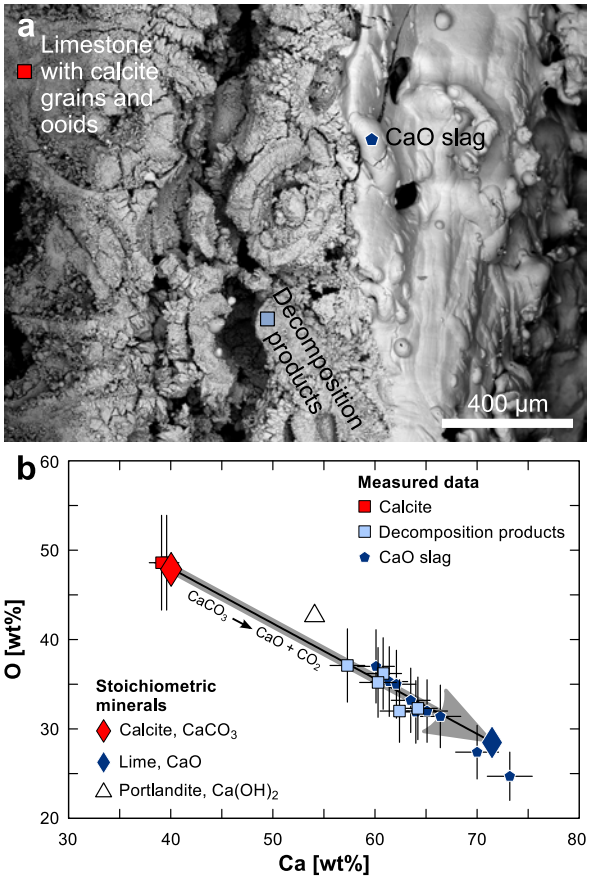

Figure 10.3 Thermal decomposition of calcite by direct laser irradiation. **a** Typical BSE image of successive thermal decomposition of calcite in experiment 891, eventually forming CaO slag (cf. Fig. 10.1b). Note the presence of melt droplets and the gradual increase in BSE brightness from left to right, reflecting increasing Ca and decreasing O and C contents, respectively, due to the decomposition reaction (R 10.1). The symbols in the BSE image (examples of analytical spots) refer to the symbols used in (b). **b** O vs. Ca concentrations of intact calcite and decomposition products compared against stoichiometric minerals (calcite, lime, and portlandite). Data were obtained from non-carbon-coated samples prior to sectioning via SEM-EDX (see Subsection 10.2.3).

features like fading grain boundaries (Fig. 10.4b) or highly vesiculated rims (Fig. 10.4a). Typical calcite decomposition products are optically isotropic (Fig. 10.5b, d), texturally complex, ultrafine-grained assemblages of several phases that are too small in dimension to be reliably analyzed by electron microprobe techniques (e.g., Fig.10.4b, c). The calcite decomposition products observed in this study are qualitatively similar to decarbonation textures known from seismic thrust faults formed in carbonate-rich rocks (Collettini et al., 2013; Collettini et al., 2014; Carpenter et al., 2015), or from thermal breakdown of calcite in carbonate-bearing raw materials used for the production of ceramics (Cultrone et al., 2001; Tschegg et al., 2009). Specifically, we detected 1-µm-diameter, remnant or newly formed calcite crystallites disseminated in ultrafine-grained or even amorphous matrices (Fig. 10.4b, c; Table 10.3). Often tube-like dark grey objects of submicrometer size as well as microvesicles surrounded by bright-white rims in the matrices were observed in BSE images (Fig. 10.4c). Moreover, volumetrically large decomposition zones that have retained the outlines of original calcite grain boundaries, including ~120° triple junctions (Fig. 10.4d), can be observed.

Apart from thermal decomposition of calcite induced by direct laser irradiation, we observed similar calcite decomposition products in those parts of the carbonate layers that are in direct contact to the silicate glasses (Figs. 10.5 and 10.6). Although in immediate vicinity of decomposed

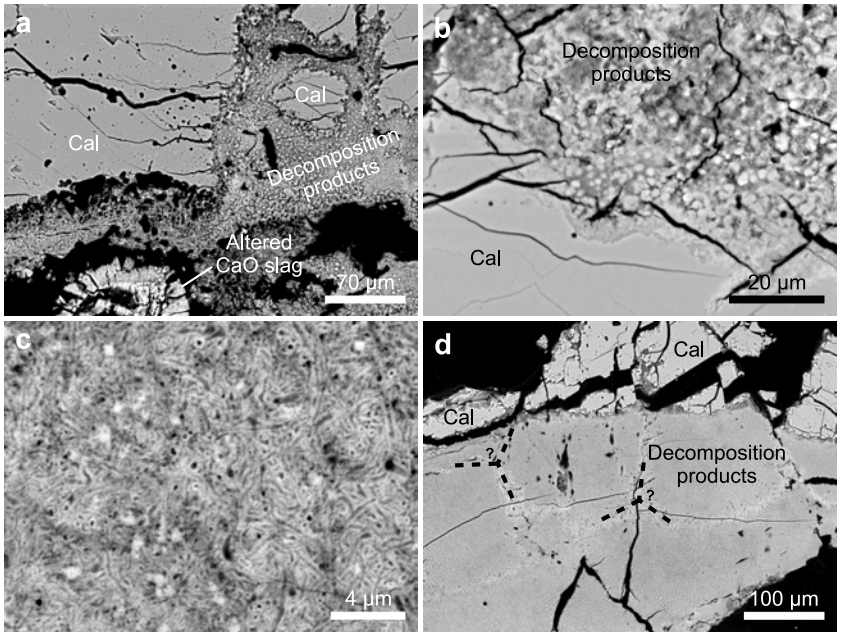

Figure 10.4 Representative BSE images of thermal decomposition of calcite in experiments 889 (sandstone–carbonate target) and 892 (basalt–carbonate target). **a** Incipient decomposition of calcite starts with the appearance of vesicles in otherwise intact grains (see calcite grain in upper left corner) and proceeds with the formation of spongy, texturally complex decomposition products. Eventually, complete devolatilization of calcite results in the formation of CaO slag (now altered; see droplet in lower left corner and cf. Fig. 10.3). **b** and **c** Close-up view of calcite decomposition products. **d** Homogeneous calcite decomposition products with possible remnants of grain-boundary triple junctions (stippled lines). Abbreviation: Cal = calcite.

calcite, the silicate glasses were never observed coexisting with or wetting the surfaces of pristine calcite crystals. Rather, a layer of calcite decomposition products similar to those described above and of variable apparent dimension (between ~10 µm and ~0.5 mm; e.g., Figs. 10.5a, e and 10.6a, b) separates calcite crystals from silicate glass. We did not detect any residual CaO in the vicinity of decomposed calcite grains that are close to the silicate glasses—as will be detailed in Subsection 10.3.4, residual CaO was incorporated into the silicate melts, yielding highly Ca-enriched melts and, depending on the composition of the silicate layer, quench crystals of Ca- or Ca,Mg-rich silicates. Remnant calcite grains in the decomposition zones usually have subround to lobate, often curved boundaries (e.g., Fig. 10.5c, d), and their interior parts are usually intact, birefringent, and generally recognizable as calcite. Twinning of the remnant calcite grains resembles twinning of the calcite grains prior to the experiments. Thus, we exclude that these grains represent calcite that formed from rapid back reactions between CaO and CO_2 (cf. Agrinier et al., 2001) or even calcite that precipitated from a melt (cf. Jones et al., 2000). However, we did observe small, submicrometer- to micrometer-size, idiomorphic calcite crystallites in the decomposition products (Fig. 10.6b, c) that are interpreted as the products of rapid and likely in situ back reactions of residual

CaO and not yet discharged, gaseous CO_2, as envisaged by Agrinier et al. (2001).

Raman spectra obtained from the calcite decomposition products (Fig. 10.7) show high background intensities and considerably reduced peak intensities compared to unreacted calcite in direct vicinity or to calcite grains prior to the experiments. Nevertheless, the spectra obtained from the calcite decomposition products can still be recognized as calcite. Some but not all of the spectra also show weak peaks at 252 and 356 cm^{-1} that are consistent with Raman bands of portlandite, $Ca(OH)_2$, which possibly formed by inevitable back reactions between highly reactive, residual CaO and H_2O from the ambient atmosphere, following the reaction

$$CaO + H_2O \rightarrow Ca(OH)_2 \qquad (R\,10.2)$$

at some time after the experiments (cf. Schmid and Dariz, 2015). Unfortunately, CaO does not possess any first-order Raman-active modes (Schmid and Dariz, 2015); hence, Raman spectroscopy is not suited to detect residual, solid CaO among decomposition products. Moreover, the spectra usually show a faint, broad hump around 1300 cm^{-1} that possibly reflects amorphous carbon. However, it is not clear where this carbon signal originates from: is it from the epoxy resin that infiltrated the pores of the material (cf. Figs. 10.4 and 10.6), or does it reflect an actual carbon (maybe graphite?) component in the material? Transmission electron microscopy techniques are required to further document the tiny decomposition products in full detail.

10.3.3 Thermal decomposition of dolomite

Thermal decomposition of dolomite is apparent in the experimental products of the iron meteorite–carbonate–sandstone powder experiment (893). Here, relict dolomite grains of variable degrees of decomposition occur frequently entrained in Ca,Mg-rich silicate glass (Figs. 10.8 and 10.9f). Compared to thermal decomposition of calcite, thermal decomposition of dolomite is more complex. Incipient or incomplete (or both) decomposition of dolomite as illustrated in Fig. 10.8a yields relict, subround to irregular dolomite grains that are surrounded by porous to spongy to even frothy decomposition products similar in appearance to those formed from calcite decomposition. In BSE images, the dolomite decomposition products show a slightly darker signal compared to the unreacted dolomite. Both the relict dolomite grains as well as the decomposition products are invariably cut by subparallel to rectangular oriented fractures (Fig. 10.8a) that are often filled with Ca-rich silicate glass (Fig. 10.8c, d).

Complete decomposition of dolomite due to heat influx from surrounding silicate melts is illustrated in Fig. 10.10c–f, in which typical BSE images are shown together with the corresponding composite X-ray maps of Si, Ca, Mg, and Fe. Decomposition of dolomite ultimately yields residual MgO (dark to light blue in the X-ray maps of Fig. 10.10d, f) that occurs

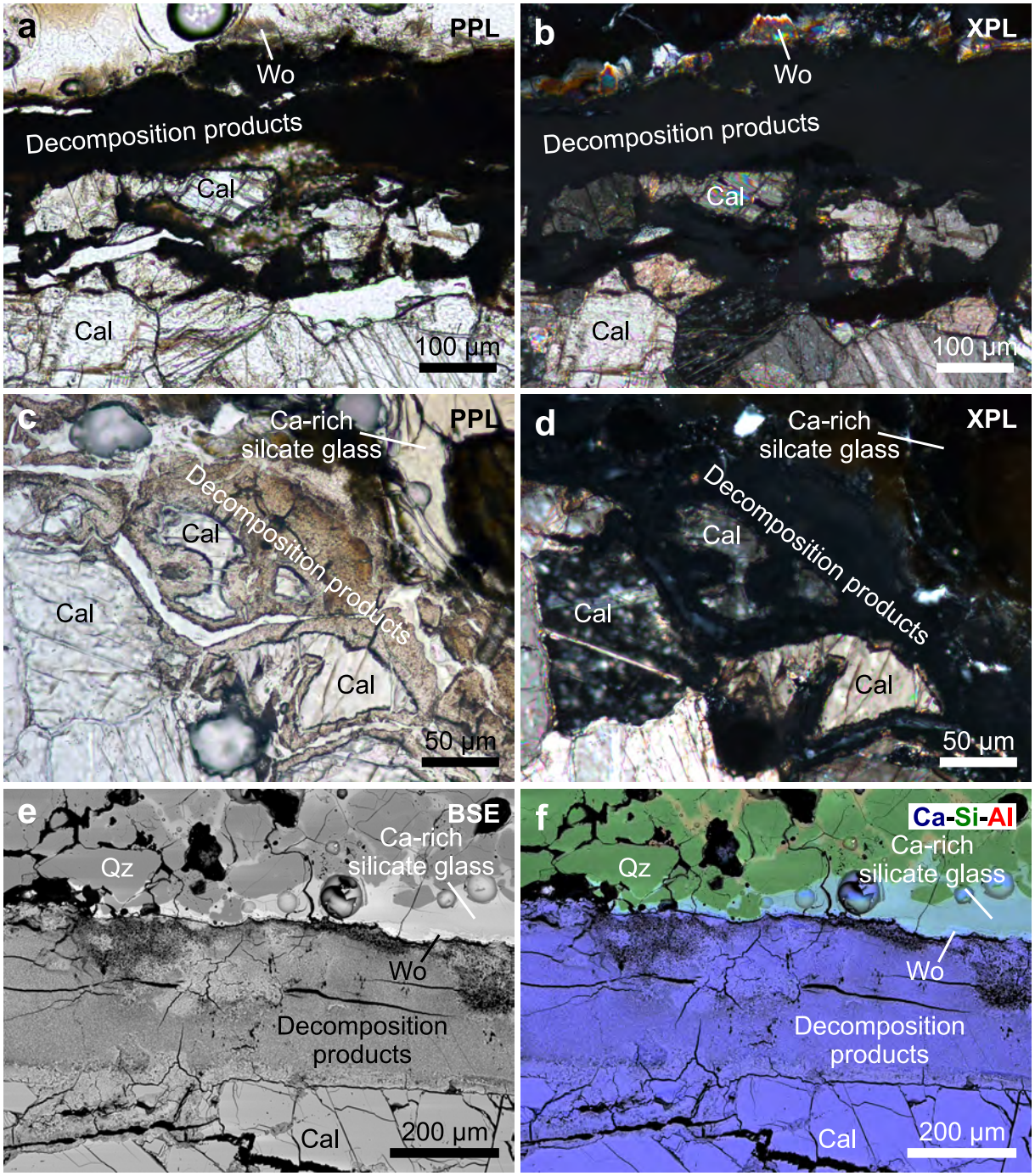

Figure 10.5 Thermal decomposition of calcite in contact to silicate melts. (a, c) Plane-polarized light; (b, d) cross-polarized light; (e) BSE image; (f) X-ray elemental distribution maps of Ca (blue), Si (green), and Al (red) superimposed onto the corresponding BSE image. **a** and **b** Partially decomposed, remnant calcite grains in optically isotropic decomposition products; experiment 889 (sandstone–carbonate target). Note the presence of feathery quench crystallites of pseudowollastonite in the Ca-rich silicate melt. **c** and **d** Partially decomposed, remnant calcite grains in optically isotropic decomposition products; experiment 892 (basalt–carbonate target). Typically, partial decomposition of calcite results in irregularly shaped, still birefringent, remnant grains that often show subrounded to lobate grain boundaries. **e** and **f** Incipient melting of the sandstone layer and thermal decomposition of the marble layer in experiment 889 yielded Ca-rich silicate melts that precipitated quench crystallites of pseudowollastonite at the carbonate–melt interface. Abbreviations: Cal = calcite; Qz = quartz; Wol = pseudowollastonite.

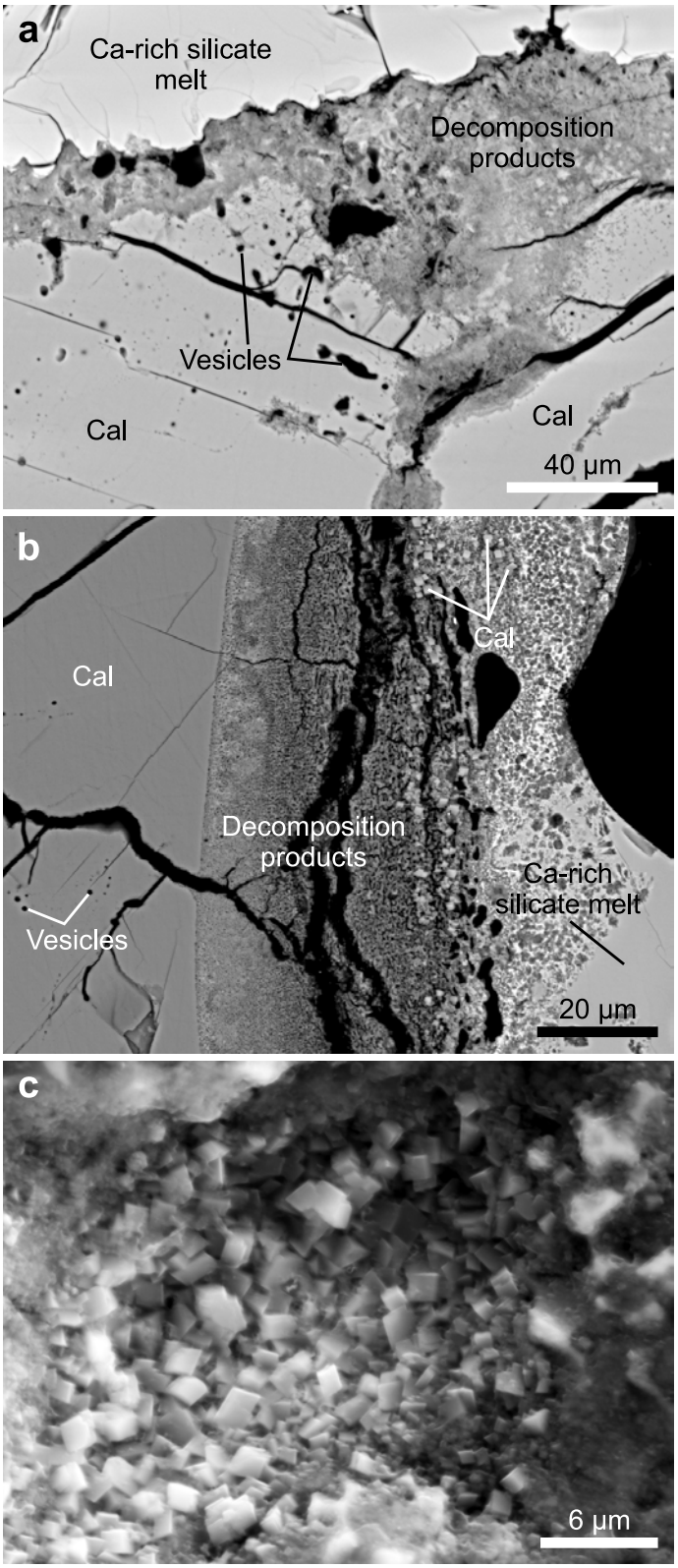

Figure 10.6 Representative BSE (**a** and **b**) and SE (**c**) images showing progressive thermal decomposition of calcite by heat influx from surrounding silicate melt. Note the presence of vesicles in the calcite grains in (a) and (b), and the submicrometer- to micrometer-size, idiomorphic calcite crystallites in (b) and (c) that were formed through rapid back reactions of residual CaO with CO_2 (cf. Agrinier et al., 2001). (a) Experiment 889 (sandstone–carbonate target); (b, c) experiment 892 (basalt–carbonate target). Abbreviation: Cal = calcite.

in the form of fine-grained (~1–3 µm size), spherical to subround particles that are either concentrated at the interfaces to the silicate melts (Fig. 10.10d) or disseminated in the silicate melts in the form of densely packed individual grains (Fig. 10.10f). The residual MgO seems to have incorporated variable amounts of FeO, yielding ferropericlase, (Mg, Fe)O, with variable Fe/Mg ratios that are illustrated in BSE images (Fig. 10.10e) and X-ray maps (Fig. 10.10f). Judging from such BSE images and X-ray maps, it seems that Mg-rich ferropericlase typically occurs close to the relict dolomite grain, whereas Fe-rich ferropericlase occurs further away in the silicate melt. It should be noted that typical EDX analyses contain limited amounts of CaO and SiO_2 that possibly represent contamination from surrounding silicate melt. Two representative analyses are: 61.1 wt.% MgO, 31.8 wt.% FeO, 5.0 wt.% CaO, and 1.4 wt.% SiO_2 (Mg-rich variety; light blue in Fig. 10.10f) and 37.0 wt.% MgO, 54.3 wt.% FeO, 4.5 wt.% SiO_2, and 3.4 wt.% CaO (Fe-rich variety; turquoise in Fig. 10.10f).

The remaining dolomite decomposition products are substantially enriched in MgO compared to pristine dolomite grains (34–48 wt.% vs. 21.86 wt.%) and slightly enriched in SiO_2 and FeO (both between 0.5 and 3.7 wt.%). The CaO concentrations of the decomposition products are highly variable (orange to purple colors in Fig. 10.10d, f) and range between 25 and 48 wt.% (pristine dolomite has 30.41 wt.% CaO). The dolomite decomposition products show high totals (between 66.8 and 94.7 wt.%) that indicate loss of CO_2, and CaO/MgO wt.% ratios of ~1.02 on average (individual values range between 0.68 and 1.22; pristine dolomite has a CaO/MgO ratio of 1.39). Hence, it appears that the solid residues of dolomite degassing are not 1:1 mixtures of pure CaO and MgO. This, in turn, suggests that thermal breakdown of dolomite could involve segregation of $CaCO_3$ and $MgCO_3$ (magnesite) that subsequently decompose individually and to possibly variable extent. Similar conclusions were reached by Agrinier et al. (2001).

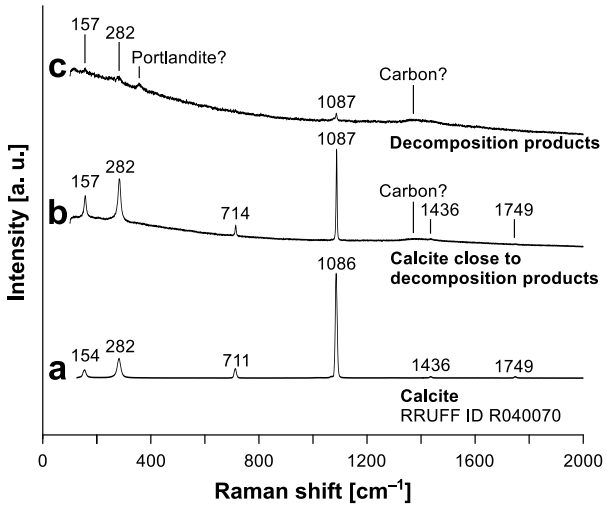

Figure 10.7 Representative Raman spectra obtained from intact calcite grains close to calcite decomposition products (**b**) and from calcite decomposition products (**c**), compared against a calcite reference spectrum from the RRUFF database (**a**). The measured spectra are given as recorded and without baseline correction.

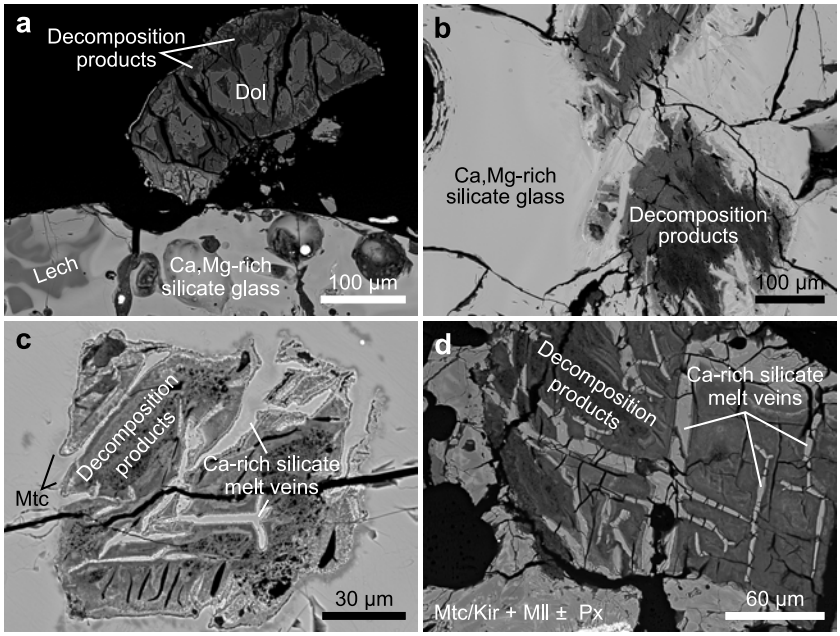

Figure 10.8 Representative BSE images of dolomite grains entrained in Ca,Mg-rich silicate glasses of experiment 893 (iron meteorite–carbonate–sandstone target). **a** Partly decomposed dolomite grain adjacent to Ca,Mg-rich silicate melt (now quenched to glass) showing intact interior parts and a rim of decomposition products. Note that large cracks pervade the decomposition products. **b** Dolomite decomposition products entrained in Ca,Mg-rich silicate melt. **c** Relict, severely decomposed dolomite grain entrained in Ca,Mg-rich silicate melt that locally precipitated ferroan monticellite. Ca-rich silicate melt veins frequently pervade the decomposition products. **d** Relict, severely decomposed dolomite grain entrained in Ca,Mg-rich silicate melt that crystallized to ferroan monticellite + magnesian kirschsteinite + melilite ± pyroxene. Abbreviations: Dol = dolomite; Kir = magnesian kirschsteinite; Lech = lechatelierite; Mll = melilite; Mtc = ferroan monticellite; Px = pyroxene.

10.3.4 Melting of the silicates and incorporation of carbonate-derived, residual oxides

As described in Subsection 10.3.1 and detailed in Chapter 7 and Ebert et al. (2017), laser-melting of pure sandstone and basalt in the parameter region considered in this study yields well-homogenized melts (see, e.g., upper left corner of Fig. 10.9c) that tend to mimic the bulk composition of the silicate starting material. However, like true impact melts (e.g., See et al., 1998), the laser-generated melts display on the micrometer scale compositional heterogeneity in the form of schlieren that arise from incomplete digestion of individual target components or from incomplete mixing of different monomineralic precursor melts (see, e.g., bottom left corner of Fig. 10.9c). Vesicles with diameters ranging from the submicrometer to the millimeter scale are widespread in the silicate glasses of all experiments. The most intensely vesiculated silicate melt was formed in the powder experiment (893), often but not exclusively yielding melt froths predominantly composed of vesicles bound together by thin, delicate glass stringers. We attribute these vesicles to the presence of an exsolved

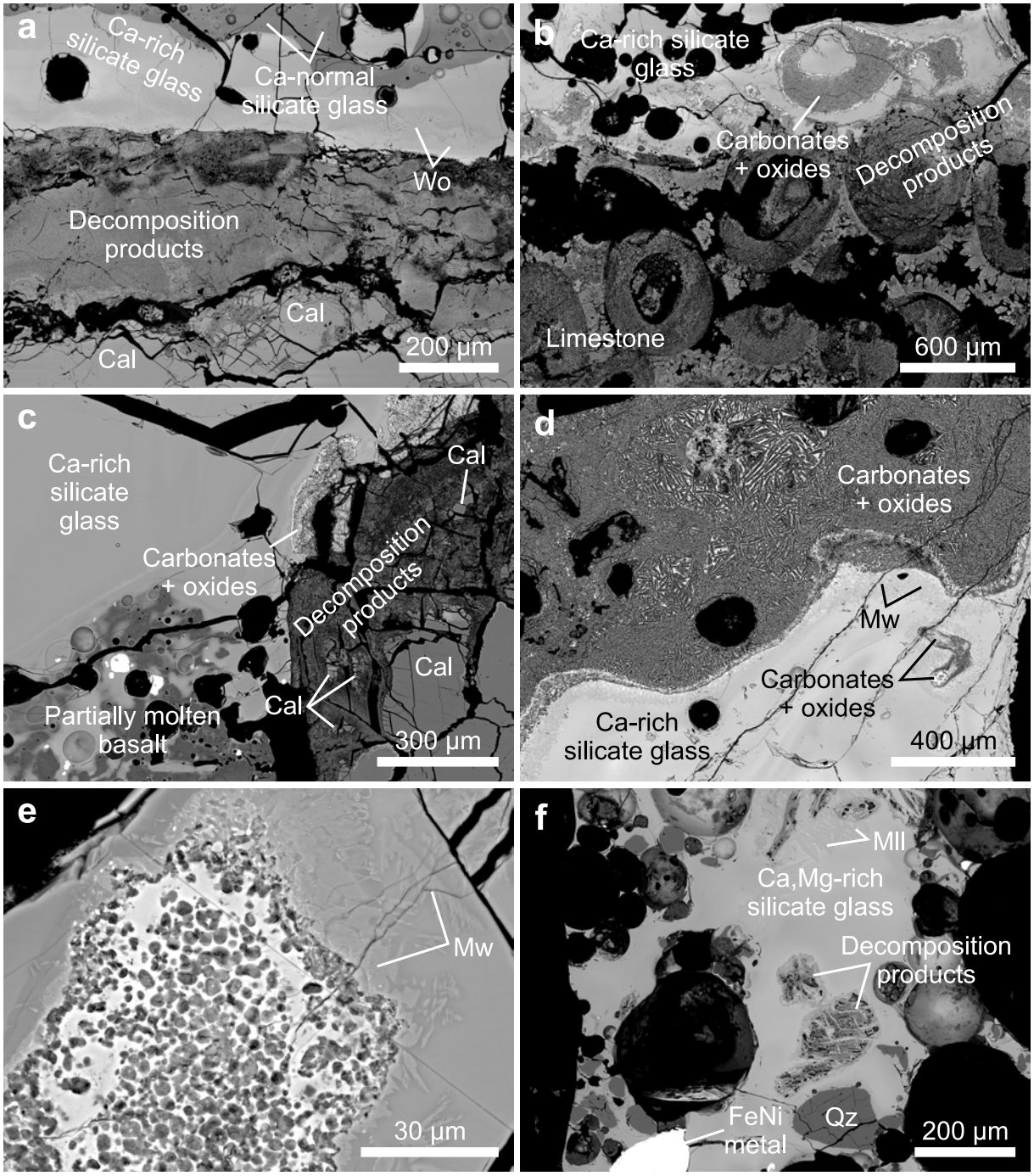

Figure 10.9 Representative BSE images of silicate glasses, carbonate decomposition products, and reaction zones. **a** Interface between calcite grains and silicate melt in experiment 889 (sandstone–carbonate target; cf. Figs. 10.2c and 10.5a, b, e, f). The strongly Ca-enriched silicate melt at the carbonate–melt interface precipitated quench crystallites of pseudowollastonite. Note the sharp meniscus between the Ca-rich and the Ca-normal silicate glasses. **b** Interface between calcite grains, ooids, and silicate melt in experiment 891. **c** Interface between calcite grains and silicate melt in experiment 891 (basalt–carbonate target). **d** Interface between Ca-rich silicate glass and quenched carbonate-rich material composed of spurrite + calcite + oxide quench phases; experiment 891. The carbonate-rich material is invariably surrounded by quench crystals of merwinite. Note the carbonate inclusion in the Ca-rich silicate glass at the lower right corner of the image. **e** Carbonate-rich inclusion, consisting of carbonate ocelli in oxide quench phases, admixed into Ca-rich silicate glass of experiment 892 (basalt–carbonate target). Merwinite crystallized in the Ca-rich silicate melt adjacent to the inclusion. **f** Dolomite decomposition products, relict quartz grains, vapor bubbles, and FeNi metal disseminated in Ca,Mg-rich silicate glass of experiment 893 (iron meteorite–carbonate–sandstone target). Abbreviations: Cal = calcite; Mll = melilite; Mw = merwinite; Qz = quartz; Wo = pseudowollastonite.

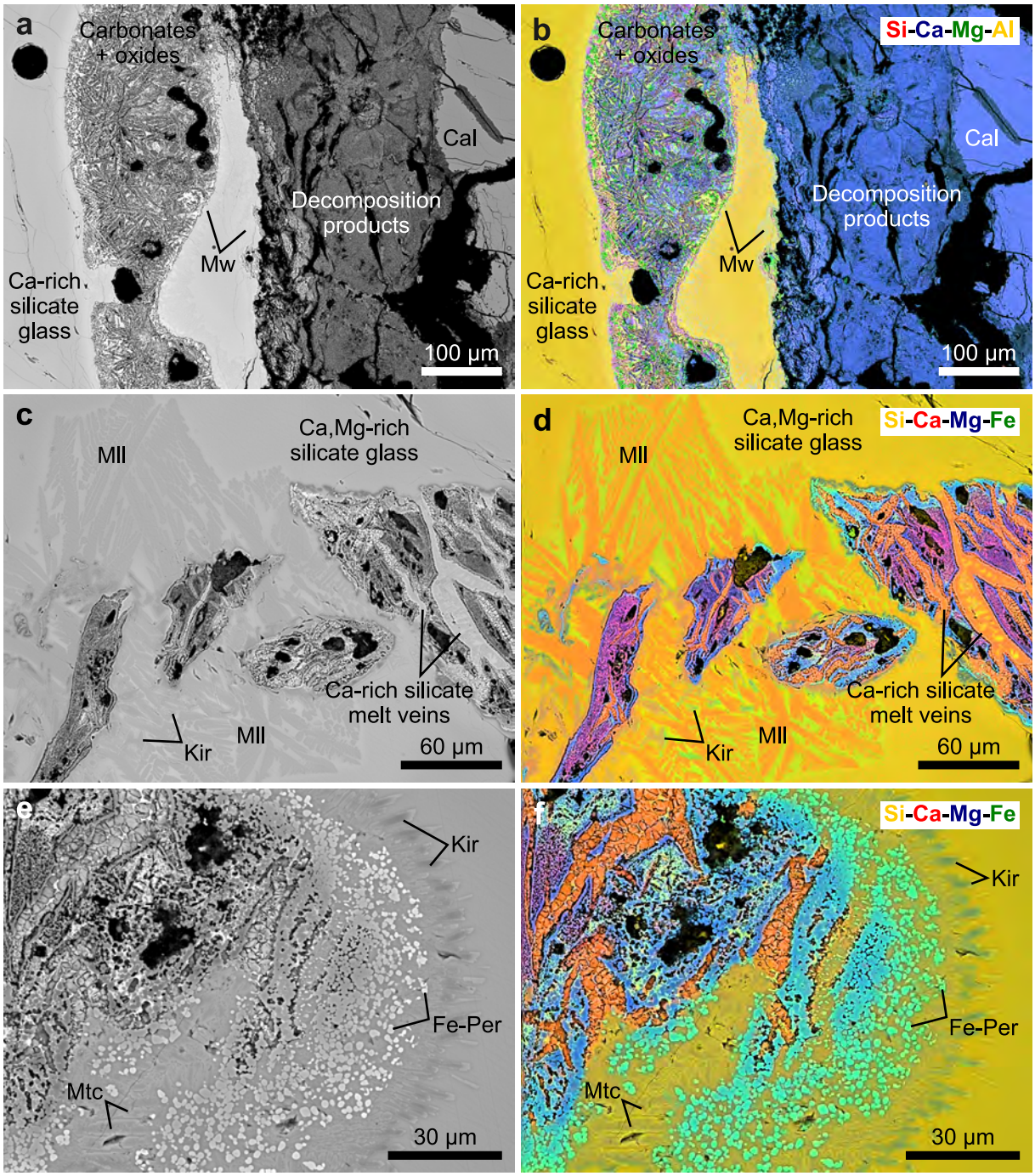

Figure 10.10 BSE images and corresponding X-ray maps of carbonate decomposition products, silicate melts (now quenched to glasses), and crystalline reaction products. **a** BSE image of Ca-rich silicate glass with fluidal-shaped inclusion of carbonates and oxide quench phases in contact to calcite in experiment 892 (basalt–carbonate target). **b** X-ray elemental distribution maps of Si (red), Ca (blue), Mg (green), and Al (yellow) superimposed onto the corresponding BSE image. **c** BSE image of relict dolomite grains in partially recrystallized, Ca,Mg-rich silicate glass of experiment 893 (iron meteorite–carbonate–sandstone target). **d** X-ray elemental distribution maps of Si (yellow), Ca (red), Mg (blue), and Fe (green) superimposed onto the corresponding BSE image. **e** BSE image of completely decomposed dolomite grain entrained in Ca,Mg-rich silicate glass of experiment 893. **f** X-ray elemental distribution maps of Si (yellow), Ca (red), Mg (blue), and Fe (green) superimposed onto the corresponding BSE image. Abbreviations: Cal = calcite; Fe-Per = ferropericlase; Kir = magnesian kirschsteinite; Mw = merwinite; Mll = melilite; Mtc = ferroan monticellite.

volatile phase (CO_2, but likely also H_2O in case of the basalt–carbonate experiments).

Owing to the fast cooling rates (Table 10.1), crystallization was largely restricted in the experiments with the layered targets (889, 891, and 892): with the exception of a thin layer of pseudowollastonite that crystallized at the interface between silicate melt and carbonates, the sandstone–carbonate experiment (889) yielded silicate glasses free of crystallites. The basalt–carbonate experiments (891 and 892) also yielded mostly silicate glasses, but crystallization of various phases in reaction zones between silicate melts and carbonates, as well as in (Figs. 10.9d, 10.10a, and 10.11b–e) and around (Figs. 10.9e, 10.11f, and 10.12c) carbonate-rich inclusions in the silicate melts is more pronounced than in experiment 889. In the iron meteorite–carbonate–sandstone experiment (893), the laser surface-fused the sandstone cover plate, but also penetrated through the cover plate into the powder mixture below (Fig. 10.2e), excavating a mixture of vapor, melt, and solid fragments. This experiment yielded silicate melts that contain spheres of FeNi metal (originating from the iron meteorite) as well as relict calcite, dolomite, and quartz fragments (originating from the dolomite and sandstone components, respectively). The silicate melts either quenched to holohyaline glasses mostly free of newly formed crystallites or precipitated a variety of crystalline phases.

As will be shown below, all silicate melts are, to variable degrees, enriched in Ca and in the case of the iron meteorite–carbonate–sandstone experiment also in Mg. Representative BSE images of the silicate glasses are given in Figs. 10.9–10.11; Figs. 10.13–10.16 and Table 10.4 summarize the glass compositions.

Silicate melts in the sandstone–carbonate experiment

The glasses of the sandstone–carbonate experiment (889) are mainly mixtures of SiO_2 and CaO with subordinate Al_2O_3 and TiO_2 (Fig. 10.13; Table 10.4) and are quite heterogeneous in terms of texture. They are highly variable in composition (56–97 wt.% SiO_2, 0.5–46 wt.% CaO, 0.1–7 wt.% Al_2O_3, and 0.1–1 wt.% TiO_2) and essentially range between Ca-normal and strongly Ca-enriched compared to the sandstone starting composition (Fig. 10.13a).

Most measured glass compositions fall onto a mixing line between the bulk composition of the sandstone and CaO (Fig. 10.13), indicating thorough mixing and homogenization of all sandstone components before admixture of carbonate-derived, residual CaO. At places where the sandstone components (mainly quartz and phyllosilicates) show incipient melting but not wholesale mixing (e.g., Figs. 10.5e, f and 10.12b), the glass is distinctly enriched in Al_2O_3, FeO, MgO, and K_2O, following mixing trends outlined in Ebert et al. (2013) and Ebert et al. (in press). Furthermore, the silicate glasses generally yield high EMPA-WDX totals ≥98.5 wt.% (averaging 99.5 wt.%), indicating that they are volatile-poor to essentially volatile-free.

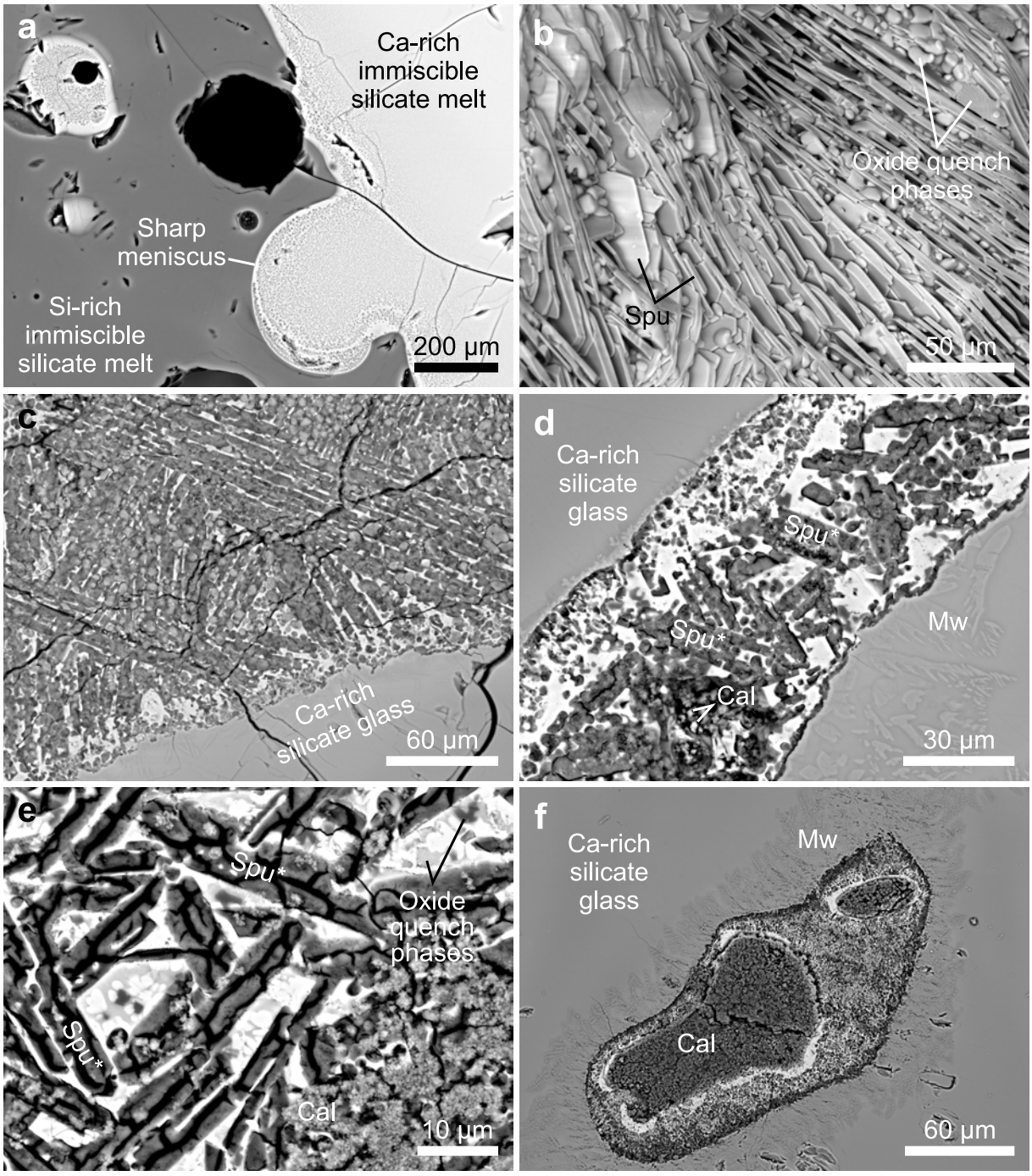

Figure 10.11 Representative BSE images of silicate glasses and reaction products of experiments 889 (a) and 891/892 (b–f). **a** Silicate emulsions in experiment 889 (sandstone–carbonate target), comprising immiscible Ca-rich (*Lca*) and Si-rich conjugate liquids (*Lsi*), separated by sharp meisci. **b** Platy spurrite quench crystals and residual oxide quench phases of experiment 891 (basalt–carbonate target) prior to thin-sectioning. **c** Spurrite quench crystals (medium grey) and oxide quench phases (white) next to Ca-rich silicate glass of experiment 892 (basalt–carbonate target). **d** and **e** Altered spurrite quench crystals (dark grey), calcite crystallites (light grey), and oxide quench phases (white and dark grey) in detail; experiments 891 and 892. **f** Sub-round inclusion of calcite and oxide quench phases (white) entrained in Ca-rich silicate glass of experiment 891 (cf. Fig. 10.12c). Note the occurrence of merwinite quench crystals around the carbonate-rich inclusion in (d) and (f). Abbreviations: Cal = calcite; Mw = merwinite; Spu = spurrite; Spu∗ = altered spurrite.

Silicate emulsions formed locally in the melt pool (Figs. 10.1a and 10.11a) and quenched to one glass rich in SiO_2 (~95 wt.%) and poor in CaO (~1 wt.%) and a second glass that contains less SiO_2 (~64 wt.%) and that is rich in CaO (~31 wt.%). Representative major element compositions of the two conjugate glasses are given in Table 10.4. The two glasses are generally separated by sharp menisci (Fig. 10.11a) and the Ca-rich glass (*Lca* for Ca-rich immiscible liquid) predominantly occurs as a distinct layer above the decomposed carbonate layer (Figs. 10.5e and 10.9a), but also exists in the form of spherical droplets of several tens of micrometers in diameter disseminated in the Si-rich, Ca-normal glass (*Lsi* for Si-rich immiscible liquid; Fig. 10.11a). Unmixing of the silicate melt was induced as the bulk composition of SiO_2 + CaO ± Al_2O_3 passed the high-temperature two-liquid field in the ternary system CaO–SiO_2–Al_2O_3 (Fig. 10.13b) upon quenching. The *Lca* phase often shows minute immiscible droplets of the *Lsi* phase that are interpreted as the result of metastable exsolution and equilibration upon quenching (see Chapter 8; cf. Freestone and Powell, 1983; Philpotts, 2008; Hamann et al., 2013). Notwithstanding differences in composition, these emulsions resemble silicate emulsions known from rapidly quenched impact glasses from the Wabar (Chapter 8; Hamann et al., 2013) and Kamil (Chapter 8; Fazio et al., 2016) impact structures, and from experimentally produced impact glasses (Chapter 8; Ebert et al., 2013; Ebert et al., 2014).

Silicate and possible carbonatite melts in the basalt–carbonate experiments

The silicate melts of the basalt–carbonate experiments (891 and 892) appear slightly more homogenized and texturally less heterogeneous compared to the sandstone–carbonate experiment. They mainly quenched to glasses, but also precipitated quench crystals of merwinite along carbonate–silicate melt interfaces. The glasses are highly variable in terms of major element composition (Figs. 10.14 and 10.15; Table 10.4), ranging, as in the sandstone–carbonate experiment, between Ca-normal and highly Ca-enriched compared to the basaltic starting composition. Electron microprobe analysis reveals that the silicate glasses range between 32–54 wt.% SiO_2, 0.3–4 wt.% TiO_2, 4–27 wt.% Al_2O_3, 2–13 wt.% FeO, 1–11 wt.% MgO, 6–43 wt.% CaO, 1–7 wt.% Na_2O, ~0.4–7 wt.% K_2O, and up to ~2 wt.% P_2O_5. Moreover, EMPA-WDX totals are generally above 98.4 wt.% (averaging 99.8 wt.%), indicating that the silicate glasses of these experiments are also volatile-poor to essentially volatile-free.

Two different compositional mixing trends are apparent from Figs. 10.14 and 10.15:

1. melting of the basalt produced monomineralic precursor melts that eventually mixed and homogenized (see Fig. 10.9c), producing a range of melt compositions that can be explained without the addition of carbonate-derived, residual CaO; and

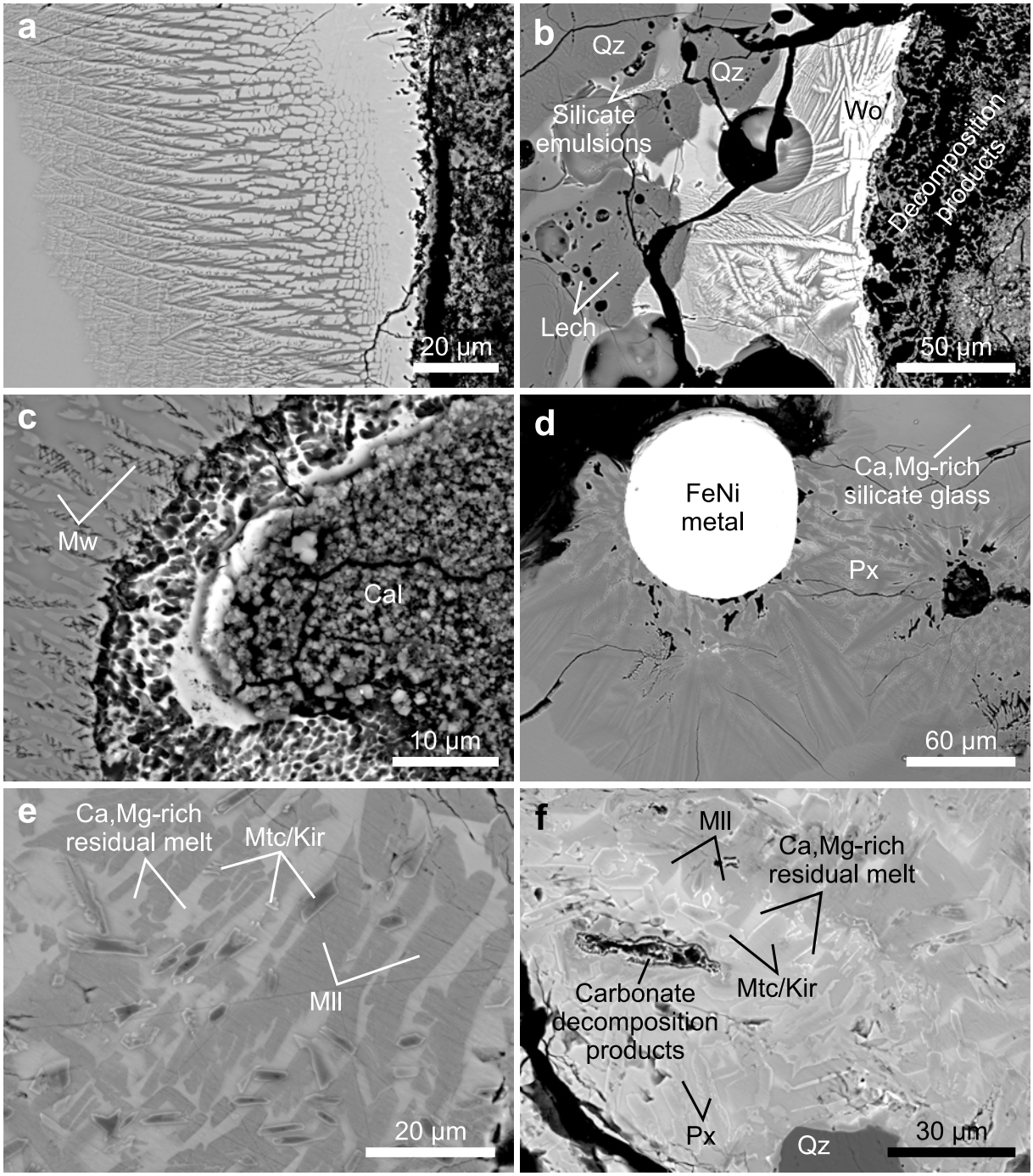

Figure 10.12 Representative BSE images of typical crystalline reaction products that document decomposition of carbonates and incorporation of residual CaO and/or MgO into silicate melts. **a** Feathery pseudowollastonite in Ca-rich silicate glass of experiment 889 (sandstone–carbonate target). **b** Acicular pseudowollastonite in Ca-rich melt adjacent to partially molten sandstone; experiment 889. **c** Carbonate inclusion in Ca-rich silicate glass that locally precipitated merwinite quench crystallites; experiment 891 (basalt–carbonate target; cf. Fig. 10.11f). Note that the carbonate inclusion is a texturally complex assemblage of equant, submicrometer size calcite crystallites, silicate glass (medium grey), and oxide quench phases (white, light grey). **d** Feathery pyroxene in Ca,Mg-rich silicate glass around a FeNi metal sphere in experiment 893 (iron meteorite–carbonate–sandstone target). **e** Partial crystallization of Ca,Mg-rich silicate melt in experiment 893, yielding laths of melilite and strongly zoned quench crystallites of magnesian kirschsteinite and ferroan monticellite. **f** Granular assemblage of melilite, magnesian kirschsteinite, ferroan monticellite, and pyroxene in experiment 893. Frequently occurring inclusions in these areas are quartz fragments (often showing partial melting) and carbonate decomposition products. Abbreviations: Cal = calcite; Kir = magnesian kirschsteinite; Lech = lechatelierite; Mw = merwinite; Mll = melilite; Mtc = ferroan monticellite; Px = pyroxene; Qz = quartz; Wo = pseudowollastonite.

2. incorporation of carbonate-derived, residual CaO into homogenized basaltic melts produced a range of melt compositions that cannot be explained by melting and mixing any combination of the basalt components.

These two mixing trends are illustrated in Figs. 10.14 and 10.15 by light green and grey fields that outline the extent of simple multicomponent melt mixtures. Most silicate glass compositions fall onto, or close to, a mixing line between the bulk composition of the basalt and the theoretical bulk composition of degassed Carrara marble (i.e., almost pure CaO), indicating thorough, laser-induced melt mixing and homogenization of the silicate melts prior to admixture of carbonate-derived CaO.

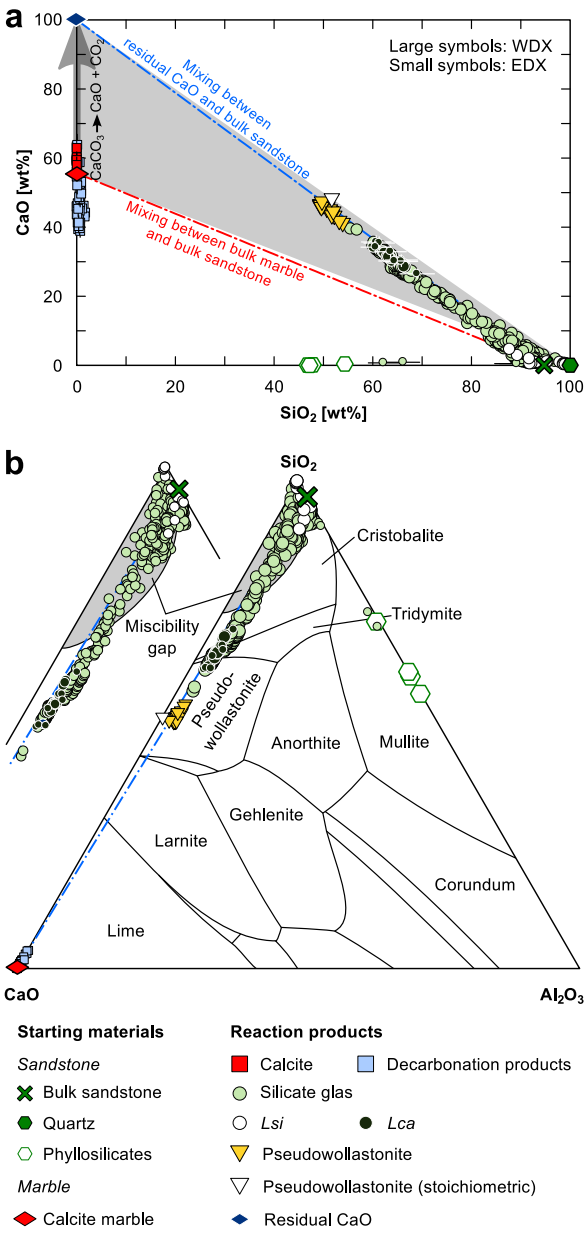

Figure 10.13 Compositions of starting materials and reaction products of experiment 889 (sandstone–carbonate target). **a** In binary diagrams such as CaO–SiO_2, the compositions of the silicate glasses, ranging between Ca-normal to strongly Ca-enriched, fall onto a mixing line between the bulk composition of the sandstone and stoichiometric CaO. This indicates complete devolatilization of $CaCO_3$ and mixing between sandstone-derived SiO_2 and carbonate-derived, residual CaO. The formation of silicate emulsions of immiscible Si-rich (*Lsi*) and Ca-rich (*Lca*) melts and of pseudowollastonite in the Ca-rich melt supports this scenario. **b** Compositions of starting materials and reaction products plotted in the ternary system CaO–SiO_2–Al_2O_3 (redrawn from Haccuria et al., 2016). Most silicate glass compositions fall into a high-temperature immiscibility field extending along the SiO_2–CaO join. The most Ca-rich melts (~50 wt.% CaO) precipitated crystallites of pseudowollastonite. Bulk sandstone and phyllosilicate data from Ebert et al. (2013) and Ebert et al. (in press).

Table 10.3 Average major element compositions of carbonates and carbonate reaction products in experiments 889 (sandstone–carbonate target), 891 and 982 (basalt–carbonate targets), and 893 (iron meteorite–carbonate–sandstone target).

	889				891 and 892	893			
	Pristine calcite[†]	Calcite adjacent to decomposition products*	Calcite decomposition products*		Bulk carbonate inclusions*	Pristine dolomite[†]	Dolomite adjacent to decomposition products[†]	Dolomite decomposition products[†]	
[wt.%]	$n = 167$	$n = 15$	$n = 46$		$n = 14$	$n = 62$	$n = 6$	$n = 9$	
SiO_2	bdl	bdl	0.5(4)	<1.7	10.6(26)	bdl	0.06(4)	1.22(102)	0.25–3.63
TiO_2	bdl	bdl	0.2(3)	<1.3	bdl	bdl	bdl	bdl	bdl
Al_2O_3	bdl	bdl	bdl	bdl	5.9(14)	bdl	bdl	0.31(47)	<1.58
FeO_t	bdl	bdl	bdl	bdl	7.1(35)	0.04	0.13(3)	0.87(103)	0.35–3.70
MnO	bdl	bdl	bdl	bdl	bdl	0.01	0.03(2)	0.03(2)	<0.07
MgO	0.80(8)	0.8(1)	0.6(2)	0.3–1.2	4.5(10)	22.5	20.4(6)	39.6(38)	33.9–47.7
CaO	55.3(2)	59.1(14)	47.2(65)	38.9–63.8	44.8(60)	30.9	31.40(84)	34.33(705)	24.85–48.18
Na_2O	bdl	bdl	bdl	bdl	0.2(1)	n.a.	bdl	0.02(1)	<0.03
K_2O	bdl	bdl	bdl	bdl	bdl	n.a.	bdl	bdl	bdl
P_2O_5	bdl	bdl	0.3(5)	<1.8	bdl	n.a.	n.a.	n.a.	n.a.
CO_2	43.8(2)[§]	40.1(14)[¶]	51.1(65)[¶]	35.2–59.8[¶]	26.8(75)[¶]	46.6 [§]	48.0(14)[§]	23.6(84)[§]	5.3–35.9[§]
Total	56.2	59.9	48.8	40.3–64.8	73.1	53.5	52.0	76.4	64.1–94.7

Data obtained by EMPA-WDX ([†]) or SEM-EDX ([*]) and given in wt.%; *n* = number of analyses included in average; uncertainty given in parentheses represents one standard deviation from the mean based on all analyses included in the average.
bdl = below detection limit; n.a. = not analyzed; total iron (FeO_t) is reported as FeO + Fe_2O_3; CO_2 in WDX analyses was calculated by difference from 100 wt.% ([§]) or obtained from EDX spectra after coating correction ([¶]).

We frequently detected texturally complex, recrystallized, carbonate-rich inclusions entrained in the Ca-rich silicate glasses that often have fluidal shapes and outlines, as well as sharp phase boundaries to the surrounding silicate glass (Figs. 10.9b, d and 10.10a). Often, a gradual transition from calcite decomposition products to this carbonate-rich material exists (Figs. 10.9b, c and 10.10a), ultimately forming large volumes of carbonate-rich material adjacent to Ca-rich silicate glasses (see Fig. 10.9d). In detail, the carbonate-rich material comprises texturally complex assemblages of (1) spurrite quench crystals (Fig. 10.11b–e), (2) residual, SiO_2-poor oxide quench phases (Fig. 10.11c–e), (3) fine-grained, euhedral crystallites of calcite (Fig. 10.11e), and (4) sub-micrometer size, dendritic to equant crystallites (Fig. 10.11e) that are too small for reliable phase identification—they are presumably ferropericlase, (Mg,Fe)O, and either brownmillerite, $Ca_2(Al, Fe^{3+})_2O_5$, or srebrodolskite, $Ca_2(Fe^{3+}, Al)_2O_5$ (see below). Obtaining a reliable bulk composition of the carbonate-rich material using EMPA-WDX methods proved difficult because defocusing of the electron beam resulted in mixed analyses between minerals, quench phases, and the epoxy resin. Hence, we determined representative bulk compositions by averaging representative areas in EDX elemental maps such as shown in Fig. 10.10b. The EDX data were corrected for coating-induced carbon content (see Subsection 10.2.3) and care was taken to avoid areas that are highly vesicular or penetrated by fractures. A number of representative analyses are averaged in Table 10.3. They reveal that the carbonate-rich material contains substantial amounts of CaO and CO_2 (ca. 45 ± 6 and 27 ± 8 wt.% on average, respectively) as well as minor amounts of SiO_2 (~11 ± 3 wt.%), FeO (~7 ± 4 wt.%), Al_2O_3 (~6 ± 1 wt.%), and MgO (~5 ± 1 wt.%); alkalis are almost absent (Na_2O ≈ 0.2 wt.%, K_2O < 0.1 wt.%). On average, the inclusions have a CaO/(CaO + MgO + FeO) wt.% ratio of 0.79, individual values range between 0.69 and 0.87. The nature and origin of the carbonate-rich material is discussed below.

Silicate melts in the iron meteorite–carbonate–sandstone experiment

The iron meteorite–carbonate–sandstone experiment (893) yielded Ca,Mg-rich, well-homogenized, vesicular, and occasionally clast-rich silicate melts that either rapidly quenched to holohyaline glasses or precipitated a variety of quench crystals. Compared to the bulk composition of the sandstone (Table 10.2), the silicate glasses are strongly enriched in Ca and Mg derived from the dolomite and in Fe and Ni derived from the iron meteorite (Table 10.4; Fig. 10.16). Compared to the layered sandstone–carbonate experiment (889), the silicate glasses of the powder experiment are less heterogeneous in composition (43–64 wt.% SiO_2, 5–31 wt.% FeO, 15–26 wt.% CaO, 7–13 wt.% MgO, and 2–5 wt.% Al_2O_3), which is probably due to the thorough homogenization of the powder components before laser irradiation (see Subsection 10.2.2).

In the pseudo-binary diagram (SiO_2 + FeO)–(CaO + MgO) (Fig. 10.16a), all analyzed glass compositions fall onto mixing lines spanned between

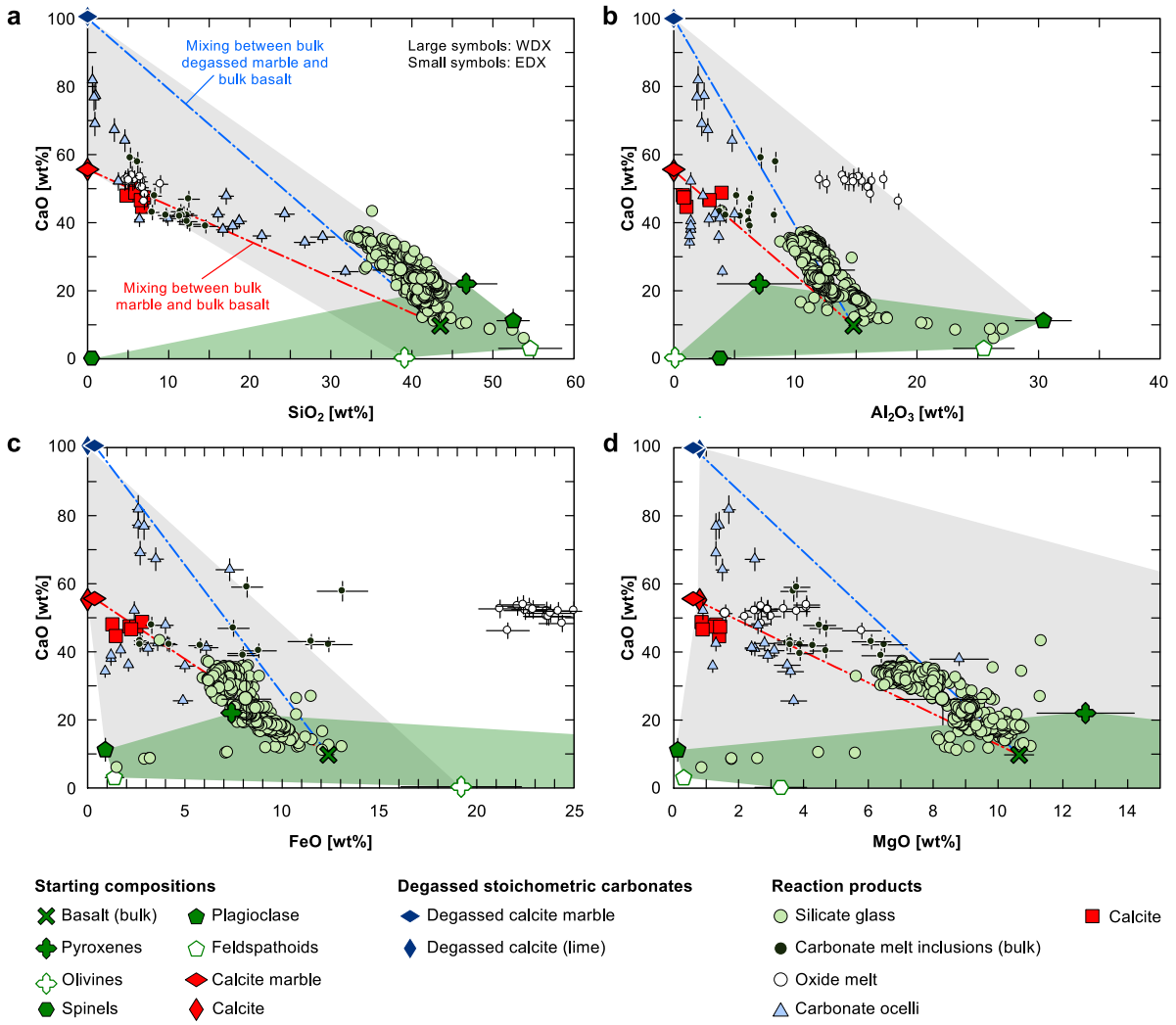

Figure 10.14 Compositions of starting materials and reaction products of experiments 891 and 892 (basalt–carbonate targets) plotted in binary mixing diagrams. **a** CaO–SiO_2; **b** CaO–Al_2O_3; **c** CaO–FeO; **d** CaO–MgO. Some silicate glass compositions can be explained by melting and mixing of the basalt components (illustrated by green fields), but most glass compositions require admixture of variable amounts of carbonate-derived material (illustrated by grey fields and mixing lines). See text for discussion.

a theoretical bulk composition of the sandstone and the iron meteorite and the theoretical bulk composition of 66% to 100% degassed dolomite (assuming residual CaO and MgO in molar proportions of 1:1). The glasses invariably show high EMPA-WDX totals ≥98.2 wt.% (99.2 wt.% on average), indicating, again, that they are volatile-poor or -free. In detail, the silicate glasses show more complex compositional trends that reflect variable admixture and incomplete homogenization of monomineralic quartz- and phyllosilicate-derived melts (e.g., Fig. 10.16d, e) and oxidized, FeO-rich, iron meteorite-derived melts (e.g., Fig. 10.16d). Notably, CaO/MgO wt.% ratios of the silicate melts (2.12 on average, individual values range between 1.78 and 2.56) deviate slightly from average bulk dolomite mar-

ble (1.85) and dolomite mineral (1.54) ratios (Fig. 10.16f). Judging from these average ratios and taking into account that the bulk dolomite also contained some calcite (see Table 10.2), these values indicate slight but distinct fractionation of Ca and Mg (i.e., enrichment in Ca over Mg in the silicate melts) during chemical interaction of the silicate melts and the entrained carbonate clasts. Now, the question that arises is: do these data really represent fractionation of Ca and Mg, or are they governed by other factors, such as segregation of $CaCO_3$ and $MgCO_3$ during thermal

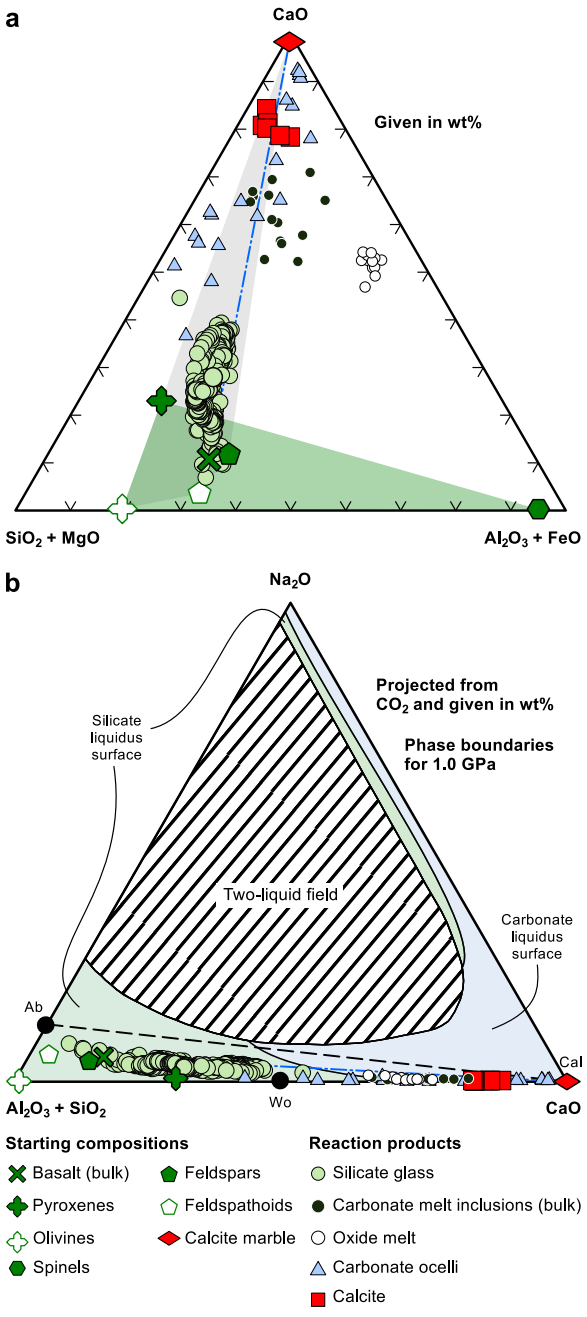

Figure 10.15 Compositions of starting materials and reaction products of experiments 891 and 892 (basalt–carbonate targets). **a** Pseudo-ternary diagram (SiO_2 + MgO)–CaO–(Al_2O_3 + FeO). **b** Pseudo-ternary system Na_2O–CaO–Al_2O_3–SiO_2–CO_2 (Lee and Wyllie, 1998). See text for discussion.

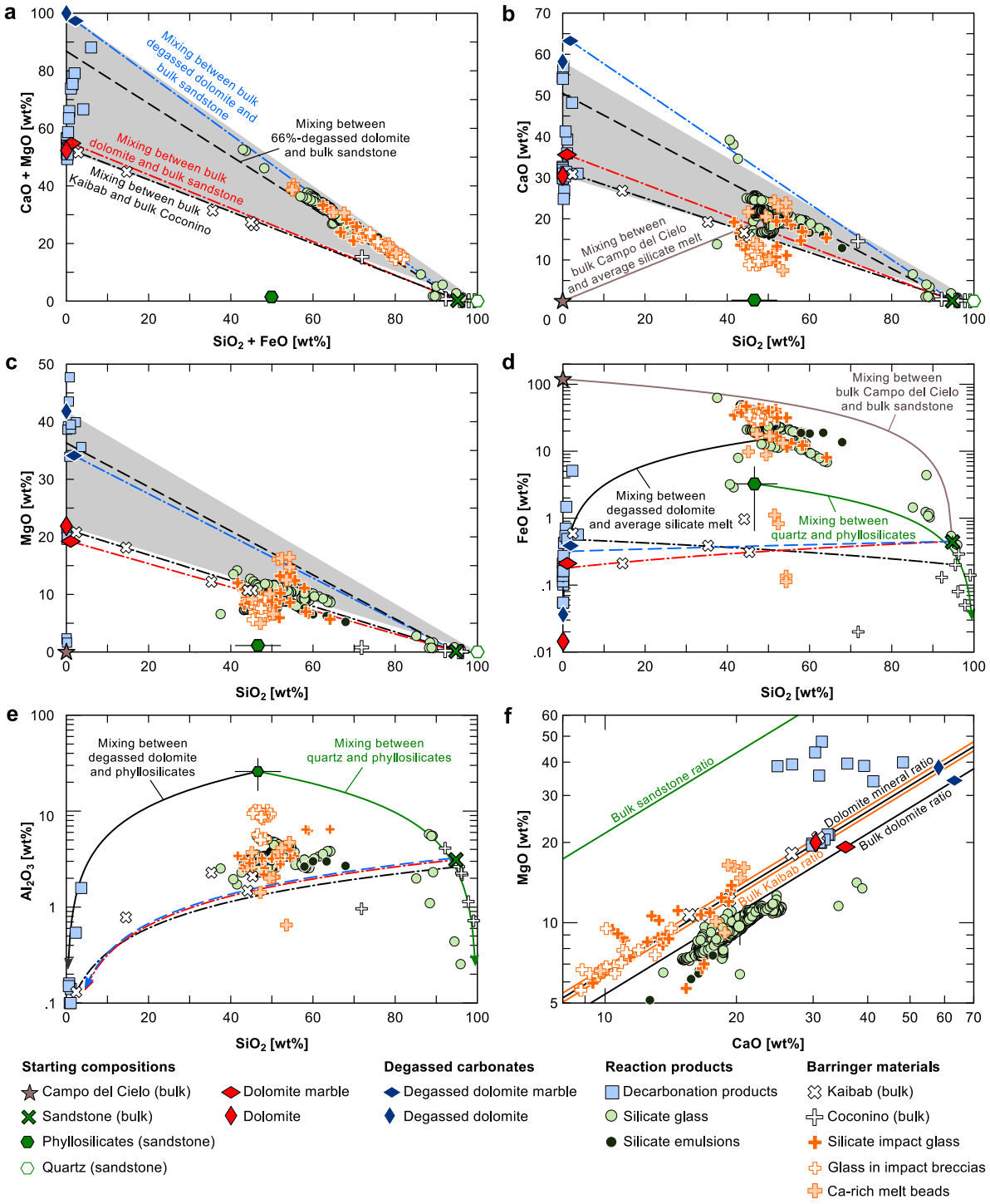

Figure 10.16 Compositions of starting materials and reaction products of experiment 893 in comparison to natural Barringer Crater silicate impact melts plotted in pseudo-binary and binary mixing diagrams. **a** (CaO + MgO)–(SiO_2 + FeO); **b** CaO–SiO_2; **c** MgO–SiO_2; **d** FeO–SiO_2; **e** Al_2O_3–SiO_2; **f** MgO–CaO. Note logarithmic scaling in (d–f). See text for discussion. Bulk Kaibab and Coconino compositions are from Mittlefehldt et al. (2005); silicate impact glass compositions are from Hörz et al. (2002) and Mittlefehldt et al. (2005); compositions of glasses in impact breccias and Ca-rich melt beads are from Osinski et al. (2015).

breakdown of dolomite as suggested above, or preferential decomposition of the calcite component of the dolomite marble?

To test these possibilities, we measured the composition of the silicate glasses immediately around partially decomposed dolomite grains. A representative electron microprobe line profile through a decomposed dolomite grain entrained in Ca,Mg-rich silicate glass is given in Fig. 10.17. The glass around the dolomite shows a CaO/MgO wt.% ratio of ~2.5, indeed indicating enrichment in CaO and depletion in MgO compared to the average silicate melt composition (CaO/MgO ≈ 2.12; Fig. 10.17d). With increasing distance from the dolomite grain, the glass shows gradually decreasing CaO/MgO ratios; within ~10–15 µm distance, the CaO/MgO ratio of the average silicate melt is reached. To the contrary, MgO seems to be enriched in the dolomite decomposition products, as emanating from the line profile of Fig. 10.17d or from the elemental distribution maps given in Fig. 10.10d, f. Moreover, the Ca-rich silicate melt veins that fill the fractures in the dolomite grains (Figs. 10.8c, d and 10.10d; Table 10.5) show CaO/MgO ratios of as high as 2.86, further corroborating the findings from the electron microprobe line profiles. Note that similar melt veins in dolomite grains have been described, although at the transmission electron microscopy scale, by Martinez et al. (1994). Although operating on a very small scale, these two processes—that is, slight but consistent preferential enrichment of CaO in the silicate melts and enrichment of residual MgO in the dolomite decomposition products—seem to be responsible for the slightly elevated bulk CaO/MgO ratios of the silicate glasses.

The glasses of the powder experiment also contain silicate emulsions that comprise a Ca,Fe,Mg-rich (*Lca*) glass and a likely Si,Al-rich (*Lsi*) glass. The emulsion textures are similar to those observed in the glasses of the sandstone–carbonate experiment (889) and the Kamil impact glasses (see Chapter 8; Fazio et al., 2016). The *Lca* phase contains ~15 wt.% CaO, ~12 wt.% FeO, ~6 wt.% MgO, and ~62 wt.% SiO_2 (Table 10.4) and melt unmixing was most likely induced in the high-temperature miscibility gap in the general pseudo-ternary system (CaO + MgO + FeO + TiO_2 + P_2O_5)–SiO_2–(Na_2O + K_2O + Al_2O_3) that extends along the (CaO + MgO + FeO + TiO_2 + P_2O_5)–SiO_2 join (see Chapter 8).

10.3.5 Subsequent partial crystallization of the melts during quenching

Partial crystallization of the silicate melts yielded in all experiments quench crystals of Ca- and/or Ca,Mg-rich silicates that are absent in laser-generated melts produced from pure silicate starting materials (cf. Chapter 7) or in mixtures of silicate and iron meteorite starting materials (cf. Ebert et al., 2017). The presence of these minerals further documents the decomposition of carbonates and incorporation of residual oxides into the silicate melts. These crystals show morphologies that are typically related to nucleation and growth at high cooling rates and/or high degrees of undercooling (e.g., Shea and Hammer, 2013, and references therein);

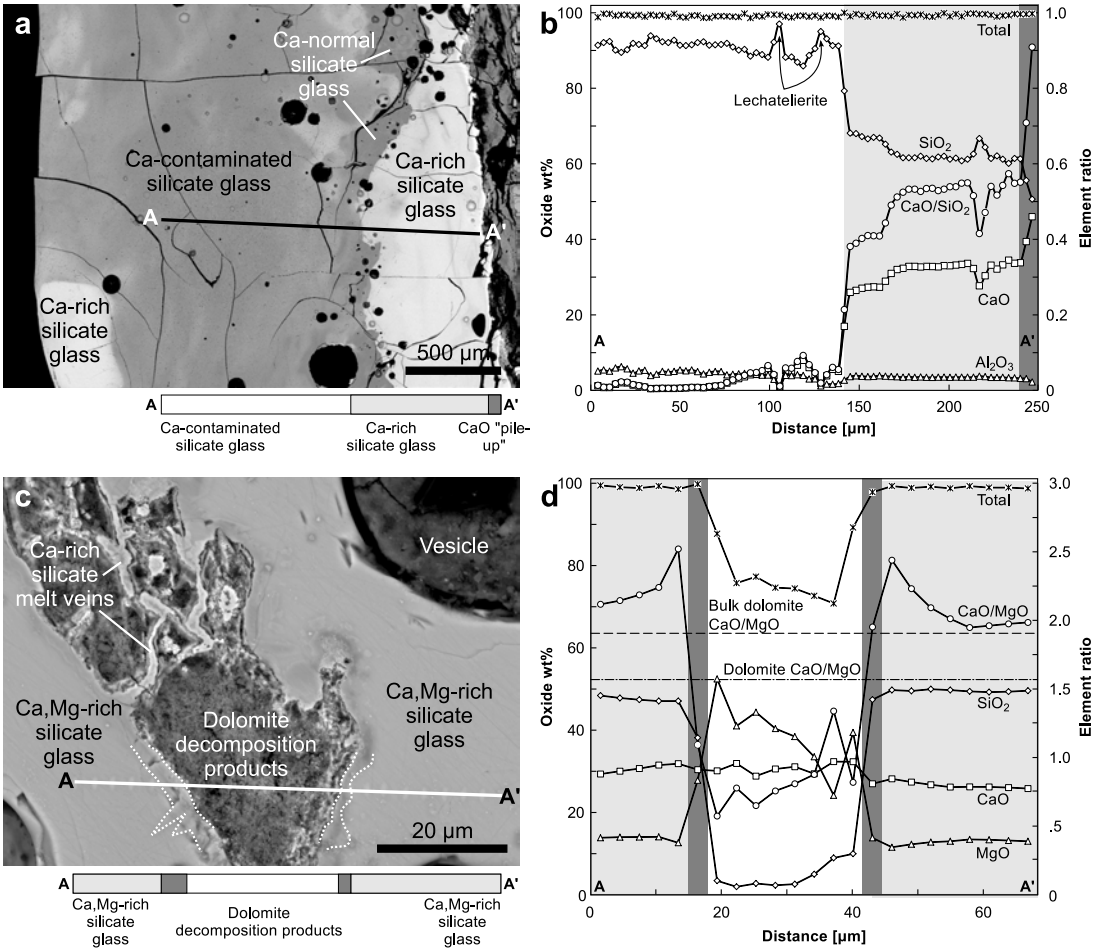

Figure 10.17 Representative BSE images (**a** and **c**) and electron microprobe line profiles (**b** and **d**) through silicate glass adjacent to calcite decomposition products of experiment 889 (sandstone–carbonate target; a and b) and through a relict dolomite grain entrained in Ca,Mg-rich silicate glass of experiment 893 (iron meteorite–carbonate–sandstone target; c and d). The positions of the traverses are drawn onto the corresponding BSE images. Specific areas are illustrated by light and dark grey shadings in the line profiles and below the BSE images. The stippled line in (c) corresponds to a mineral phase that crystallized in the Ca,Mg-rich melt (presumably magnesian kirschsteinite or ferroan monticellite).

similar quench crystals are frequently encountered in rapidly cooled impact melts (e.g., Hörz et al., 2002; Schultze et al., 2016). Moreover, all experiments yielded small, equant, idiomorphic calcite crystallites like those depicted in Figs. 10.6c and 10.12c that we interpret as back-reaction products (see Subsection 10.3.2). However, in most cases (especially in the sandstone–carbonate and the powder experiment), the calcite crystallites were too small to be reliably analyzed for their major-element composition; only a hand full of WDX point analyses could be obtained from experiment 891 (basalt–carbonate target). Representative major-element compositions of the crystalline phases present were analyzed and are given in Table 10.5; Figs. 10.10–10.12 illustrate typical morphologies and Fig. 10.18 gives representative Raman spectra of some of the crystalline phases.

Mineral phases in the sandstone–carbonate experiment

In the sandstone–carbonate experiment (889), feathery crystals of pseudowollastonite, β-$CaSiO_3$, occur in Ca-rich glass in contact with the carbonate layer (e.g, Figs. 10.5b and 10.12a, b). These crystals have nucleated exclusively in the Ca-rich melt immediately at the carbonate–silicate melt interface, where CaO and SiO_2 are likely present in molar ratios of 1:1. Typical crystal shapes grade from stubby, almost equant forms immediately adjacent to the decomposition products to skeletal, acicular crystals to delicate, feathery swallowtails that grew into the surrounding Ca-rich melt (Fig. 10.12a). Raman spectra agree well with pseudowollastonite reference spectra taken from the RRUFF database (Fig. 10.18a, b) and electron microprobe data are largely consistent with wollastonite stoichiometry (Table 10.5). We note, however, that due to the small size of these crystallites, the point analyses presented in Table 10.5 are likely contaminated by surrounding Ca-rich glass (e.g., note the high K_2O or Al_2O_3 concentrations).

Mineral phases in the basalt–carbonate experiments

The melts in the basalt–carbonate experiments (891 and 892) precipitated spurrite, merwinite, and calcite as the dominant crystalline phases. Additionally, we detected several small (<1 μm size), dendritic crystallites in the

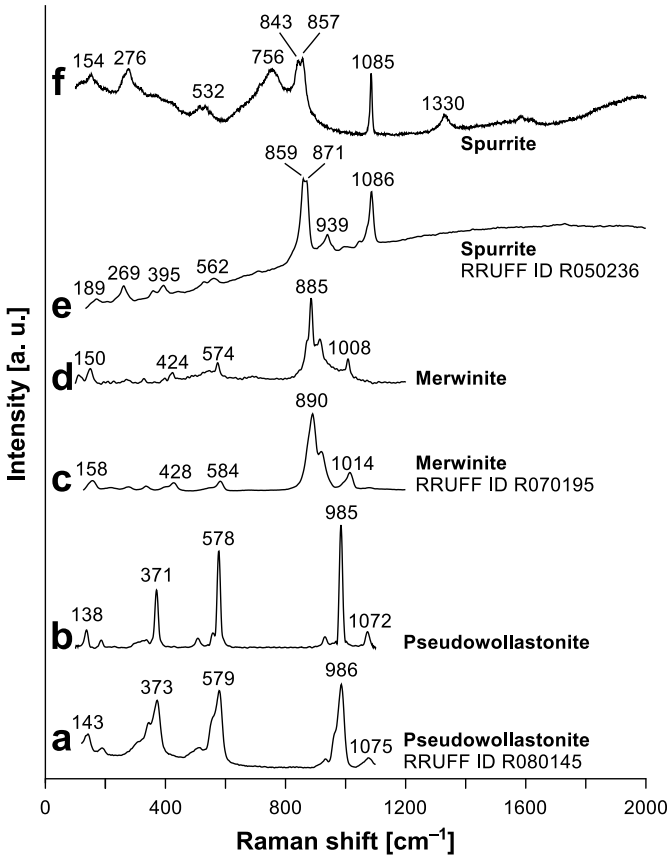

Figure 10.18 Representative Raman spectra obtained from crystalline reaction products of experiments 889 (sandstone–carbonate target; pseudowollastonite) and 891/892 (basalt–carbonate targets; merwinite and spurrite) compared against reference spectra obtained from the RRUFF database.

Table 10.4 Average major element compositions of silicate glasses in experiments 889 (sandstone–carbonate target), 891 and 982 (basalt–carbonate targets), and 893 (iron meteorite–carbonate–sandstone target).

	889				891 and 892		893		
	Silicate glass		Immiscible silicate glasses		Silicate glass		Silicate glass	Immiscible silicate glass	Silicate melt veins[a]
[wt.%]	*n* = 505		*Lca*; *n* = 14	*Lsi*; *n* = 14	*n* = 640		*n* = 497	*Lca*; *n* = 5	*n = 3*
SiO_2	78.7(123)	55.6–97.1	63.7(17)	95.3(39)	38.7(35)	32.4–53.9	50.1(31)	62.0(35)	41.8(8)
TiO_2	0.52(15)	0.05–1.06	0.37(3)	0.15(17)	1.97(33)	0.30–4.06	0.28(5)	0.25(4)	0.15(4)
Al_2O_3	4.24(106)	0.09–4.26	3.31(17)	2.25(22)	12.78(209)	3.98–27.11	3.10(55)	2.80(15)	1.96(23)
FeO_t	0.33(8)	0.08–0.57	0.27(3)	0.31(31)	8.16(126)	1.53–13.09	15.38(401)	11.67(126)	3.30(155)
MnO	bdl	<0.06	bdl	bdl	0.14(3)	0.04–0.23	0.01(1)	bdl	bdl
MgO	0.33(16)	0.03–0.71	0.5(4)	0.11(13)	8.30(143)	0.88–11.34	9.63(116)	6.34(78)	12.96(108)
CaO	15.14(1280)	0.45–45.98	31.03(16)	0.98(121)	26.08(751)	5.89–43.20	20.38(232)	15.84(168)	37.11(196)
Na_2O	bdl	<0.07	bdl	bdl	2.45(5)	1.24–7.17	0.17(10)	0.02(1)	0.04(2)
K_2O	0.18(7)	0.05–0.49	0.11(1)	0.32(3)	0.97(29)	0.38–4.26	0.07(2)	0.12(2)	0.32(5)
P_2O_5	bdl	bdl	bdl	bdl	0.27(12)	<2.32	n.a.	n.a.	n.a.
NiO	n.a.	n.a.	n.a.	n.a.	n.a.	n.a.	0.06(5)	0.03(2)	bdl
Total	99.5	98.5–100.5	99.3	99.4	99.8	98.4–100.7	99.2	99.0	97.6

Data obtained by EMPA-WDX and given in wt.%; *n* = number of analyses included in average; uncertainty given in parentheses represents one standard deviation from the mean based on all analyses included in the average.

bdl = below detection limit; n.a. = not analyzed; total iron (FeO_t) is reported as FeO + Fe_2O_3; *Lca* = Ca-rich immiscible glass; *Lsi* = Si-rich immiscible glass.

[a] Ca-rich silicate melt veins in dolomite.

Table 10.5 Average major element compositions of crystalline reaction products in experiments 889 (sandstone–carbonate target), 891 and 982 (basalt–carbonate targets), and 893 (iron meteorite–carbonate–sandstone target).

	889	891 and 892		
	Pseudowollastonite[†]	Spurrite[a,*]	Calcite[b,†]	Merwinite[*]
[wt.%]	$n = 19$	$n = 7$	$n = 6$	$n = 14$
SiO_2	50.8(14)	21.6(18)	6.42(48)	34.4(30)
TiO_2	0.32(4)	0.1(1)	0.10(7)	0.1(1)
Al_2O_3	2.53(40)	1.5(8)	1.73(124)	2.8(16)
FeO_t	0.18(5)	1.2(5)	2.07(54)	2.8(8)
MnO	bdl	bdl	0.04(1)	bdl
MgO	0.60(17)	1.6(6)	1.17(23)	9.5(5)
CaO	45.1(17)	61.1(24)	47.2(13)	49.5(20)
NiO	n.a.	bdl	n.a.	bdl
Na_2O	bdl	0.3(1)	0.12(2)	0.6(1)
K_2O	0.06(5)	bdl	0.10(2)	0.2(1)
CO_2	—	12.5(12)[¶]	40.7(24)[§]	—
Total	99.5	87.4	58.9	99.9
Number of cations on the basis of X (O)				
(apfu)	18 (O)	11 (O)	3 (O)	8 (O)
Si	5.875	1.593	0.106	1.910
Ti	0.028	0.006	0.001	0.004
Al	0.345	0.130	0.034	0.183
Fe	0.018	0.074	0.029	0.130
Mn	0.000	0.000	0.001	0.000
Mg	0.103	0.176	0.029	0.786
Ca	5.581	4.826	0.837	2.945
Ni	0.000	0.000	0.000	0.000
Na	0.000	0.043	0.004	0.065
K	0.009	0.000	0.002	0.014
C	0.000	1.258	0.919	0.000
Sum	11.960	8.110	1.960	6.040
En	2	—	—	—
Fs	0	—	—	—
Wo	98	—	—	—
Fo	—	—	—	—
Fa	—	—	—	—

Data obtained by EMPA-WDX ([†]) or SEM-EDX ([*]) and given in wt.%; n = number of analyses included in average; uncertainty given in parentheses represents one standard deviation from the mean based on all analyses included in the average. bdl = below detection limit; n.a. = not analyzed; apfu = atoms per formula unit on the basis of X (O); total iron (FeO_t) is reported as $FeO + Fe_2O_3$; CO_2 was either calculated by difference from 100 wt.% ([§]) or obtained from EDX spectra after coating correction ([¶]). En = molar enstatite component calculated as $100 \times Mg/(Mg + Fe + Ca)$; Fs = molar ferrosilite component calculated as $100 \times Fe/(Fe + Mg + Ca)$; Wo = molar wollastonite component calculated as $100 \times Ca/(Ca + Mg + Fe)$; Fo = molar forsterite component calculated as $100 \times Mg/(Mg + Fe)$; Fa = molar fayalite component calculated as $100 \times Fe/(Fe + Mg)$.

[a] Data obtained immediately after performing the experiments by SEM-EDX surface analysis; contamination by surrounding phases possible (see Fig. 10.11b).

[b] Small equant crystallites (see Fig. 10.6).

Table 10.5 (cont.) Average major element compositions of crystalline reaction products in experiments 889 (sandstone–carbonate target), 891 and 982 (basalt–carbonate targets), and 893 (iron meteorite–carbonate–sandstone target).

	893				
	Pyroxene[c,†]	Olivine[d,†]	Olivine[e,*]	Melilite[f,†]	Melilite[g,*]
[wt.%]	$n = 6$	$n = 4$	$n = 6$	$n = 6$	$n = 5$
SiO_2	52.2(6)	41.2(14)	34.4(6)	42.9(4)	43.1(2)
TiO_2	0.17(4)	0.13(8)	bdl	0.02(2)	bdl
Al_2O_3	1.65(58)	1.18(78)	bdl	1.52(5)	1.2(2)
FeO_t	10.91(121)	15.7(16)	21.0(11)	4.04(54)	3.6(12)
MnO	bdl	bdl	bdl	bdl	bdl
MgO	13.50(122)	31.3(42)	18.5(16)	11.51(35)	13.0(0)
CaO	21.03(52)	10.93(108)	26.1(14)	38.98(24)	38.7(4)
NiO	0.16(6)	0.14(4)	bdl	bdl	bdl
Na_2O	0.07(3)	bdl	bdl	0.04(2)	0.4(1)
K_2O	0.02(2)	0.16(13)	bdl	0.11(3)	bdl
CO_2	—	—	—	—	—
Total	99.7	100.7	100.0	99.1	100.0
Number of cations on the basis of X (O)					
(apfu)	6 (O)	4 (O)	4 (O)	14 (O)	14 (O)
Si	1.964	1.054	0.970	3.979	3.955
Ti	0.005	0.003	0.000	0.001	0.000
Al	0.073	0.036	0.000	0.166	0.130
Fe	0.343	0.336	0.495	0.313	0.276
Mn	0.000	0.000	0.000	0.001	0.000
Mg	0.757	1.194	0.777	1.592	1.779
Ca	0.848	0.300	0.788	3.874	3.805
Ni	0.005	0.003	0.000	0.001	0.000
Na	0.005	0.000	0.000	0.007	0.071
K	0.001	0.005	0.000	0.013	0.000
C	0.000	0.000	0.000	0.000	0.000
Sum	4.000	2.930	3.030	9.950	10.020
En	39	—	—	—	—
Fs	18	—	—	—	—
Wo	44	—	—	—	—
Fo	—	78	61	—	—
Fa	—	22	39	—	—

Data obtained by EMPA-WDX (†) or SEM-EDX (*) and given in wt.%; n = number of analyses included in average; uncertainty given in parentheses represents one standard deviation from the mean based on all analyses included in the average. bdl = below detection limit; n.a. = not analyzed; apfu = atoms per formula unit on the basis of X (O); total iron (FeO_t) is reported as $FeO + Fe_2O_3$; CO_2 was either calculated by difference from 100 wt.% (§) or obtained from EDX spectra after coating correction (¶). En = molar enstatite component calculated as $100 \times Mg/(Mg + Fe + Ca)$; Fs = molar ferrosilite component calculated as $100 \times Fe/(Fe + Mg + Ca)$; Wo = molar wollastonite component calculated as $100 \times Ca/(Ca + Mg + Fe)$; Fo = molar forsterite component calculated as $100 \times Mg/(Mg + Fe)$; Fa = molar fayalite component calculated as $100 \times Fe/(Fe + Mg)$.

[c] Salite, feathery variety (see Fig. 10.12d).

[d] Ferroan monticellite (see Figs. 10.10c–f and 10.12e, f).

[e] Magnesian kirschstinite (see Figs. 10c–f and 12e, f).

[f] Melilite, feathery variety (see Fig. 10.12e).

[g] Melilite, granular variety (see Fig. 10.12f).

oxide melts that are presumably ferropericlase and a so-far unidentified mineral (possibly brownmillerite or srebrodolskite).

Spurrite, $Ca_5(SiO_4)_2(CO_3)$, a nesosilicate typical of high-temperature contact metamorphism of siliceous limestones (e.g., Tilley, 1929; Tilley and Harwood, 1931; Walter, 1965; Joesten, 1976; Marineca et al., 2001; Pascal et al., 2001), occurs frequently in the carbonate-rich material of both basalt–carbonate experiments. Fresh crystals of spurrite were observed under the SEM immediately after performing the experiments, that is, without applying any sample preparation (Fig. 10.11b). Some semi-quantitative EDX point analyses obtained from the surface of the irradiated target of experiment 891 are given in Table 10.5. The fresh crystallites occur as nests of platy, subhedral to euhedral crystallites up to ~50 µm long and ~5 µm thick. The composition of the fresh crystallites agrees reasonably well with theoretical stoichiometry and previously published compositions (e.g., Marineca et al., 2001; Rosa and Martin, 2010). Compared to ideal stoichiometry, the spurrite analyses presented in Table 10.5 contain less SiO_2 (~21.6 wt.%) and more CO_2 (~12.5 wt.%), with limited amounts of MgO (1.6 wt.%), Al_2O_3 (1.5 wt.%), and FeO (1.2 wt.%) that likely result from the poor analytical conditions under which these analyses were obtained. In the thin sections (Fig. 10.11c–e), spurrite appears heavily altered: in BSE images, the most abundant pattern of spurrite alteration involves the formation of black cracks in dark grey spurrite laths and the formation of small, submicrometer size, equant calcite crystallites (e.g., Fig. 10.11e). Nevertheless, Raman spectra obtained from individual laths still agree reasonably well with spurrite reference spectra (Fig. 10.18e, f).

Immediately around most of the spurrite-bearing carbonate-rich material, merwinite, $Ca_3Mg(SiO_4)_2$, another nesosilicate typical of high-temperature contact metamorphism of siliceous limestones (see references above), occurs frequently in the Ca-rich silicate glass (Figs. 10.9d, 10.10a, and 10.11d). Merwinite invariably occurs in the form of small, needle- or dendrite-shaped crystallites some 2–20 µm in size. Compositionally, the crystallites are close to ideal stoichiometry, with 1.964 apfu (atoms per formula unit) Si, 2.945 apfu Ca, and a cation sum of 6.040 apfu (Table 10.5); Raman spectra identify the minerals as merwinite (Fig. 10.18c, d). Most merwinites seemingly contain limited amounts of Al_2O_3 and FeO (~2.8 wt.% each) that might arise from mixed analyses between merwinite and the surrounding silicate glass, but also could be caused by impurities present in the minerals, or by possible solid solutions (e.g., replacement of Mg by Fe^{2+}). Moreover, high-magnification BSE images (Fig. 10.12c) reveal fine exsolution lamellae in most of the merwinite quench crystals that might explain the observed deviation from ideal stoichiometry.

The basalt–carbonate experiments yielded abundant newly grown, submicrometer to micrometer size, equant, idiomorphic calcite crystallites (Figs. 10.6b, c and 10.12c). The calcites usually occur in clusters of individual crystallites (e.g., Figs. 10.11e and 10.12c), but are also present in the form of individual crystals surrounded by calcite decomposition products (Fig. 10.6b). Due to their small sizes it was difficult to obtain precise

compositional data; the analyses presented in Table 10.5 are possibly contaminated by surrounding phases (e.g., spurrite) or by impurities residing in minute interstices or surface deposits (see Fig 10.12c). The significant amounts of SiO_2 (~6.4 wt.% or 0.106 apfu Si) and Al_2O_3 (~1.7 wt.% or 0.034 apfu Al) are interpreted as major contaminants given the fact that Si^{4+} and Al^{3+} are usually not incorporated in such large amounts into the calcite crystal lattice (e.g., Chang et al., 1996, and references therein). Divalent cations other than Ca^{2+} are, however, readily incorporated into the calcite crystal lattice. Thus, these calcites might indeed show limited amounts of siderite or magnesite in solid solution (e.g., ~2 wt.% FeO and ~1 wt.% MgO; Table 10.5).

Apart from these readily identified minerals, the basalt–carbonate experiments contain a number of crystalline phases that are difficult to identify due to their small dimensions. Ferropericlase is likely present in the oxide melts, where it forms submicrometer size, subhedral to euhedral crystallites that appear dark grey in BSE images (Fig. 10.11d, e). Point analyses obtained by SEM-EDX are, however, ambiguous (a representative composition is: 77.5 wt.% MgO, 10.7 wt.% CaO, 6.8 wt.% FeO, 2.6 wt.% Al_2O_3, and 1.3 wt.% SiO_2) and possibly reflect contamination by surrounding oxide melt. Moreover, in BSE images we detected a dendritic bright-white phase of submicrometer to micrometer size (Fig. 10.11e) that might represent either brownmillerite, $Ca_2(Al, Fe^{3+})_2O_5$, or srebrodolskite, $Ca_2(Fe^{3+}, Al)_2O_5$. These oxides have been reported from metamorphosed limestone at West Clearwater Lake by Rosa and Martin (2010). Compositionally, both brownmillerite and srebrodolskite are close to the composition of the oxide melt, hence, nucleation of these minerals seem plausible.

Mineral phases in the iron meteorite–carbonate–sandstone experiment

The silicate melts of the iron meteorite–carbonate–sandstone experiment (893) precipitated (1) feathery, Ca-rich clinopyroxene, (2) hopper-shaped, strongly zoned, Ca-bearing olivine, and (3) elongated, occasionally hopper-shaped melilite.

The pyroxenes were frequently found radiating from spheres of FeNi metal (Fig. 10.12d) and usually comprise feathery or acicular grains some 10 to 100 µm along their long axis; stubby and more equant varieties some 10 to 20 µm in size also exist, but the feathery forms dominate. Overall, the pyroxene compositions conform closely to the expected stoichiometry: normalized to six oxygen atoms, the sum of cations is 4.000 apfu (Table 10.5). Individual crystals range between $En_{35}Fs_{20}Wo_{45}$ and $En_{40}Fs_{20}Wo_{41}$; thus, the pyroxenes contain substantial amounts of CaO (~21 wt.%) and MgO (~13.5 wt.%) that obviously reflect the incorporation of refractory residues from the decomposition of dolomite. Moreover, they contain limited amounts of NiO (~0.2 wt.%) reflecting admixture and oxidation of FeNi metal of the Campo del Cielo iron meteorite in the silicate melts. The pyroxenes also show slight compositional variations

with respect to FeO (~11 ± 1 wt.%) and MgO (~14 ± 1 wt.%), but individual pyroxene needles were too thin to evaluate whether this reflects any systematic compositional zoning.

The olivines comprise skeletal, hopper, and subhedral to euhedral grains, usually with sizes of ~10–20 µm (Fig. 10.12e, f). They contain significant amounts of CaO (ranging between ~9 and ~28 wt.%; Table 10.5) and thin, likely more Fe-rich rims. Thus, they deviate substantially from the forsterite–fayalite solid solution and represent ferroan monticellite or magnesian kirschsteinite, $Ca(Mg, Fe)SiO_4$. Both olivine varieties are close to the expected stoichometry in terms of cation sums (2.930 and 3.030 apfu, respectively, when normalized to four oxygen atoms) and show considerable ($Mg + Fe^{2+}$)-for-Ca substitution: the ferroan monticellites have 1.194 apfu Mg, 0.336 apfu Fe, and 0.300 apfu Ca, whereas the magnesian kirschsteinites have 0.777 apfu Mg, 0.495 apfu Fe, and 0.788 apfu Ca. Manganese is absent in all analyses, but the ferroan monticellites show small amounts of Al_2O_3 (~1.2 wt.%, translating into 0.036 apfu Al).

The third typical mineral that is frequently encountered in the powder experiment is melilite, $(Ca, Na, K)_2[(Mg, Fe^{2+}, Fe^{3+}, Al, Si)_3O_7]$. The melilites typically occur in the form of elongated, subhedral and occasionally hopper-shaped laths (Fig. 10.12e), but more euhedral, equant forms also exist (Fig. 10.12f). They show appreciable amounts of iron (~4 wt.% FeO_t) and are low in Al_2O_3 (~1.5 wt.%) and Na_2O (<0.1 wt.%), reflecting the iron meteorite and sandstone starting compositions.

10.4 Discussion

10.4.1 Pressure–temperature paths during laser melting and impact melting

The experiments performed in this study were designed to simulate post-shock impact melting of mixed silicate–carbonate targets. As briefly outlined before, most, if not all, terrestrial impact structures that contain carbonates as major target components also contain silicate components (Osinski et al., 2008); no monolithic carbonate impact melt volumes are known or have been recognized so far. Prominent cases of such mixed silicate–carbonate targets are Barringer, Haughton, Ries, Tenoumer, and Chicxulub. For example, the pre-impact target stratigraphy at Haughton consisted of Lower Paleozoic sedimentary rocks (mainly carbonates, but also calcite-bearing sandstones) overlying Precambrian metamorphic basement of the Canadian Shield (Osinski, 2007, and references therein), whereas the target stratigraphy at Barringer Crater was composed of a mixture of Moenkopi sandstone, Kaibab dolomite, and Coconino sandstone (Hörz et al., 2015, and references therein).

While our starting materials are, thus, appropriate for carbonate-bearing targets at typical terrestrial impact structures, a major issue of our experimental setup is that direct CW laser irradiation does not exert high pressures commensurate with typical terrestrial impact scenarios. While local pressure excursions might have existed during the experiments that could

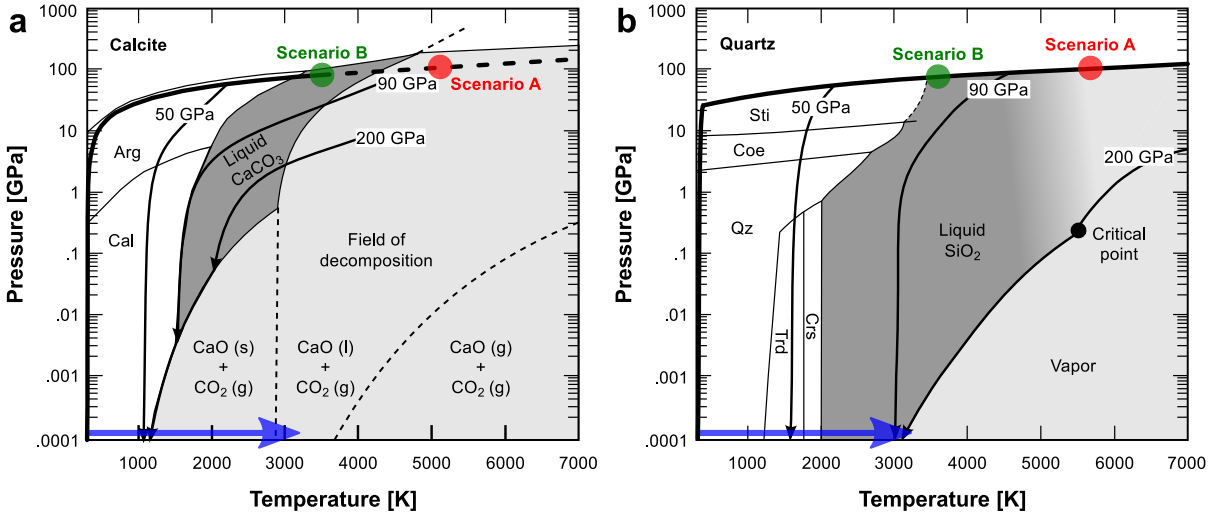

Figure 10.19 Thermodynamic paths of the adiabatic release of shocked, single-crystal, non-porous calcite (**a**) and quartz (**b**) on log *P* vs. *T* diagrams, superimposed onto the phase diagrams of $CaCO_3$ (modified after Ivanov and Deutsch, 2002) and SiO_2 (modified after Melosh, 2007), respectively. The Hugoniot curves for calcite and quartz are shown as heavy lines, whereas medium lines with arrows denote decompression isentropes for 50, 90, and 200 GPa, respectively. Thin solid and dotted lines are phase boundaries. The decompression isentropes for calcite are a courtesy of Natasha Artemieva and were calculated using the equation of state program ANEOS; the decompression isentropes for quartz are from Melosh (2007) and were also calculated using ANEOS (the particle velocities in Melosh's original version of this diagram were converted to shock pressures using the Hugoniot equations). The transparent blue arrows qualitatively illustrate prograde *P*–*T* paths during laser irradiation (i.e., quasi-isobaric heating). Note that depending on the temperature increase of the materials during laser irradiation, the thermodynamic states of the resulting melts are similar to the thermodynamic states of the resulting impact melts (cf. Chapter 7). The green and red dots denoted "Scenario A" and "Scenario B" qualitatively refer to the initial shock conditions discussed for the two different scenarios of the working model presented in Fig. 10.20.

explain rare melt textures in some calcite grains (small vesicles in otherwise intact calcite; see Figs. 10.4a and 10.5a, b), the gross of the irradiated materials (solids and liquids) remained at atmospheric pressure. General "prograde" *P*–*T* paths during laser melting of carbonates and silicates are illustrated in Fig. 10.19 (transparent blue arrows) by exemplarily using the phase diagrams of calcite (Ivanov and Deutsch, 2002) and quartz (Melosh, 2007) as a first-order approximation of the "carbonate" and "silicate" portions of a mixed sedimentary target. Our experiments are, thus, neither able to produce high-pressure phases (e.g., coesite, aragonite, ringwoodite, etc.), nor are they able to trigger the formation of planar deformation features or diaplectic glasses. However, considering general *P*–*T* relations of materials during shock compression (e.g., Zel'dovich and Raizer, 1967; Ahrens and O'Keefe, 1972; Melosh, 1989) and thermodynamic reasoning (Chapter 7 and, e.g., Ahrens and O'Keefe, 1972; Pierazzo et al., 1997; Kadono et al., 2002; Pierazzo et al., 2005), it follows that impact melts generally form *after* unloading, that is, during adiabatic decompression after passage of the impact-induced shock wave, and only if the residual heat that remains in the target is sufficient to induce melting (or even incipient vaporization). In Fig. 10.19, thermodynamic paths for the adiabatic release of shocked calcite and quartz from high shock pressures (50, 90, and 200 GPa, respectively) are shown to illustrate typical *P*–*T*

conditions during and after unloading. From Fig. 10.19 and the arguments outlined in Kadono et al. (2002) and Chapter 7, it follows that although the P–T paths during impact melting and laser melting are different, the resulting thermodynamic states (temperatures, entropies, densities, etc.) of the resulting melts are similar if appropriate experimental settings (laser intensity, duration of irradiation, etc.) are used.

10.4.2 Comparison of experimental products to natural impactites

The laser-generated melts of this study indeed bear many similarities to true impact melts formed in similar lithologies. For example, laser melting of the pure sandstone or basalt starting materials yields silicate glasses that mimic the composition and texture of silicate impact glasses known from the Wabar (Hörz et al., 1989; See et al., 1998; Hamann et al., 2013), Kamil (Fazio et al., 2016), or Lonar (Kieffer et al., 1976b) impact structures. Adding carbonate and iron meteorite components to the sandstone starting material obviously results in laser-generated glasses that mimic textural (e.g., Fig. 10.12d, f) and compositional (Fig. 10.16) trends known from impact glasses at Barringer Crater (Hörz et al., 2002; Mittlefehldt et al., 2005; Osinski et al., 2015). Furthermore, Martinez et al. (1994) described evidence for high-temperature reactions between silicate impact melts and carbonates in the impactites from Haughton (e.g., Ca,Mg-rich silicate glasses and Ca-rich silicates such as augite or larnite, Ca_2SiO_4). They also described dolomite assimilation by intruding silicate melt and hypothesized that certain calcite microtextures as well as oxygen- and carbon-isotopic signatures are indicative of calcite formation by back reactions between residual CaO and CO_2. Deutsch and Langenhorst (2007) documented in situ reactions of carbonates entrained in silicate impact melts from Chicxulub and described reaction fronts in which diopside ($En_{33–43}Fs_{12–19}Wo_{44–48}$) formed around carbonate clasts due to carbonate assimilation by surrounding silicate melt. Rosa and Martin (2010) described thermal metamorphosis of limestone xenoliths associated with silicate impact melt at West Clearwater Lake, yielding a variety of skarn minerals that are typically associated with contact metamorphism of limestone, some of which were encountered in our experiments (e.g., spurrite, merwinite, monticellite, srebrodolskite, and periclase). As already stated above, Hörz et al. (2002) and subsequently Hörz et al. (2015) and Osinski et al. (2015) ascribed Ca,Mg,Fe-rich silicate impact glasses and a variety of Ca,Mg,Fe-rich silicates at Barringer Crater to decomposition of carbonates and recombination of residual oxides with target-derived SiO_2 and Al_2O_3, as well as impactor-derived FeO and NiO. While Hörz et al. (2015) and Osinski et al. (2015) agreed that the Ca,Mg,Fe-rich silicate impact glasses reflect decomposition of carbonates in a specific part of the crater's melt zone, they disagreed on the nature and origin of globular or spherical calcite entrained in these glasses.

10.4.3 Decomposition or melting of carbonates upon impact? Or both?

Barringer Crater in Arizona, USA, provides a natural test site for impact melt formation in a mixed silicate–carbonate sedimentary target. Target and projectile compositions and properties are well-known (e.g., Hörz et al., 2002; Mittlefehldt et al., 2005; Hörz et al., 2015; Osinski et al., 2015) and impact glasses at Barringer mainly comprise four varieties:

1. extremely projectile-contaminated (~15–20% meteoritic component), high-Fe, Ca,Mg-bearing silicate glass ejecta (Hörz et al., 2002);
2. highly projectile-contaminated (~5% meteoritic component), low-Fe, Ca,Mg-rich silicate glass ejecta (Hörz et al., 2002);
3. high-Fe, Ca,Mg-bearing silicate glasses in impact-melt bearing breccias (Osinski et al., 2015); and
4. low-Fe, calcite-bearing silicate glass beads (Osinski et al., 2015).

The fate of carbonates at Barringer Crater—and, by analogy, also at other impact structures—is a subject of continuous debate, with some authors favoring wholesale decomposition of dolomite (e.g., Hörz et al., 2015) and others favoring a combination of decomposition and melting of dolomite in different parts of the crater's melt zone, followed by precipitation of globular calcite as a liquidus phase (e.g., Osinski et al., 2015).

Our iron meteorite–carbonate–sandstone experiment was designed to reproduce prominent textural and compositional characteristics of typical impact melts at Barringer Crater under idealized conditions. From the data presented above (Figs. 10.8, 10.10, and 10.16) it is apparent that the dominant response of dolomite to superheated silicate melts is thermal decomposition. Due to the fast quenching rates and pristine state of preservation of our experimental products, dolomite decomposition was fixed in various stages, ranging from incipient decomposition (Fig. 10.8a), to severe decomposition (e.g., Figs. 10.8c and 10.10c), to near-total decomposition (Fig. 10.10e), and, ultimately, to wholesale decomposition (represented by Ca,Mg-rich silicate glasses; e.g., Figs. 10.9f, 10.10, and 10.16). Residual CaO and MgO combined with SiO_2 derived from the sandstone component (at Barringer: derived from Moenkopi and Coconino) and FeO and NiO derived from the meteorite. Notably, in terms of major-element chemistry, our laser-generated glasses show similar, if not essentially identical, compositional ranges when compared to the impact melts at Barringer (Fig. 10.16). Subsequent crystallization of the silicate melts yielded a variety of minerals that reflect high contents of FeO, CaO, MgO, and NiO in the melts. In keeping with some of the previous investigators (e.g., Hörz et al., 2002; Hörz et al., 2015), we envisage that similar processes took place at Barringer, the clearest evidence being Fe,Ca,Mg-rich silicate glasses, Ca,Mg-rich pyroxenes, and Ca-bearing olivine.

These findings reinforce the view of Hörz et al. (2002) and Hörz et al. (2015): decomposition was the dominant response of dolomite during impact melt formation and evolution at Barringer Crater, followed by assimilation of CaO and MgO in the silicate impact melts. Similar evidence for the decomposition of calcite and assimilation of CaO in silicate impact melts at other impact structures (e.g., Haughton, Chicxulub, or West Clearwater Lake) has been summarized in the previous subsection. Here, we will use the phase diagrams of calcite (Fig. 10.19a; Ivanov and Deutsch, 2002) and quartz (Fig. 10.19b; Melosh, 2007) as first-order approximations of the "carbonate" and "silicate" portions of a mixed target to illustrate that these findings are not surprising. As outlined above, impact melts are generally considered as decompression melts that form after unloading from high pressure, following adiabatic release paths in pressure–temperature (Fig. 10.19) or pressure–volume planes. Typical adiabatic release paths of coexisting calcite and quartz shocked to high pressures, say, 90 GPa in the case of a completely non-porous target, will encounter the $CaCO_3$ liquid field (Fig. 10.19a) and the SiO_2 liquid field (Fig. 10.19b), respectively, producing true carbonate and silicate impact melts. Upon further pressure release, the $CaCO_3$ P–T path will encounter the field of solid $CaCO_3$ (i.e., crystallization of the melt, forming aragonite or calcite), whereas SiO_2 remains liquid (i.e., forming lechatelierite). Temperatures in the "carbonate" portion of the target will rapidly drop (<2000 K) during decompression, whereas temperatures in the "silicate" portion will remain high (>3000 K). As pressure drops towards normal, temperatures in the silicate melt will still be high (>3000 K), whereas temperatures in the newly formed calcite will be rather low (~1000 K), thereby inducing (partial) decomposition of the newly formed calcite and cooling of the silicate melt (i.e., isobarically moving to the right in Fig. 10.19a and isobarically moving to the left in Fig. 10.19b). Thus, we envisage that the initial response of calcite to high shock pressures is melting, but evidence of this melt phase is later readily destroyed by heat influx from coexisting silicate melts. In our view, textural and compositional evidence of this scenario is documented, for instance, in fig. 2a of Martinez et al. (1994) and fig. 2i of Osinski et al. (2008), which both show round calcite blebs surrounded by Ca-rich pyroxene. In this scenario, the amount of degassed calcite in a mixed carbonate–silicate target will obviously depend on several factors, including porosity, initial shock pressure, impedance contrast between carbonates and silicates, initial lithostatic pressure, final lithostatic pressure, final CO_2 partial pressure, final temperature, time span of pressure release, reaction kinetics, and amount of coexisting silicates (cf. Agrinier et al., 2001; Ivanov and Deutsch, 2002).

Consideration of the purely exemplary Fig. 10.19 also offers an explanation for the postulated existence of carbonate impact melts, for example, at the Ries (Graup, 1999; Osinski, 2003; Osinski et al., 2008) or Haughton impact structures (Osinski and Spray, 2001; Osinski, 2007; Osinski et al., 2008). We envisage that if a mixed carbonate–silicate target is shocked to pressures marginally capable of inducing melting of both carbonates and

silicates, the final temperature difference among the crystallized carbonate (i.e., calcite) and the silicate impact melt will be much closer than in the above example. This will especially be the case if silicates with lower shock-melting thresholds than quartz (e.g., feldspars, phyllosilicates) are abundant. Moreover, it is likely that if combined with other factors such as slightly elevated final pressures (e.g., lithostatic pressure in case of large volumes of impact melt), rapid cooling rates (e.g., in the case of small ejecta; cf. Chapter 7), or inhibited reaction kinetics (e.g., induced by high CO_2 partial pressures), the protracted thermal degassing of carbonates (cf. Deutsch and Langenhorst, 2007) might effectively be restrained, if not completely suppressed.

In conclusion, we argue that both decomposition *and* melting of carbonates takes place in mixed carbonate–silicate targets. Carbonate impact melts are readily produced in mixed carbonate–silicate targets, but coexisting high-T silicate impact melts subsequently induce thermal degassing of re-crystallized carbonate melts, thereby destroying the evidence of a primary carbonate melt phase. Under certain circumstances, however, post-shock P–T paths are favorable for the production and survival of a true, primary carbonate melt phase. We will later combine these thoughts into a working model that is presented in Fig. 10.20 and discussed in Subsection 10.4.7.

10.4.4 Melting of carbonates and silicate–carbonate liquid immiscibility in our experiments?

In situ melting of carbonates (i.e., production of liquid $CaCO_3$) was not unequivocally identified in our experiments. In all experiments, calcite grains in the immediate vicinity of calcite decomposition products often show vesicles that could be taken as evidence for incipient melting and degassing of the material (see Figs. 10.4a and 10.6a). However, all calcite decomposition products encountered in our experimental products have textures, compositions, and Raman spectra that suggest that they represent (non-stoichiometric?) quench phases rather than magmatic calcite that crystallized from a melt (cf. Jones et al., 2000; Deutsch and Langenhorst, 2007). Dolomite grains entrained in silicate glasses of the iron meteorite–carbonate–sandstone experiment (893) invariably show textures and compositions indicative of thermal decomposition. The fractures documented in the dolomite grains are filled with Ca-rich silicate glass (see Fig. 10.10c, d and Table 10.4) that formed as the result of mixing residual CaO and, to lesser extent, MgO into infiltrating silicate melt. In agreement with previous studies investigating magma–carbonate interaction at 1200 °C and 0.5 GPa (Deegan et al., 2010; Jolis et al., 2013), these findings indicate that thermal decomposition is the major mechanism that governs the fate of subcentimeter size carbonate clasts entrained in (superheated) silicate melts under non-equilibrium, high-T, low-P conditions.

There are, however, several textural and compositional observations that suggest that true calcio-carbonatite melts could have been formed

in the basalt–carbonate experiments (891/892) due to incorporation of carbonate components from proximally dissociating carbonates into the silicate melts (i.e., melting of carbonated basalt). The assemblages spurrite + calcite + oxide quench phases that occur in experiments 891 and 892 are rich in CaO, FeO, MgO, and CO_2 and contain substantial amounts of SiO_2 and Al_2O_3. Alkalis are extremely low (~0.2 wt.%; Table 10.3), reflecting either the alkali-poor composition of the average laser-generated basaltic melt ($Na_2O + K_2O \approx 3.5$ wt.%) or loss of alkalis due to high temperatures during the experiments (i.e., partial vaporization). In terms of textures, this material strongly resembles quenched carbonatite liquids in experiments performed to constrain the genesis of carbonatites (cf. fig. 3 in Lee and Wyllie, 1997; fig. 2 in Brooker and Kjarsgaard, 2011; or fig. 5 in Martin et al., 2013). In the pseudo-ternary system Na_2O–CaO–Al_2O_3–SiO_2–CO_2 (Fig. 10.15b; Lee and Wyllie, 1998), bulk compositions obtained from the material plot inside the carbonate liquidus field. Note that the exact arrangement of phase elements in the system Na_2O–CaO–Al_2O_3–SiO_2–CO_2 is poorly constrained for atmospheric pressure and that the phase relationships shown in Fig. 10.15b are valid for 1 GPa. Generally, with decreasing pressure and increasing temperature, the two-liquid field becomes smaller (e.g, Lee and Wyllie, 1996; Lee and Wyllie, 1997; Lee and Wyllie, 1998; Brooker and Kjarsgaard, 2011) until it is completely surrounded by the silicate liquidus surface, whereas with decreasing pressure, the silicate–carbonate liquidus field boundary moves toward the carbonate side (Lee and Wyllie, 1996; Lee and Wyllie, 1998). In the generalized tetrahedron CaO–(MgO + FeO)–($Na_2O + K_2O$)–($SiO_2 + Al_2O_3 + TiO_2$), the bulk compositions also plot inside the carbonate liquidus field for 1 GPa (Fig. D.2; Lee and Wyllie, 1998). If we consider melting of carbonated basalt at 1 GPa, we would expect to observe a range of melt compositions ranging from:

1. monomineralic, CO_2-free silicate precursor melts (e.g., partial melting of the feldspar component); to
2. well-mixed silicate melts that mimic the bulk composition of the basalt; to
3. Ca-enriched, vesicle-rich melts that assimilated substantial amounts of carbonate but that still are on the silicate side of the silicate–carbonate liquidus field boundary; and ultimately to
4. true carbonatite melts that are on the carbonate side of the silicate–carbonate liquidus field boundary.

Indeed, this is what we observe when individual melt compositions are plotted together with the bulk compositions of typical spurrite + calcite + oxide quench phase assemblages in the pseudo-ternary system Na_2O–CaO–Al_2O_3–SiO_2–CO_2 (Fig. 10.15a; Lee and Wyllie, 1998) or in the generalized pseudo-quaternary system CaO–(MgO + FeO)–($Na_2O + K_2O$)–($SiO_2 + Al_2O_3 + TiO_2$)–CO_2 (Fig. D.2; Lee and Wyllie, 1998).

However, our experiments were performed at atmospheric pressure, and temperatures were high enough to produce liquid CaO (e.g., Fig. 10.3) that rapidly back-reacted to form small, equant calcite crystallites (Fig. 10.6), even when incorporated in Ca-rich silicate melts (Figs. 10.11f, and 10.12c). It is, thus, questionable whether a carbonate liquid can be produced under these P–T conditions (cf. Deegan et al., 2010; Jolis et al., 2013). Instead, one might envisage other (simpler?) processes that would explain the carbonate-rich ("carbonatite-like") assemblage spurrite + calcite + oxide quench phases in the basalt–carbonate experiments (891/892).

Similar to the formation of calcic skarns, the most likely scenario is that the carbonate-rich inclusions in the silicate melts resemble high-T, low-P reaction zones known from contact metamorphism and metasomatism of limestone, as during shallow emplacement of plutonic bodies (e.g., Tilley, 1929; Tilley and Harwood, 1931; Joesten, 1976; Marineca et al., 2001; Pascal et al., 2001). Typical high-T skarn minerals include calcite, spurrite, tilleyite, $Ca_5(Si_2O_7)_3(CO_3)_2$, galuskinite, $Ca_7(SiO_4)_3(CO_3)$, wollastonite, larnite, rankinite, $Ca_3Si_2O_7$, merwinite, melilite, and, where silica is low or deficient, also brownmillerite and srebrodolskite. Thus, we envisage that spurrite was initially formed as a high-temperature phase at the interface between proximally decomposing carbonate and basaltic melt. At this interface, residual, possibly liquid CaO and volatile CO_2 from decomposing carbonate was incorporated into basaltic melt, leading to the formation of spurrite after the general reactions

$$CaO + SiO_2 + CaCO_3 \rightarrow Ca_2SiO_4 + CO_2 \qquad (R\,10.3)$$

and

$$2\ Ca_2SiO_4 + CaCO_3 \rightarrow Ca_5(SiO_4)(CO_3) \qquad (R\,10.4)$$

Rapid back-reactions between excess CaO and CO_2 produced small, equant crystallites of calcite (cf. Agrinier et al., 2001) that obviously differ from feathery (cf. Jones et al., 2000) or dendritic (cf. Lee et al., 1994; Brooker and Kjarsgaard, 2011) calcite that grew from a melt, or from round calcite equilibrium mineral phases (cf. Lee et al., 1994; Brooker and Kjarsgaard, 2011). Occasionally present MgO from decomposition of accessory dolomite did not react to magnesite or calcite–dolomite solid solution (cf. Agrinier et al., 2001) and, therefore, remained in the residual melt. Here, it combined with FeO and formed quench crystals of ferropericlase. The residual melt—depleted in SiO_2 and CaO but enriched in Al_2O_3 and, depending on the amount of carbonate-derived, residual MgO, also FeO (Fig. 10.14)—eventually precipitated upon quenching dendritic crystallites of either brownmillerite or srebrodolskite. Due to mechanical stirring during laser irradiation, these assemblages were either mixed into the silicate melts in the form of carbonate-rich inclusions (e.g., Figs. 10.10a and 10.11d) or remained at the interface between proximally dissociating carbonate and Ca-contaminated basaltic melt (e.g., Fig. 10.9c, d). In situ formation of this assemblage is possibly frozen-in in Fig. 10.10a. In this scenario,

CO_2 would primarily be present as a vapor phase and we would expect only limited amounts of CO_2 to be solved in the carbonate-precipitating silicate melts.

We conclude that the textures presented above are possibly not the result of silicate–carbonate liquid immiscibility *sensu stricto* (i.e., the unmixing of two liquids from a homogeneous precursor melt; see Chapter 8), nor do they represent quenched carbonatite liquids. The most likely interpretation is that they represent high-*T*, low-*P* contact zones known from calcic skarns produced during contact metamorphism of limestone. We expect that similar processes take place in impact melts or hot melt-bearing breccias, the most obvious evidence being documented in the impactites from Haughton (Martinez et al., 1994), Chicxulub (Deutsch and Langenhorst, 2007), and West Clearwater Lake (Rosa and Martin, 2010).

10.4.5 Silicate–carbonate liquid immiscibility in impact melts?

Liquid immiscibility between silicate and carbonate melts occurs across a wide range of compositions (see Figs. 10.15b and D.2 and, e.g., Koster van Groos and Wyllie, 1966; Koster van Groos and Wyllie, 1973; Freestone and Hamilton, 1980; Lee and Wyllie, 1996; Lee and Wyllie, 1997; Lee and Wyllie, 1998; Brooker and Kjarsgaard, 2011; Martin et al., 2013), but there are also continuous liquidus paths between alkali-poor silicate and carbonate-rich melts (e.g., Otto and Wyllie, 1993; Lee et al., 1994; Gudfinnsson and Presnall, 2005; Martin et al., 2013). In some studies (Kjarsgaard and Hamilton, 1988; Kjarsgaard and Hamilton, 1989; Brooker and Hamilton, 1990), a miscibility gap was postulated to exist at 0.5 GPa and 1250 °C that extends into alkali-free silicate-carbonate systems and that was envisaged to separate out an almost-pure $CaCO_3$ phase as an immiscible liquid. This interpretation was based on the presence of round globules or spheres of almost-pure $CaCO_3$ that showed several textural characteristics of a liquid phase (e.g., coalescing, vesiculation, budding, sharp menisci, etc.; see Chapter 8) in many experimental studies. Subsequently, it was shown that the round calcite globules are equilibrium mineral phases (Lee et al., 1994; Lee and Wyllie, 1996; Brooker and Kjarsgaard, 2011) rather than quenched $CaCO_3$ liquids whose shapes are controlled by surface tension (Lee et al., 1994). Further reports of silicate–carbonate liquid immiscibility in alkali-poor (Dasgupta et al., 2006; Thomsen and Schmidt, 2008) and alkali-free (Novella and Keshav, 2010) systems were later challenged and re-interpreted as carbonate-bearing quench products of CO_2-rich silicate melts (Martin et al., 2013).

While the influence of alkalis on the extent of the two-liquid field is controversial, the influence of pressure and temperature on the extent of the two-liquid field is much better constrained. In a series of experiments, Lee and Wyllie (1996) and Brooker and Kjarsgaard (2011) showed that the extent of the two-liquid field increases with decreasing temperatures and/or increasing pressures. According to these studies, the maximum extent of the two-liquid field is either reached at 1.5 GPa and ~1225 °C

(producing alkali-poor carbonatite liquids) or at 2.5 GPa and ~1300 °C (potentially producing alkali-free carbonatite liquids, but see Martin et al., 2013 for a different interpretation). Brooker and Kjarsgaard (2011) furthermore showed that the shape of the two-liquid field excludes exsolution of a pure $CaCO_3$ conjugate liquid and that alkali-poor immiscible carbonatite liquids will have SiO_2 + Al_2O_3 contents greater than 10–15 wt.%. At low pressures of 0.1 to 0.2 GPa and moderate temperatures of 1250 °C, the two-liquid field extends to alkali-poor compositions that have ~10 wt.% SiO_2 + Al_2O_3 (Brooker and Kjarsgaard, 2011).

Based on textural arguments, the occurrence of calcite spheres and globules in silicate impact glass from the Ries was first interpreted by Graup (1999) to represent genuine immiscibility between carbonate and silicate liquids. Unfortunately, the original description of Graup (1999) focused on textures alone and did not include detailed compositional data. Subsequently, Osinski and co-workers observed similar textures in impact glass from Ries (Osinski, 2003), Haughton (Osinski and Spray, 2001), and Barringer (Osinski et al., 2015) and provided major-element compositions of globular calcite surrounded by silicate impact glass. Ultimately, Osinski et al. (2008) came to the conclusion that these textures "provide unequivocal evidence for carbonates and silicate glasses being in the liquid state at the same time".

Given the arguments outlined above and illustrated in Figs. 10.15b and D.2, we respectfully submit that is it not unequivocally possible to identify silicate–carbonate liquid immiscibility based on putative "melt" textures alone. Liquid immiscibility *sensu stricto* refers to the unmixing of an initially homogeneous liquid into two conjugate liquids (e.g., a silicate and a carbonatite liquid, or Fe-rich and Si-rich silicate liquids) as the liquid encounters a miscibility gap upon cooling (Chapter 8; James, 1975; Roedder, 1978; Brooker and Kjarsgaard, 2011). As unmixing due to liquid immiscibility is governed by thermodynamics and structural properties (e.g., Schmidt, 2006; Veksler et al., 2006; Martin et al., 2013; Veksler and Charlier, 2015, and references therein), the compositions of the conjugate melts are controlled by the shape and position of the miscibility gap. Specifically, major- and trace-element partitioning between conjugate silicate and carbonatite liquids (expressed as carbonatite/silicate melt partition coefficients) is systematically governed by the melt's composition and, thus, its structure (e.g., Veksler et al., 1998; Veksler et al., 2012; Martin et al., 2013)—this has recently also been shown to be true for rapidly quenched silicate impact melts (Chapter 8; cf. Hamann et al., 2013). Considering the position of the miscibility gap in the system CaO–(MgO + FeO)–(Na_2O + K_2O)–(SiO_2 + Al_2O_3 + TiO_2)–CO_2 (Fig. D.2; Lee and Wyllie, 1998) and the arguments presented by Lee et al. (1994) and Brooker and Kjarsgaard (2011) concerning rounded/globular calcite, it is seems, thus, questionable that the calcite spheres and globules present in the Ries (Graup, 1999; Osinski, 2003; Osinski et al., 2008) and Haughton (Osinski and Spray, 2001; Osinski et al., 2008) impact glasses represent quenched liquids that unmixed from a homogeneous precursor melt (i.e., true liquid immisci-

bility) and not just solid mineral phases that underwent various degrees of assimilation by surrounding silicate impact melt, or a primary calcite impact melt phase that subsequently re-crystallized upon decompression (Fig. 10.19a). A more robust test for genuine immiscibility would be to determine carbonate/silicate melt partition coefficients and diffusion profiles (both assuming that the assemblages quenched in situ, thus reflecting the original silicate melt composition) in a similar fashion to those of Martin et al. (2013) for carbonatite liquids or Chapter 8 for silicate impact melts.

As noted by Graup (1999) and Osinski et al. (2008), some of the calcite in the Ries and Haughton impact glasses do contain certain amounts of SiO_2, Al_2O_3, MgO, and FeO (in terms of bulk composition enough to be considered as "carbonatite") that might indeed originate from liquid–liquid phase separation. Hörz et al. (2015) dismissed this possibility and concluded that elevated contents of SiO_2 and Al_2O_3 simply reflect contamination from material residing in minute interstices or as surface deposits on individual grains. In our view, these occurrences are potential candidates for subsequent studies focusing on major- and possibly trace-element partitioning between potentially shock-melted carbonates and silicate impact melts. In summary, we argue that positive identification of *sensu stricto* silicate–carbonate liquid immiscibility in impact glasses cannot be based on textures alone. In keeping with Osinski et al. (2008), who suggested that "the term 'carbonate–silicate liquid immiscibility' [should] be avoided unless there is unequivocal evidence for the unmixing of originally homogeneous impact melt", we propose that a robust test for *sensu stricto* silicate–carbonate liquid immiscibility in impact melts has to be based on textural *and* compositional data.

10.4.6 Carbonate assimilation in silicate impact melts

The principal and dominant mechanism of carbonate assimilation observed in our experiments is dissolution after carbonate decomposition, that is, breakdown of $CaCO_3$ or $CaMg(CO_3)_2$ molecules into their component parts CaO, MgO, and CO_2. Both CaO and MgO are readily incorporated into silicate melts of variable composition and structure, although initially homogeneous silicate melts may undergo unmixing during quenching if they encounter a silicate–silicate two-liquid field (see Figs. 10.9a, 10.11a, and 10.13b; cf. Chapter 8). In our experiments, transport and homogenization of carbonate-derived CaO and MgO in the silicate melts is probably initially dominated by agitating effects induced by direct laser irradiation. This would explain the well-homogenized nature of most melt volumes (e.g., top right and top left corners of Figs. 10.2d and 10.9c, respectively) as well as the mixing trends observed, for example, in the basalt–carbonate or iron meteorite–carbonate–sandstone experiment. Transport of CaO and MgO in the silicate melts after cease of laser irradiation is probably mainly governed by diffusion in response to the strong chemical gradient imposed by the dissociating carbonate (Figs. 10.2c, 10.9a, 10.10d, and 10.17). For example, Figs. 10.17a illustrates

that dissociation of calcite due to heat influx from surrounding silicate melt locally results in enrichment of CaO in the melt, forming a layer of Ca-rich, vesicular melt that separates calcite crystals and calcite decomposition products from Ca-normal or slightly Ca-contaminated sandstone melt. In this case, the compositional contrast between the dissociating carbonate and the sandstone melt is large. The Ca-rich melt seems to have remained in contact with the marble layer and eventually became saturated in dissolving components, yielding pseudowollastonite crystallites that nucleated at places were CaO and SiO_2 had molar proportions of ca. 1:1 ("CaO pile-up" in Fig. 10.17b). With increasing distance from the proximally dissociating calcite, CaO contents of the Ca-rich melt drop from ~46 wt.% to ~33 wt.%, whereas SiO_2 increases from ~51 wt.% to ~62 wt.%.

Comparing this scenario to the line profile given in Fig. 10.17d, it seems that carbonate assimilation in silicate melts that are less contrasting in composition is less pronounced. The Ca,Mg-rich glass around the relict dolomite grain has ~23–25 wt.% CaO and ~13 wt.% MgO. The effective length of diffusion of Ca into the surrounding Ca,Mg-rich silicate melt is some 10–20 μm at best as illustrated by increased CaO/MgO ratios, whereas in Fig. 10.17a it is on the order of ~100 μm. This indicates that carbonate assimilation is obviously limited by the time during which the silicate melt was in contact to dissociating carbonate, but also that carbonate assimilation is governed by compositional gradients between the dissociating carbonate and the silicate melt (no diffusion without a chemical gradient). To some extent, carbonate assimilation is probably also limited by the diffusivity of Ca (and Mg in case of dolomite assimilation) through the surrounding silicate melt (cf. Deegan et al., 2010; Jolis et al., 2013). In large, slowly cooled volumes of impact melt (e.g., melt sheets in complex craters), we would expect convection due to compositional gradients, temperature and density differences within the melt, or mechanical agitation of the melt to remove Ca- or Ca,Mg-rich melts from the reaction interface—this would possibly increase the rate of assimilation because a large compositional gradient would be maintained at the interface between carbonate fragment and silicate melt (cf. Deegan et al., 2010). In rapidly cooled impact melt volumes, we would, however, expect to find similar textural evidence of diffusion/composition-controlled carbonate assimilation. We envisage that fig. 2a of Martinez et al. (1994) or fig. 2i of Osinski et al. (2008)—both showing subround calcite (representing relict, re-crystallized carbonate melts?) surrounded by Ca-rich, feathery pyroxene (representing quenched, Ca-rich silicate melts)—experienced such diffusion/composition-controlled carbonate assimilation in silicate impact melts.

In addition to mechanical agitation or diffusion/composition-controlled homogenization, viscosity differences between carbonate-contaminated and carbonate-free silicate impact melts might also influence melt mixing and mingling (cf. Deegan et al., 2010). Using the model of Giordano et al. (2008) and the silicate glass compositions presented in Table 10.4, we

can exemplarily calculate melt viscosities for the Ca- and Ca,Mg-rich melts in comparison to melt viscosities of the starting materials. Note, however, that (1) the model does not take pressure into account; (2) that it is only calibrated for SiO_2 contents between 41 and 79 wt.%, CaO contents below 26 wt.%, and FeO contents below 12 wt.%; and (3) that the model database only covers temperatures below 1705 °C (anhydrous melts) or 1580 °C (volatile-bearing melts). Hence, we cannot estimate the viscosities of the most Ca-rich melts (with CaO contents exceeding 40 wt.%; e.g., experiments 889 and 891), nor can we estimate melt viscosities at "typical" impact melt temperatures (i.e., >1700 °C; cf. Fig. 10.19b). However, one also might argue that in impact melts mixing and mingling of different melts takes place within rather large temperature intervals (e.g., from >1700 °C to some 1000 °C). By arbitrarily setting the temperature to 1200 °C, we calculate the following viscosities for the average melt compositions presented in Table 10.4: $\log \eta = 6.68$ Pa s for experiment 889 (~15 wt.% CaO), $\log \eta = 0.26$ Pa s for experiments 891 and 892 (~26 wt.% CaO), and $\log \eta = 1.82$ Pa s for experiment 893 (~20 wt.% CaO; ~10 wt.% MgO; note that this melt has ~15 wt.% FeO and is, thus, slightly outside the model calibration). Relative to the database of silicate melt viscosities of Giordano et al. (2008), the average Ca- and Ca,Mg-rich melts of our experiments have low viscosities. For comparison, at ~1200 °C pure SiO_2 melt (lechatelierite; e.g., Fig. 10.17a, b) has a viscosity of $\log \eta = 279.9$ Pa s (Urbain et al., 1982), whereas at 1200 °C the basaltic starting composition has a calculated viscosity of $\log \eta = 0.57$ Pa s. Widely contrasting viscosities between silicate melts can effectively hinder melt homogenization (e.g., Grasset and Albarède, 1994; Troll et al., 2004; Deegan et al., 2010, and references therein), which partially explains why the melts of experiment 889 are substantially less homogenized compared to experiments 891, 892, and 893 (cf. Figs. 10.2c, d or Figs. 10.17a and 10.9c). However, as has been shown above (e.g., Figs. 10.9a and 10.11a), the silicate melts of experiment 889 are also affected by liquid immiscibility, which, apart from physical separation, is the most effective mechanism for suppressing melt homogenization. We envisage that similar viscosity differences effectively hinder or even completely suppress melt homogenization of rapidly cooled impact melts, especially if CaO-rich or even $CaCO_3$-rich melts are mixed into felsic silicate impact melts.

10.4.7 Impact melting of mixed carbonate–silicate sedimentary targets: a working model

Assessing whether carbonate decomposition or melting dominates upon impact is obviously a difficult task, given the contrasting reports of evidence for both processes in impactites from one and the same impact structure (e.g., Martinez et al., 1994; Osinski and Spray, 2001; Hörz et al., 2015; Osinski et al., 2015, and others). Based on theoretical considerations of the calcite phase diagram (Fig. 10.19a; Ivanov and Deutsch, 2002), it is highly likely that primary calcite melts are readily formed upon

decompression from high (>70 GPa?) shock pressures in typical terrestrial impact scenarios. The reports of calcite ocelli, blebs, and deformed spherules in the impactites from Ries (Graup, 1999), Chicxulub (Jones et al., 2000), Haughton (Osinski and Spray, 2001), and Barringer Crater (Osinski et al., 2015) might indeed attest to this process. In contrast, the numerous reports of silicate melt-induced decomposition reactions in the same impactites argue that impact melting of carbonates can only be part of the story. Although confined to Barringer Crater, Hörz et al. (2015) even applied a temporary coupe de grâce by arguing that whilst universally accepted criteria for the recognition of primary carbonate impact melts as well as modal data on abundance and distribution of these melts are lacking, the postulate that melting is the dominant response of carbonates to hypervelocity impacts is premature and unjustified.

By combining our findings of carbonate assimilation by silicate melts under low pressure with petrographic findings of previous studies (e.g., Martinez et al., 1994; Graup, 1999; Jones et al., 2000; Agrinier et al., 2001; Osinski and Spray, 2001; Deutsch and Langenhorst, 2007; Osinski et al., 2008; Stöffler et al., 2013; Hörz et al., 2015; Osinski et al., 2015) and theoretical considerations of the phase diagrams of calcite (Ivanov and Deutsch, 2002) and typical silicates (e.g., Ahrens and O'Keefe, 1972; Melosh, 2007), we propose the following working model of impact melting of mixed carbonate–silicate sedimentary targets. As a caveat, we note that caution is needed when generalizing findings from different impact structures and different experiments, as hypervelocity impacts are highly idiosyncratic events, each of which being unique and controlled by a variety of factors that differ for every single impact structure (see discussion in Hörz et al., 2015).

Figure 10.20 summarizes our working model, which distinguishes between two major cases: Fig. 10.20a illustrates the *protracted degassing* of initially formed and subsequently crystallized carbonate impact melt by heat influx due to surrounding silicate melt (Scenario A), whereas Fig. 10.20b illustrates formation and *conservation* of primary, subsequently crystallized carbonate impact melt in coexistence with silicate impact melt (Scenario B). In both cases, we assume that carbonates and silicates are initially juxtaposed in the form of individual strata, for example, as in the case of the Ries (Graup, 1999) or Haughton (Osinski and Spray, 2001) impact structures (Stage 1 in Fig. 10.20). We envisage that, depending on their pre-impact positions, certain volumes of this mixed target are

1. either shocked to high pressures, commensurate with the production of whole-rock melts of both the silicate and the carbonate portion (Fig. 10.20a; "Scenrio A" Fig. 10.19); or

2. shocked to somewhat lower pressures that are only marginally capable of producing carbonate and silicate melts, thereby producing a mixture of silicate and carbonate melts and lithic and/or mineral clasts (Fig. 10.20b; "Scenario B" in Fig. 10.19).

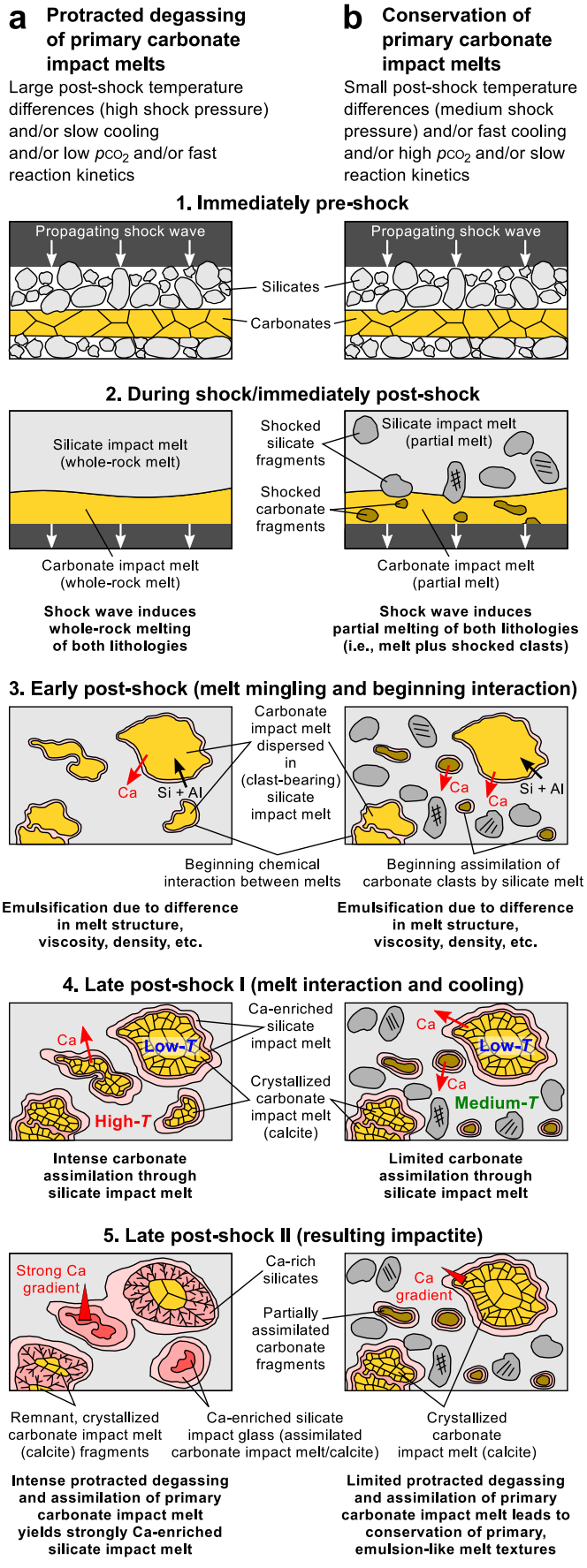

Figure 10.20 Sketch of a potential working model of impact melting of mixed carbonate–silicate sedimentary targets. **a** Scenario A favoring the intense protracted degassing of initially produced carbonate impact melt, potentially yielding textures like those depicted in fig. 2a of Martinez et al. (1994) or fig. 2i of Osinski et al. (2008). **b** Scenario B favoring the conservation of initially produced carbonate impact melt, potentially yielding textures like those depicted in figs. 5–7 of Graup (1999), fig. 2d–e of Deutsch and Langenhorst (2007), or fig. 2a–f of Osinski et al. (2008). Note that the protracted outgassing of cold carbonate clasts entrained in silicate impact melt is not explicitly shown as an individual scenario, but is included in the scenario on the right (Stages 3–5). See text for discussion.

The pressure thresholds that govern incipient and complete melting of the carbonate and the silicate portion of the target obviously depend on a variety of factors, the most important ones being the type and modal abundance of specific minerals (e.g., Ahrens and O'Keefe, 1972) and the target's porosity (e.g., Wünnemann et al., 2008; Kowitz et al., 2016). Therefore, discussion of the phase diagrams presented in Fig. 10.19 and definition of exact shock conditions for the two scenarios can only be purely qualitative. During decompression, that is, along the release isentropes (Fig. 10.19), both melts form individually (Stage 2) and begin to mingle during the subsequent excavation stage (starting between Stage 2 and Stage 3 in Fig. 10.20). During excavation it is also likely that rock/melt volumes originating from different zones in the opening crater are mixed (e.g., Dressler and Reimold, 2001), thereby relativizing the need of an initially stratified target to some extent. Homogenization of the silicate and carbonate impact melts at Stage 3 and subsequent stages is effectively hindered due to large differences in melt structure and viscosity (see Subsection 10.4.6), yielding emulsion-like melt textures documented, for instance, in the Ries suevites (Graup, 1999). However, both melts will start to chemically equilibrate by diffusion, the clearest evidence being Ca-enriched silicate melts around fluidal-shaped carbonate fragments that are, in turn, enriched in Si and Al, as mentioned by Graup (1999). Since typical carbonate melts are ionic liquids that do not satisfy the requirements for glass formation (Genge et al., 1995), the carbonate melt will rapidly crystallize upon decompression and subsequent cooling (Stage 4 in Fig. 10.20; cf. the carbonate release paths in Fig. 10.19a), forming igneous calcite as reported from the Ries (Graup, 1999) or Chicxulub (Jones et al., 2000; Deutsch and Langenhorst, 2007) impactites. To the contrary, the silicate melt will remain liquid much longer (see the silicate release paths in Fig. 10.19b) and, depending on the cooling rate, either quench to a glass or crystallize to an impact melt rock.

Up to this stage, both scenarios result in the formation of a primary carbonate impact melt phase that subsequently crystallizes and that exchanges, to various extents, Ca (as well as Mg in the case of dolomite) with surrounding silicate impact melt. Incorporation of other elements (e.g., Si and Al) into the carbonate impact melt due to diffusional equilibration could also explain the documented abundance of these elements in putative carbonate melt phases (e.g., Graup, 1999; Osinski and Spray, 2001; Osinski et al., 2008), although these findings have been questioned by others (e.g., Hörz et al., 2015). However, it is nevertheless tempting to speculate that highly elevated concentrations of Si and Al in fluidal-shaped calcite could indeed be a potential recognition criterion for quenched calcite impact melts, as it has been demonstrated that globular, rounded calcite precipitated as a liquidus phase is always pure $CaCO_3$ (Lee et al., 1994; Lee and Wyllie, 1997; Brooker and Kjarsgaard, 2011).

Once this carbonate impact melt has been produced, we conceive that two alternative mechanisms may operate that either result in intense protracted decomposition of the crystallized carbonate melt in Scenario A

(Fig. 10.20a), or favor conservation of the crystallized carbonate melt due to limited, if not effectively prevented, carbonate assimilation in Scenario B (Fig. 10.20b). As outlined above, the major factor governing either decomposition or conservation of the crystallized carbonate melt might be temperature differences between the silicate melt and the crystallized carbonate melt—"large" differences favoring decomposition, "small" differences conservation—, but other factors can be envisaged that would also influence the chance of survival of the crystallized carbonate melt. For instance, the final post-shock pressure immediately influences the temperature threshold for carbonate decomposition (Fig. 10.19a), with higher final pressures stabilizing solid carbonates to higher temperatures. Depending on the CO_2 partial pressure and reaction kinetics, the decomposition reaction (R 10.1) might be shifted to either the products or educts side (cf. Agrinier et al., 2001; Ivanov and Deutsch, 2002), thus either favoring or hindering carbonate decomposition. More obviously, carbonate decomposition will also depend on exact cooling rates (which in the case of impact melts can be quite heterogeneous, even in small melt volumes; e.g., Hörz et al., 2002) and, thus, the time span that allows high-T reactions between the materials (which can be quite variable over short distances).

In conclusion we argue that both decomposition *and* melting of carbonates can occur in parallel in specific volumes of impact melt or melt-bearing breccia that originate from different pre-impact positions, or that experience different P–T–pCO_2 conditions and/or cooling rates during and after decompression. It is, however, beyond doubt that the reaction of carbonates to hypervelocity impact is a complex, highly idiosyncratic process. Hence, answering the question of which process dominates might not be universally possible, but requires careful consideration of the unique makeup of projectile (velocity, size, composition/density, impact direction, etc.) and target (composition, porosity, stratification, water content, etc.), as well as the post-impact geological history (hydrothermal activity, tectonic overprint, etc.) of every single impact structure (Hörz et al., 2015). It remains that many observations on naturally shocked carbonate–silicate targets (especially containing dolomite instead of calcite as the main carbonate mineral) are still enigmatic and demand further, multidisciplinary investigation.

10.5 Summary and conclusions

High-T interactions between silicates and carbonates during meteorite impacts were simulated by 1-bar laser melting of composite targets, using sandstone, basalt, calcite marble, limestone, dolomite marble, and iron meteorite as natural planetary starting materials. Our experiments demonstrate that carbonate assimilation by silicate melts of various compositions is extremely fast, operating on time scales of tens of seconds to minutes, and invariably results in silicate melts that are contaminated with carbonate-derived, solid or liquid residual oxides (CaO and/or MgO)

and release of CO_2 at the carbonate–silicate melt interface. Depending on the starting materials (e.g., sandstone vs. basalt, calcite vs. dolomite), we identify several major processes at the carbonate–silicate melt interface.

1. Thermal decomposition of calcite and/or dolomite due to heat influx from surrounding silicate melt yields residual oxides (CaO and/or MgO) and CO_2.

2. Incorporation of residual oxides from proximally dissociating carbonates into silicate melt yields Ca- or Ca,Mg-enriched ("contaminated") silicate melts.

3. Rapid back-reactions between residual, highly reactive CaO and CO_2 produces micrometer-size, equant calcite crystallites at the carbonate–silicate melt interface. Residual MgO does not back-react to magnesite or dolomite, but may combine with FeO to ferropericlase.

4. High-temperature reactions between Ca- or Ca,Mg-contaminated silicate melts and carbonates may result in a variety of typical calc-silicate skarn minerals such as spurrite and merwinite. Formation of a residual, Si,Ca-depleted and Al,Fe-enriched oxide melt due to precipitation of calc-silicates yields oxide phases such as brownmillerite or srebrodolskite.

5. Physical and chemical (diffusion/composition-controlled) mixing and mingling between Ca- or Ca,Mg-contaminated and unaffected silicate melts.

6. Precipitation of Ca- or Ca,Mg-rich silicates such as pseudowollastonite, melilite, monticellite, kirschsteinite, or Ca-rich clinopyroxene in the contaminated silicate melts upon quenching.

Our experiments reproduce many textural and compositional petrographic features of true impact melts from impact structures that formed in mixed silicate–carbonate targets, such as Barringer Crater, Haughton, Ries, and Chicxulub. Our experiments reinforce hypotheses that thermal decomposition of carbonates, rapid back-reactions between highly reactive, residual CaO and CO_2, as well as incorporation of residual oxides into silicate melts are abundant, if not dominant, processes during impact melting of mixed silicate–carbonate targets. However, by comparing our 1-bar experimental results with previous petrographic studies and thermodynamic considerations on the phase diagrams of calcite and typical silicate minerals (e.g., quartz), we envisage that primary carbonate impact melts are readily produced during adiabatic decompression from high shock pressures, but subsequently decompose/alter upon pressure release due to heat influx from coexisting silicate impact melts. Under certain circumstances, depending on temperature differences between carbonate and silicate melt, final post-shock pressure, CO_2 partial pressure, reaction kinetics, etc., post-shock conditions may favor production

and conservation of primary carbonate impact melts (e.g., documented at the Chicxulub, Ries, or Haughton impact structures), possibly in one and the same samples that also bear evidence of carbonate decomposition. Thus, the response of mixed carbonate–silicate targets to impact might involve melting and decomposition of carbonates, the dominant response being governed by a complex and idiosyncratic variety of internal and external factors.

Acknowledgments

We appreciate the assistance of Dominic Heunoske during the experimental campaign and are furthermore indebted to Hendryk Schneider and Hans-Rudolf Knöfler for skillful preparation of parts of our experimental setup and samples. We thank Kirsten Born for assistance at the SEM, Kathrin Krahn for XRF sample preparation, Ralf-Thomas Schmitt for XRF analysis, and Peter Czaja for assistance at the microprobe. Ralf-Thomas Schmitt generously opened his mineralogical collection and provided some reference samples of spurrite, larnite, brownmillerite, and srebrodolskite from the Eifel mountains, Germany, that were used as internal Raman standards. We furthermore thank Natasha Artemieva for fruitful discussions and for providing ANEOS calculations of adiabatic release paths of calcite used in Fig. 10.19, as well as Sanni Siegert for insightful discussions on the Ries suevites and our working model. This publication is part of the PhD thesis of CH, who acknowledges the Barringer Crater Company for sponsoring two travel grants to MetSoc Meetings and the Lunar and Planetary Institute for granting a LPI Career Development Award. This work was conducted in the framework of the DFG-funded Multidisciplinary Experimental and Modeling Impact Research Network MEMIN. The research unit is DFG FOR 887 and this is project He-2893/8-2.

Associate editor: Mike Zolensky

Part IV

Conclusions and outlook

Chapter 11

Conclusions

The collision of solid bodies at cosmic encounter velocities is a fundamental process in the solar system. Impact processes played a dominant role during early formation stages of our solar system, shaped the surfaces of most solid planetary bodies (including Earth), and even affected the evolution of life on our planet (Chapter 1). However, due to the complexity of planetary-scale impact events, the short time scales involved, and the extreme pressure and temperature conditions during impact (Chapter 2), the process itself, in its entirety, is difficult to study in nature.

Very early time steps of crater formation as well as the physical and chemical interaction between projectile and target during these early time steps are especially difficult to assess from impactites. For example, in large, complex impact structures, the projectiles are dominantly vaporized, the resulting impactites are typically poor in projectile material, the original interface between projectile and target is lost and impossible to reconstruct, and postimpact processes further impede reconstruction of transient processes and products of early time steps of crater formation (Chapter 3; Dressler and Reimold, 2001). At some small terrestrial craters, such as Meteor Crater (Hörz et al., 2002; Hörz et al., 2015; Osinski et al., 2015), Wabar (Hörz et al., 1989; Hamann et al., 2013), or Kamil (Fazio et al., 2016), general conditions and preservation state of the resulting impactites are more fortuitous (Chapter 8). These circumstances have allowed reconstruction of melt-mixing process during cratering (e.g., Chapter 8 and See et al., 1998) and delivered insights into the general formation of impact melts (e.g., Chapters 8, 9, and Hörz et al., 1989; Mittlefehldt et al., 1992; Hörz et al., 2002; Mittlefehldt et al., 2005; Hamann et al., 2013; Hörz et al., 2015; Osinski et al., 2015; Fazio et al., 2016) under conditions as ideal as possible in nature. Apart from studies on terrestrial craters and terrestrial as well as extraterrestrial impactites, impact experiments—both in the laboratory (e.g., Chapters 5, 6, and Wozniakiewicz et al., 2011; Ebert et al., 2013; Ebert et al., 2014; Wozniakiewicz et al., 2015) and by means of numerical modeling (e.g., Chapter 6 and Wünnemann et al., 2016; Svetsov and Shuvalov, 2016; Goderis et al., 2017)—are an important tool to gain insight into transient processes that operate during crater formation. However,

experiments and, more so, numerical models must be validated against observations on terrestrial impact structures and terrestrial as well as extraterrestrial impactites.

The major goals of this dissertation (cf. Chapter 3) were: (1) to reconstruct early physical and chemical processes at the projectile–target interface; (2) to contribute to our understanding of mixing processes between impact melts of different structure and/or composition under dynamic disequilibrium conditions; (3) to reconstruct petrogenetic processes in compositionally complex impact melts, in particular those originating from carbonate-bearing targets; (4) to constrain minimum time scales associated with these processes, particularly in ballistic melt ejecta (e.g., melt spherules, tektites etc.); and (5) to evaluate whether melts that are produced in impact- and laser-irradiation experiments are veritable analogs to impact melts produced in nature. To this end, findings from conventional hypervelocity impact experiments and newly designed laser irradiation experiments were combined with observations on pristine planetary impact glasses and impact melt rocks that were found to document melt-mixing and petrogenetic processes virtually ideally. Although evident, this *integrated* approach of combining experiments with observations within a single study is insofar novel as that the experiments were performed with similar planetary materials (e.g., sandstone, basalt, iron meteorite, limestone) that were also involved in the formation of the natural examples.

Apart from answering specific scientific questions that were outlined in the respective results chapters (Chapters 5–10 in Parts II and III), direct, continuous-wave laser irradiation was further developed and established in this dissertation (Chapters 7, 8, and 10) as an adequate experimental technique that allows melting and vaporization of planetary materials virtually instantaneously. This was done on the basis of thermodynamic reasoning (Chapter 7) and a petrologic comparison of the experimental products against terrestrial impact melts (Chapters 8 and 10). These experiments allow simulation of impact-melt formation (and, by analogy, also impact vaporization; cf. Gerasimov et al., 1998; Kadono et al., 2002; Ohno et al., 2004; Ishibashi et al., 2013) in high-fidelity scenarios under dynamic disequilibrium conditions typical of hypervelocity impact. Such conditions are otherwise rarely encountered in "conventional" petrologic experiments (e.g., piston-cylinder experiments, diamond anvil press, etc.), and are much harder to achieve in conventional hypervelocity impact experiments performed with two-stage light-gas guns.[16] Furthermore, the laser irradiation experiments allowed for the first time to combine real-time imaging and temperature measurements of the melts with subsequent petrographic investigations of the resulting glasses. This has so far neither been done in previous laser irradiation experiments (e.g., Gerasimov et al., 1998; Kadono et al., 2002; Ohno et al., 2004; Ishibashi et al., 2013),[17] nor in conventional hypervelocity impact experiments (cf., e.g., Ebert et al., 2013; Ebert et al., 2014; Wozniakiewicz et al., 2015; Daly and Schultz, 2016), and is generally not possible in confined shock-reverberation experiments

[16] The major limitations of conventional hypervelocity impact experiments with macroscopic projectiles are comparatively low impact velocities (some 7 or 8 km s^{-1} at best) and small melt volumes that are produced

[17] An exception is the study of Ebert et al. (2017), which was also done in the framework of MEMIN and under participation of the PhD candidate (laser experiment 887 was investigated both in Chapter 7 and in Ebert et al., 2017)

(cf., e.g., Kowitz et al., 2016). Although not capable of creating high shock pressures, the experiments allowed production of superheated melts with temperatures >2100 °C that have been shown (Chapters 7, 8, and 10) to thermodynamically, texturally, and mineralogically resemble true impact melts formed during adiabatic decompression. In particular, the laser-generated melts, formed from various combinations of natural planetary materials, resembled genuine impact melts from terrestrial impact structures (e.g., Wabar, Kamil, Barringer, Haughton; Chapters 8 and 10) and the conventional MEMIN two-stage light-gas gun impact experiments (Chapter 8).

Each of the chapters presented in Parts II and III is self-contained, that is, results have been discussed and distinct conclusions have been drawn in each of these chapters. In the following, this chapter picks up the five general points that were presented in Chapter 3 and discusses the findings of Parts II and III in the light of these topics.

11.1 Early physical and chemical processes at the projectile–target interface

One of the major driving forces that stimulated this study was the question:

- What physical and chemical processes occur immediately at the *projectile–target interface*?

A complete and in situ reconstruction of a projectile–target interface was documented in conventional hypervelocity impact experiments (Chapter 5); this finding was independently confirmed by numerical modeling techniques (Chapter 6 and Wünnemann et al., 2016). A major result that emerges from this dissertation is that in decimeter-size craters formed in porous materials in low-velocity (~4–6 km s^{-1}) scenarios such as impacts of micrometeoroids into asteroidal regoliths, physical mixing between projectile and target is inefficient, and projectile-derived melts are preserved as discrete melt volumes (melt spheres or even continuous melt coatings) that are intimately associated with target-derived melts. This is particularly the case for metallic impactors such as iron meteorites (Chapters 5 and 6), but similar impact experiments performed with basaltic projectiles (Daly and Schultz, 2016) showed that this is also the case for silicate impactors such as chondrites or achondrites. The physical mixing between projectile and target melts is limited in such scenarios,[18] but the chemical interaction between these two melt volumes, although confined to only a small fraction of the crater's melt zone, is exceptionally fast and efficient (Chapters 5 and 6). Based on the comparison with the numerical model (Chapter 6), it was suggested that the chemical interaction between projectile and target melts may operate on time scales measured in fractions of total crater-growth time (i.e., within microseconds in the case of the experiments). The major outcomes of Chapters 5 and 6 are:

[18] The majority of the projectile remains as a continuous melt coating; minor volumes of largely immiscible, metallic projectile melt are disseminated in the form of individual melt spherules within silicate melts (see Chapter 5)

- Reconstruction of the projectile–target interfaces in hypervelocity impact experiments that simulated impacts of metallic micrometeoroids into asteroidal regoliths at ~6 km s^{-1} revealed that layered impact melt particles essentially sample the floors of the transient craters during very early time steps of crater formation
- Physical and chemical processes along the projectile–target interface involve complete melting of the projectile, partial melting of the target, redox reactions between the liquid projectile and the partially molten target, and physical dissemination of immiscible projectile melt spheres in target melts
- Under these impact conditions, the liquid projectile is spread over the partially molten and shock-lithified target during crater formation, thereby becoming an integral part of centimeter-size impact melt particles
- Planetary implications are that impacts of millimeter-size projectiles into regolith-covered surfaces, for example on 1 Ceres or 4 Vesta, at typical impact velocities in the main belt (4–6 km s^{-1}) should yield qualitatively similar impact melt particles
- Projectile-derived melts are likely preserved in such regoliths in the form of discrete, sizeable melt volumes that potentially influence surface reflectance spectra
- Subsequent studies are needed to evaluate whether this is also the case for oblique impacts, in which projectile-coated impactites may be ejected from the crater at velocities in excess of escape velocity and in trajectories that favor escape from the planetary surface into open space

In the terrestrial impact structures studied here, ranging between 45 m and 1.9 km in diameter and generally involving much higher impact velocities >10 km s^{-1}, the physical mixing between projectile- and target-derived melts was much more efficient. However, as attested by abundant projectile melt spherules present in the impactites from Wabar, Kamil, and Barringer, complete homogenization of both melt volumes was still not achieved before the melts quenched to glasses or crystallized to impact melt rocks (Chapter 8). At larger (mid-sized) impact structures such as the Ries (26 km diameter), heterogeneity of impact melt has been recently described (e.g., Siegert et al., 2017), indicating incomplete mixing of impact melts at the initial projectile–target interface and/or during later stages of crater formation. Taking into account findings from even larger complex impact structures whose impact melts are typically described as "well-mixed" and "homogeneous" (e.g., Dressler and Reimold, 2001, and references therein), the general picture that emerges is that both the efficiency of projectile admixture as well as the subsequent homogenization of projectile- and target-derived melts is positively correlated with

crater size. However, in the case of large craters and/or high impact velocities, additional physical processes can be envisaged to operate along the projectile–target interface that are not reproduced by the impact experiments presented in Part II, and that are apparently not documented in the terrestrial impactites studied in Part III. These include bulk vaporization and possible melt–vapor interaction (e.g., Svetsov and Shuvalov, 2016), as well as development of Kelvin–Helmholtz instabilities between projectile- and target-derived melt volumes (e.g., Goderis et al., 2017).

Based on the presence of a substantial meteoritic component in the ballistic ejecta studied in Chapter 8 and consideration of the findings of Chapters 5 and 6, it follows that physical admixture of projectile melts into target melts is essentially an early process that happens *prior* to ejection and, thus, within very short time scales that are measured in fractions of total crater-growth time. Subsequent dilution of projectile melts within volumetric dominant target melts as well as chemical interaction (e.g., chemical diffusion, element exchange, melt unmixing) between individual melt volumes and other petrogenetic processes such as crystallization occur on much longer time scales, that is, during cooling and emplacement of the melt mixture.[19] These processes are governed by factors like total melt volume, initial melt temperature, and cooling rate (Chapters 5 and 8), but are probably also influenced by structural or compositional differences of individual melts (Chapters 8 and 10) as well as the presence or absence of volatiles (e.g., Kieffer and Simonds, 1980; Siegert et al., 2017). Physical mixing due to differential particle velocities of individual melt volumes during crater growth probably further enhances the degree of melt homogenization prior to ejection (cf. See et al., 1998). This is evident when laser-generated melts formed from layered targets (e.g., iron meteorite layer on top of sandstone layer) are compared to the impact melts from Wabar or Kamil: although petrologically largely similar, the terrestrial impactites are substantially more well-mixed (yet still not completely homogenized; Chapter 8). Laser-melting of pre-homogenized, multicomponent targets such as the powder target investigated in Chapter 10 can, however, effectively simulate physical mixing in the dynamic crater environment. Such a setup was found to be capable of producing well-mixed melts similar to those of terrestrial craters (e.g., Barringer; Chapter 10).

The interfaces between FeNi metal host and silicate impact melt in the Netschaëvo IIE iron meteorite allowed to study the chemical interaction between these two materials in a different planetary setting (Chapter 9). The impact history of Netschaëvo was previously recognized (Van Roosbroek et al., 2016), and a careful reconstruction of the thermal history of this impact breccia was subsequently presented in Chapter 9. The major findings from Chapter 9 are:

- In keeping with Van Roosbroek et al. (2016), the fine-grained, hyaline silicate melt inclusions preserved in the Netschaëvo IIE iron meteorite are silicate impact melts

[19] Thus, petrogenesis of small melt ejecta such as melt spherules and tektites differs from petrogenesis of large impact-melt pools or sheets—the former obviously involves short time scales and fast cooling rates, whereas the latter involves long time scales and slower cooling rates

- The silicate impact melt shows compositional variations that result from element exchange with the surrounding FeNi metal (i.e., partitoning of P and Fe from the metal into the silicate melt)
- Crystal morphologies, mineral compositions, and the presence of phase-separated silicate glass droplets in the silicate inclusions hint at fast cooling rates that are commensurate with hypervelocity impacts, but incompatible with endogenic models involving slow cooling rates over geologic time scales
- Impact processes may have played an important role on the IIE parent body

Regarding the chemical interaction between metal and silicate lithologies (i.e., between projectile and target),[20] it was found that similar processes as discussed in Chapters 5 and 8 have occurred in Netschaëvo (Chapter 9). These include partitioning of elements (e.g., P and Fe) from the metal into the silicate melt, unmixing of silicate impact melt, emulsification of metal or sulfide melts and silicate melts, and incorporation of metal-derived elements in silicate minerals. Specifically, the P-rich silicate melt close to the metal host documents that in Netschaëvo a similar process took place like in the terrestrial impactites and experimental analogs (see Chapter 8). In the latter, Fe was partitioned from projectile-derived FeNi metal into target-derived silicate impact melt (cf. Ebert et al., 2013; Hamann et al., 2013; Fazio et al., 2016). These findings suggest that such processes could be largely insensitive to the presence or absence of atmospheric oxygen; however, subsequent studies as well as immediate comparisons to lunar impactites are necessary to fully evaluate the role of oxygen for such processes during impact.

[20] However, it remains to be seen which of the two materials was the projectile and which the target

In conclusion, it has been shown in this dissertation that the chemical interaction between projectile- and target-derived melts at the projectile–target interface is extremely fast and efficient. Depending largely on the materials involved, this interaction may include redox reactions (e.g., oxidation of FeNi metal or artificial aluminum alloy by silicate impact melt; Chapters 5, 8, and 9), contamination of target melts by projectile melts (Chapters 5, 8, and 10), melt unmixing in miscibility gaps (Chapter 8), emulsification of structurally incompatible melts (Chapter 8), as well as inter-element fractionation during melt mixing (Chapters 5, 8, 9, and 10).[21] The experiments presented in Chapters 5–8 showed that such processes may operate on time scales measured in fractions of crater-growth time, thus bearing on our understanding of projectile signatures documented in ballistically ejected melt volumes that originate at early time steps of crater formation from shallow depths in the crater's melt zone (e.g., melt spherules at Wabar, Kamil, and Barringer: Hörz et al., 1989; Hörz et al., 2002; Hamann et al., 2013; Fazio et al., 2016, or tektites: Goderis et al., 2017). For example, it seems plausible that tektites can indeed carry a significant projectile component that was admixed into target-derived, shallow melts during earliest time steps of crater formation. However, this

[21] Some of these processes will be further discussed below

assumes that tektites are produced along the projectile–target interface and under involvement of projectile melts (i.e., during or after melting of the projectile; see Goderis et al., 2017).

11.2 Mixing of structurally or compositionally different impact melts under disequilibrium conditions

After the initial physical contact between projectile and target, the stage is set for mixing and homogenization between projectile- and target-derived melts, as well as for mixing and homogenization of individual target-derived melts. In Chapter 3, the following two questions were asked that aim at understanding such mixing and homogenization processes:

- What happens during physical and chemical *mixing* of structurally or compositionally diverse impact melts under dynamic disequilibrium conditions?
- In which respect differs mixing and homogenization of miscible, yet structurally or compositionally diverse impact melts from mixing and homogenization of immiscible impact melts?

Mixing of structurally compatible (e.g., two or more silicate melts; Chapter 8) as well as of structurally incompatible impact melts (e.g., silicate melt and metal melt; Chapters 5 and 8–9) was investigated in this dissertation. Focus was given on centimeter to decimeter size ballistic ejecta originating from simple terrestrial impact craters (Chapter 8), but melt-mixing processes were also investigated in impact (Chapters 5 and 8) and laser irradiation experiments (Chapters 8 and 10) as well as in an extraterrestrial impact melt (Chapter 9).

Mixing of structurally compatible, perfectly *miscible* impact melts[22] at high temperatures (generally >1700 °C) in the dynamic crater environment typically results in schlieren of variable chemical composition. Such schlieren are abundant in the terrestrial impactites studied here (e.g., Wabar, Barringer; see Chapter 8; Hörz et al., 1989; Hörz et al., 2002; Hamann et al., 2013; Hörz et al., 2015; Osinski et al., 2015), and they are also abundant in the experimentally generated melts (Chapters 7, 8, and 10). With increasing degree of homogenization—which seemingly depends primarily on crater size, initial temperature, and the time span at which the melt mixture is held above liquidus or above the glass transformation range—differences in composition among individual schlieren become less pronounced, until a well-mixed, essentially homogeneous hybrid melt is formed. Such melts were produced in the larger craters studied here (Barringer, Tenoumer; see Chapter 8; Hörz et al., 2002; Hörz et al., 2015; Osinski et al., 2015; Schultze et al., 2016) as well as in the laser irradiation experiments that employed an initially well-mixed target (the powder mixture of Campo del Cielo, sandstone, and dolomite studied in Chapter 10). An important observation (cf. also the previous section) is that mechanical mixing, for example, induced by differential particle

[22] For example, digestion of silicates entrained into superheated silicate impact melt; melting and mixing of monomineralic precursor melts derived from melting of individual silicates comprised within a lithologic unit; or mixing of whole-rock silicate melts originating from different parts of the crater's melt zone

velocities in the dynamic crater environment, appears much more efficient than simple "chemical" mixing that is or is not induced by, for example, differences in density, temperature, or viscosity of the participating melt batches. This becomes apparent from laser-generated melt mixtures that formed within "deep" melt zones from layered targets. These were much less well-mixed than those melt mixtures that formed at "shallower" melt zones, and which presumably experienced pronounced stirring by direct laser irradiation.

Mixing of miscible silicate impact melts has been shown in this dissertation to typically produce a range of compositions that follow mixing lines defined by the compositions of the individual melt volumes (e.g., Chapters 8 and 10). In simple scenarios that involve only a limited number of starting compositions (e.g., Wabar, Kamil, Barringer, all experiments presented here), detailed reconstruction of melt-mixing processes is feasible (cf. also Hörz et al., 1989; Mittlefehldt et al., 2005; Hamann et al., 2013; Ebert et al., 2013; Fazio et al., 2016; Ebert et al., 2017). Such reconstructions become more involved with increasing number of participating lithologic components (e.g., Tenoumer), up to the point were modal abundances of participating starting compositions cannot be given with reasonable confidence (cf. Schultze et al., 2016). Furthermore, some petrogenetic processes during cooling, such as crystallization or emulsification (see below), tend to obscure primary mixing signatures by inducing fractionation, yet this is seemingly only operating on the micrometer scale and only when individual phases are considered (Chapters 8 and 10; cf. Mittlefehldt et al., 1992; Hamann et al., 2013; Ebert et al., 2013; Ebert et al., 2014; Ebert et al., 2017). If bulk compositions or modal recombinations of all phases are considered, mixing of miscible silicate impact melts seems to be essentially unaffected by fractionation (cf. also Mittlefehldt et al., 2005). However, partial vaporization of those elements or chemical species with the lowest vaporization temperatures (e.g., H_2O, CO_2, Na, K; trace elements such as Rb or Cs) may readily induce fractionation even on non-microsopic scales (e.g., Floss et al., 1996; Gerasimov et al., 2005), for example, when bulk compositions or large batches of melt are considered, yet this was not unequivocally documented in this dissertation.

Mixing of structurally incompatible, *immiscible* impact melts[23] at high temperatures in the dynamic crater environment differs from mixing of structurally compatible, miscible impact melts. For example, metallic projectile melts have been shown to be largely immiscible to silicate impact melts (Chapters 5 and 8; cf. Hamann et al., 2013; Ebert et al., 2013; Ebert et al., 2014; Fazio et al., 2016), forming emulsions in which metal droplets are disseminated within a silicate melt matrix.[24] These two melts have been shown to chemically interact with each other during the mixing process (Chapters 5 and 8; cf. also Hörz et al., 1989; Hamann et al., 2013; Ebert et al., 2013; Ebert et al., 2014; Fazio et al., 2016; Ebert et al., 2017), inducing fractionation, on the micrometer scale, due to selective partitioning of projectile-derived elements into the coexisting silicate melt (e.g., Hamann et al., 2013; Ebert et al., 2013; Fazio et al., 2016). Partitioning of Fe

[23] For example, admixture of impactor-derived FeNi metal into silicate impact melt, or mixing of carbonate and silicate impact melts

[24] Similar assemblages are also known from impact-melt veins in chondrites (e.g., Stöffler et al., 1991)—these form in situ by melting and emulsification of the silicate, metal, and sulfide components of the meteorite (e.g., Moreau et al., in press) and, thus, usually do not represent chemical interaction between projectile and target

from the projectile melt into the silicate melt was furthermore recognized (Chapters 8 and 9) as the main cause of phase-separation in the Wabar, Kamil, and Netschaëvo melts (cf. also Hamann et al., 2013; Fazio et al., 2016), as well as in the experimental analogs (cf. also Ebert et al., 2014; Ebert et al., 2017).

Although true carbonate melts were not produced in the laser irradiation experiments, emulsification of immiscible carbonate and silicate impact melts, as envisaged by Graup (1999) or Osinski et al. (2008), was discussed in Chapter 10 in the light of mixing between carbonate decomposition products (CaO, MgO, and CO_2) and silicate impact melt. In contrast to mixing between silicate impact melt and carbonate decomposition products, which results in heavily Ca- or Ca,Mg-enriched silicate melts (as discussed in Chapter 10 and in the next section), mingling and mixing between carbonate and silicate impact melts results in silicate–carbonate emulsions (e.g., Graup, 1999; Osinski et al., 2008). It was discussed (Chapter 10) that these melts do not represent emulsions formed by *unmixing* of a single, homogeneous precursor melt (i.e., liquid immiscibility *sensu stricto*),[25] but rather represent emulsions that form due to the stark contrast in structure and viscosity of the two melts as they become admixed to another (e.g., as in the case of metal–silicate or sulfide–silicate emulsions documented in Chapters 8 and 9). Thus, it is entirely plausible and to be expected that such silicate–carbonate emulsions exchange elements among the two phases (Chapter 10), which would explain, for example, elevated contents of SiO_2 and Al_2O_3 in some carbonate occurrences (e.g., Osinski et al., 2008). However, subsequent experimental studies are necessary to quantify element exchange between silicate and carbonate melts in such emulsions.

[25] This possibility was dismissed in Chapter 10 based on findings from quenching experiments aimed at understanding the petrogenesis of carbonatites: the silicate–carbonatite miscibility gap does not extend to pure $CaCO_3$ (e.g., Lee and Wyllie, 1998; Martin et al., 2013); hence, carbonate melts formed by unmixing cannot be pure $CaCO_3$, but rather contain several percent by weight of alkalis, SiO_2, and Al_2O_3

11.3 Petrogenetic processes in impact melts, with special emphasis to carbonate-bearing targets

In Chapter 3, two questions were asked that informed investigation of rock-forming processes in impact melts:

- What *petrogenetic processes* operate during cooling of compositionally complex impact melts, in particular of those originating from carbonate-bearing targets?
- Can experiments shed light onto transient petrogenetic processes during melt formation and cooling that are inaccessible from natural impactites?

The studies on silicate liquid immiscibility in impact melts (Chapters 8 and 9) and silicate melt–carbonate interaction (Chapter 10) provided new insights into rock-forming processes in impact melts.

Chapter 8 represents the first comprehensive study of silicate liquid immiscibility in terrestrial impact melts. It was backed up by Chapter 9, which represents the first clear evidence of silicate liquid immiscibility

in meteorites. Although silicate liquid immiscibility is well-known from terrestrial and lunar magmas (e.g., Roedder, 1951; Roedder and Weiblen, 1970; Roedder and Weiblen, 1971; Philpotts, 1982; Charlier et al., 2013; Veksler and Charlier, 2015, and references therein), it was so far only marginally studied in the context of impact melts (the most detailed previous studies being Zolensky and Koeberl, 1991 and Hamann et al., 2013). It was shown in Chapter 8 that unmixing of silicate impact melt follows similar thermodynamic and structural causes as unmixing of endogenous terrestrial magmas of, for example, basaltic composition: the tendency of a system to minimize its Gibb's free energy and the poor steric compatibility between network-forming (mainly Si^{4+}) and network-modifying (e.g., Fe^{2+}, Mg^{2+}, and Ca^{2+}) cations is the driving force behind melt unmixing. Although formed under chemical disequilibrium, the resulting emulsion textures and liquid compositions were shown to represent those known from terrestrial magmas and melts formed in conventional petrologic experiments, which both generally tend to form and cool under chemical equilibrium.[26] However, in impact melts, bulk compositions and temperatures can be reached that are unknown from terrestrial magmas (e.g., Wabar). Unique to impact melts is also that miscibility gaps can be reached by melting and mixing various progenitor lithologies, forming an "exotic" bulk melt composition that coincides with this miscibility gap (e.g., Wabar, Kamil, Netschaëvo). Moreover, bulk impact melt compositions (e.g., Wabar black melt) may also coincide with high-temperature, "quasi-binary" miscibility gaps (e.g., SiO_2–FeO; $T > 1700\,^{\circ}C$) that are usually inaccessible to endogenous magmatic systems (Chapter 8). On the other hand, crystallization of initially homogeneous (i.e., non-phase-separated) impact melt might shift the composition of a residual liquid into a miscibility gap (e.g., Barringer, Tenoumer) in a similar way as in the case of more slowly crystallizing, endogenous terrestrial magmas (cf. Philpotts, 1982). Chapter 8 also presented petrologic tools to distinguish between true melt unmixing (liquid immiscibility *sensu stricto*) and emulsification caused by mixing and incomplete homogenization of structurally incompatible impact melts (e.g., FeNi metal spherules disseminated within silicate impact melt). In conclusion, silicate liquid immiscibility was appreciated as a much more common petrogenetic process in impact melts than previously thought.

[26] Attainment of chemical equilibrium is often exhaustively discussed in experimental petrology, as this is one of the major factors that governs application of experimental findings to nature (e.g., Bogaerts and Schmidt, 2006; Veksler et al., 2007; Charlier and Grove, 2012; Martin et al., 2013)

The reaction between carbonates and superheated silicate melts, taken as impact melt analogs, was investigated in Chapter 10 by using newly designed laser irradiation experiments. In particular, the interaction between silicate melts and carbonates during postshock stages of impact crater formation were investigated by using direct laser irradiation to melt (and partially vaporize) carbonate–silicate composite targets under P–T conditions typical of postshock stages of crater formation. In contrast to previous studies—hypervelocity impact experiments and confined shock-recovery experiments performed mostly with calcite or dolomite single crystals and generally in absence of silicates (see Bell, 2016, and references therein)—this approach is novel in several aspects:

- It allowed for melting of mixed carbonate–silicate rock targets under ambient pressure, and, thus, realistically simulated impact-melt formation, mixing, and interaction after pressure release
- It allowed for a detailed petrologic investigation of the reaction of carbonates to superheated silicate (impact) melts
- It allowed to constrain reaction times and cooling rates associated with carbonate decomposition by coexisting silicate melts

It was shown in Chapter 10 that carbonate decomposition by coexisting silicate impact melt is extremely fast (tens of seconds), resulting in contamination of silicate melt with carbonate-derived CaO and MgO and release of CO_2 at the silicate melt–carbonate interface. Specifically, the following (partially transient) processes were shown to occur at the silicate melt–carbonate interface: (1) thermal decomposition of carbonate releases CO_2 and produces residual oxides (CaO, MgO); (2) incorporation of residual oxides from proximally dissociating carbonate into silicate melt; (3) rapid back-reactions between residual CaO and CO_2 form equant calcite crystallites and porous carbonate quench products; (4) high-temperature reactions between Ca-contaminated silicate melt and carbonate yield typical skarn minerals and residual oxide melt; (5) mixing and mingling between Ca- or Ca,Mg-contaminated and unaffected silicate melts; (6) precipitation of Ca- or Ca,Mg-rich silicates in contaminated silicate melt upon quenching. The experiments were shown to reproduce many textural, compositional, and mineralogical features of impact melts produced in carbonate-bearing terrestrial craters such as Barringer (Hörz et al., 2002; Hörz et al., 2015; Osinski et al., 2015), Haughton (Martinez et al., 1994; Osinski and Spray, 2001; Osinski et al., 2008), Chicxulub (Jones et al., 2000; Claeys et al., 2003; Deutsch and Langenhorst, 2007), or West Clearwater Lake (Rosa and Martin, 2010). These findings suggest that upon pressure release, "protracted" decomposition of carbonates by heat influx from coexisting silicate impact melt—as envisaged by Deutsch and Langenhorst (2007)—is the dominant process during impact melting of mixed silicate–carbonate targets. A combination of the experimental findings presented in Chapter 10, findings from previous studies (e.g., Martinez et al., 1994; Graup, 1999; Jones et al., 2000; Agrinier et al., 2001; Osinski and Spray, 2001; Osinski et al., 2015; Hörz et al., 2015), and consideration of the phase diagrams of calcite (Ivanov and Deutsch, 2002) and quartz (Melosh, 2007) suggests, however, that carbonate impact melts are indeed readily produced during adiabatic decompression from high shock pressures, as envisaged by a number of studies (e.g., Graup, 1999; Jones et al., 2000; Osinski et al., 2008). It was discussed that the preservation of this primary carbonate melt phase depends on a complex variety of idiosyncratic factors (e.g., differences in postshock temperature between carbonate melt and silicate melt, final lithostatic pressure, CO_2 partial pressure, reaction kinetics, etc.) that likely differ from impact structure to impact structure. Eventually, a working model was presented

that suggests that carbonate impact melts are readily produced during adiabatic decompression, but preservation of this primary melt phase depends on a complex variety of idiosyncratic factors that are governed by the unique makeup of each impact event. In conclusion, it was suggested that hypervelocity impacts into mixed silicate–carbonate targets may involve both melting *and* decomposition of carbonates, thus bringing together seemingly contrasting findings on terrestrial impact structures like Haughton (e.g., Martinez et al., 1994; Osinski and Spray, 2001), Ries (e.g., Graup, 1999; Stöffler et al., 2013), or Chicxulub (e.g., Claeys et al., 2003; Deutsch and Langenhorst, 2007). The working model also suggests that impact-induced CO_2 degassing of carbonate-bearing targets during hypervelocity impact is more complex than previously thought, which has in turn implications for estimating the net amount of CO_2 that is discharged into the atmosphere immediately after such impacts (e.g., as in the case of Chicxulub; cf. Pierazzo et al., 1998; Deutsch and Langenhorst, 2007; Brugger et al., 2017.

11.4 Time scales and cooling rates involved in formation and cooling of ballistic melt ejecta

As this thesis was concerned mainly with ballistic melt ejecta, one initial question (cf. Chapter 3) was:

- What are typical *time scales* and *cooling rates* involved in formation and cooling of millimeter- to centimeter-sized ballistic melt ejecta (e.g., melt spherules, tektites, etc.)?

The laser irradiation experiments presented in Chapters 7, 8, and 10 allowed to constrain time scales and cooling rates associated with formation and cooling of millimeter- to centimeter-size melt volumes formed from various combinations of natural planetary materials (i.e., sandstone, basalt, iron meteorite, calcite and dolomite marbles, limestone). The measured cooling profiles were found to follow power laws with negative exponents, and found to match cooling profiles that were modeled using thermodynamic data. In particular, it was shown that cooling rates depend both on melt volume (larger volumes cool slower than smaller ones) and material properties (density, heat capacity; e.g., metallic melts cool faster than silicate melts), and typically involve initial cooling rates of several hundred Kelvin per second (e.g., quenching of droplets of sandstone melt a few millimeter in size from >2373 K to ~773 K took ~7 seconds, translating to a cooling rate of 300 K s^{-1}). For largely similar melt volumes, the cooling rates obtained in Chapter 7 agree well with modeled cooling rates of, for example, Stöffler et al. (2002), who modeled the thermal evolution of tektite melts ejected from the Ries crater by means of numerical modeling (e.g., see cooling profile for a 0.7-cm-diameter melt droplet in fig. 8 of Stöffler et al., 2002). Furthermore, the good agreement between measured cooling profiles and simple thermal models (Chapter 7) bestows confidence in planetary applications such as investigation of impact flashes on

the Moon (e.g., Bouley et al., 2012; Luther et al., 2017) that rely, in part, on such thermal models.

The measured and modeled cooling profiles constrain general time scales of melt-mixing, glass formation, crystallization, and other petrogenetic processes in ballistic ejecta of similar size and similar thermodynamic properties. For example, it is suggested that the abundant, centimeter-sized ballistic melt ejecta of Meteor Crater (Chapters 8 and 10; Hörz et al., 2002; Hörz et al., 2015; Osinski et al., 2015) have fully solidified on time scales measured in tens of seconds. Depending on the initial temperature, millimeter- to centimeter-size melt ejecta (e.g., tektites, impact melt spherules) will cool within several seconds to temperatures below the glass transformation range of typical silicate melts, thus constraining the time scales of the rock-forming processes discussed in the previous sections to similar time scales.

11.5 Application of experiments to nature

This thesis is heavily based on experimental findings. Consequently, two of the initial questions that were asked in Chapter 3 were:

- Are hypervelocity impact and laser irradiation experiments a suitable tool to study melt-mixing processes in and petrogenesis of impact melts?
- Can such results be "scaled up" to natural impact scenarios?

Although not the prime objective of this thesis, these questions can be partially answered by comparing the experimental products of both impact- and laser-melting experiments against terrestrial impactites formed from similar starting materials. For example, in Chapter 8, it was shown that the impact- as well as the laser-irradiation experiments indeed produced melts that, in terms of mineralogy, chemical composition, texture, and thermodynamics, are similar to true impact melts (ballistic ejecta) formed in the Wabar, Kamil, Barringer, and Tenoumer impact structures. In this chapter it was also shown that both unmixing of silicate melt as well as mixing or emulsification of diverse progenitor melts in the experiments is similar to the natural examples, resulting in melts that share typical characteristics of the natural examples. These findings are backed up by the other MEMIN experiments described by Ebert et al. (2013), Ebert et al. (2014), and Ebert et al. (2017), who compared their experimentally generated impact melts against the Wabar and Barringer melts and showed that similar chemical processes (e.g., impactor fractionation, physical dissemination of the impactor melts, emulsification of metal and silicate melts, etc.) occurred in both nature and experiment (cf. also Hamann et al., 2013; Fazio et al., 2016). It was furthermore shown in Chapter 10 that if appropriate materials similar to the target and projectile materials in natural impact scenarios are used, the laser irradiation experiments are capable of producing melts that are—leaving the generation of *sensu*

stricto shock effects such as PDF or diaplectic glasses aside—in all petrologic aspects similar to the impact melts known from that specific impact structure (e.g., Meteor Crater).

On the other hand, conventional state-of-the-art hypervelocity impact experiments are obviously not suited to investigate the petrogenesis of large volumes of impact melt (e.g., impact-melt pools or sheets), and the CW laser irradiation experiments described here neither produce dominantly pressure-dependent schock effects (e.g., PDF, high-pressure polymorphs, diaplectic glasses, etc.), nor do they produce typical structural features of impact craters (e.g., craters, crater rims, ejecta blankets, etc.). Despite these limitations, one of the major findings that emerges from this dissertation is that if natural planetary materials are used in hypervelocity impact or laser irradiation experiments, melts can be produced that allow detailed investigations of petrogenetic processes in impact melts such as the interaction between projectile and target melts along the projectile–target interface (Chapter 5), mixing of impact melts under highly dynamic disequilibrium conditions (Chapters 5, 8, and 10), the interaction between carbonates and superheated silicate melts (Chapters 10), melt unmixing in miscibility gaps (Chapter 8), as well as crystallization during cooling (Chapters 8 and 10). In particular, the many similarities between

1. the impactites produced in the MEMIN impact experiments (A20-5339 in Chapter 8; also D3-3298 described by Ebert et al., 2013) and the Wabar and Kamil melts (Chapter 8);

2. the laser-generated basaltic melts of experiment 892 and the impact melts known from Lonar (Chapter 7; Kieffer et al., 1976b);

3. the laser-generated melts of experiments 887 and LE-I and the Wabar and Kamil melts (Chapter 8); and

4. the laser-generated melts from carbonate–silicate composite targets (e.g., experiment 893) and the impact melts from, for example, Barringer (Chapter 10)

bestow confidence in such experimental approaches. These comparisons show that the experiments employed here are indeed a suitable tool to investigate the general petrogenesis of impact glasses and impact melt rocks, with the caveat that only ballistic melt ejecta have been considered in this dissertation.

Chapter 12

Outlook

This thesis has delivered several new brushstrokes to the greater picture of impact-melt genesis, yet much remains to be done until this picture is complete.

In Part II, discussion of projectile retention in asteroidal regoliths was based on impact experiments that were performed at angles of 90° to the target surface. Oblique impacts were not simulated in the experiments, although these are statistically much more frequent than vertical impacts. The impact experiments of Daly and Schultz (2016) included oblique impacts and clearly showed that projectile retention is sensitive to impact angle, ranging from 7% for 30° impacts to 72% for vertical impacts (averaging 17% of the mass of the projectile retained over all probable impact angles). However, such experiments have one common, inevitable problem that makes transfer of results to asteroidal environments questionable: gravity. Numerical models (e.g., the ones presented in one of the conference abstracts that served as the foundation of Chapter 6) can overcome this problem and are able to simulate impacts under reduced gravity. If combined with impact experiments aimed at investigating structure, mineralogy, and composition of resulting impactites (which are so far not accessible in numerical models), future studies could shed light onto standing issues like the paucity of agglutinates in asteroidal regolith breccias, or the paucity of impact melt products in the Hayabusa samples.

It also remains to be seen if numerical models can actually benefit from the direct comparison presented in Chapter 6. Such comparisons already validate numerical models, as shown by Wünnemann et al. (2016), but the small scale of the impact experiments raises the question if results can be scaled up to impact structures of several kilometers, or even hundreds of kilometers, in diameter. In the case of the experiments, it is evident that the models tend to treat the projectile as a strength-less fluid that is smeared along the floor of the transient crater up to very late time steps, eventually forming a thin, infinitesimal veneer that covers the bottom of the transient crater. In the experiments, however, it could be shown that the projectile does not thin out infinitesimally, but is preserved as a discrete, lens-shaped object coating the target-derived impact melt particles. Interestingly, the layers of the impact melt particles—from top to bottom: projectile coating,

heavily projectile-contaminated silicate melt, projectile-free silicate melt, brecciated and shock-lithified target—can be qualitatively transferred to reconstructed melt zones of much larger craters, such as Kamil (45 m diameter; Fazio et al., 2016) or Wabar (116 m diameter; Hörz et al., 1989; Mittlefehldt et al., 1992; Hamann et al., 2013). For these craters, it was shown that heavily projectile-contaminated silicate impact melt (black melt; cf. Chapter 8) existed in the uppermost parts of the craters' melt zones, whereas the lowermost parts of the melt zones were occupied by projectile-free silicate impact melt (white melt; cf. Hörz et al., 1989; Fazio et al., 2016). Obviously, there is much left to do to correlate the initial findings presented in Chapter 6 to small, simple impact structures.

Pulsed laser irradiation has been shown to be well-suited to simulate impact vaporization (e.g., Gerasimov et al., 1998; Kadono et al., 2002; Ohno et al., 2004; Ishibashi et al., 2013). However, as already alluded to in Chapter 7, the high irradiation intensities used in previous studies resulted in laser-generated vapor plumes that were thermodynamically similar to vapor plumes generated in impact scenarios with extreme impact velocities (50–120 km s^{-1}). Using continuous-wave laser irradiation and the setup described in Chapter 7, less laser intensity is delivered to the target, and much more realistic impact energies and, thus, impact velocities (a conservative estimate is 4–50 km s^{-1}, depending in the laser intensity) can be simulated. Hence, the obvious next step would be to investigate impact vaporization and condensation processes using the experimental setup of Chapter 7. Direct, continuous-wave laser irradiation under the conditions presented in Chapter 7 could be further developed and adapted to investigate other flash-heating events, such as the formation of chondrules in the solar nebular, melting of soil during lightning strikes, or any other dominantly thermal process that requires near-instantaneous heating followed by rapid cooling.

A standing issue in the planetary sciences that was touched upon in Chapter 10 is: what definite recognition criteria could be established to unequivocally identify carbonate impact melts? Most previous attempts have relied on textures (e.g., Graup, 1999) or internal structures (e.g., Jones et al., 2000; Claeys et al., 2003), although some others (e.g., Osinski et al., 2008) also consulted "anomalous" major-element compositions of the carbonate. However, textures alone can be misleading, as shown by round carbonate crystals produced in quenching experiments (e.g., Lee et al., 1994; Brooker and Kjarsgaard, 2011), and enrichment of Si or Al in the carbonate has been discussed as representing impurities present along grain boundaries (e.g., Hörz et al., 2015). To overcome these issues, on possible approach could be to investigate element exchange between silicate melt and carbonate melt, in hope to find diffusion profiles or other chemical indicators of chemical interaction. Obviously, unified recognition criteria for primary carbonate impact melts are needed; establishing these will be a major task for future studies.

Bibliography

Agrell, S. O., Charnley, N. R., and Chinnger, G. A. (1998). Phosphoran olivine from Pine Canyon, Piute Co., Utah. *Mineralogical Magazine* 62, 265–269.

Agrinier, P., Deutsch, A., Schärer, U., and Martinez, I. (2001). Fast back-reactions of shock-released CO_2 from carbonates: an experimental approach. *Geochimica et Cosmochimica Acta* 65, 2615–2632.

Ahrens, T. J. and O'Keefe, J. D. (1972). Shock melting and vaporization of lunar rocks and minerals. *Earth Moon Planets* 4, 214–249.

Ahrens, T. J. and O'Keefe, J. D. (1977). Equations of state and impact-induced shock-wave attenuation on the moon. *Impact and explosion cratering.* Ed. by D. J. Roddy, R. O. Pepin, and R. B. Merrill. New York: Pergamon Press, 639–656.

Alvarez, L. W., Alvarez, W., Asaro, F., and Michel, H. V. (1980). Extraterrestrial cause for the Cretaceous–Tertiary extinction. *Science* 208, 1095–1108.

Anders, D., Kegler, P., Buchner, E., and Schmieder, M. (2011). Carbonate melt lithologies from the Steinheim impact crater (SW Germany). *42nd Lunar and Planetary Science Conference, #1997 (abstr.),* Houston.

Anders, E., Ganapathy, R., Krähenbühl, U., and Morgan, J. W. (1973). Meteoritic material on the Moon. *The Moon* 8, 3–24.

Anderson, J. L. B., Schultz, P. H., and Heineck, J. T. (2004). Experimental ejection angles for oblique impacts: implications for the subsurface flow-field. *Meteoritics & Planetary Science* 39, 303–320.

Armstrong, J. T., Kennedy, A. K., Carpenter, P. K., and Albee, A. L. (1990). Petrography and trace element chemistry of Colomera (IIE) silicate inclusions: rhyolitic plums in the pudding. *21st Lunar and Planetary Science Conference, #22 (abstr.),* Houston.

Artemieva, N. and Pierazzo, E. (2009). The Canyon Diablo impact event: projectile motion through the atmosphere. *Meteoritics & Planetary Science* 44, 25–42.

Artemieva, N. and Pierazzo, E. (2011). The Canyon Diablo impact event: 2. projectile fate and target melting upon impact. *Meteoritics & Planetary Science* 46, 805–829.

Artemieva, N., Wünnemann, K., Krien, F., Reimold, W. U., and Stöffler, D. (2013). Ries crater and suevite revisited – observations and modeling, Part II: modeling. *Meteoritics & Planetary Science* 48, 590–627.

Asimov, P. D. and Ghiorso, M. S. (1998). Algorithmic modifications extending MELTS to calculate subsolidus phase relations. *The American Mineralogist* 83, 1127–1132.

Baratoux, D. and Reimold, W. U. (2016). The current state of knowledge about shatter cones: introduction to the special issue. *Meteoritics & Planetary Science* 51, 1–46.

Bargossi, G. M., Del Moro, A., Ferrari, M., Gasparotto, G., Mordenti, A., Rottura, A., and Tateo, F. (1999). Caratterizzazione petrografico–geochimica e significato dell'associazione monzogranito-inclusi femici microgranulari della Vetta di Cima d'Asta (Alpi Meridionali). *Mineralogica et Petrographica Acta* 42, 155–179.

Basilevsky, A. T., Yakovlev, O. I., Fisenko, A. V., Semjonova, L. F., Moroz, L. V., Pieters, C. M., Hiroi, T., Zinovieva, N. G., Keller, H. U., Semenova, A. S., Barsukova, L. D., Roshchina, I. A., Galuzinskaya, A. K., and Stroganov, I. A. (2000). Simulation of impact melting effect on optical properties of Martian regolith. *31st Lunar and Planetary Science Conference, #1214 (abstr.),* Houston.

Basurah, H. M. (2003). Estimating a new date for the Wabar meteorite impact. *Meteoritics & Planetary Science* 38, A155–A156.

Bell, M. S. (2016). CO_2 release due to impact devolatilization of carbonate: results of shock experiments. *Meteoritics & Planetary Science* 51, 619–646.

Bence, A. E. and Burnett, D. S. (1969). Chemistry and mineralogy of the silicates and metal of the Kodaikanal meteorite. *Geochimica et Cosmochimica Acta* 33, 387–407.

Benedix, G. K., McCoy, T. J., Keil, K., and Love, S. G. (2000). A petrologic study of the IAB iron meteorites: constraints on the formation of the IAB–Winonaite parent body. *Meteoritics & Planetary Science* 35, 1127–1141.

Bindi, L., Eiler, J. M., Yunbin, G., Hollister, L. S., MacPherson, G. J., Steinhardt, P. J., and Yao, N. (2012). Evidence for the extraterrestrial origin of a natural quasicrystal. *Proceedings of the National Academy of Sciences of the United States of America* 109, 1396–1401.

Bischoff, A. and Lange, M. A. (1984). Experimental shock-lithification of chondritic powder: implications for ordinary chondrite regolith breccias. *15th Lunar and Planetary Science Conference, #60 (abstr.),* Houston.

Bishop, F. C., Smith, J. V., and Dawson, J. B. (1976). Na, P, Ti and coordination of Si in garnet from peridotite and eclogite xenoliths. *Nature* 260, 696–697.

Bland, P. A., Collins, G. S., Davison, T. M., Abreu, N. M., Ciesla, F. J., Muxworthy, A. R., and Moore, J. (2014). Pressure–temperature evolution

of primordial solar system bodies during impact-induced compaction. *Nature Communications* 5, 5451.

Boag, A., Hughes, A. E., Wilson, N. C., Torpy, A., MacRae, C. M., Glenn, A. M., and Muster, T. H. (2009). How complex is the microstructure of AA2024-T3? *Corrosion Science* 51, 1565–1568.

Boehnke, P. and Harrison, T. M. (2016). Illusory late heavy bombardments. *Proceedings of the National Academy of Sciences* 113, 10802–10806.

Boesenberg, J. S. (2006). Wrought iron from the USS Monitor: mineralogy, petrology and metallography. *Archaeometry* 48, 613–631.

Boesenberg, J. S., Delaney, J. S., and Hewins, R. H. (2012). A petrological and chemical reexamination of Main Group pallasite formation. *Geochimica et Cosmochimica Acta* 89, 134–158.

Boesenberg, J. S. and Hewins, R. H. (2010). An experimental investigation into the metastable formation of phosphoran olivine and pyroxene. *Geochimica et Cosmochimica Acta* 74, 1923–1941.

Bogaerts, M. and Schmidt, M. W. (2006). Experiments on silicate melt immiscibility in the system Fe_2SiO_4–$KAlSi_3O_8$–SiO_2–CaO–MgO–TiO_2–P_2O_5 and implications for natural magmas. *Contributions to Mineralogy and Petrology* 152, 257–274.

Bogard, D., Garrison, D. H., and McCoy, T. J. (2000). Chronology Chronology and petrology of silicates from IIE iron meteorites: evidence of a complex parent body evolution. *Geochimica et Cosmochimica Acta* 64, 2133–2154.

Boslough, M. B., Ahrens, T. J., Vizgirda, J., Becker, R. H., and Epstein, S. (1982). Shock-induced devolatilization of calcite. *Earth and Planetary Science Letters* 61, 166–170.

Bottke, W. F., Nesvorny, D., Grimm, R. E., Morbidelli, A., and O'Brien, D. P. (2006). Iron meteorites as remnants of planetesimals formed in the terrestrial planet region. *Nature* 439, 821–824.

Bottke, W. F., Nolan, M. C., Greenberg, R., and Kolvoord, R. A. (1994). Velocity distribution among colliding asteroids. *Icarus* 107, 255–268.

Bouhifd, M. A., Besson, P., Courtial, P., Gérardin, C., Navrotsky, A., and Richet, P. (2007). Thermochemistry and melting properties of basalt. *Contributions to Mineralogy and Petrology* 153, 689–698.

Bouley, S., Baratoux, D., Vaubaillon, J., Mocquet, A., Le Feuvre, M., Colas, F., Benkhaldoun, Z., Daassou, A., Sabil, M., and Lognonné, P. (2012). Power and duration of impact flashes on the Moon: implications for the cause of radiation. *Icarus* 218, 115–124.

Bowen, N. L. (1928). *The evolution of the igneous rocks.* Princeton: Princeton University Press.

Bowen, N. L., Schairer, J. F., and Posnjak, E. (1933). The system CaO–FeO–SiO_2. *American Journal of Science* 26, 193–284.

Braslau, D. (1970). Partitioning of energy in hypervelocity impact against loose sand targets. *Journal of Geophysical Research* 75, 3987–3999.

Brett, R. (1967). Metallic spherules in impactite and tektite glasses. *The American Mineralogist* 52, 721–733.

Brooker, R. A. and Hamilton, D. L. (1990). Three-liquid immiscibility and the origin of carbonatites. *Nature* 346, 459–462.

Brooker, R. A. and Kjarsgaard, B. O. (2011). Silicate–carbonate liquid immiscibility and phase relations in the system SiO_2–Na_2O–Al_2O_3–CaO–CO_2 at 0.1–2.5 GPa with applications to carbonatite genesis. *Journal of Petrology* 52, 1281–1305.

Brown, P. G., Assink, J. D., Astiz, L., Blaauw, R., Boslough, M. B., Borovička, J., Brachet, N., Brown, D., Campbell-Brown, M., Ceranna, L., Cooke, W., Groot-Hedlin, C. de, Drob, D. P., Edwards, W., Evers, L. G., Garces, M., Gill, J., Hedlin, M., Kingery, A., Laske, G., Le Pichon, A., Mialle, P., Moser, D. E., Saffer, A., Silber, E., Smets, P., Spalding, R. E., Spurný, P., Tagliaferri, E., Uren, D., Weryk, R. J., Whitaker, R., and Krzeminski, Z. (2013). A 500-kiloton airburst over Chelyabinsk and an enhanced hazard from small impactors. *Nature* 35, 1441.

Brugger, J., Feulner, G., and Petri, S. (2017). Baby, it's cold outside: climate model simulations of the effects of the asteroid impact at the end of the Cretaceous. *Geophysical Research Letters* 44, 419–427.

Buchheit, R. G., Grant, R. P., Hlava, P. F., Mckenzie, B., and Zender, G. L. (1997). Local dissolution phenomena associated with S phase (Al_2CuMg) particles in aluminum alloy 2024-T3. *Journal of The Electrochemical Society* 144, 2621–2628.

Buchwald, V. F. (1975). *Handbook of iron meteorites: their history, distribution, composition and structure.* Berkeley: University of California Press.

Buhl, E., Poelchau, M. H., Dresen, G., and Kenkmann, T. (2013). Deformation of dry and wet sandstone targets during hypervelocity impact experiments, as revealed from the MEMIN program. *Meteoritics & Planetary Science* 48, 71–86.

Bunch, T. E., Keil, K., and Olsen, E. J. (1970). Mineralogy and petrology of silicate inclusions in iron meteorites. *Contributions to Mineralogy and Petrology* 25, 240–297.

Burnett, D. S. and Wasserburg, G. J. (1967). Evidence for the formation of an iron meteorite at 3.8×10^9 years. *Earth and Planetary Science Letters* 2, 137–147.

Buseck, P. R. (1977). Pallasite meteorites – mineralogy, petrology, and geochemistry. *Geochimica et Cosmochimica Acta* 41, 711–740.

Buseck, P. R. and Clark, J. (1984). Zaisho – a pallasite containing pyroxene and phosphoran olivine. *Mineralogical Magazine* 48, 229–235.

Canup, R. M. and Asphaug, E. (2001). Origin of the Moon in a giant impact near the end of the Earth's formation. *Nature* 412, 708–712.

Capdevilla, R. (1967). Répartition et habitus de l'apatite dans le granite de Neira (Espagne): comparaisons avec des données expérimentales et applications petrogénétiques. *Comptes Rendus de l'Académie des Sciences – Series I – Mathematics* 264, 1694–1697.

Carpenter, B. M., Mollo, S., Viti, C., and Collettini, C. (2015). Influence of calcite decarbonation on the frictional behavior of carbonate-bearing gouge: implications for the instability of volcanic flanks and fault slip. *Tectonophysics* 658, 128–136.

Casanova, I., Graf, T., and Marti, K. (1995). Discovery of an unmelted H-chondrite inclusion in an iron meteorite. *Science* 268, 540–542.

Chabot, N. L. and Drake, M. J. (2000). Crystallization of magmatic iron meteorites: the effects of phosphorus and liquid immiscibility. *Meteoritics & Planetary Science* 35, 807–816.

Chakrabarti, D. J. and Laughlin, D. E. (2004). Phase relations and precipitations in Al–Mg–Si alloys with Cu additions. *Progress in Materials Science* 49, 389–410.

Chang, L., Howie, R. A., and Zussman, J. (1996). *Rock-forming minerals, Vol. 5B, non-silicates: sulphates, carbonates, phosphates, halides.* London: Longman.

Chao, E. C. T., Fahey, J. J., and Littler, J. (1961). Coesite from Wabar crater, near Al Hadida, Arabia. *Science* 133, 882–883.

Chao, E. C. T., Fahey, J. J., Littler, J., and Milton, D. J. (1962). Stishovite, SiO_2, a very high pressure new mineral from Meteor Crater, Arizona. *Journal of Geophysical Research* 67, 419–421.

Chao, E. C. T. and Shoemaker, E. (1961). New evidence for the impact origin of the Ries Basin, Bavaria, Germany. *Journal of Geophysical Research* 66, 3371–3378.

Charlier, B. and Grove, T. L. (2012). Experiments on liquid immiscibility along tholeiitic liquid lines of descent. *Contributions to Mineralogy and Petrology* 164, 27–44.

Charlier, B., Namur, O., and Grove, T. L. (2013). Compositional and kinetic controls on liquid immiscibility in ferrobasalt–rhyolite volcanic and plutonic series. *Geochimica et Cosmochimica Acta* 113, 79–93.

Charlier, B., Namur, O., Latypov, R., and Tegner, C., eds. (2015). *Layered intrusions.* Dordrecht: Springer.

Charlier, B., Namur, O., Toplis, M. J., Schiano, P., Cluzel, N., Higgins, M. D., and Auwera, J. V. (2011). Large-scale silicate liquid immiscibility during differentiation of tholeiitic basalt to granite and the origin of the Daly gap. *Geology* 39, 907–910.

Chase, M. W. (1998). *NIST–JANAF thermochemical tables.* Forth Edition. Gaithersburg, Maryland: National Institute of Standards and Technology.

Choi, B.-G., Ouyang, X., and Wasson, J. T. (1995). Classification and origin of IAB and IIICD iron meteorites. *Geochimica et Cosmochimica Acta* 59, 593–612.

Christiansen, E. L. (2003). *Meteoroid/debris shielding. NASA Technical Report TP–2003-210788.* Houston: NASA.

Chyba, C. F., Owen, T. C., and Ip, W.-H. (1994). Impact delivery of volatiles and organic molecules to Earth. *Hazards due to comets and asteroids.* Ed. by T. Gehrels. Tucson: University of Arizona, 9–58.

Chyba, C. F. and Sagan, C. (1992). Endogenous production, exogenous delivery and impact-shock synthesis of organic molecules: an inventory for the origins of life. *Nature* 355, 125–132.

Chyba, C. F., Thomas, P. J., and Zahnle, K. J. (1993). The 1908 Tunguska explosion: atmospheric disruption of a stony asteroid. *Nature* 361, 40–44.

Cintala, M. J., Berthoud, L., and Hörz, F. (1999). Ejection–velocity distributions from impacts into coarse-grained sand. *Meteoritics & Planetary Science* 34, 605–623.

Cintala, M. J. and Grieve, R. A. F. (1998). Scaling impact-melt and crater dimensions: implications for the lunar cratering record. *Meteoritics & Planetary Science* 33, 889–912.

Cintala, M. J. and Hörz, F. (1990). Regolith evolution in the laboratory: scaling dissimilar comminution experiments. *Meteoritics & Planetary Science* 25, 27–40.

Claeys, P., Heuschkel, S., Lounejeva-Baturina, E., Sanchez-Rubio, G., and Stöffler, D. (2003). The suevite of drill hole Yucàtan 6 in the Chicxulub impact crater. *Meteoritics & Planetary Science* 38, 1299–1317.

Cohen, B. A., Swindle, T. D., and Kring, D. A. (2000). Support for the lunar cataclysm hypothesis from lunar meteorite impact melt ages. *Science* 290, 1754–1755.

Collettini, C., Carpenter, B. M., Viti, C., Cruciani, F., Mollo, S., Tesei, T., Trippetta, F., Valoroso, L., and Chiaraluce, L. (2014). Fault structure and slip localization in carbonate-bearing normal faults: an example from the Northern Apennines of Italy. *Jorunal of Structural Geology* 67, 154–166.

Collettini, C., Viti, C., Tesei, T., and Mollo, S. (2013). Thermal decomposition along natural carbonate faults during earthquakes. *Geology* 41, 927–930.

Collins, G. S., Melosh, H. J., Morgan, J. V., and Warner, M. R. (2002). Hydrocode simulations of Chicxulub crater collapse and peak-ring formation. *Icarus* 157, 24–33.

Cultrone, G., Rodriguez-Navarro, C., Sebastian, E., Cazalla, O., and De La Torre, M. J. (2001). Carbonate and silicate phase reactions during ceramic firing. *European Journal of Mineralogy* 13, 621–634.

Daly, R. A. (1914). *Igneous rocks and their origin.* New York: McGraw-Hill.

Daly, T. R. and Schultz, P. H. (2016). Delivering a projectile component to the vestan regolith. *Icarus* 264, 9–19.

Dasgupta, R., Hirschmann, M. C., and Stalker, K. (2006). Immiscible transition from carbonate-rich to silicate-rich melts in the 3 GPa melting interval of eclogite + CO_2 and genesis of silica-undersaturated ocean island lavas. *Journal of Petrology* 47, 647–671.

Dauphas, N. (2003). The dual origin of the terrestrial atmosphere. *Icarus* 165, 326–339.

Davis, A. M. and Olsen, E. J. (1991). Phosphates in pallasite meteorites as probes of mantle processes in small planetary bodies. *Nature* 353, 637–640.

Davison, T. M., Collins, G. S., and Ciesla, F. J. (2010). Numerical modeling of heating in porous planetesimal collisions. *Icarus* 208, 468–481.

Day, J. M. D., Floss, C., Taylor, L. A., Anand, M., and Patchen, A. D. (2006). Evolved mare basalt magmatism, high Mg/Fe feldspathic crust, chondritic impactors, and the petrogenesis of Antarctic lunar breccia meteorites Meteorite Hills 01210 and Pecora Escarpment 02007. *Geochimica et Cosmochimica Acta* 70, 5957–5989.

De Bresser, J. H. P., Urai, J. L., and Olgaard, D. L. (2005). Effect of water on the strength and microstructure of Carrara marble axially compressed at high temperature. *Jorunal of Structural Geology* 27, 265–281.

Deegan, F. M., Troll, V. R., Freda, C., Misiti, V., Chadwick, J. P., McLeod, C. L., and Davidson, J. P. (2010). Magma–carbonate interaction processes and associated CO_2 release at Merapi volcano, Indonesia: insights from experimental petrology. *Journal of Petrology* 51, 1027–1051.

Dence, M. R., Engelhardt, W. von, Plant, A. G., and Walter, L. S. (1974). Indications of fluid immiscibility in glass from West Clearwater Lake impact crater, Quebec, Canada. *Contributions to Mineralogy and Petrology* 46, 81–97.

Desai, P. D. (1986). Thermodynamic properties of iron and silicon. *Journal of Physical and Chemical Reference Data* 15, 967–983.

Desai, P. D. (1987). Thermodynamic properties of selected binary aluminum alloy systems. *Journal of Physical and Chemical Reference Data* 16, 109–124.

Deutsch, A. and Langenhorst, F. (2007). On the fate of carbonates and anhydrite in impact processes – evidence from the Chicxulub event. *Geologiska Forenigens I Stockholm Forhandlingar* 129, 155–160.

D'Orazio, M., Folco, L., Zeoli, A., and Cordier, C. (2011). Gebel Kamil: the iron meteorite that formed the Kamil crater (Egypt). *Meteoritics & Planetary Science* 46, 1179–1196.

Dressler, B. O. and Reimold, W. U. (2001). Terrestrial impact melt rocks and glasses. *Earth Science Reviews* 56, 205–284.

Ebert, M., Hamann, C., Hecht, L., Deutsch, A., and Kenkmann, T. (2015). Bridging the gap between laboratory and nature: geochemical clues from experimental approaches. *Bridging the Gap III, #1055 (abstr.),* Freiburg.

Ebert, M., Hecht, L., Deutsch, A., and Kenkmann, T. (2013). Chemical modification of projectile residues and target material in a MEMIN cratering experiment. *Meteoritics & Planetary Science* 48, 134–149.

Ebert, M., Hecht, L., Deutsch, A., Kenkmann, T., Wirth, R., and Berndt, J. (2014). Geochemical processes between steel projectiles and silica-rich targets in hypervelocity impact experiments. *Geochimica et Cosmochimica Acta* 133, 257–279.

Ebert, M., Hecht, L., Hamann, C., and Luther, R. (2017). Laser-induced melting experiments: simulation of short-term high-temperature impact processes. *Meteoritics & Planetary Science* 52, 1475–1494.

Ebert, M., Kowitz, A., Schmitt, R.-T., Reimold, W. U., Mansfeld, U., and Langenhorst, F. (in press). Localized shock-induced melting of sandstone at low impact pressures (<17.5 GPa): an experimental study. *Meteoritics & Planetary Science.*

Ehlmann, B. L., Mustard, J. F., Murchie, S. L., Pouler, F., Bishop, J. L., Brown, A. J., Calvin, W. M., Clark, R. N., Des Marais, D. J., Miliken, R. E., Roach, L. H., Roush, T. L., Swayze, G. A., and Wray, J. J. (2008). Orbital identification of carbonate-bearing rocks on Mars. *Science* 322, 1828–1832.

Engelhardt, W. von (1970). Gesteine und Mineralien des Mondes. *ZEISS Informationen* 76, 50–53.

Essene, E. J. and Fisher, D. C. (1986). Lightning strike fusion: extreme reduction and metal–silicate liquid immiscibility. *Science* 234, 189–193.

Evans, N. J., Gregoire, D. C., Grieve, R. A. F., Goodfellow, W. D., and Veizer, J. (1993). Use of platinum-group elements for impactor identification: terrestrial impact craters and Cretaceous–Tertiary boundary. *Geochimica et Cosmochimica Acta* 57, 3737–3748.

Evans, N. J., Shahinpoor, M., and Ahrens, T. J. (1994). Hypervelocity impact: ejecta velocity, angle, and composition. *Geological Society of America Special Paper* 293, 93–101.

Farrow, C. E. G. and Watkinson, D. H. (1997). Diversity of precious-metal mineralization in footwall Cu-Ni-PGE deposits, Sudbury, Ontario: implications for hydrothermal models of formation. *The Canadian Mineralogist* 35, 817–840.

Fazio, A., D'Orazio, M., Cordier, C., and Folco, L. (2016). Target–projectile interaction during impact melting at Kamil Crater, Egypt. *Geochimica et Cosmochimica Acta* 180, 33–50.

Fazio, A., D'Orazio, M., Folco, L., and Cordier, C. (2014a). Target–projectile interaction during impact melting at Kamil crater, Egypt. *77th Annual Meteoritical Society Meeting, #5030 (abstr.),* Casablanca.

Fazio, A., Folco, L., D'Orazio, M., Frezzotti, M. L., and Cordier, C. (2014b). Shock metamorphism and impact melting in small impact craters on Earth: evidence from Kamil crater, Egypt. *Meteoritics & Planetary Science* 49, 2175–2200.

Fiske, P. S., Nellis, W. J., Lipp, M., Lorenzana, H., Kikuchi, M., and Syono, Y. (1995). Pseudotachylites generated in shock experiments: implications for impact cratering products and processes. *Science* 270, 281–283.

Floss, C., El Goresy, A., Zinner, E., Kransel, G., Rammensee, W., and Palme, H. (1996). Elemental and isotopic fractionations produced through evaporation of the Allende CV chondrite: implications for the origin of HAL-type hibonite inclusions. *Geochimica et Cosmochimica Acta* 60, 1975–1997.

Fogel, R. A., Hess, P. C., and Rutherford, M. J. (1989). Intensive parameters of enstatite chondrite metamorphism. *Geochimica et Cosmochimica Acta* 53, 2735–2746.

Folco, L., Di Martino, M., El Barkooky, A., D'Orazio, M., Lethy, A., Urbini, S., Nicolosi I., Hafez, M., Cordier, C., van Ginneken, M., Zeoli, A., Randwan, A. M., El Khrepy, S., El Gabry, M., Gomaa, M., Barakat, A. A., Serra, R., and El Sharkawi, M. (2010). The Kamil crater in Egypt. *Science* 329, 804.

Folco, L., Di Martino, M., El Barkooky, A., D'Orazio, M., Lethy, A., Urbini, S., Nicolosi I., Hafez, M., Cordier, C., van Ginneken, M., Zeoli, A., Randwan, A. M., El Khrepy, S., El Gabry, M., Gomaa, M., Barakat, A. A., Serra, R., and El Sharkawi, M. (2011). Kamil crater (Egypt): ground truth for small-scale meteorite impacts on Earth. *Geology* 39, 179–182.

Folco, L., D'Orazio, M., Fazio, A., Cordier, C., Zeoli, A., van Ginneken, M., and El Barkooky, A. (2015). Microscopic impactor debris in the soil around Kamil Crater (Egypt): inventory, distribution, total mass, and implications for the impact scenario. *Meteoritics & Planetary Science* 50, 382–400.

Fonseca, R. O. C., Campbell, I. H., O'Neill, H. S. C., and Fitzgerald, J. D. (2008). Oxygen solubility and speciation in sulphide-rich mattes. *Geochimica et Cosmochimica Acta* 72, 2619–2635.

Fowler-Gerace, N. A. and Tait, K. T. (2015). Phosphoran olivine overgrowths: implications for multiple impacts to the Main Group pallasite parent body. *The American Mineralogist* 100, 2043–2052.

Freestone, I. C. and Hamilton, D. L. (1980). The role of liquid immiscibility in the genesis of carbonatites: an experimental study. *Contributions to Mineralogy and Petrology* 73, 105–117.

Freestone, I. C. and Powell, R. (1983). The low temperature field of liquid immiscibility in the system K_2O–Al_2O_3–FeO–SiO_2 with special reference to the join fayalite–leucite–silica. *Contributions to Mineralogy and Petrology* 82, 291–299.

French, B. M. (1998). *Traces of catastrophe: a handbook of shock-metamorphic effects in terrestrial meteorite impact structures.* Houston: Lunar and Planetary Institute, LPI Contribution No. 954.

French, B. M., Hartung, J. B., and Short, N. M. (1970). Tenoumer crater, Mauritania: age and petrologic evidence for origin by meteorite impact. *Journal of Geophysical Research* 75, 4396–4406.

Frost, B. R. (1991). Introduction to oxygen fugacity and its petrologic importance. *Reviews in mineralogy volume 25. Oxide minerals: petrologic and magnetic significance.* Ed. by D. H. Lindsley. Blacksburg, Virginia: Mineralogical Society of America, 1–9.

Fudali, R. F. (1974). Genesis of the melt rocks at Tenoumer crater, Mauretania. *Journal of Geophysical Research* 79, 2115–2121.

Gao, M., Feng. C. R., and Wei, R. P. (1998). An analytical electron microscopy study of constituent particles in commercial 7075-T6 and 2024-T3 alloys. *Metallurgical and Materials Transactions A* 92A, 1145–1151.

Gault, D. E., Quaide, W. I., and Oberbeck, V. R. (1968). Impact cratering mechanics and structures. *Shock metamorphism of natural materials.* Ed. by B. M. French and N. M. Short. Baltimore: Mono Book Corps., 87–100.

Genge, M. J., Jones, A. P., and Price, G. D. (1995). An infrared and Raman study of carbonate glasses: implications for the structure of carbonatite magmas. *Geochimica et Cosmochimica Acta* 59, 927–937.

Gerasimov, M. B. V., Ivanov, B. A., Yakovlev, O. I., and Yu, P. (1998). Physics and chemistry of impacts. *Earth Moon Planets* 80, 209–259.

Gerasimov, M. B. V., Yakovlev, O. I., Yu, P., Dikov, Y. P., and Wlotzka, F. (2005). Evaporative differentiation of impact-produced melts: laser-simulation experiments and comparison with impact glasses from the Logoisk crater. *Geological Society of America Special Paper* 384, 351–366.

Gibbons, R. V., Hörz, F., and Schaal, R. B. (1976a). The chemistry of some individual lunar soil agglutinates. *Proceedings, 7th Lunar Science Conference,* 405–421.

Gibbons, R. V., Hörz, F., Thompson, T. D., and Brownlee, D. E. (1976b). Metal spherules in Wabar, Monturaqui, and Henbury impactites. *Proceedings, 7th Lunar Science Conference,* 863–880.

Giordano, D., Russell, J. K., and Dingwell, D. B. (2008). Viscosity of magmatic liquids: a model. *Earth and Planetary Science Letters* 271, 123–134.

Girault, J. (1966). Sur la genése des cristaux d'apatite des carbonatites d'Oka (Canada). *Comptes Rendus de l'Académie des Sciences – Series I – Mathematics* 263, 97–100.

Gnos, E., Hofmann, B. A., Al-Halawani, M. A., Tarabulsi, Y., Hakeem, M., Al-Shanti, M., Greber, N. D., Holm, S., Alwmark, C., Greenwood, R. C., and Ramseyer, K. (2013). The Wabar impact craters, Saudi Arabia, revisited. *Meteoritics & Planetary Science* 48, 2000–2014.

Goderis, S., Tagle, R., Belza, J., Smit, J., Montanari, A., Vanhaeke, F., Erzinger, J., and Claeys, P. (2013). Reevaluation of siderophile element abundances and ratios across the Cretaceous–Paleogene (K–Pg) boundary: implications for the nature of the projectile. *Geochimica et Cosmochimica Acta* 120, 417–446.

Goderis, S., Tagle, R., Fritz, J., Bartoschewitz, R., and Artemieva, N. (2017). On the nature of the Ni-rich component in splash-form Australasian tektites. *Geochimica et Cosmochimica Acta* 217, 28–50.

Goderis, S., Tagle, R., Schmitt, R.-T., Erzinger, J., and Claeys, P. (2007). Platinum group elements provide no indication of a meteoritic component in ICDP cores from the Bosumtwi crater, Ghana. *Meteoritics & Planetary Science* 42, 731–741.

Goldstein, J. I. (1967). The iron meteorites, their thermal history and parent bodies. *Geochimica et Cosmochimica Acta* 31, 1733–1770.

Goldstein, J. I., Scott, E. R. D., and Chabot, N. L. (2009). Iron meteorites: crystallization, thermal history, parent bodies, and origin. *Chemie der Erde* 69, 293–325.

Goodrich, C. A. (1984). Phosphoran pyroxene and olivine in silicate inclusions in natural iron–carbon alloy, Disko island, Greenland. *Geochimica et Cosmochimica Acta* 48, 1115–1126.

Goodrich, C. A. (2003). Petrogenesis of olivine-phyric shergottites Sayh al Uhaymir 005 and Elephant Moraine A79001 lithology A. *Geochimica et Cosmochimica Acta* 67, 3753–3771.

Govindaraju, K. (1994). Compilation of working values and sample description for 383 geostandards. *Geostandards Newsletter* 18, 1–158.

Grady, M. M. (2000). *Catalogue of meteorites.* Cambridge: Cambridge University Press.

Grasset, O. and Albarède, F. (1994). Hybridization of mingling magmas with different densities. *Earth and Planetary Science Letters* 121, 327–332.

Graup, G. (1999). Carbonate–silicate liquid immiscibility upon impact melting: Ries Crater, Germany. *Meteoritics & Planetary Science* 34, 425–438.

Greig, J. W. (1927). Immiscibility in silicate melts; Part II. *American Journal of Science* 13, 133–154.

Grieve, R. A. F., Stöffler, D., and Deutsch, A. (1991). The Sudbury structure: controversial or misunderstood? *Journal of Geophysical Research* 96, 22753–22764.

Gudfinnsson, G. H. and Presnall, D. C. (2005). Continuous gradations among primary carbonatitic, kimberlitic, melilititic, basaltic, picritic, and komatiitic melts in equilibrium with garnet lherzolite at 3–8 GPa. *Journal of Petrology* 46, 1645–1659.

Güldemeister, N., Wünnemann, K., Durr, N., and Hiermaier, S. (2013). Propagation of impact-induced shock waves in porous sandstone using mesoscale modeling. *Meteoritics & Planetary Science* 48, 115–133.

Gupta, S. C., Love, S. G., and Ahrens, T. J. (2000). Shock temperatures in calcite ($CaCO_3$): implication for shock induced decomposition. *Shock compression of condensed matter.* Ed. by M. D. Furnish, L. C. Chhabildas, and R. S. Hixson. College Park, Maryland: American Institute of Physics, 1263–1266.

Haack, H. and McCoy, T. J. (2004). Iron and stony-iron meteorites. *Treatise on geochemistry (Vol. 1): meteorites, comets, and planets.* Ed. by A. M. Davis. Elsevier, 325–345.

Haccuria, E., Crivits, T., Hayes, P. C., and Jak, E. (2016). Selected phase equilibria studies in the Al_2O_3–CaO–SiO_2 system. *Journal of the American Ceramic Society* 99, 691–704.

Hamann, C., Fazio, A., Schultze, D., Ebert, M., Hecht, L., Reimold, W. U., and Wirth, R. (2015). Silicate liquid immiscibility in natural and experimental impact melts. *46th Lunar and Planetary Science Conference, #2071 (abstr.)* Houston.

Hamann, C., Hecht, L., Ebert, M., and Wirth, R. (2013). Chemical projectile–target interaction and liquid immiscibility in impact glass from the Wabar craters, Saudi Arabia. *Geochimica et Cosmochimica Acta* 121, 291–310.

Hart, S. R. (1978). Nickel partitioning between olivine and silicate melt. *Earth and Planetary Science Letters* 40, 203–219.

Hartmann, W. K. (1966). Early lunar cratering. *Icarus* 5, 406–418.

Hartmann, W. K. (2003). Megaregolith evolution and cratering cataclysm models–lunar cataclysm as a misconception (28 years later). *Meteoritics & Planetary Science* 38, 579–593.

Hecht, L., Freiberger, R., Gilg, H. A., Grundmann, G., and Kostitsyn, Y. A. (1999). Rare earth and isotope (C, O, Sr) characteristics of hydrothermal carbonates: genetic implications for dolomite-hosted talc mineralization at Göpfersgrün (Fichtelgebirge, Germany). *Chemical Geology* 155, 115–130.

Heiken, G., Vaniman, D., and French, B. M., eds. (1991). *Lunar sourcebook.* Cambridge: Cambridge University Press.

Hermalyn, B. and Schultz, P. H. (2011). Time-resolved studies of hypervelocity vertical impacts into porous particulate targets: effects of projectile density on early-time coupling and crater growth. *Icarus* 216, 269–279.

Hess, P. C. (1977). Structure of silicate melts. *The Canadian Mineralogist* 15, 162–178.

Hess, P. C. (1995). Thermodynamic mixing properties and the structure of silicate melts. *Reviews in mineralogy volume 32. Structure, dynamics and properties of silicate melts.* Ed. by J. F. Stebbins, McMillan P. F., and D. B. Dingwell. Washington, DC: Mineralogical Society of America, 145–190.

Hiesinger, H. and Head, J. W. (2006). New views of lunar geoscience: an introduction and overview. *New views of the moon.* Ed. by B. L. Jolliff, M. A. Wieczorek, C. K. Shearer, and C. R. Neal. Washington, DC: Mineralogical Society of America and Geochmical Society, 1–81.

Hiesinger, H., van der Bogert, C. H., Pasckert, J. H., Funcke, L., Gioacomini, L., Ostrach, L. R., and Robinson, M. S. (2012). How old are young lunar craters? *Journal of Geophysical Research* 117, E00H10.

Hildebrand, A. R., Penfield, G. T., Kring, D. A., Pilkington, M., Zanoguera, A. C., Jacobsen, S. B., and Boynton, W. V. (1991). Chicxulub Crater; a possible Cretaceous/Tertiary boundary impact crater on the Yucatán Peninsula, Mexico. *Geology* 19, 867–871.

Hollister, L. S., Bindi, L., Yao, N., Poirier, G. R., Andronicos, C. L., MacPherson, G. J., Lin, C., Distler, V. V., Eddy, M. P., Kostin, A., Kryachko, V., Steinhardt, W. M., Yudovskaya, M., Eiler, J. M., Guan, Y., Clarke, J. J., and Steinhardt, P. J. (2014). Impact-induced shock and the formation of natural quasicrystals in the early solar system. *Nature Communications* 5, 4040.

Hollister, L. S., MacPherson, G. J., Bindi, L., Lin, C., Guan, Y., Yao, N., Eiler, J. M., and Steinhardt, P. J. (2015). Redox reactions between Cu–Al metal and silicates in the Khatyrka meteorite. *46th Lunar and Planetary Science Conference, #2394 (abstr.),* Houston.

Holm-Alwmark, S., Rae, A. S. P., Ferrière, L., Alwmark, C., and Collins, G. S. (in press). Combining shock barometry with numerical modeling: insights into complex crater formation—the example of the Siljan impact structure (Sweden). *Meteoritics & Planetary Science.*

Horak, J., Heunoske, D., Lueck, M., Osterholz, J., and Wickert, M. (2015). Numerical modeling and characterization of the laser–matter interaction during high-power continuous wave laser perforation of thin metal plates. *Journal of Laser Applications* 27, S28003.

Horneck, G., Stöffler, D., Ott, S., Hornemann, U., Cockell, C. S., Moeller, R., Meyer, C., deVera, J. P., Fritz, J., Schade, S., and Artemieva, N. (2008). Microbial rock inhabitants survive hypervelocity impacts on Mars-like host planets: first phase of lithopanspermia experimentally tested. *Astrobiology* 8, 17–44.

Hörz, F., Archer Jr., P. D., Niles, P. B., Zolensky, M. E., and Evans, M. (2015). Devolatilization or melting of carbonates at Meteor Crater, AZ? *Meteoritics & Planetary Science* 50, 1050–1070.

Hörz, F., Brownlee, D. E., Fechting, H., Hartung, J. B., Morrison, D. A., Neukum, G., Schneider, E., Vedder, J. F., and Gault, D. E. (1975). Lunar microcraters: implications for the micrometeoroid complex. *Planetary and Space Science* 23, 151–172.

Hörz, F. and Cintala, M. J. (1997). Impact experiments related to the evolution of planetary regoliths. *Meteoritics & Planetary Science* 32, 179–209.

Hörz, F., Cintala, M. J., See, T. H., and Le, L. (2005). Shock melting of ordinary chondrite powders and implications for asteroidal regoliths. *Meteoritics & Planetary Science* 40, 1329–1346.

Hörz, F., Fechting, H., Janicke, J., and Schneider, E. (1983). Morphology and chemistry of projectile residues in small experimental impact craters. *Journal of Geophysical Research* 88, B353–B363.

Hörz, F., Mittlefehldt, D. W., See, T. H., and Galindo, C. (2002). Petrographic studies of the impact melts from Meteor Crater, Arizona, USA. *Meteoritics & Planetary Science* 37, 501–531.

Hörz, F., See, T. H., Murali, A. V., and Blanchard, D. P. (1989). Heterogeneous dissemination of projectile materials in the impact melts from Wabar crater, Saudi Arabia. *Proceedings, 19th Lunar and Planetary Science Conference,* 697–709.

Hsu, W. (2003). Rare earth element geochemistry and petrogenesis of Miles (IIE) silicate inclusions. *Geochimica et Cosmochimica Acta* 67, 4807–4821.

Hu, H.-N. and Taylor, L. A. (1977). Lack of chemical fractionation in major and minor elements during agglutinate formation. *Proceedings, 8th Lunar Science Conference,* 3645–3656.

Hudon, P. and Baker, D. R. (2002). The nature of phase separation in binary oxide melts and glasses. I. Silicate systems. *Journal of Non-Crystalline Solids* 303, 299–345.

Hutcheon, I. and Olsen, E. J. (1991). Cr isotopic composition of differentiated meteorites: a search for 53 Mn. *22nd Lunar and Planetary Science Conference, #605 (abstr.),* Houston.

Hwang, J. Y., Doty, H. W., and Kaufman, M. J. (2008). The effects of Mn additions on the microstructure and mechanical properties of Al–Si–Cu casting alloys. *Materials Science and Engineering A* 488, 496–504.

Ikeda, Y., Ebihara, M., and Prinz, M. (1997). Petrology and chemistry of the Miles IIE iron. I: description and petrology of twenty new silicate inclusions. *Antarctic Meteorite Research* 10, 355–372.

Ikeda, Y. and Prinz, M. (1996). Petrology of silicate inclusions in the Miles IIE iron. *Proceedings, NIPR Symposium on Antarctic Meteorites* 9, 143–173.

Ishibashi, K., Ohno, S., Sugita, S., Kadono, T., and Matsui, T. (2013). Oxidation of carbon compounds by silica-derived oxygen within impact-induced vapor plumes. *Earth Planets Space* 85, 811–822.

Ivanov, B. A. and Deutsch, A. (2002). The phase diagram of $CaCO_3$ in relation to shock compression and decomposition. *Physics of the Earth and Planetary Interiors* 129, 131–143.

Jakobsen, J. K., Veksler, I. V., Tegner, C., and Brooks, C. K. (2005). Immiscible iron- and silica-rich melts in basalt petrogenesis documented in the Skaergaard intrusion. *Geology* 33, 885–888.

James, P. F. (1975). Liquid-phase separation in glass-forming systems. *Journal of Materials Science* 10, 1802–1825.

Jammes, C. (1984). "Experimentelle Stoßwellenmetamorphose von Quartzsand durch Hochgeschwindigkeits-Impakt von Aluminiumprojektilen". Diploma thesis. Münster, Germany: Westfälische Wilhelms-Universität.

Jammes, C., Stöffler, D., Bischoff, A., Reimold, W. U., and Gault, D. E. (1983). Reduction of SiO_2 to Si and metallurgical transformations in Al by hypervelocity impacts of Al-projectiles into quartz sand. *14th Lunar and Planetary Science Conference, #1176 (abstr.),* Houston.

Jana, D. and Walker, D. (1997a). The influence of silicate melt composition on distribution of siderophile elements among metal and silicate liquids. *Earth and Planetary Science Letters* 150, 463–472.

Jana, D. and Walker, D. (1997b). The influence of sulfur on partitioning of siderophile elements. *Geochimica et Cosmochimica Acta* 61, 5255–5277.

Jaret, S. J., Kah, L. C., and French, B. M. (2009). Petrographic investigation of ejecta from Tenoumer impact crater, Mauritania. *40th Lunar and Planetary Science Conference, #1281 (abstr.),* Houston.

Jarosewich, E., Nelen, J. A., and Norberg, J. A. (1980). Reference samples for electron microprobe analysis. *Geostandards and Geoanalytical Research* 4, 43–47.

Joesten, R. (1976). High-temperature contact metamorphism of carbonate rocks in a shallow crustal environment, Christmas Mountains, Big Bend region, Texas. *The American Mineralogist* 61, 776–781.

Jolis, E. M., Freda, C., Troll, V. R., Deegan, F. M., Blythe, L. S., McLeod, C. L., and Davidson, J. P. (2013). Experimental simulation of magma–carbonate interaction beneath Mt. Vesuvius, Italy. *Contributions to Mineralogy and Petrology* 166, 1335–1353.

Jolliff, B. L., Korotev, R. L., and Haskin, L. A. (1993). An iridium-rich iron micrometeorite with silicate inclusions from the Moon. *24th Lunar and Planetary Science Conference, #729 (abstr.),* Houston.

Jones, A. P., Claeys, P., and Heuschkel, S. (2000). Impact melting of carbonates from the Chicxulub crater. *Impacts and the early Earth: lecture notes in earth sciences, 91.* Ed. by I. Gilmour and C. Koeberl. Berlin: Springer, 343–361.

Joy, K., Zolensky, M. E., Nagashima, K., Huss, G. R., Ross, D. K., McKay, D. S., and Kring, D. A. (2012). Direct detection of projectile relics from the end of the lunar basin-forming epoch. *Science* 336, 1426–1429.

Kadono, T., Sugita, S., Mitani, N. K., Fuyuki M., Ohno, S., Sekine, Y., and Matsui, T. (2002). Vapor clouds generated by laser ablation and hypervelocity impact. *Geophysical Research Letters* 29, 40-1–40-4.

Kargel, J. S., Kirk, R. L., Fegley Jr., B., and Treiman, A. H. (1994). Carbonate–sulfate volcanism on Venus. *Icarus* 112, 219–252.

Kearsley, A., Graham, G., McDonnell, T., Bland, P. A., Hough, R., and Helps, P. (2004). Early fracturing and impact residue emplacement: can modeling help to predict their location in major craters? *Meteoritics & Planetary Science* 39, 247–265.

Keller, L. P. and McKay, D. S. (1992). Micrometer-sized glass spheres in Apollo 16 Soil 61181: implications for impact volatilization and condensation. *Proceedings, 22nd Lunar and Planetary Science Conference,* 137–141.

Kelly, W. R., Holdsworth, E., and Moore, C. B. (1974). The chemical composition of metallic spheroids and metallic particles within impactite from Barringer Meteorite Crater, Arizona. *Geochimica et Cosmochimica Acta* 38, 533–543.

Kenkmann, T., Deutsch, A., Thoma, K., Ebert, M., Poelchau, M. H., Bulh, E., Carl, E.-R., Danilewsky, A. N., Dresen, G., Dufresne, A., Durr, N., Ehm, L., Hecht, L., Hiermaier, S., Hoerth, T., Grosse, T., Gulde, M., Güldemeister, N., Hamann, C., Kowitz, A., Langenhorst, F., Lexow, B., Liermann, H.-P., Luther, R., Mansfeld, U., Moser, D., Raith, M., Reimold, W. U., Sauer, M., Schäfer, F., Schmitt R. T., Sommer, F., Wilk, J., Winkler,

R., and Wünnemann, K. (in press). Experimental impact cratering: a summary of the major results of the MEMIN research unit. *Meteoritics & Planetary Science.*

Kieffer, S. W. (1971). Schock metamorphism of the Coconino sandstone at Meteor Crater, Arizona. *Journal of Geophysical Research* 76, 5449–5473.

Kieffer, S. W., Phakey, D. P., and Christie, J. M. (1976a). Shock processes in porous quartzite: transmission electron mircroscope observations and theory. *Contributions to Mineralogy and Petrology* 59, 41–93.

Kieffer, S. W., Schaal, R. B., Gibbons, R. V., Hörz, F., Milton, D. J., and Dube, A. (1976b). Shocked basalt from Lonar Impact Crater, India, and experimental analogues. *Proceedings, 7th Lunar Science Conference,* 1391–1412.

Kieffer, S. W. and Simonds, C. H. (1980). The role of volatiles and lithology in the impact cratering process. *Reviews of Geophysics* 18, 143–181.

Kjarsgaard, B. O. and Hamilton, D. L. (1988). Liquid immiscibility and the origin of alkali-poor carbonatites. *Mineralogical Magazine* 52, 43–55.

Kjarsgaard, B. O. and Hamilton, D. L. (1989). The genesis of carbonatites by immiscibility. *Carbonatites: genesis and evolution.* Ed. by K. Bell. London: Unwin Hyman, 388–404.

Koeberl, C., Claeys, P., Hecht, L., and McDonald, I. (2012). Geochemistry of impactites. *Elements* 8, 37–42.

Koeberl, C., Shukolyukov, A., and Lugmair, G. W. (2007). Chromium isotopic studies of terrestrial impact craters: identification of meteoritic components at Bosumtwi, Clearwater East, Lappajärvi, and Rochechouart. *Earth and Planetary Science Letters* 256, 534–546.

Koeberl, C. (1998). Identification of meteoritic components in impactites. *Meteorites: flux with time and impact effects.* Ed. by M. M. Grady, R. Hutchison, G. J. H. McCall, and D. A. Rothery. London: Geological Society Special Publications 140, 133–153.

Koeberl, C., Sharpton, V. L., Schuraytz, B. C., Shirey, S. B., Blum, J. D., and Marin, L. E. (1994). Evidence for a meteoritic component in impact melt rock from the Chicxulub structure. *Geochimica et Cosmochimica Acta* 58, 1679–1684.

Kokubo, E. and Ida, S. (2000). Formation of protoplanets from planetesimals in the solar nebula. *Icarus* 143, 15–27.

Korhonen, F. J., Clark, C., Brown, M., and Taylor, R. J. M. (2014). Taking the temperature of Earth's hottest crust. *Earth and Planetary Science Letters* 408, 341–354.

Koster van Groos, A. F. and Wyllie, P. J. (1966). Liquid immiscibility in the system Na_2O–Al_2O_3–SiO_2–CO_2 at pressures to 1 kilobar. *American Journal of Science* 264, 234–255.

Koster van Groos, A. F. and Wyllie, P. J. (1973). Liquid immiscibility in the join $NaAlSi_3O_8$–$CaAl_2Si_2O_8$–Na_2CO_3–H_2O. *American Journal of Science* 273, 465–487.

Kowitz, A., Güldemeister, N., Reimold, W. U., Schmitt, R.-T., and Wünnemann, K. (2013a). Diaplectic quartz glass and SiO_2 melt experimentally generated at only 5 GPa shock pressure in porous sandstone: laboratory observations and meso-scale numerical modeling. *Earth and Planetary Science Letters* 384, 17–26.

Kowitz, A., Güldemeister, N., Schmitt, R.-T., Reimold, W. U., Wünnemann, K., and Holzwarth, A. (2016). Revision and recalibration of existing shock classifications for quartzose rocks using low-shock pressure (2.5–20 GPa) recovery experiments and mesoscale numerical modeling. *Meteoritics & Planetary Science* 51, 1741–1761.

Kowitz, A., Schmitt, R.-T., Reimold, W. U., and Hornemann, U. (2013b). The first MEMIN shock recovery experiments at low shock pressure (5–12.5 GPa) with dry, porous sandstone. *Meteoritics & Planetary Science* 48, 99–114.

Kracher, A. (1983). Notes on the evolution of the IIIAB/pallasite parent body. *14th Lunar and Planetary Science Conference, #405 (abstr.),* Houston.

Kraus, R. G., Root, S., Lemke, R. W., Stewart, S. T., Jacobsen, S. B., and Mattsson, T. R. (2015). Impact vaporization of planetesimal cores in the late stages of planet formation. *Nature Geoscience* 8, 296–272.

Kraus, R. G., Stewart, S. T., Swift, D. C., Bolme, C. A., Smith, R. F., Hamel, S., Hammel, B. D., Spaulding, D. K., Hicks, D. G., Eggert, J. H., and Collins, G. W. (2012). Shock vaporization of silica and the thermodynamics of planetary impact events. *Journal of Geophysical Research: Planets* 117, E09009.

Kring, D. A. (1997). Air blast produced by the Meteor Crater impact event and a reconstruction of the affected environment. *Meteoritics & Planetary Science* 32, 517–530.

Kring, D. A. (2007). *Guidebook to the geology of Barringer Meteorite Crater (a.k.a. Meteor Crater).* Houston: Lunar and Planetary Institute, LPI Contribution No. 1355.

Kurosawa, K., Ohno, S., Sugita, S., Mieno, T., Matsui, T., and Hasegawa, S. (2012). The nature of shock-induced calcite ($CaCO_3$) devolatilization in an open system investigated using a two-stage light gas gun. *Earth and Planetary Science Letters* 337-338, 68–76.

Lange, M. A. and Ahrens, T. J. (1986). Shock-induced CO_2 loss from $CaCO_3$: implications for early planetary atmospheres. *Earth and Planetary Science Letters* 77, 409–418.

Langenhorst, F. (2002). Shock metamorphism of some minerals: basic introduction and microstructural observations. *Bulletin of the Czech Geoloical Survey* 77, 265–282.

Langenhorst, F. and Deutsch, A. (2012). Shock metamoprhism of minerals. *Elements* 8, 31–36.

Le Bas, M. J., Le Maitre, R. W., Streckeisen, A., and Zanettin, B. (1986). A chemical classification of volcanic rocks based on the total alkali–silica diagram. *Journal of Petrology* 27, 745–750.

Lee, W.-J. and Wyllie, P. J. (1996). Liquid immiscibility in the join $NaAlSi_3O_8$–$CaCO_3$ to 2.5 GPa and the origin of calciocarbonatite magmas. *Journal of Petrology* 37, 1125–1152.

Lee, W.-J. and Wyllie, P. J. (1997). Liquid immiscibility between nephelinite and carbonatite from 1.0 to 2.5 GPa compared with mantle melt compositions. *Contributions to Mineralogy and Petrology* 127, 1–16.

Lee, W.-J. and Wyllie, P. J. (1998). Petrogenesis of carbonatite magmas from mantle to crust, constrained by the system CaO–(MgO + FeO*)–(Na_2O + K_2O)–(SiO_2 + Al_2O_3 + TiO_2)–CO_2. *Journal of Petrology* 39, 495–517.

Lee, W.-J., Wyllie, P. J., and Rossmann, G. R. (1994). CO_2-rich glass, round calcite crystals, and no liquid immiscibility in the system CaO–SiO_2–CO_2 at 2.5 GPa. *The American Mineralogist* 79, 1135–1144.

Leuw, S. D., Rubin, A. E., and Wasson, J. T. (2010). Carbonates in CM chondrites: complex formational histories and comparison to carbonates in CI chondrites. *Meteoritics & Planetary Science* 45, 513–530.

Lin, B., Zhang, W., Lou, Z., Zhang, D., and Li, Y. (2014). Comparative study on microstructures and mechanical properties of the heat-treated Al–5.0Cu–0.6Mn–xFe alloys prepared by gravity die casting and squeeze casting. *Materials and Design* 59, 10–18.

Lin, C., Hollister, L. S., MacPherson, G. J., Bindi, L., Ma, C., Andronicos, C. L., and Steinhardt, P. J. (2017). Evidence of cross-cutting and redox reaction in Khatyrka meteorite reveals metallic-Al minerals formed in outer space. *Scientific Reports* 7, 1637.

Lindsley, D. H. and Andersen, D. J. (1983). A two-pyroxene thermometer. *Journal of Geophysical Research* 88, A887.

Lodders, K. (2003). Solar system abundances and condensation temperatures of the elements. *Astrophysical Journal* 591, 1220–1247.

Longhi, J. (1990). Silicate liquid immiscibility in isothermal crystallization experiments. *Proceedings, 19th Lunar and Planetary Science Conference,* 13–24.

Lucey, P., Korotev, R. L., Gillis, J. J., Taylor, L. A., Lawrence, D., Campbell, B. A., Elphic, R., Feldman, B., Hood, L. L., Hunten, D., Mendillo, M., Noble, S. K., Papike, J. J., Reedy, R., Lawson, S., Prettyman, T., Gas-

nault, O., and Maurice, S. (2006). Understanding the lunar surface and space–moon interaction. *New views of the moon.* Ed. by B. L. Jolliff, M. A. Wieczorek, C. K. Shearer, and C. R. Neal. Washington, DC: Mineralogical Society of America and Geochmical Society, 83–220.

Luther, R., Prieur, N. C., Wünneman, K., and Werner, S. C. (2017). Crater formation and shock melt production for the 17th March 2013 lunar impact flash event. *48th Lunar and Planetary Science Conference, #3012 (abstr.),* Houston.

MacPherson, G. J., Andronicos, C. L., Bindi, L., Distler, V. V., Eddy, M. P., Eiler, J. M., Guan, Y., Hollister, L. S., Kostin, A., Kryachko, V., Steinhardt, W. M., Yudovskaya, M., and Steinhardt, P. J. (2013). Khatyrka, a new CV3 find from the Koryak Mountains, Eastern Russia. *Meteoritics & Planetary Science* 48, 1499–1514.

Marchi, S., Bottke, W. F., Cohen, B. A., Wünnemann, K., Kring, D. A., McSween, H. Y., de Sanctis, M. C., O'Brien, D. P., Schenk, P., Raymond. C. A., and Russell, C. T. (2013). High-velocity collisions from the lunar cataclysm recorded in asteroidal meteorites. *Nature Geoscience* 6, 303–307.

Marchi, S., Bottke, W. F., Elkins-Tanton, L. T., Bierhaus, M., Wünnemann, K., Morbidelli, A., and Kring, D. A. (2014). Widespread mixing and burial of Earth's Hadean crust by asteroid impacts. *Nature* 511, 578–582.

Marineca, S., Bilal, E., Verkaeren, J., Pascal, M.-L., and Fonteilles, M. (2001). Superposed paragenesis in the spurrite-, tilleyite-, and gehlenite-bearing skarns from Cornet Hill, Apuseni Mountains, Romania. *The Canadian Mineralogist* 39, 1435–1453.

Martin, L. H., Schmidt, M. W., Mattsson, H. B., and Guenther, D. (2013). Element partitioning between immiscible carbonatite and silicate melts for dry and H_2O-bearing systems at 1–3 GPa. *Journal of Petrology* 54, 2301–2338.

Martinez, I., Agrinier, P., Schärer, U., and Javoy, M. (1994). A SEM–ATEM and stable isotope study of carbonates from the Haughton impact crater, Canada. *Earth and Planetary Science Letters* 121, 559–574.

Martinez, I., Deutsch, A., Schärer, U., Ildefonse, P., Guyot, F., and Agrinier, P. (1995). Shock recovery experiments on dolomite and thermodynamical calculations of impact induced decarbonation. *Journal of Geophysical Research* 100, 15465–15476.

Marvin, U. B., Wood, J. A., Taylor, G. J., Reid, J. B., Powell, B. N., Dickey, J. S., and Bower, J. F. (1971). Relative proportions and probable sources of rock fragments in the Apollo 12 soil samples. *Proceedings, 2nd Lunar Science Conference,* 679–699.

Masaitis, V. L. (1998). Popigai crater: origin and distribution of diamond-bearing impactites. *Meteoritics & Planetary Science* 33, 349–359.

McCoy, T. J. (1995). Silicate-bearing IIE irons: early mixing and differentiation in a core mantle environment and shock resetting of ages. *Meteoritics* 30, 542–543.

McKay, D. S., Heiken, G., Basu, A., Blanford, G., Simon, S., Reedy, R., French, B. M., and Papike, J. J. (1991). The lunar regolith. *Lunar sourcebook.* Ed. by G. Heiken, D. Vaniman, and B. M. French. Cambridge: Cambridge University Press, 285–356.

McKibbin, S. J. and Claeys, P. (2014). Heterogeneous, rapid crystallization of the Main-Group pallasite parent body: planetesimal history from principle component analysis of metal geochemistry and accessory phase mineralogies. *37th Symposium on Antarctic Meteorites, (abstr.),* Tokyo.

McKibbin, S. J., Ireland, T. R., Holden, P., O'Neill, H. S. C., and Mallmann, G. (2016). Rapid cooling of planetesimal core–mantle reaction zones from Mn–Cr isotopes in pallasites. *Geochemical Perspective Letters* 2, 68–77.

McKibbin, S. J., Pittarello, L., and Claeys, P. (2015). Contrasting styles of interaction between core and mantle reservoirs in the Main-group pallasite source. *25th Goldschmidt Conference, #2079 (abstr.),* Prague.

McSween, H. Y., Mittlefehldt, D. W., Beck, A. W., Rhiannon, G. M., and McCoy, T. J. (2011). HED meteorites and their relationship to the geology of Vesta and the Dawn mission. *Space Science Reviews* 163, 141–174.

Melosh, H. J. (1989). *Impact cratering: a geologic process.* New York: Oxford University Press.

Melosh, H. J. (2007). A hydrocode equation of state for SiO_2. *Meteoritics & Planetary Science* 42, 2079–2098.

Melosh, H. J., Ryan, E. V., and Asphaug, E. (1992). Dynamic fragmentation in impacts: hydrocode simulation of laboratory impacts. *Journal of Geophysical Research* 97, 14735–14759.

Michalski, J. R. and Niles, P. B. (2010). Deep crustal carbonate rocks exposed by meteor impact on Mars. *Nature Geoscience* 3, 751–755.

Miliken, R. E., Grotzinger, J. P., and Thomson, B. J. (2010). Paleoclimate of Mars as captured by the stratigraphic record in Gale Crater. *Journal of Geophysical Research* 37, L04201.

Mittlefehldt, D. W., Hörz, F., See, T. H., Scott, E. R. D., and Mertzman, S. A. (2005). Geochemistry of target rocks, impact-melt particles, and metallic spherules from Meteor Crater, Arizona: empirical evidence on the impact process. *Geological Society of America Special Paper* 384, 367–390.

Mittlefehldt, D. W., McCoy, T. J., Goodrich, C. A., and Kracher, A. (1998). Non-chondritic meteorites from asteroidal bodies. *Reviews in miner-*

alogy, Vol. 36: planetary materials. Ed. by J. J. Papike. Mineralogical Society of America, 4.1–4.196.

Mittlefehldt, D. W., See, T. H., and Hörz, F. (1992). Dissemination and fractionation of projectile materials in the impact melts from Wabar crater, Saudi Arabia. *Meteoritics* 27, 361–370.

Morbidelli, A., Chambers, J., Lunine, J. I., Petit, J. M., Robert, F., Valsecchi, G. B., and Cyr, K. E. (2000). Source regions and time scales for the delivery of water to Earth. *Meteoritics & Planetary Science* 35, 1309–1320.

Moreau, J., Kohout, T., and Wünnemann, K. (in press). Shock-darkening in ordinary chondrites: determination of the pressure–temperature conditions by shock physics mesoscale modeling. *Meteoritics & Planetary Science.*

Morgan, J. V., Gulick, S. P. S., Bralower, T., Chenot, E., Christeson, G., Claeys, P., Cockell, C., Collins, G. S., Coolen, M. J. L., Ferrière, L., Gebhardt, C., Goto, K., Jones, H., Kring, D. A., Le Ber, E., Lofi, J., Long, X., Lowery, C., Mellett, C., Ocampo-Torres, R., Osinski, G. R., Perez-Cruz, L., Pickersgill, A., Poelchau, M., Rae, A., Rasmussen, C., Rebolledo-Vieyra, M., Riller, U., Sato, H., Schmitt, D. R., Smit, J., Tikoo, S., Tomioka, N., Urrutia-Fucugauchi, J., Whalen, M., Wittmann, A., Yamaguchi, K. E., and Zylberman, W. (2016). The formation of peak rings in large impact craters. *Science* 354, 878–882.

Myers, J. and Eugster, H. P. (1983). The system Fe–Si–O: oxygen buffer calibrations to 1, 500K. *Contributions to Mineralogy and Petrology* 82, 75–90.

Mysen, B. and Richet, P. (2005). *Silicate glasses and melts.* Amsterdam: Elsevier.

Nagaki, K., Kadono, T., Sakaiya, T., Kondo, T., Kurosawa, K., Hironaka, Y., Shigemori, K., and Arakawa, M. (2016). Recovery of entire shocked samples in a range of pressure from ~100 GPa to Hugoniot elastic limit. *Meteoritics & Planetary Science* 51, 1153–1162.

Nakazawa, S., Watanabe, S., Iijima, Y., and Kato, M. (2002). Experimental investigation of shock wave attenuation in basalt. *Icarus* 156, 539–550.

Nazarov, M. A., Shornikov, S. I., and Demidova, S. I. (2015). Origin of native silicon and iron silicides in the Dhofar 280 lunar meteorite. *Petrology* 23, 168–175.

Neukum, G. (1983). "Meteoritenbombardement und Datierung planetarer Oberflächen". PhD thesis. Munich, Germany: University of Munich.

Neukum, G. and Ivanov, B. A. (1994). Crater size distributions and impact probabilities on Earth from lunar, terrestrial-planet, and asteroid cratering data. *Hazards due to comets and asteroids.* Ed. by T. Gehrels. Tucson: University of Arizona, 359–416.

Neukum, G., Ivanov, B. A., and Hartmann, W. K. (2001). Cratering records in the inner solar system in relation to the lunar reference system. *Space Science Reviews* 96, 55–86.

Newsom, H. E. and Drake, M. J. (1983). Experimental investigations of the partitioning of phosphorus between metal and silicate phases: implications for the Earth, Moon and eucrite parent body. *Geochimica et Cosmochimica Acta* 47, 93–100.

Nininger, H. H. (1954). *Arizona's Meteorite Crater.* Denver: World Press.

Nishiizumi, K., Kohl, C., Shoemaker, E., Arnold, J., Klein, J., Fink, D., and Middleton, R. (1991). In situ 10Be–26Al exposure ages at Meteor Crater, Arizona. *Geochimica et Cosmochimica Acta* 55, 2699–2703.

Novella, D. and Keshav, S. (2010). Silicate melt–carbonatite liquid immiscibility reconsidered in the system CaO–MgO–Al_2O_3 at 2–3 GPa. *EMPG XIII, (abstr.),* Toulouse.

Oberst, J., Christou, A., Suggs, R., Moser, D., Daubar, I. J., McEwen, A. S., Burchell, M., Kawamura, T., Hiesinger, H., Wünnemann, K., Wagner, R., and Robinson, M. S. (2012). The present-day flux of large meteoroids on the lunar surface—a synthesis of models and observational techniques. *Planetary and Space Science* 74, 179–193.

Ohno, S., Sugita, S., Kadono, T., Hasegawa, S., and Igarashi, G. (2004). Sulfur chemistry in laser-simulated impact vapor clouds: implications for the K/T impact event. *Earth and Planetary Science Letters* 218, 347–361.

O'Keefe, J. D. and Ahrens, T. J. (1989). Impact production of CO_2 by the Cretaceous/Tertiary extinction bolide and the resultant heating of the Earth. *Nature* 388, 247–249.

O'Keefe, J. D. and Ahrens, T. J. (1993). Planetary cratering mechanincs. *Journal of Geophysical Research* 98, 17011–17028.

Olsen, E. J., Davis, A., Clarke, R. S. J., Schultz, L., Weber, H. W., Clayton, R., Mayeda, T., Lipschutz, M. E., Steele, I. M., and Schwade, J. (1994). Watson: a new link in the IIE iron chain. *Meteoritics* 29, 200–2013.

Olsen, E. J. and Jarosewich, E. (1971). Chondrules: first occurence in an iron meteorite. *Science* 174, 853–858.

Olsen, E. J., Kracher, A., Davis, A. M., Steele, I. M., Hutcheon, I., and Bunch, T. E. (1999). The phosphates of IIIAB iron meteorites. *Meteoritics & Planetary Science* 34, 285–300.

Olsson-Steel, D. (1990). The asteroidal impact rate upon the terrestrial planets: an update. *Proceedings of the Astronomical Society of Australia* 8, 303–307.

Osadchii, E. G., Baryshnikova, G. V., and Novikov, G. V. (1981). The Elga meteorite: silicate inclusions and shock metamorphism. *Proceedings, Lunar and Planetary Science Conference 12B,* 1049–1068.

Osinski, G. R. (2003). Impact glasses in fallout suevites from the Ries impact structure, Germany: an analytical SEM study. *Meteoritics & Planetary Science* 38, 1641–1668.

Osinski, G. R. (2007). Impact metamorphism of $CaCO_3$-bearing sandstones at the Haughton structure, Canada. *Meteoritics & Planetary Science* 42, 1945–1960.

Osinski, G. R., Bunch, T. E., Flemming, R. L., Buitenhuis, E., and Wittke, J. H. (2015). Impact melt- and projectile bearing ejecta at Barringer Crater, Arizona. *Earth and Planetary Science Letters* 432, 283–292.

Osinski, G. R., Grieve, R. A. F., Chanou, A., and Sapers, H. M. (2016). The "suevite" conundrum, Part 1: the Ries suevite and the Sudbury Onaping Formation compared. *Meteoritics & Planetary Science* 51, 2316–2333.

Osinski, G. R. and Pierazzo, E. (2012). *Impact cratering: processes and products.* Chichester, UK: John Wiley and Sons.

Osinski, G. R. and Spray, J. G. (2001). Impact-generated carbonate melts: evidence from the Haughton structure, Canada. *Earth and Planetary Science Letters* 194, 17–29.

Osinski, G. R., Spray, J. G., and Grieve, R. A. F. (2008). Impact melting in sedimentary target rocks: an assessment. *Geological Society of America Special Paper* 437, 1–17.

Ott, U., Merchel, S., Herrmann, S., Pavetich, S., Rugel, G., Faestermann, T., Fimiani, L., Gomez-Guzman, J. M., Hain, K., Korschinek, G., Ludwig, P., D'Orazio, M., and Folco, L. (2014). Cosmic ray exposure and preatmospheric size of the Gebel Kamil iron meteorite. *Meteoritics & Planetary Science* 49, 1365–1374.

Otto, J. W. and Wyllie, P. J. (1993). Relationships between silicate melts and carbonate-precipitating melts in $CaO–MgO–SiO_2–CO_2–H_2O$ at 2 kbar. *Mineralogy and Petrology* 48, 343–365.

Pak, J. J. and Fruehan, R. J. (1986). Soda slag system for hot metal dephosphorization. *Metallurgical and Materials Transactions B* 17B, 797–804.

Palme, H., Janssens, M.-J., Takahasi, H., Anders, E., and Hertogen, J. (1978). Meteorite material at five large impact craters. *Geochimica et Cosmochimica Acta* 42, 313–323.

Pascal, M.-L., Fonteilles, M., Verkaeren, J., Piret, R., and Marineca, S. (2001). The melilite-bearing high-temperature skarns of the Apuseni Mountains, Carparthians, Romania. *The Canadian Mineralogist* 39, 1405–1434.

Philby, H. S. J. B. (1933). *The Empty Quarter: being a description of the great south desert of Arabia known as Rub 'al Khali.* New York: H. Holt and Company.

Phillips, F. M., Zreda, M. G., Smith, S. S., Elmore, D., Kubik, P. W., Dorn, R. I., and Roddy, D. J. (1991). Age and geomorphic history of Meteor Crater, Arizona, from cosmogenic ^{36}Cl and ^{14}C in rock varnish. *Geochimica et Cosmochimica Acta* 55 (9), 2695–2698.

Philpotts, A. R. (1978). Textural evidence for liquid immiscibility in tholeiites. *Mineralogical Magazine* 42, 417–425.

Philpotts, A. R. (1982). Compositions of immiscible liquids in volcanic rocks. *Contributions to Mineralogy and Petrology* 80, 201–218.

Philpotts, A. R. (2008). Comments on: liquid immiscibility and the evolution of basaltic magma. *Journal of Petrology* 49, 2171–2175.

Philpotts, A. R. and Ague, J. J. (2009). *Principles of igneous and metamorphic petrology.* Cambridge: Cambridge University Press.

Philpotts, A. R. and Doyle, C. D. (1983). Effect of magma oxidation state on the extent of silicate liquid immiscibility in a tholeiitic basalt. *American Journal of Science* 283, 967–986.

Piccoli, P. M. and Candela, P. (2002). Apatite in igneous systems. *Reviews in mineralogy volume 48. Phosphates: geochemical, geobiological, and materials importance.* Ed. by M. L. Kohn, J. Rakovan, and J. M. Hughes. Mineralogical Society of America, 255–292.

Pierazzo, E. and Artemieva, N. (2012). Local and global environmental effects of impacts on Earth. *Elements* 8, 55–60.

Pierazzo, E., Artemieva, N., and Ivanov, B. A. (2005). Starting conditions for hydrothermal systems underneath Martian craters: hydrocode modeling. *384,* 443–457.

Pierazzo, E., Hahmann, A. N., and Sloan, L. C. (2003). Chicxulub and climate: effects of stratospheric injections of impact-produced S-bearing gases. *Astrobiology* 3, 99–118.

Pierazzo, E., Kring, D. A., and Melosh, H. J. (1998). Hydrocode simulation of the Chicxulub impact event and the production of climatically active gases. *Journal of Geophysical Research* 103, 28607–28625.

Pierazzo, E. and Melosh, H. J. (1999). Hydrocode modeling of Chicxulub as an oblique impact event. *Earth and Planetary Science Letters* 165, 163–176.

Pierazzo, E., Vickery, A. M., and Melosh, H. J. (1997). A reevaluation of impact melt production. *Icarus* 127, 408–423.

Pilkington, M., Hildebrand, A. R., and Ortiz-Aleman, C. (1994). Gravity and magnetic field modeling and structure of the Chicxulub Crater, Mexico. *Journal of Geophysical Research: Planets* 99, 13147–13162.

Poelchau, M. H., Kenkmann, T., Hoerth, T., Schäfer, F., Rudolf, M., and Thoma, K. (2014). Impact cratering experiments into quartzite, sandstone and tuff: the effects of projectile size and target properties on spallation. *Icarus* 242, 211–224.

Poelchau, M. H., Kenkmann, T., Thoma, K., Hoerth, T., Dufresne, A., and Schäfer, F. (2013). The MEMIN research unit: scaling impact cratering experiments in porous sandstones. *Meteoritics & Planetary Science* 48, 8–22.

Pratesi, G., Morelli, M., Rossi, A. P., and Ori, G. G. (2005). Chemical compositions of impact melt breccias and target rocks from the Tenoumer impact crater, Mauritania. *Meteoritics & Planetary Science* 40, 1653–1672.

Prescott, J. R., Robertson, G. B., Shoemaker, C., Shoemaker, E., and Wynn, J. (2004). Luminescence dating of the Wabar meteorite craters, Sauid Arabia. *Journal of Geophysical Research* 109, E01008.

Prinz, M., Nehru, C. E., and Delaney, J. S. (1982). Sombrerete: an iron with highly fractionated amphibole-bearing Na–P silicate inclusions. *13th Lunar and Planetary Science Conference, #634 (abstr.),* Houston.

Prinz, M., Nehru, C. E., Delaney, J. S., Weisberg, M. K., and Olsen, E. J. (1983). Globular silicate inclusions in IIE irons and Sombrerete: highly fractionated minimum melts. *14th Lunar and Planetary Science Conference, #618 (abstr.),* Houston.

Putirka, K. D. (2005). Mantle potential temperatures at Hawaii, Iceland, and the mid-ocean ridge system, as inferred from olivine phenocrysts: evidence for thermally driven mantle plumes. *Geochemistry, Geophysics, Geosystems* 6, 1–14.

Quaide, W. I. and Bunch, T. E. (1970). Impact metamorphism of lunar surface materials. *Proceedings, Apollo 11 Lunar Science Conference.* Vol. 1, 711–729.

Rae, A. S. P., Collins, G. S., Grieve, R. A. F., Osinski, G. R., and Morgan, J. V. (in press). Complex crater formation: insights from combining observations of shock pressure distribution with numerical models at the West Clearwater Lake impact structure. *Meteoritics & Planetary Science.*

Raymond, S. N., O'Brien, D. P., Morbidelli, A., and Kaib, N. A. (2009). Building the terrestrial planets: constrained accretion in the inner Solar System. *Icarus* 203, 644–662.

Reese, C. C. and Solomatov, V. S. (2010). Early martian dynamo generation due to giant impacts. *Icarus* 207, 82–97.

Reese, C. C., Solomatov, V. S., Baumgardner, J. R., Stegman, D. R., and Vezolainen, A. V. (2004). Magmatic evolution of impact-induced Martian mantle plumes and the origin of Tharsis. *Journal of Geophysical Research* 109, E08009.

Reimold, W. U. and Koeberl, C. (2014). Impact structures in Africa: a review. *Journal of African Earth Sciences* 93, 57–175.

Rietmeijer, J. M., Nakamura, T., Tsuchiyama, A., Uesugi, K., Nakano, T., and Leroux, H. (2008). Origin and formation of iron silicide phases in the aerogel of the Stardust mission. *Meteoritics & Planetary Science* 43, 121–134.

Righter, K. and Drake, M. J. (2000). Metal/silicate equilibrium in the early Earth: new constraints from the volatile moderately siderophile elements Ga, Cu, P and Sn. *Geochimica et Cosmochimica Acta* 64, 3581–3597.

Righter, K., Pando, K. M., Danielson, L., and Lee, C.-T. (2010). Partitioning of Mo, P and other siderophile elements (Cu, Ga, Sn, Ni, Co, Cr, Mn, V, and W) between metal and silicate melt as a function of temperature and silicate melt composition. *Earth and Planetary Science Letters* 291, 1–9.

Robie, R. A., Hemingway, B. S., and Fisher, J. R. (1995). *Thermodynamic properties of minerals and related substances at 298.15 K and 1 bar (105 pascals) pressure and at higher temperature. U.S. Geological Survey Bulletin 2131.* Washington, DC: United States Government Printing Office.

Roddy, D. J. (1978). Pre-impact geological conditions, physical properties, energy calculations, meteorite and initial crater dimensions and orientations of joints, faults and walls at Meteor Crater, Arizona. *Proceedings, 9th Lunar and Planetary Science Conference,* 3891–3930.

Roddy, D. J., Pepin, R. O., and Merrill, R. B., eds. (1977). *Impact and explosion cratering.* New York: Pergamon Press.

Roedder, E. (1951). Low temperature liquid immiscibility in the system K_2O–FeO–Al_2O_3–SiO_2. *The American Mineralogist* 36, 282–286.

Roedder, E. (1978). Silicate liquid immiscibility in magmas and the system K_2O–FeO–Al_2O_3–SiO_2: an example of serendipity. *Geochimica et Cosmochimica Acta* 42, 1597–1617.

Roedder, E. (1979). Silicate liquid immiscibility in magmas. *The evolution of igneous rocks.* Ed. by H. S. Yoder. Princeton: Princeton University Press, 15–57.

Roedder, E. and Weiblen, P. W. (1970). Lunar petrology of silicate melt inclusions, Apollo 11 rocks. *Proceedings, Apollo 11 Lunar Science Conference* 1, 801–837.

Roedder, E. and Weiblen, P. W. (1971). Petrology of silicate melt inclusions, Apollo 11 and Apollo 12 and terrestrial equivalents. *Proceedings, 2nd Lunar Science Conference* 2, 507–528.

Roeder, P. L. and Emslie, R. F. (1970). Olivine liquid equilibrium. *Contributions to Mineralogy and Petrology* 29, 275–289.

Roels, S., Carmeliet, J., and Hens, H. (2003). Modelling unsaturated moisture transport in heterogeneous limestone. *Transport in Porous Media* 52, 333–350.

Rosa, D. F. and Martin, R. F. (2010). A spurrite-, merwinite- and srebrodolskite-bearing skarn assemblage, West Clearwater Lake impact crater, Northern Quebec. *The Canadian Mineralogist* 48, 1519–1532.

Rowan, L. R. and Ahrens, T. J. (1994). Observations of impact-induced molten metal–silicate partitioning. *Earth and Planetary Science Letters* 122, 71–88.

Rubin, A. E. (1997). The Hadley Rille enstatite chondrite and its agglutinate-like rim: impact melting during accretion of the moon. *Meteoritics & Planetary Science* 32, 135–141.

Rubin, A. E., Jerde, E. A., Zong, P., Wasson, J. T., Westcott, J. W., Mayeda, T., and Clayton, R. (1986). Properties of the Guin ungrouped iron meteorite: the origin of Guin and of group-IIE irons. *Earth and Planetary Science Letters* 76, 209–226.

Ruzicka, A. (2014). Silicate-bearing iron meteorites and their implications for the evolution of asteroidal parent bodies. *Chemie der Erde* 74, 3–48.

Ruzicka, A., Boynton, W. V., and Ganguly, J. (1994). Olivine coronas, metamorphism, and the thermal history of the Morristown and Emery mesosiderites. *Geochimica et Cosmochimica Acta* 58, 2725–2741.

Ruzicka, A., Fowler, G. W., Snyder, G. A., Prinz, M., Papike, J. J., and Taylor, L. A. (1999). Petrogenesis of silicate inclusions in the Weekeroo Station IIE iron meteorite: differentiation, remelting, and dynamic mixing. *Geochimica et Cosmochimica Acta* 63, 2123–2143.

Ruzicka, A. and Hutson, M. (2010). Comparative petrology of silicates in the Udei Station (IAB) and Miles (IIE) iron meteorites: implications for the origin of silicate-bearing irons. *Geochimica et Cosmochimica Acta* 74, 394–433.

Ruzicka, A., Hutson, M., and Floss, C. (2006). Petrology of silicate inclusions in the Sombrerete ungrouped iron meteorite: implictaions for the origins of IIE-type silicate-bearing irons. *Meteoritics & Planetary Science* 41, 1797–1831.

Ryerson, F. J. and Hess, P. C. (1978). Implications of liquid–liquid distribution coefficients to mineral–liquid partitioning. *Geochimica et Cosmochimica Acta* 42, 921–932.

Sack, R. O. and Ghiorso, M. S. (1991). Chromian spinels as petrogenetic indicators; thermodynamics and petrological applications. *The American Mineralogist* 76, 827–847.

Schaal, R. B. and Hörz, F. (1977). Shock metamorphism of lunar and terrestrial basalts. *Proceedings, 8th Lunar Science Conference,* 1697–1729.

Schaal, R. B. and Hörz, F. (1980). Experimental shock metamorphism of lunar soil. *Proceedings, 11th Lunar and Planetary Science Conference,* 1679–1695.

Schaal, R. B., Hörz, F., Thompson, T. D., and Bauer, J. F. (1979). Shock metamorphism of granulated lunar basalt. *Proceedings, 10th Lunar and Planetary Science Conference,* 2547–2571.

Schmid, T. and Dariz, P. (2015). Shedding light onto the spectra of lime: Raman and luminescence bands of CaO, $Ca(OH)_2$ and $CaCO_3$. *Journal of Raman Spectroscopy* 46, 141–146.

Schmidt, M. W. (2006). Element partitioning: the role of melt structure and composition. *Science* 312, 1646–1650.

Schmitt, W., Palme, H., and Wanke, H. (1989). Experimental determination of metal/silicate partition coefficients for P, Co, Ni, Cu, Ga, Ge, Mo, W and some implications for the early evolution of the Earth. *Geochimica et Cosmochimica Acta* 53, 173–186.

Schulte, P., Alegret, L., Arenillas, I., Arz, J. A., Barton, P. J., Bown, P. R., Bralower, T. J., Christeson, G. L., Claeys, P., Cockell, C. S., Collins, G. S., Deutsch, A., Goldin, T. J., Goto, K., Grajales-Nishimura, J. M., Grieve, R. A. F., Gulick, S. P. S., Johnson, K. R., Kiessling, W., Koeberl, C., Kring, D. A., MacLeod, K. G., Matsui, T., Melosh, J., Montanari, A., Morgan, J. V., Neal, C. R., Nichols, D. J., Norris, R. D., Pierazzo, E., Ravizza, G., Rebolledo-Vieyra, M., Reimold, W. U., Robin, E., Salge, T., Speijer, R. P., Sweet, A. R., Urrutia-Fucugauchi, J., Vajda, V., Whalen, M. T., and Willumsen, P. S. (2010). The Chicxulub asteroid impact and mass extinction at the Cretaceous–Paleogene boundary. *Science* 327, 1214–1218.

Schultze, D., Jourdan, F., Hecht, L., Reimold, W. U., and Schmitt, R.-T. (2016). Tenoumer impact crater, Mauretania: impact melt genesis from a lithologically diverse target. *Meteoritics & Planetary Science* 51, 323–350.

Scott, E. R. D. (1972). Chemical fractionation in iron meteorites and its interpretation. *Geochimica et Cosmochimica Acta* 36, 1205–1236.

Scott, E. R. D. and Wasson, J. T. (1976). Chemical classification of iron meteorites – VIII. Groups IC, IIE, IIIF and 97 other irons. *Geochimica et Cosmochimica Acta* 40, 103–115.

See, T. H., Wagstaff, J., Yang, V., Hörz, F., and McKay, G. A. (1998). Compositional variation and mixing of impact melts on microscopic scales. *Meteoritics & Planetary Science* 33, 937–948.

Sensarma, S. and Palme, H. (2013). Silicate liquid immiscibility in the ~2.5 Ga Fe-rich andesite at the top of the Dongargarh large igneous province (India). *Lithos* 170-171, 239–251.

Shannon, R. D. (1976). Revised effective ionic radii and systematic studies of interatomic distances in halides and chalcogenides. *Acta Crystallographica A* 32, 751–767.

Shea, T. and Hammer, J. E. (2013). Kinetics of cooling- and decompression-induced crystallization in hydrous mafic-intermediate magmas. *Journal of Volcanology and Geothermal Research* 260, 127–145.

Shelby, J. E. (2005). *Introduction to glass science and technology.* Cambridge: The Royal Society of Chemistry.

Shoemaker, E. (1963). Impact mechanics at Meteor Crater, Arizona. *The Moon, Meteorites and Comets.* Ed. by B. M. Middlehurst and G. P. Kuiper. Chicago: University of Chicago Press, 301–336.

Shoemaker, E. (1987). Meteor Crater, Arizona. *Rocky Mountain Section of the Geological Society of America Centennial Field Guide.* Ed. by S. S. Beus. Boulder: Geological Society of America, 399–404.

Shoemaker, E. and Wynn, J. (1997). Geology of the Wabar meteorite craters, Saudi Arabia. *28th Lunar and Planetary Science Conference, #1660 (abstr.),* Houston.

Shuvalov, V. (2009). Atmospheric erosion induced by oblique impacts. *Meteoritics & Planetary Science* 44, 1095–1105.

Siegert, S., Branney, M. J., and Hecht, L. (2017). Density current origin of a melt-bearing impact ejecta blanket (Ries suevite, Germany). *Geology* 45, 855–858.

Sighinolfi, G. P., Sibilia, E., Contini, G., and Martini, M. (2015). Thermoluminescence dating of the Kamil impact crater (Egypt). *Meteoritics & Planetary Science* 50, 204–213.

Sigurdsson, H., D'Hondt, S., Arthur, M. A., Bralower, T. J., Zachos, J. C., van Fossen, M., and Channell, E. T. (1991). Glass from the Cretaceous/Tertiary boundary in Haiti. *Nature* 349, 482–487.

Skála, R., Ederová, J., Matìka, P., and Hörz, F. (2002). Mineralogical investigation of experimentally shocked dolomite: implications for the outgassing of carbonates. *Geological Society of America Special Paper* 356, 571–586.

Smit, J. (1999). The global stratigraphy of the cretaceous-tertiary boundary impact ejecta. *Annual Review of Earth and Planetary Sciences* 27, 75–113.

Spear, F. S. (1993). *Metamorphic phase equilibria and pressure–temperature–time paths.* Washington, DC: Mineralogical Society of America.

Spencer, L. J. (1933). Meteoritic iron and silica glass from the meteorite craters of Henbury (central Australia) and Wabar (Arabia). *Mineralogical Magazine* 23, 387–404.

Spicuzza, M. J., Valley, J. W., Fournelle, J., Huberty, J. M., and Treiman, A. (2011). Native silicon and Fe-silicides from the Apollo 16 lunar regolith: extreme reduction, metal-silicate liquid immiscibility, and shock melting. *42nd Lunar and Planetary Science Conference, #2231 (abstr.),* Houston.

Stöffler, D. (1972). Deformation and transformation of rock-forming minerals by natural and experimental shock processes. I. Behavior of minerals under shock compression. *Fortschritte der Mineralogie* 49, 5477–5488.

Stöffler, D. (1974). Deformation and transformation of rock forming minerals by natural and experimental shock processes. II. Physical properties of shocked minerals. *Fortschritte der Mineralogie* 51, 256–289.

Stöffler, D., Artemieva, N., and Pierazzo, E. (2002). Modeling the Ries-Steinheim impact event and the formation of the moldavite strewn field. *Meteoritics & Planetary Science* 37, 1893–1907.

Stöffler, D., Artemieva, N., Wünnemann, K., Reimold, W. U., Jacob, J., Hansen, B. K., and Summerson, I. A. T. (2013). Ries crater and suevite revisited—observations and modeling. Part I: observations. *Meteoritics & Planetary Science* 48, 515–589.

Stöffler, D., Gault, D. E., and Reimold, W. U. (1980a). Experimental hypervelocity impact into quartz sand: pre-impact location of ejecta. *Meteoritics* 15, 371.

Stöffler, D., Gault, D. E., Wedekind, J., and Polkowski, G. (1975). Experimental hypervelocity impact into quartz sand: distribution and shock metamorphism of ejecta. *Journal of Geophysical Research* 80, 4062–4077.

Stöffler, D. and Grieve, R. A. F. (2007). Impactites, Chapter 2.11. *Metamorphic rocks.* Ed. by D. Fettes and J. Desmons. Cambridge: Cambridge University Press, 82–91, 111–125, and 126–242.

Stöffler, D., Hamann, C., and Metzler, K. (2017). Shock metamorphism of planetary silicate rocks and sediments: proposal for an updated classification system. *Meteoritics & Planetary Science.*

Stöffler, D., Keil, K., and Scott, E. R. D. (1991). Shock metamorphism of ordinary chondrites. *Geochimica et Cosmochimica Acta* 55, 3845–3867.

Stöffler, D., Knöll, H.-D., Marvin, U. B., Simonds, C. H., and Warren, P. H. (1980b). Recommended classification and nomenclature of lunar highland rocks – a committee report. *Proceedings, Lunar and Planetary Institute Compiler Conference on the Lunar Highlands Crust,* 51–70.

Stöffler, D. and Langenhorst, F. (1994). Shock metamorphism of quartz in nature and experiment: I. basic observation and theory. *Meteoritics* 29, 155–181.

Stöffler, D. and Ryder, G. (2001). Stratigraphy and isotope ages of lunar geological units: chronological standards for the inner solar system. *Space Science Reviews* 96, 9–54.

Stöffler, D., Ryder, G., Ivanov, B. A., Artemieva, N., Cintala, M. J., and Grieve, R. A. F. (2006). Cratering history and lunar chronology. *New views of the moon.* Ed. by B. L. Jolliff, M. A. Wieczorek, C. K. Shearer,

and C. R. Neal. Washington, DC: Mineralogical Society of America and Geochmical Society, 519–596.

Storzer, D., Sélo, M., Latouche, L., and Fabre, J. (2003). The age of Tenoumer crater, revisited. *34th Lunar and Planetary Science Conference, #1183 (abstr.),* Houston.

Svetsov, V. V. and Shuvalov, V. (2016). Silicate impact-vapor condensate on the Moon: theoretical estimates versus geochemical data. *Geochimica et Cosmochimica Acta* 173, 50–63.

Tagle, R. and Hecht, L. (2006). Geochemical identification of projectiles in impact rocks. *Meteoritics & Planetary Science* 41, 1721–1735.

Takeda, H., Hsu, W., and Huss, G. R. (2003). Mineralogy of silicate inclusions of the Colomera IIE iron and crystallization of Cr-diopside and alkali feldspar from a partial melt. *Geochimica et Cosmochimica Acta* 67, 2269–2288.

Taylor, G. J., Marvin, U. B., Reid, J. B., and Wood, J. A. (1972). Noritic fragments in the Apollo 14 and 12 soils and the origin of Oceanus Procellarum. *Proceedings, 3rd Lunar Science Conference,* 955–1014.

Tera, F., Papanastassiou, D. A., and Wasserburg, G. J. (1974). Isotopic evidence for a terminal lunar cataclysm. *Earth and Planetary Science Letters* 22, 1–21.

Thoma, K., Schäfer, F., Hiermaier, S., and Schneider, E. (2004). An approach to achieve progress in spacecraft shielding. *Advances in Space Research* 34, 1063–1075.

Thompson, R. N. (1975). Is upper-mantle phosphorus contained in sodic garnet? *Earth and Planetary Science Letters* 26, 417–424.

Thompson, S. L. (1990). *ANEOS: analytic equations of state for shock physics codes input manual.* Albuquerque: Sandia National Laboratory.

Thompson, S. L. and Lauson, H. S. (1972). *Improvements in the Chart D radiation-hydrodynamic code 3: revised analytic equations of state. Report SC-RR-71 0714.* Albuquerque: Sandia National Laboratory.

Thomsen, T. B. and Schmidt, M. W. (2008). Melting of carbonated pelites at 2.5–5.0 GPa, silicate–carbonatite liquid immiscibility, and potassium–carbon metasomatism of the mantle. *Earth and Planetary Science Letters* 467, 17–31.

Tilley, C. E. (1929). On larnite (calcium orthosilicate, a new mineral) and its associated minerals from the limestone contact-zone of Scawt Hill, Co. Antrim. *Mineralogical Magazine* 22, 77–86.

Tilley, C. E. and Harwood, H. F. (1931). The dolerite–chalk contact of Scawt Hill, Co. Antrim. The production of basic alkali-rocks by the assimilation of limestone by basaltic magma. *Mineralogical Magazine* 22, 439–468.

Timms, N. E., Erickson, T. M., Zanetti, M. R., Pearce, M. A., Cayron, C., Cavosie, A. J., Reddy, S. M., Wittmann, A., and Carpenter, P. K. (2017). Cubic zirconia in >2370 °C impact melt records Earth's hottest crust. *Earth and Planetary Science Letters* 477, 52–58.

Tollari, N., Baker, D. R., and Barnes, S.-J. (2008). Experimental effects of pressure and fluorine on apatite saturation in mafic magmas, with reference to layered intrusions and massif anorthosites. *Contributions to Mineralogy and Petrology* 156, 161–175.

Tollari, N., Toplis, M. J., and Barnes, S.-J. (2006). Predicting phosphate saturation in silicate magmas: an experimental study of the effects of melt composition and temperature. *Geochimica et Cosmochimica Acta* 70, 1518–1536.

Toplis, M. J., Dingwell, D. B., and Libourel, G. (1994). The effect of phosphorus on the iron redox ratio, viscosity and density of an evolved ferro-basalt. *Contributions to Mineralogy and Petrology* 117, 239–304.

Troll, V. R., Donaldson, C. H., and Emeleus, C. H. (2004). Pre-eruptive magma mixing in ash-flow deposits of the Tertiary Rum Igneous Centre, Scotland. *Contributions to Mineralogy and Petrology* 147, 722–739.

Tropper, P., Recheis, A., and Konzett, J. (2004). Pyrometamorphic formation of phosphorous-rich olivines in partially molten metapelitic gneisses from a prehistoric sacrificial burning site (Otz valley, Tyrol, Austria). *European Journal of Mineralogy* 16, 631–640.

Trunin, R. F., Gudarenko, L. F., Zhernokletov, M. V., and Simakov, G. V. (2001). *Experimental data on shock compression and adiabatic expansion of condensed matter.* Sarov: Russian Federal Nuclear Center VNIEF.

Tschegg, C., Ntaflos, T., and Hein, I. (2009). Thermally triggered two-stage reaction of carbonates and clay during ceramic firing – a case study on Bronze Age Cypriot ceramics. *Applied Clay Science* 43, 69–78.

Tyburczy, J. A. and Ahrens, T. J. (1986). Dynamic compression and volatile release of carbonates. *Journal of Geophysical Research* 91, 4730–4744.

Ulff-Møller, F. (1985). Solidification history of the Kitdlît lens: immiscible metal and sulfide liquids from a basaltic dike on Disko, Central West Greenland. *Journal of Petrology* 26, 64–91.

Ulff-Møller, F. (1998). Solubility of chromium and oxygen in metallic liquids and the co-crystallization of chromite and metal in iron meteorite parent bodies. *24th Lunar and Planetary Science Conference, #1969 (abstr.),* Houston.

Urbain, G., Bottinga, Y., and Richet, P. (1982). Viscosity of liquid silica, silicates and alumo-silicates. *Geochimica et Cosmochimica Acta* 46, 1061–1072.

Urbini, S., Nicolosi I., Zeoli, A., El Khrepy, S., Lethy, A., Hafez, M., El Gabry, M., El Barkooky, A., Barakat, A. A., Gomaa, M., Randwan, A. M., El Sharkawi, M., D'Orazio, M., and Folco, L. (2012). Geological

and geophysical investigation on Kamil crater, Egypt. *Meteoritics & Planetary Science* 47, 1842–1868.

Usui, T., Jones, J., and Mittlefehldt, D. W. (2015). A partial melting study of an ordinary (H) chondrite composition with application to the unique achondrite Graves Nunataks 06128 and 06129. *Meteoritics & Planetary Science* 50, 759–781.

Van Roosbroek, N., Debaille, V., Pittarello, L., Goderis, S., Humayun, M., Hecht, L., Jourdan, F., Spicuzza, M. J., Vanhaeke, F., and Claeys, P. (2015). The formation of IIE iron meteorites investigated by the chondrule-bearing Mont Dieu meteorite. *Meteoritics & Planetary Science* 50, 1173–1196.

Van Roosbroek, N., Pittarello, L., Greshake, A., Debaille, V., and Claeys, P. (2016). First finding of impact melt in the IIE Netschaëvo meteorite. *Meteoritics & Planetary Science* 51, 372–389.

Veksler, I. V. and Charlier, B. (2015). Silicate liquid immiscibility in layered intrusions. *Layered intrusions.* Ed. by B. Charlier, O. Namur, R. Latypov, and C. Tegner. Dordrecht: Springer, 229–258.

Veksler, I. V., Dorfman, A. M., Borisov, A. A., Wirth, R., and Dingwell, D. B. (2007). Liquid immiscibility and the evolution of basaltic magma. *Journal of Petrology* 48, 2187–2210.

Veksler, I. V., Dorfman, A. M., Danyushevsky, L. V., Jakobsen, J. K., and Dingwell, D. B. (2006). Immiscible silicate liquid partition coefficients: implications for crystal-melt element partitioning and basalt petrogenesis. *Contributions to Mineralogy and Petrology* 152, 685–702.

Veksler, I. V., Dorfman, A. M., Dulski, P., Kamenetsky, V. S., Danyushevsky, L. V., Jeffries, T., and Dingwell, D. B. (2012). Partitioning of elements between silicate melt and immiscible fluoride, chloride, carbonate, phosphate and sulfate melts, with implications to the origin of natrocarbonatite. *Geochimica et Cosmochimica Acta* 79, 20–40.

Veksler, I. V., Dorfman, A. M., Rhede, D., Wirth, R., Borisov, A. A., and Dingwell, D. B. (2008). Liquid unmixing kinetics and the extent of immiscibility in the system K_2O–CaO–FeO–Al_2O_3–SiO_2. *Chemical Geology* 256, 119–130.

Veksler, I. V., Kähn, J., and Dingwell, D. B. (2010). Interfacial tension between immiscible liquids in alkaline earth–boron oxide binary systems. *Journal of Non-Crystalline Solids* 356, 1163–1167.

Veksler, I. V., Petibon, C., Jenner, G. A., Dorfman, A. M., and Dingwell, D. B. (1998). Trace element partitioning in immiscible silicate–carbonate liquid systems: an initial experimental study using a centrifuge autoclave. *Journal of Petrology* 39, 2095–2104.

Vickery, A. M. and Melosh, H. J. (1990). Atmospheric erosion and impactor retention in large impacts, with applications to mass extinction. *Geological Society of America Special Paper* 247, 289–300.

Visser, W. and Koster van Groos, A. F. (1979). Phase relations in the system K_2O–FeO–Al_2O_3–SiO_2 at 1 atmosphere with special emphasis on low temperature liquid immiscibility. *American Journal of Science* 279, 70–91.

Vizgirda, J. and Ahrens, T. J. (1982). Shock compression of aragonite and implications for the equation of state for carbonates. *Journal of Geophysical Research* 87, 4747–4758.

Walter, L. S. (1965). Experimental studies on Bowen's decarbonation series. III. *P–T* univariant equilibrium of the reaction: spurrite + monticellite ↔ merwinite + calcite and analysis of assemblages found at Crestmore, California. *American Journal of Science* 263, 64–77.

Wang, S. C. and Starink, M. J. (2005). Precipitates and intermetallic phases in precipitation hardening Al–Cu–Mg–(Li) based alloys. *International Materials Reviews* 50, 193–215.

Wang, Y., Hua, X., and Hsu, W. (2006). Phosphoran-olivine in opaque assemblages of the Ningqiang carbonaceous chondrite: implication to their precursors. *37th Lunar and Planetary Science Conference, #1504 (abstr.),* Houston.

Warren, P. H. (2008). Lunar rock-rain: diverse silicate impact-vapor condensates in an Apollo-14 regolith breccia. *Geochimica et Cosmochimica Acta* 72, 3562–3585.

Wasserburg, G. J., Sanz, G. J., and Bence, A. E. (1968). Potassiumfeldspar phenocrysts in the surface of Colomera, an iron meteorite. *Science* 161, 684–687.

Wasson, J. T. and Choi, B.-G. (2003). Main-group pallasites: chemical composition, relationship to IIIAB irons, and origin. *Geochimica et Cosmochimica Acta* 67, 3079–3096.

Wasson, J. T., Lange, D. E., Francis, C. A., and Ulff-Møller, F. (1999). Massive chromite in the Brenham pallasite and the fractionation of Cr during the crystallization of asteroidal cores. *Geochimica et Cosmochimica Acta* 63, 1219–1232.

Wasson, J. T. and Ouyang, X. (1990). Compositional range in the Canyon Diablo meteoroid. *Geochimica et Cosmochimica Acta* 54, 3175–3183.

Wasson, J. T. and Wang, J. (1986). A nonmagmatic origin of group-IIE iron meteorites. *Geochimica et Cosmochimica Acta* 50, 725–732.

Watson, E. B. (1979). Apatite saturation in basic to intermediate magmas. *Geophysical Research Letters* 6, 937–940.

Watson, E. B. (1980). Apatite and phosphorus in mantle source regions—an experimental study of apatite/melt equilibria at pressures to 25 Kbar. *Earth and Planetary Science Letters* 51, 322–335.

Watters, W. A., Zuber, M. T., and Hager, B. H. (2009). Thermal perturbations caused by large impacts and consequences for mantle convection. *Journal of Geophysical Research* 114, E02001.

Williams, J. P. and Nimmo, F. (2004). Thermal evolution of the Martian core: implications for an early dynamo. *Geology* 32, 97–100.

Wirth, R. (2009). Focused Ion Beam (FIB) combined with SEM and TEM: advanced analytical tools for studies of chemical composition, microstructure and crystal structure in geomaterials on a nanometre scale. *Chemical Geology* 261, 217–229.

Wood, M. I. and Hess, P. C. (1980). The structural role of Al_2O_3 and TiO_2 in immiscible silicate liquids in the system SiO_2–MgO–CaO–FeO–TiO_2–Al_2O_3. *Contributions to Mineralogy and Petrology* 72, 319–328.

Wozniakiewicz, P. J., Ishii, H. A., Kearsley, A., Bradley, J. P., Price, M. C., Burchell, M. J., Teslich, N., and Cole, M. J. (2015). The survivability of phyllosilicates and carbonates impacting Stardust Al foils: facilitating the search for cometary water. *Meteoritics & Planetary Science* 50, 2003–2023.

Wozniakiewicz, P. J., Ishii, H. A., Kearsley, A., Burchell, M. J., Bland, P. A., Bradley, J. P., Dai, Z., Teslich, N., Collins, G. S., Cole, M. J., and Russell, S. S. (2011). Investigation of iron sulfide impact crater residues: a combined analysis by scanning and transmission electron microscopy. *Meteoritics & Planetary Science* 46, 1007–1024.

Wozniakiewicz, P. J., Kearsley, A., Ishii, H. A., Burchell, M. J., Bradley, J. P., Teslich, N., Cole, M. J., and Price, M. C. (2012). The origin of crystalline residues in Stardust Al foils: surviving cometary dust or crystallized impact melts? *Meteoritics & Planetary Science* 47, 660–670.

Wünnemann, K., Engelmann, J., Luther, R., and Hamann, C. (2017). Impact-induced shock melting and ejection of material in an asteroidal environment—implications for the deficit in melt agglutinates in Itokawa samples. *48th Lunar and Planetary Science Conference, #2023 (abstr.),* Houston.

Wünnemann, K., Collins, G. S., and Melosh, H. J. (2006). A strain-based porosity model for use in hydrocode simulations of impacts and implications for transient crater growth in porous targets. *Icarus* 180, 514–527.

Wünnemann, K., Collins, G. S., and Osinski, G. R. (2008). Numerical modeling of impact melt production in porous rocks. *Earth and Planetary Science Letters* 269, 530–539.

Wünnemann, K., Zhu, M.-H., and Stöffler, D. (2015). Insights into crater formation, shock metamorphism and ejecta distribution from laboratory experiments and modeling. *Bridging the Gap III, #1067 (abstr.),* Freiburg.

Wünnemann, K., Zhu, M.-H., and Stöffler, D. (2016). Impacts into quartz sand: crater formation, shock metamorphism, and ejecta distribution in laboratory experiments and numerical models. *Meteoritics & Planetary Science* 51, 1762–1794.

Wyllie, P. J., Cox, K. G., and Biggar, G. M. (1962). The habit of apatite in synthetic systems and igneous rocks. *Journal of Petrology* 3, 238–243.

Yang, J., Goldstein, J. I., and Scott, E. R. D. (2010). Main-group pallasites: thermal history, relationship to IIIAB irons, and origin. *Geochimica et Cosmochimica Acta* 74, 4471–4492.

Young, R. W., Duffy, J. A., Hassall, G. J., and Xu, Z. (1992). Use of optical basicity concept for determining phosphorus and sulphur slag–metal partitions. *Ironmaking Steelmaking* 19, 201–219.

Zel'dovich, Y. B. and Raizer, Y. P. (1967). *The physics of shock waves and high-temperature hydrodynamic phenomena.* New York: Academic Press.

Zolensky, M. E. (1997). Structural water in the Bench Crater chondrite returned from the Moon. *Meteoritics & Planetary Science* 32, 15–18.

Zolensky, M. E. and Koeberl, C. (1991). Why are blue zhamanshinites blue? Lqiuid immiscibility in an impact melt. *Geochimica et Cosmochimica Acta* 55, 1483–1486.

Zook, H. A. (1975). The state of meteoritic material on the Moon. *Proceedings, 6th Lunar Science Conference,* 1653–1672.

Part V

Appendices

Appendix A

Supplementary information, Chapter 5

Standards for XRF analysis Calibration curves for XRF data are based on analysis of the following 40 certified international rock standards: CERAM 2CAS11, CCRMP MRG-1, CCRMP SY-3, HUN BAH, IGEM MK-1 (VS 2125-81), IGEM MO-2 (VS 2116-81), IGEM MO-3 (VS 2117-81), IGEM MO-5 (VS 2119-81), IGEM MO-6 (VS 2120-81), IGEM MO-7 (VS 1046-94), IGEM MO-13 (VS 1044-94), IGEM MO-15 (VS 1017-94), IGEM MW-1 (VS 2121-81), IGEM MW-2 (VS 2122-81), IGEM MW-3 (VS 2123-81), IGI BIL-1 (VS 7126-95), IGI BIL-2 (VS 7176-95), MINTEK NIM-D (SARM 6), MINTEK NIM-G (SARM 1), MINTEK NIM-L (SARM 3), MINTEK NIM-N (SARM 4), MINTEK NIM-P (SARM 5), MINTEK NIM-S (SARM 2), MINTEK SARMMINTEK SARM 39 (X-39), MINTEK SARM 40 (X-40), MINTEK SARM 41 (X-41), MINTEK SARM 44 (X-44), MINTEK SARM 45 (X-45), MINTEK SARM 46 (X-46), MINTEK SARM 50 (X-50), RIAP OOPE401 (VS 5370-90), RIAP OOPE501 (VS 5372-90), UNS SPS, ZGI BM, ZGI FK, ZGI GM, ZGI GNA, ZGI SW, ZGI TB, ZGI TB2, and ZGI TS. For petrographic descriptions and analytical data, see Govindaraju (1994). Furthermore, ten reference standards, that is, SIEM-01 to SIEM-10 by SIEMENS AG, Karlsruhe, Germany, were used in addition to the rock standards.

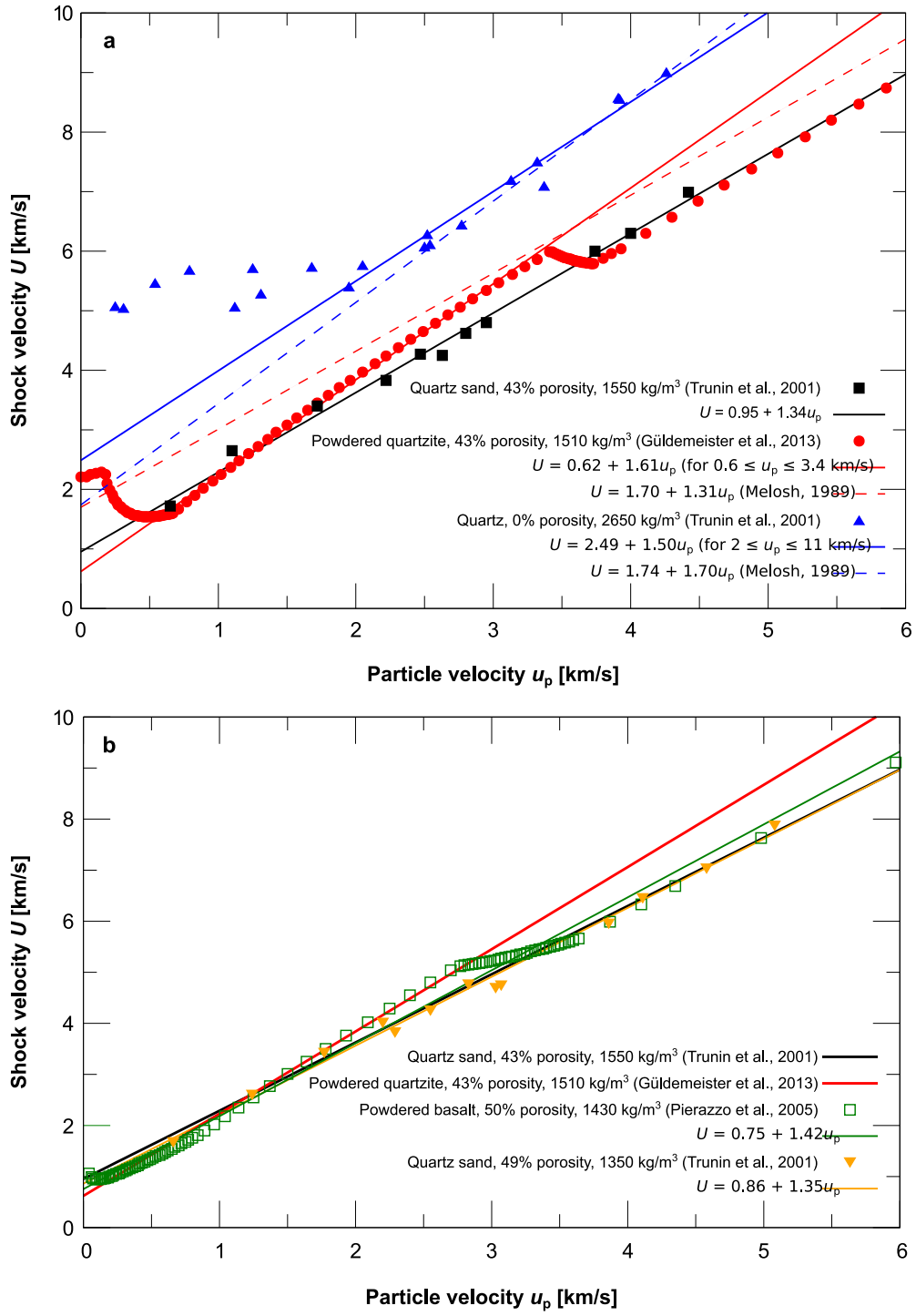

Figure A.1 a Linear relation between shock velocity U and particle velocity u_p for quartz sand (black; porosity 43%, density 1550 kg m^{-3}; Hugoniot data from Trunin et al., 2001), powdered quartzite (red; porosity 43%, density 1510 kg m^{-3}; Hugoniot data from Güldemeister et al., 2013), and quartz (blue; porosity 0%, density 2650 kg m^{-3}; Hugoniot data from Trunin et al., 2001). These different parameter sets were used to obtain a measure of uncertainty for the shock pressure estimates calculated from the planar impact approximation (cf. Table 5.1): for the Trunin et al. (2001) data set for quartz sand, C = 0.95 km s^{-1} and S = 1.34, and for the Güldemeister et al. (2013) data set for powdered quartzite, C = 0.62 km s^{-1}, S = 1.61. In comparison, Melosh (1989) quoted C = 1.70 km s^{-1} and S = 1.31 for dry sand. **b** In order to estimate the difference in shock pressure between our experiments and that of Daly and Schultz (2016), we used Hugoniot data for powdered basalt (shown in green, porosity 50%, density 1430 kg m^{-3}, Hugoniot data from Pierazzo et al., 2005) and quartz sand (shown in orange, porosity 49%, density 1350 kg m^{-3}, Hugoniot data from Trunin et al., 2001) as a proxy for the powdered pumice target (porosity ~43%, density 1300 kg m^{-3}) used by Daly and Schultz (2016). The Hugoniot curves for powdered basalt and quartz sand are close to that of quartz sand with 43% porosity and 1550 kg m^{-3} density.

Table A.1 Detection limits and measurement error of XRF major element analysis.

	Detection limit (wt.%)	Measurement error (wt.%)
SiO_2	1.0	0.5
TiO_2	0.01	0.01
Al_2O_3	0.5	0.1
Fe_2O_3[a]	0.05	0.05
MnO	0.01	0.01
MgO	0.01	0.05
CaO	0.01	0.05
Na_2O	0.01	0.05
K_2O	0.01	0.05
P_2O_5	0.01	0.01
Cu	27	27
Sr	17	17
LOI	0.1	0.1

[b] Total Fe reported as Fe_2O_3.

Table A.2 Analytical conditions for EMPA of the bulk aluminum projectile.

				Counting time (s)		Detection limit
Element	Standard	Spectral line	Spectrometer	Peak	Background	(ppm)
Si	Si metal	Kα	PETH	20	10	34
Al	Al metal	Kα	TAP	20	10	39
Fe	Fe metal	Kα	LIFH	20	10	111
Mn	Mn metal	Kα	PETJ	20	10	119
Mg	Mg metal	Kα	TAP	20	10	43
Cu	Cu metal	Kα	LIF	20	10	269

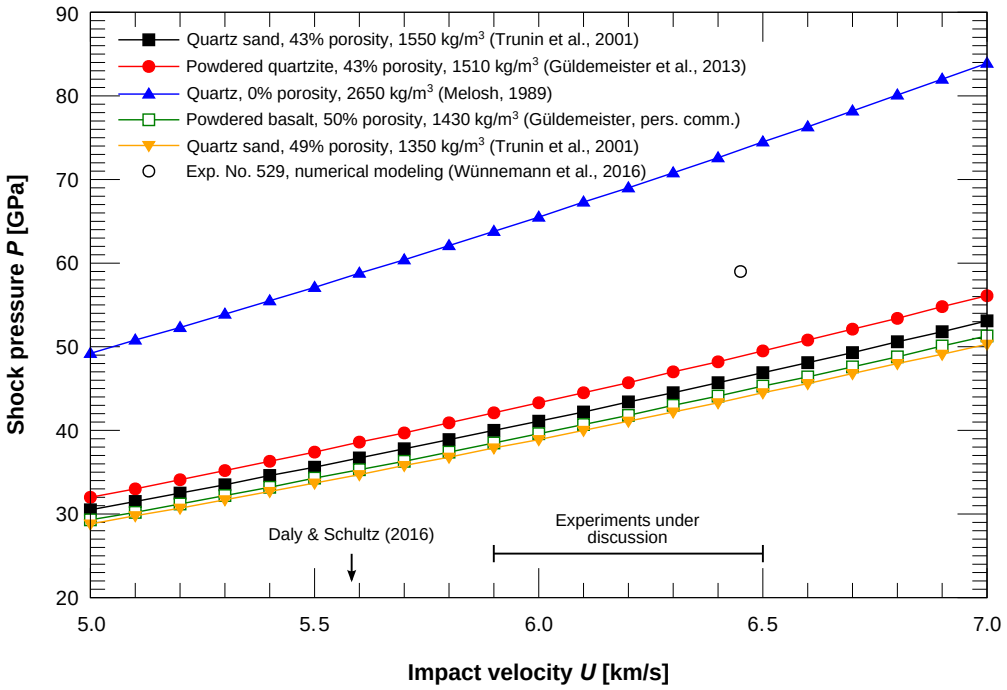

Figure A.2 Estimated peak shock pressure as a function of impact velocity for impacts of aluminum impactors (density 2750 kg m^{-3}, mass 0.38 g) on quartz sand (porosity 43%, density 1550 kg m^{-3}; black) and powdered quartzite (porosity 43%, density 1510 kg m^{-3}; red). For the impact velocities under discussion (5.9–6.5 km s^{-1}), shock pressures between 41 ± 3 and 48 ± 3 GPa were reached. The Hugoniot curve for non-porous quartz (porosity 0%, density 2650 kg m^{-3}; blue) places an upper limit for peak shock pressures at different impact velocities: ~64 GPa at 5.9 km s^{-1} and ~75 GPa at 6.5 km s^{-1}. However, for a porous target, shock pressure at the projectile–target interface is influenced by localized pore crushing, which amplifies shock pressure and temperature. Using Hugoniot data for powdered basalt and quartz sand as a proxy (cf. Fig. A.1), we find that the shock pressure in the impact experiment of Daly and Schultz (2016), using powdered pumice as target (porosity ~43%, density 1300 kg m^{-3}), was slightly lower compared to the experiments under discussion here, that is, ~35 GPa at ~5.6 km s^{-1}.

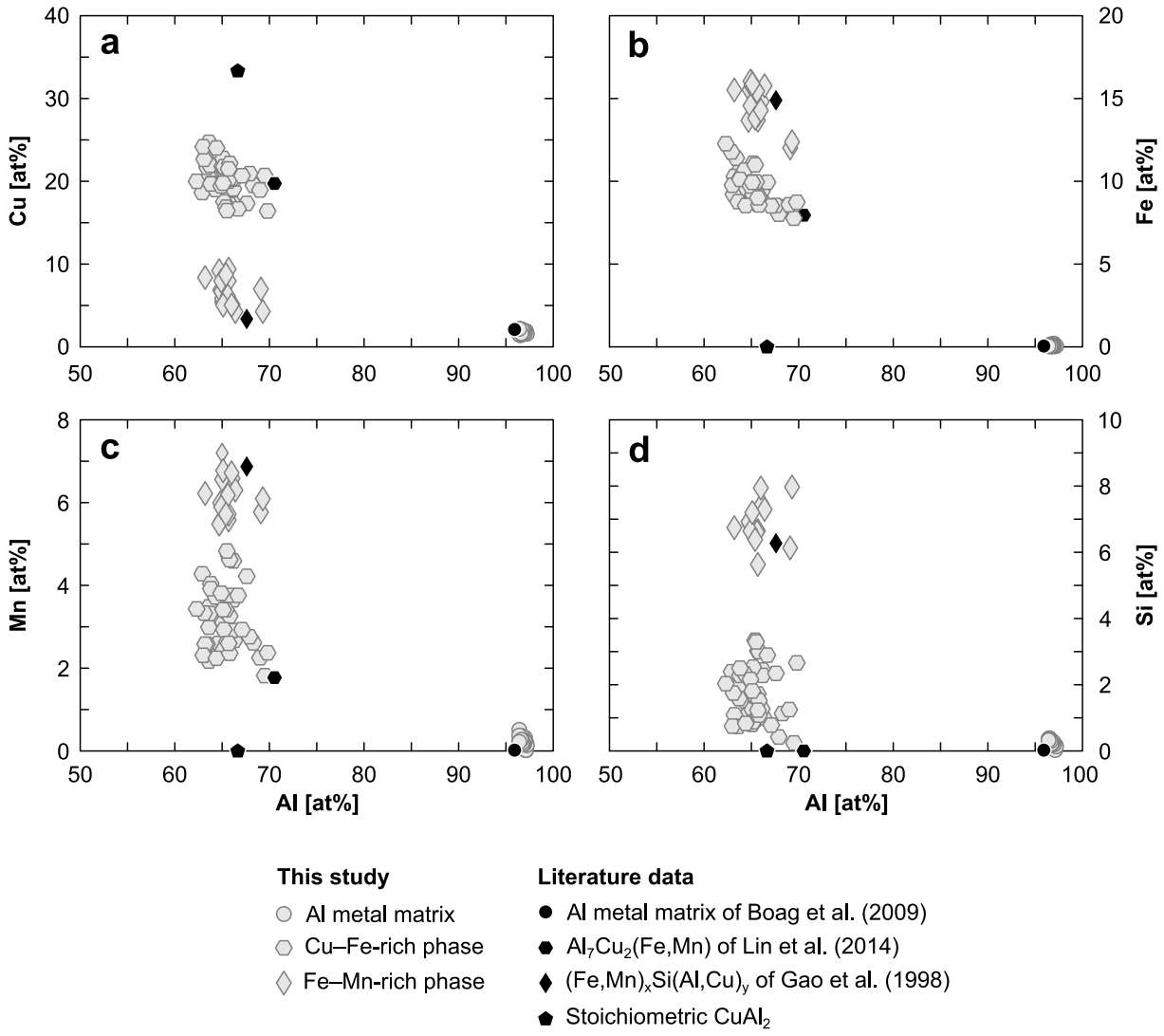

Figure A.3 Chemical composition of Al metal matrix and intermetallic phases of the unshocked aluminum projectile (open symbols) in comparison to literature data (filled symbols) of phases typically encountered in commercial aluminum alloys of the AA2xxx series. **a** Al vs. Cu, **b** Al vs. Fe, **c** Al vs. Mn, and **d** Al vs. Si (all data are reported in at.%). Note that most of the data obtained from the Cu–Fe-rich phase fall onto a theoretical mixing line between Al metal matrix and the most Al-poor (~65 at.% Al) composition, indicating mixed analyses.

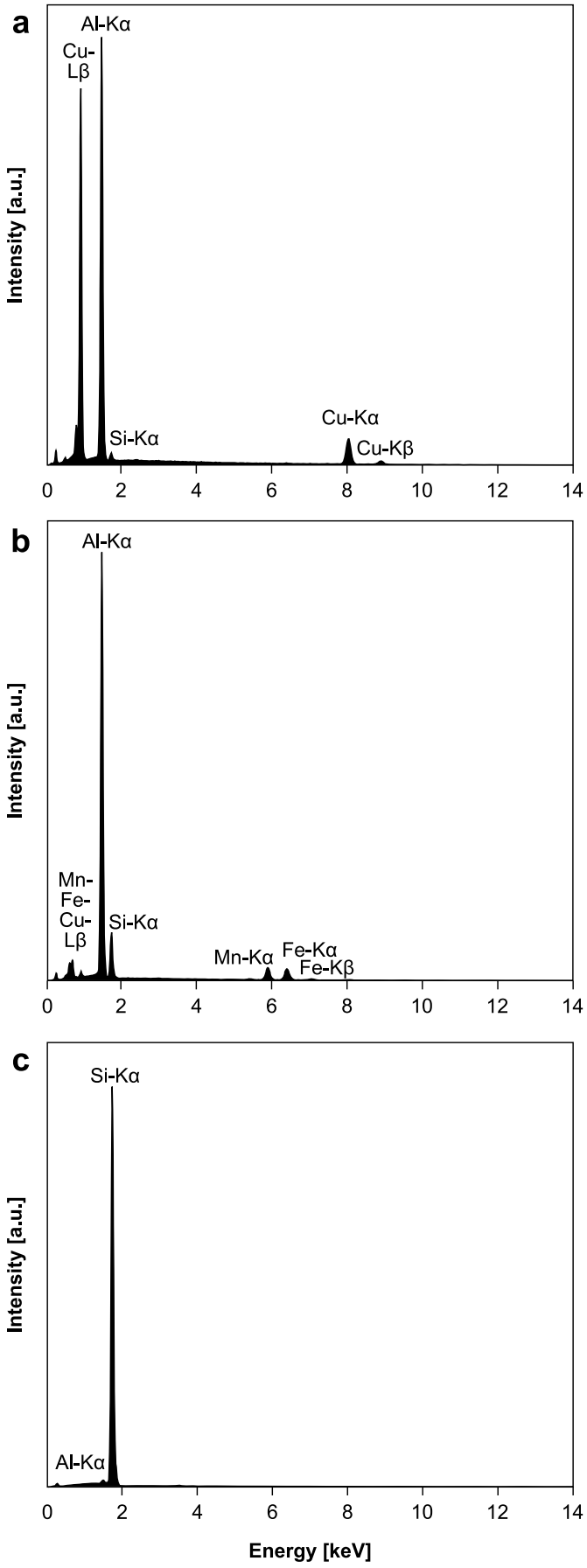

Figure A.4 Typical EDX spectra of **a** khatyrkite ($CuAl_2$), **b** the Fe–Mn-rich phase [$(Fe,Mn)_xSi(Al,Cu)_y$], and **c** silicon encountered in the impact melt particles. The faint peak at ~0.28 keV is C-Kα caused by carbon-coating. Spectra were obtained from experiment 534 (cf. Table A.1).

Appendix B

Supplementary information, Chapter 7

This chapter includes an overview of the experimental setup (Fig. B.1), a detailed description of the target materials used in this study (Texts B.1–B.3; Table B.1), additional images of the experimental setup (Figs. B.2–B.3), details on the temperature measurements (Text B.4) and the approach used to model the cooling of the generated melts (Text B.5), details on the melting and boiling points of the materials used in the experiments (Table B.2), a graphic representation of the heat capacity data used to calculate the changes in entropy during laser melting (Figs. B.4–B.6), and the results of impedance matching calculations for planar impacts of iron projectiles onto non-porous quartz (Fig. B.7).

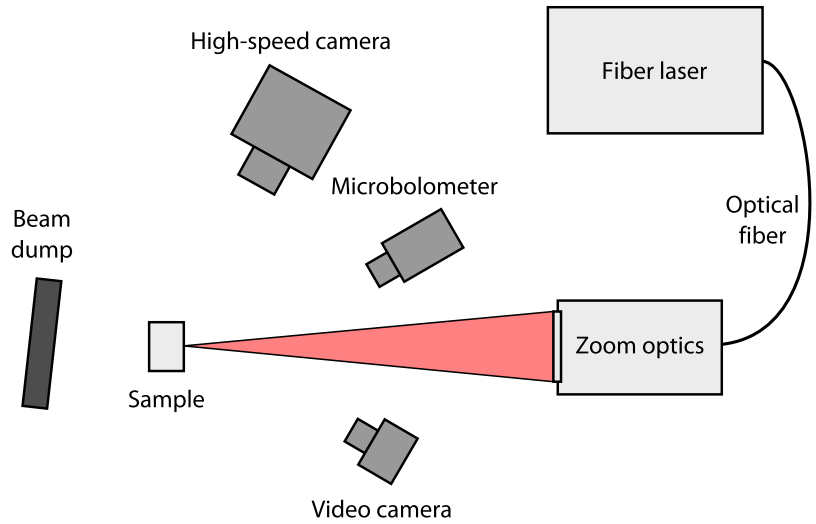

Figure B.1 Experimental setup (not to scale) used in this study. The light of a CW fiber laser is coupled into an optical fiber and subsequently focused onto the sample by a high-power zoom optics. The laser–matter interaction zone is observed with a video camera. An uncooled infrared microbolometer camera is used to measure the temperature distribution on the front surface of the target. In addition, a high-speed camera is used to record the expansion of the laser-generated plasma and the melting process.

Table B.1 Bulk chemical composition of the sandstone and the basalt used in this study.

	Seeberger sandstone[a,b]	Hoffelder basalt[a]
SiO_2	94.77(90)	43.50(30)
TiO_2	0.36(4)	2.36(1)
Al_2O_3	3.11(10)	14.78(38)
Cr_2O_3	0.01(1)	0.04(1)
Fe_2O_3	0.45(9)	12.38(28)
MnO	bdl	0.18(1)
MgO	0.12(2)	10.65(45)
CaO	0.05(1)	9.78(5)
Na_2O	0.15(5)	3.69(4)
K_2O	0.23(1)	1.53(2)
P_2O_5	0.03(1)	0.49(1)
LOI	1.29(30)	0.76(12)
Total	100.57	100.11

[a] Data determined by ICP-AES.
[b] Data from Ebert et al. (2013).
All data are given in wt.% and reported with 2σ in parentheses; Fe is reported as Fe_2O_3.
bdl = below detection limit; LOI = loss on ignition.

B.1 Seeberger sandstone

Sandstone, so-called Seeberger sandstone, was used in previous MEMIN impact (e.g., Poelchau et al., 2013; Ebert et al., 2013) and shock recovery experiments (Kowitz et al., 2013a). In this study, we used the material in experiment 887 to simulate impact melting of sandstone impacted by an iron meteorite. Briefly, the material is a well-sorted, porous, quartz-dominated sandstone with an average grain size of 100 ± 25 µm and a porosity of 23.1 ± 0.5 vol.%. It consists of ~89 vol.% quartz, ~10 vol.% phyllosilicates (kaolinite along with muscovite and illite), and ~1 vol.% accessory minerals (rutile, altered ilmenite, zircon, and rare iron oxides/hydroxides). The bulk composition of the sandstone is given in Table B.1.

B.2 Campo del Cielo

The Campo del Cielo iron meteorite was also used in previous MEMIN impact experiments (Ebert et al., 2013); here, we us it in experiment 887 to simulate impact melting of iron meteorite and sandstone. A detailed petrologic description can be found elsewhere (Ebert et al., 2013, and references therein). Briefly, Campo del Cielo is a IAB coarse oxahedrite (Og) with a Widmannstätten bandwidth of 3.0 ± 0.6 mm. It has a homogeneous kamacite matrix and shows minor amounts of taenite, plessite, schreibersite, and rhabdite, which are irregularly distributed, as well as some rare silicate inclusions. The bulk composition of the meteorite is 92.9 wt.% Fe, 6.3 wt.% Ni, and 0.5 wt.% Co (Ebert et al., 2013).

B.3 Hoffelder basalt

Basalt, so-called Hoffelder basalt, was used in laser melting experiment 892 to simulate impact melting of a chondritic target. The material is a dense, aphanitic, holocrystalline, porphyritic, ultramafic rock with olivine phenocrysts in a fine-grained matrix of plagioclase, pyroxene, ilmenite, feldspathoids, and Fe,Ti oxides. The olivine phenocrysts show sizes between 200 and ~800 µm, whereas the matrix shows grain sizes ≤100 µm. The bulk composition of the basalt is given in Table B.1.

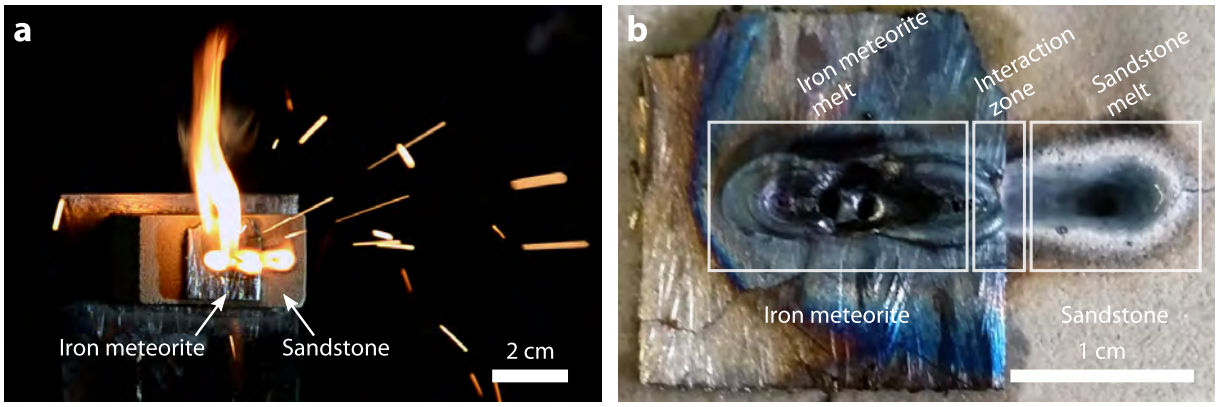

Figure B.2 Experimental setup (**a**) and irradiation products (**b**) of experiment 887. The composite setup of this experiment allows for constraining the melting behavior of the two materials, as well as their interaction during melting and cooling.

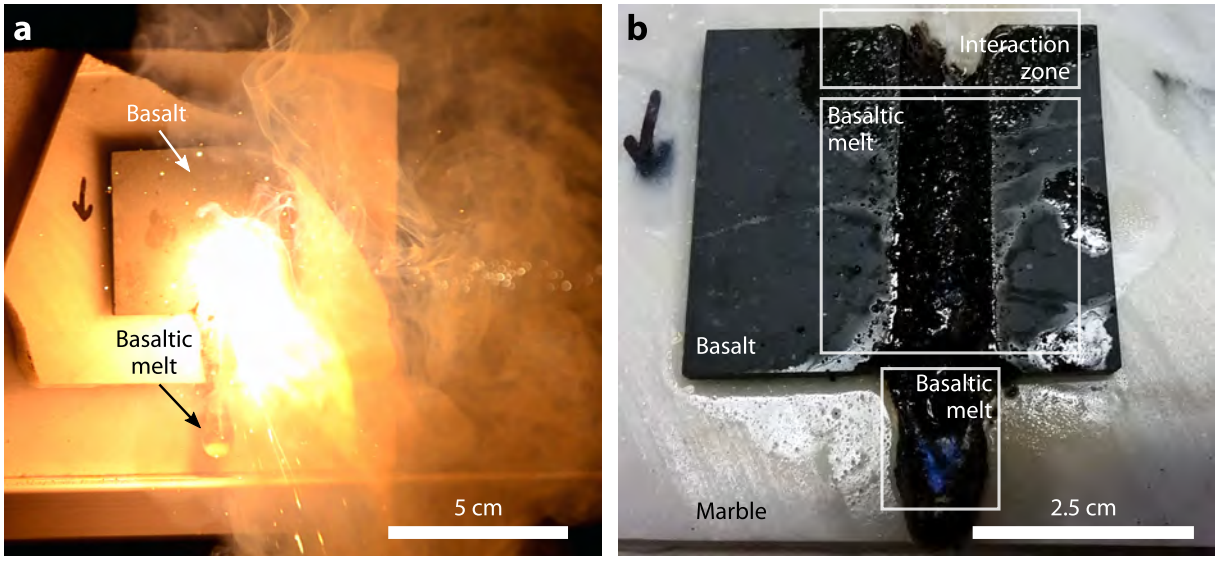

Figure B.3 Experimental setup (**a**) and irradiation products (**b**) of experiment 892. Although two separate materials were used in this experiment, we focus on the melting behavior of the basalt. The response of the marble target to laser irradiation will be detailed in a separate publication (see Chapter 10).

B.4 Temperature measurements

The infrared microbolometer was calibrated prior to the experiments following ISO 9001:2008. Specifically, calibration of the microbolometer was done by measuring the radiance of a certain number of blackbody emitters at known temperatures, emissivities, and distances. The digital counts on the thermal detector are then transformed into radiance values and then converted into temperatures based on the emissivity ε of the object. Using these data, the calibration software generates a calibration curve that relates radiance values to temperatures over a certain range. Additionally, calibration involved ambient temperature compensation, that is, contributions from the materials surrounding and temperature changes of the laboratory equipment are taken into account.

The temperature measured by the bolometer camera depends on the emissivity of the target material. In general, the emissivity of a material varies with temperature and surface finish. During the irradiation process, the sample surface is modified (molten, vaporized), which also affects the emissivity of the material. This *emissivity shift* is a common problem in thermography experiments and leads to a measuring inaccuracy. In addition, the irradiated planetary materials have complex spectral characteristics since they are composed of a variety of individual phases (e.g., the basalt). Therefore, a distinct and immediate correlation of emissivity and absolute temperature values is unfeasible and defective. However, apart from the measuring uncertainty of the *absolute temperature*, the method nonetheless allows to estimate *temperature gradients* and *cooling rates*. For the iron meteorite, we assumed a conservative emissivity of $\varepsilon = 0.95$, which is close to $\varepsilon = 0.94$ commonly used for dull wrought iron. For the silicates, we assumed that ε varies between ~0.6 and ~0.95, which translates to a measurement inaccuracy of the absolute temperature of about 100 K (cf. Fig. 7.2).

B.5 Thermal modeling

We modeled the thermal evolution of the laser-generated melts following the approach of Bouley et al. (2012). To this end, we first estimated the dimensions of the melt volumes from which the cooling profiles shown in Fig. 7.2e, f were obtained using the high-speed framing camera and infrared camera videos (Fig. 7.2a, b) and the recovered samples (Fig. B.2b and B.3b). For the sandstone melt zone shown in Fig. B.2, we estimate that the volume of the melt from which the cooling profile was obtained corresponds to a droplet with a diameter of ~1–2 mm. For the basaltic melt droplet shown in Fig. 7.2b, we estimate a diameter of ~6–8 mm.

The thermal evolution of a given melt volume can be modeled by solving the equation of heat transport by conduction in the melt with the radiative condition at the melt's surface (see Bouley et al., 2012). For melt droplets with small diameters (millimeters to centimeters), heat transport by conduction is small with respect to heat transport by thermal radia-

tion. Moreover, the temperature distribution within the droplet can be regarded as uniform. In case of small melt droplets such as those depicted in Fig. 7.2, cooling of the melt may be approximated by an equation in the form of:

$$\frac{4}{3}\pi r^3 \rho c_p \frac{\mathrm{d}T}{\mathrm{d}t} = -4\pi r^2 \sigma T^4 \tag{B.1}$$

(Bouley et al., 2012), where r is the droplet radius, ρ is the density, c_p is the heat capacity, T is the temperature, t is the time, and σ is the Stefan–Boltzmann constant (not to be confused with the Boltzmann constant, k_B). Following Bouley et al. (2012), this equation has the analytical solution

$$T(t) = \frac{T_0}{\left(1 + \frac{t}{\tau}\right)^{\frac{1}{3}}} \tag{B.2}$$

where T_0 is the initial temperature at $t = 0$ and τ is a characteristic time depending on the initial temperature and the radius of the droplet:

$$\tau = \frac{\rho r c_p}{9\sigma T_0^3} \tag{B.3}$$

For the sandstone melt, we assume a constant heat capacity of 1298 J kg^{-1} K^{-1}, a density of 2400 kg m^{-3}, and an initial temperature of 2373 K. For the basalt melt, we assume a constant heat capacity of 1522 J kg^{-1} K^{-1}, a density of 2850 kg m^{-3}, and an initial temperature of 2373 K.

The thermal evolution of the sandstone and basalt melt, respectively, was then modeled as a function of t. In both cases, r was varied between 1 mm and 5 cm in order to estimate the influence of melt volume on the cooling rate. The modeled cooling profiles (Fig. 7.2e, f) agree well with the measured cooling profiles. In case of the sandstone melt, the data agree well with the modeled profiles for $r = 1$ mm and $r = 2$ mm and in case of the basalt melt, the data agree well with the modeled profiles for $r = 5$ mm and $r = 1$ cm. Moreover, the shapes of the modeled profiles agree with the shapes of the measured profiles, indicating that the assumptions made above are essentially correct. However, for temperatures <1000 K, the modeled profiles deviate from the measured data. This discrepancy is due to the fact that heat capacity is held constant in the model (representing the high-temperature melts, but not the solid phases that exist at lower temperatures), whereas it varies with temperature in reality (see Figs. B.4 and B.6).

The modeled profiles may be used to constrain cooling rates of impact melts of variable composition (reflected mainly by density and heat capacity) and volume. A major outcome of these simple models is that the thermal evolution of small volumes of impact melt (e.g., ballistic ejecta) is mainly a function of melt volume; melt composition seems to play only a minor effect.

Table B.2 Inferred 1 bar melting and boiling temperatures of the target materials.

Material	Melting temperature at 1 bar pressure [K]	Boiling temperature at 1 bar pressure [K]	Enthalpy of melting at 1 bar pressure [kJ kg^{-1}]
Quartz[a,c,e]	1996	3157	236.918
Iron[b]	1811	3130	247.283
Basalt[a,d]	1430	3800	400.800
Diopside[a,b]	1668	3800	137.700
Anorthite[a,b]	1830	3800	133.000
Forsterite[a,b,c]	2163	3350	142.000

[a] Ahrens and O'Keefe (1972).
[b] Desai (1986) and Robie et al. (1995).
[c] NIST–JANAF thermochemical tables (Chase, 1998).
[d] Bouhifd et al. (2007).
[e] For cristobalite.

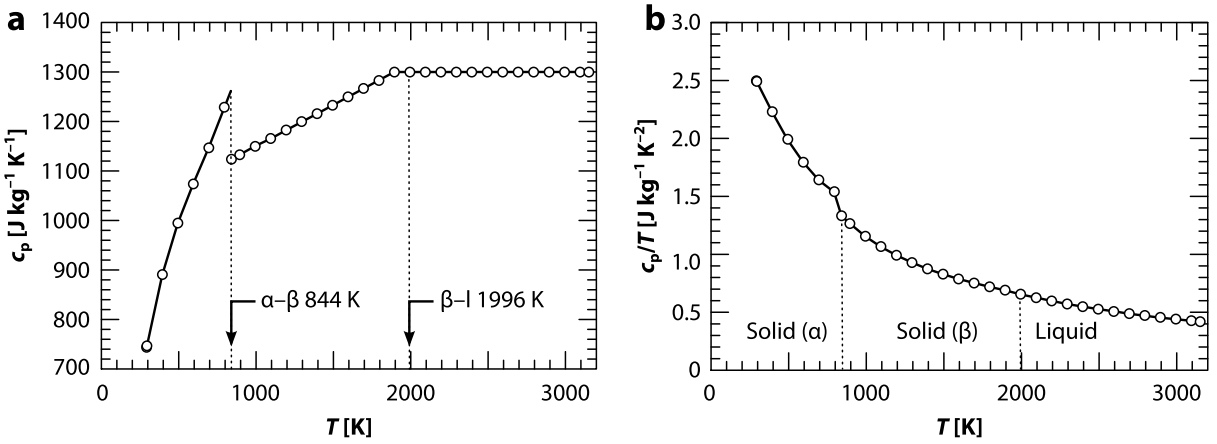

Figure B.4 Isobaric specific heat capacity of quartz (**a**) and plot of c_p/T versus T (**b**). Data taken from Chase (1998), covering a temperature range from 298 to 3157 K.

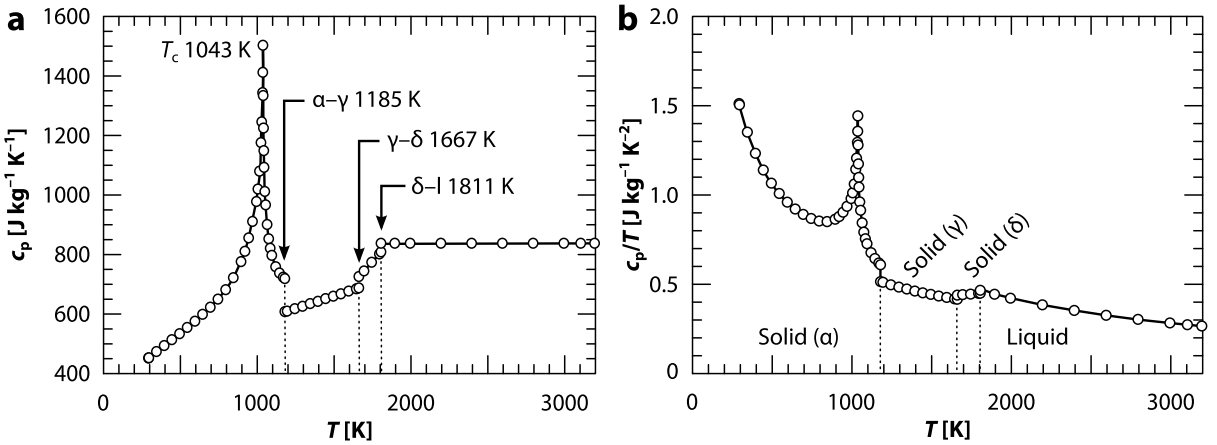

Figure B.5 Isobaric specific heat capacity of iron (**a**) and plot of c_p/T versus T (**b**). Data taken from Desai (1986), covering a temperature range from 298 to 3200 K.

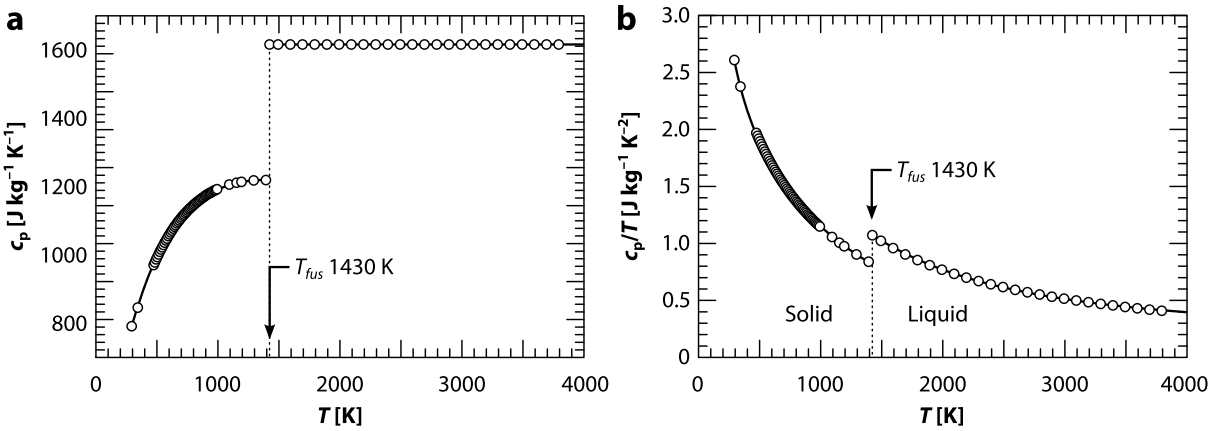

Figure B.6 Isobaric specific heat capacity of basalt (**a**) and plot of c_p/T versus T (**b**). Data calculated following the methods outlined by Bouhifd et al. (2007). For $T > 1700$ K, we assume that c_p remains constant up to the vaporization temperature.

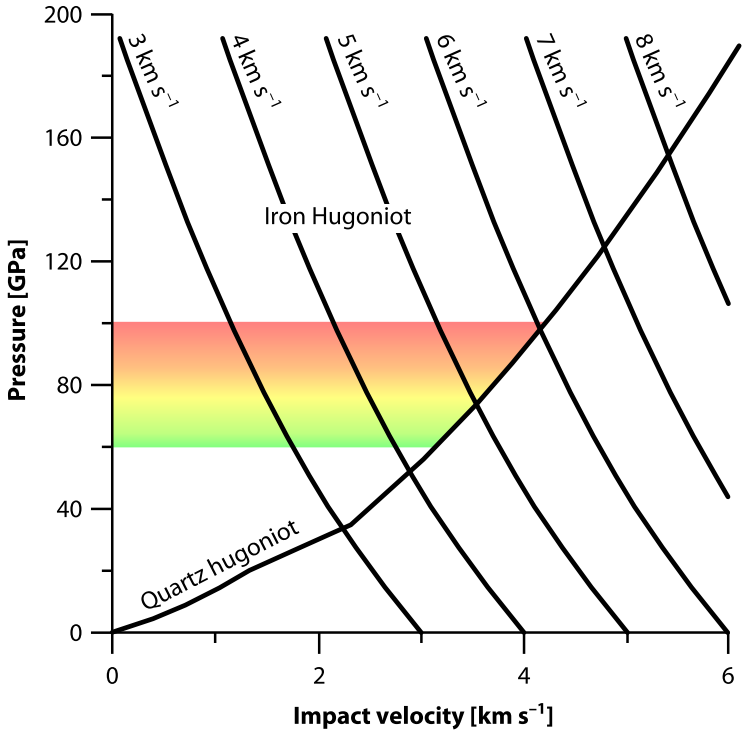

Figure B.7 Estimation of peak shock pressures for iron projectiles impacting a non-porous quartz target at impact velocities between 3 and 8 km s^{-1} using the planar impact approximation (cf. Melosh, 1989). The colored part corresponds to the entropy range covered by the laser-generate sandstone melt (cf. Figs 7.2c and 7.3a), representing "effective" shock pressures of ~60–100 GPa.

Appendix C

Supplementary information, Chapter 9

Table C.1 Measurement conditions for EMPA of bulk glasses at 15 kV and 15 nA.

				Counting time [s]		Detection limit†
Element	Standard	X-ray	Crystal	Peak	Background	[ppm]
Si	Cr-augite	Kα	TAP	20	10	104(1)
Ti	Rutile	Kα	PETJ	20	10	162(1)
Al	Cr-augite	Kα	TAP	20	10	101(1)
Cr	Cr-augite	Kα	LIFH	20	10	186(3)
Fe	Cr-augite	Kα	LIFH	20	10	199(1)
Mn	Bustamite	Kα	PETJ	20	10	210(1)
Mg	Cr-augite	Kα	TAP	20	10	78(1)
Ca	Cr-augite	Kα	PETH	20	10	58(1)
Na	Albite	Kα	TAP	10	5	182(7)
K	Sanidine	Kα	PETH	10	5	71(1)
P	Apatite	Kα	TAP	20	10	123(1)
Ni	Ni metal	Kα	LIFH	20	10	198(2)
Cl	Tugtupite	Kα	PETH	20	10	48(1)

† Given as average ± standard error.

Appendix D

Supplementary information, Chapter 10

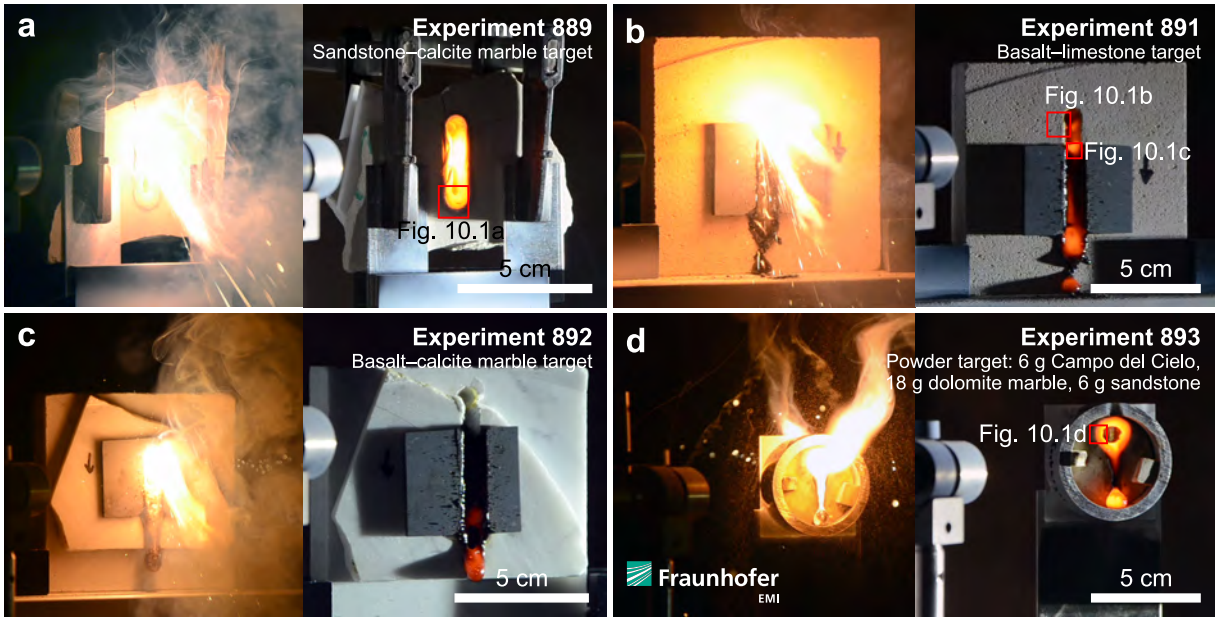

Figure D.1 Representative video snapshots of the laser experiments during (left panels) and immediately after laser irradiation (right panels). **a** Experiment 889 involved irradiation of an alternating sequence of sandstone and calcite marble plates. **b** Experiment 891 involved irradiation of a basalt plate on top of a limestone plate. **c** Experiment 892 involved irradiation of a basalt plate on top of a calcite marble plate. **d** Experiment 893 involved irradiation of a powder mixture prepared from 6 g Campo del Cielo iron meteorite, 18 g dolomite marble, and 6 g sandstone.

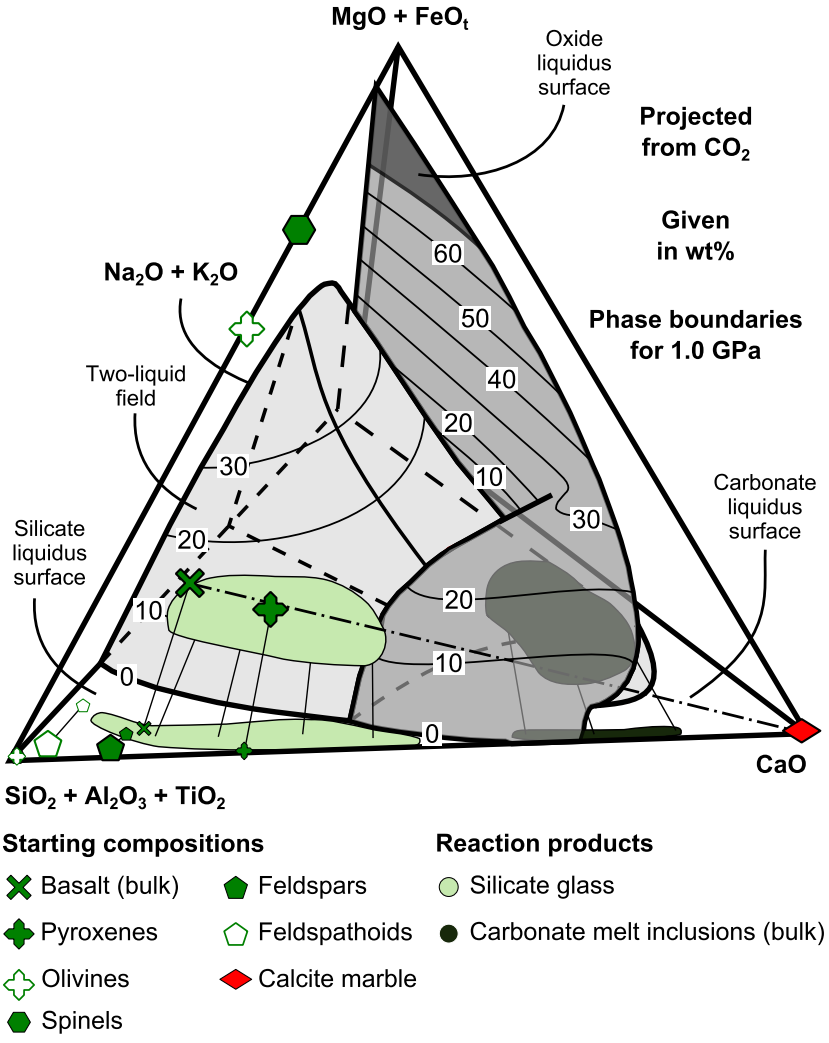

Figure D.2 Partly schematic phase relationships in the tetrahedron CaO–(MgO + FeO)–(Na_2O + K_2O)–(SiO_2–Al_2O_3–TiO_2) at 1.0 GPa and projected from CO_2, showing the three major liquidus volumes for the silicate liquidus field, the carbonate liquidus field, and the miscibility gap, as well as the liquidus surfaces between them. Diagram redrawn after Lee and Wyllie (1998). The measured data are also projected onto the basal plane for comparison with Fig. 10.15b. The contours and values are drawn in steps of 10 wt.% of (MgO + FeO_t).

Table D.1 Average major-element compositions of individual minerals in the starting materials.

	Carrara marble, Savonnières limestone, and dolomite marble		Seeberger sandstone				Hoffelder basalt			
	Calcite	Dolomite	Muscovite[b]	Kaolinite[b]	Illite (low K_2O)[b]	Illite (high K_2O)[b]	Olivine	Pyroxene	Plagioclase	Ulvöspinel
n	167	34	22	15	14	15	137	96	93	12
SiO_2	n.a.	n.a.	47.2(12)	47.9(15)	54.3(9)	46.8(13)	39.1(7)	46.7(38)	52.2(12)	0.5
TiO_2	n.a.	n.a.	0.98(58)	0.01(1)	0.18(14)	0.81(39)	0.04(3)	2.77(135)	0.19(3)	21.5
Al_2O_3	n.a.	n.a.	30.37(298)	36.94(154)	21.56(148)	31.23(200)	0.10(8)	7.04(347)	31.16(81)	3.8
FeO_t	0.01	0.04	4.01(236)	0.36(24)	7.92(117)	3.38(115)	19.2(31)	7.37(54)	0.84(11)	70.6
MnO	0.01	0.01	n.a.	n.a.	n.a.	n.a.	0.39(14)	0.13(4)	0.01(1)	0.4
MgO	0.80(8)	22.5	2.97(60)	0.51(14)	2.55(20)	1.56(54)	41.4(30)	12.7(147)	0.09(3)	3.3
CaO	55.3(2)	30.9	bdl	0.13(7)	0.41(10)	0.07(3)	0.34(14)	22.04(36)	12.51(95)	0.2
NiO	n.a.	n.a.	n.a.	n.a.	n.a.	n.a.	bdl	bdl	bdl	bdl
Na_2O	n.a.	n.a.	0.56(17)	0.03(4)	0.07(2)	0.56(29)	0.04(4)	0.54(11)	4.09(50)	bdl
K_2O	n.a.	n.a.	9.74(83)	0.37(50)	5.44(39)	8.63(120)	0.01(1)	0.03(1)	0.31(6)	bdl
Total	56.1	53.5	95.8	86.3	92.4	93.0	100.6	99.3	101.4	100.3
H2O*	—	—	4.74	13.96	6.76	6.87	—	—	—	—
CO_2*	43.8	46.6	—	—	—	—	—	—	—	—

Data are given in wt.% and reported with 2σ in parentheses; total iron (FeO_t) is reported as FeO + Fe_2O_3.
n = number of analyses; bdl = below detection limit; n.a. = not analyzed.
[a] Ebert et al. (2013);
[b] Ebert et al. (in press).
* Calculated by difference from 100 wt.%.

Eigenständigkeitserklärung

Hiermit versichere ich, dass ich die vorliegende Arbeit selbstständig verfasst und keine anderen als die angegebenen Hilfsmittel benutzt habe. Die Stellen der Arbeit, die anderen Werken wörtlich oder inhaltlich entnommen sind, wurden durch entsprechende Angaben der Quellen kenntlich gemacht.

Diese Arbeit hat in gleicher oder ähnlicher Form noch keiner anderen Prüfungsbehörde vorgelegen.

Christopher Hamann
Berlin, den 5. November 2017

Curriculum vitae

Due to the protection of privacy, the CV has been removed from the online version of this thesis. (The CV is included on the following pages in the print version.)